

A.O. Weissenberg

MUONS



MUONS

A. O. WEISSENBERG

Translated by

S. CHOMET
Kings College London

English translation edited by

J. S. IMRIE
University College London



1967

NORTH-HOLLAND PUBLISHING COMPANY - AMSTERDAM

© North-Holland Publishing Company – Amsterdam – 1967

No part of this book may be reproduced in any form by print, photoprint, microfilm or any other means without written permission from the publisher

First published in 1964 by Nauka, Moscow, under the title Mu-Meson

Translated by Scripta Technica Limited, London

Library of Congress Catalogue Card Number 67-30881

Printed in The Netherlands

CONTENTS

Chapter 1	Properties of muons	1
1.1	Discovery of the muon	1
1.2	Masses of pions and muons	5
1.3	Muon decay scheme	8
1.4	Spin of the muon	12
1.5	Lifetime of the muon	13
1.6	Interaction of negative muons with nuclei	14
1.7	The universal Fermi interaction	22
1.8	Electron and muon neutrinos	25
Chapter 2	Pion decay	33
2.1	Non-conservation of parity in weak interactions	33
2.2	Elements of π - μ -e decay theory	46
2.3	Lifetime of the free muon	52
2.4	Energy spectrum of electrons from μ -e decay. Measurement of the Michel parameter	54
2.5	Measurements of asymmetry in the electron angular distribution	60
2.6	Energy dependence of asymmetry in the electron angular distribution	64
2.7	Helicity of the electron neutrino	69

2.8	The helicity of electrons from μ -e decay	72
2.9	Helicity of muons	75
2.10	Comparison of experimental data on weak-interaction constants in β and μ -e decay	83
2.11	Decay of the pion into an electron and a neutrino	87
2.12	Decay of the pion	94
2.13	Radiative corrections to π - μ -e decay	96
2.14	Searches for rare muon decay modes	107
Chapter 3 Negative-muon capture		121
3.1	Neutrons from nuclear μ^- capture	121
3.2	Emission of charged particles in nuclear μ^- capture	127
3.3	Nuclear γ rays from μ^- capture	133
3.4	Theoretical conclusions	134
3.5	μ^- capture in hydrogen	139
3.6	Transition of nuclei to definite states on μ^- capture	143
3.7	Measurements of the effective constant for the mixed transition ($\frac{1}{2}^+ \rightarrow \frac{1}{2}^+$) in μ^- capture	146
3.8	Determination of the effective constant for the Gamow-Teller transition in μ^- capture	147
3.9	Measurements of the total μ^- capture probability	152
3.10	The Z^4 law. Primakoff's formula	167
3.11	μ^- decay probability in a bound state	171
3.12	Isotopic effect in nuclear μ^- capture	177
3.13	Effect of the hyperfine structure of the mesonic atom on nuclear μ^- capture	179
3.14	Non-conservation of parity in nuclear μ^- capture	185
3.15	Radiative μ^- capture by nuclei	196
Chapter 4 Electromagnetic interactions of muons		198
4.1	Preliminary remarks	198
4.2	Muonic atoms	199
4.3	Production of μ^+ , μ^- pairs by photons	227
4.4	Scattering of muons by nuclei	233
4.5	The magnetic moment of the muon	245
4.6	Measurements of $g-2$	256
4.7	Dipole moment of the muon	262

Chapter 5	Mesomolecular phenomena	265
5.1	Catalytic effect of negative muons in fusion reactions involving hydrogen isotopes	265
5.2	Kinetics of negative-muon catalysis of the $p + d \rightarrow \text{He}^3 + \gamma$ reaction	273
5.3	Negative-muon capture by impurity nuclei in hydrogen	280
Chapter 6	Depolarization of muons. Muonium	283
6.1	Kinematic depolarization of muons	283
6.2	Depolarization of positive muons in matter	287
6.3	Search for the triplet state of muonium	298
6.4	Depolarization of negative muons	302
Chapter 7	Cosmic-ray muons	306
7.1	Origin of the muon component	306
7.2	Main cosmic-ray components	307
7.3	Muon energy spectrum at sea level	309
7.4	The energy spectrum of muons at large zenith angles	314
7.5	Energy spectrum of low-energy cosmic-ray muons	316
7.6	Positive excess in the muon component	320
7.7	Muon intensity at great depths	323
References		328

Chapter 1

PROPERTIES OF MUONS

1.1 DISCOVERY OF THE MUON

The muon was discovered by Anderson and Neddermeyer [1] and by Street and Stevenson [2] in 1936-1938, and was originally called the mesotron. In 1947, after the discovery of the pion and the phenomenon of $\pi - \mu$ decay, the mesotron was re-named the muon. This was intended to emphasize the fact that in contrast to the 'primary' pions, which are produced directly in nuclear interactions, muons are of a secondary origin and appear during the decay of pions.

The muon was the second 'elementary' particle discovered in cosmic radiation. The existence of the first particle - the positron - was established by Anderson in 1932.

The discovery of the muon was not as unexpected as the discovery of the positron. It was the result of two years' careful study whose aim was to resolve the various apparent paradoxes in the properties of cosmic rays. The experiments were carried out by Anderson and Neddermeyer with the same Wilson cloud chamber which was used in the discovery of the positron. They showed that a high proportion of cosmic-ray particles at sea level are highly penetrating. These particles were found to pass through thick layers of

heavy matter, e.g. lead, and lost their energy only through ionization. The aim of the experiments was to establish the nature of these penetrating, charged particles, which at that time were thought to be either electrons and positrons or protons.

Attempts to identify these particles as protons produced various difficulties. For example, there were too many high-energy electrons among the δ rays produced by these particles. This was in conflict with the expected electron spectrum due to protons but was in agreement with the δ -ray spectrum expected if the particles ejecting the electrons were much lighter than protons. Moreover, at sea level, the number of positively and negatively charged particles was approximately the same, which again precluded their identification as protons. At the same time, the particles could not be identified as positrons and electrons. It became evident as a result of the theoretical work of Bethe, Heitler and Sauter that high-energy electrons should lose a considerable proportion of their energy by bremsstrahlung. This conclusion was confirmed by qualitative observations of cosmic-ray electrons. The penetrating particles did not exhibit such energy losses but could still be electrons if electrons of energy greater than about 100 MeV did not lose energy by bremsstrahlung.

In order to verify this hypothesis, which was in fact the last attempt to explain the observed facts in terms of known particles, Anderson and Neddermeyer placed a platinum plate in the Wilson chamber. They found that particles of a given energy passing through the plate could be divided into two groups: strongly absorbed particles (electrons) and highly penetrating particles. This result finally excluded explanations of existing data in terms of known particles. It was necessary to postulate the existence of positive and negative singly charged particles with a mass intermediate between the masses of the proton and the electron. Street and Stevenson arrived at similar conclusions.

During the decade that followed, muons were identified with the heavy mesons of the Yukawa theory which were thought to be responsible for nuclear forces. The main difficulty with this hypothesis was quite clear even then: fast muons arriving in the form of cosmic rays must have traversed the entire earth's atmosphere without appreciable absorption, whilst the Yukawa mesons were expected to interact strongly with nuclei and should be rapidly absorbed

in the atmosphere. This contradiction became even more acute after the work of Conversi, Pancini and Piccioni [38], who showed that cosmic-ray muons had an exceedingly weak interaction with nuclei. This was followed by the discovery of pions by Lattes, Muirhead, Occhialini and Powell in 1947 [4, 5]. It became clear that cosmic-ray muons were of secondary origin and were formed as a result of the decay of pions in the atmosphere.

Fig. 1.1 shows a typical $\pi - \mu - e$ decay recorded in a nuclear emulsion: the muon is produced after the pion comes to rest and then decays with the emission of an electron. Fig. 1.2 shows a photograph of three $\pi - \mu - e$ decays in a propane bubble chamber. By measuring the ranges of muons from the $\pi - \mu$ decays, it was found that they formed a group of monochromatic particles. This can be seen from Fig. 1.3 which shows the range distribution in nuclear emulsion for 500 muons from $\pi - \mu$ decays as reported by Menon [6]. The mean range is 596 ± 1 microns and the observed spread in the range can be explained by fluctuations in ionization losses.

The appearance of monochromatic muons from $\pi - \mu$ decays shows that the pion decays into two particles, one of which is neutral. If the latter is assumed to be the neutrino, the decay scheme for the pion becomes

$$\pi^{\pm} \rightarrow \mu^{\pm} + \nu \quad (1.1)$$

The decay of kaons is another source of muons. About 70% of such decays occur according to the scheme

$$K_{\mu 2}^{\pm} \rightarrow \mu^{\pm} + \nu$$

Since the mass of kaons exceeds the pion mass by a factor of about 3.5, the monochromatic muons which are produced in this process have long ranges (approximately 20 cm in nuclear emulsion). Yet another source of muons is the $K_{\mu 3}$ decay

$$K_{\mu 3}^{\pm} \rightarrow \mu^{\pm} + \pi^0 + \nu$$

whose probability is about 6% of the $K_{\mu 2}$ -decay probability. The muons produced in $K_{\mu 3}$ decays have a continuous spectrum. Long-lived neutral kaons and the leptonic decays of hyperons are also sources of muons. All these processes are, however, of secondary importance as sources of muons by comparison with $\pi - \mu$ decays.

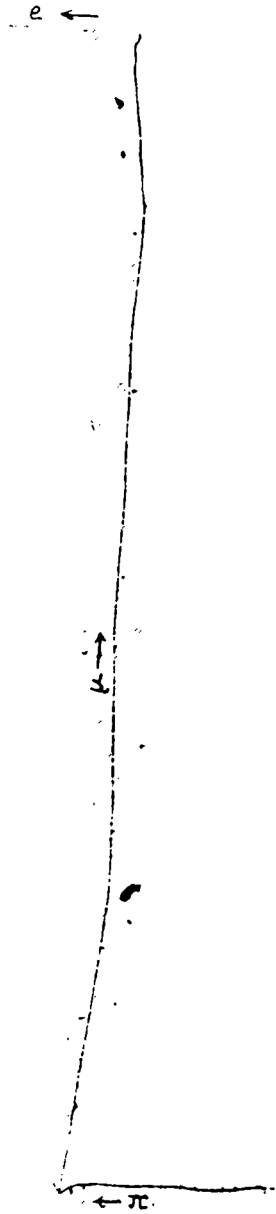


Fig. 1.1 π - μ - e decay in a nuclear emulsion sensitive to relativistic electrons

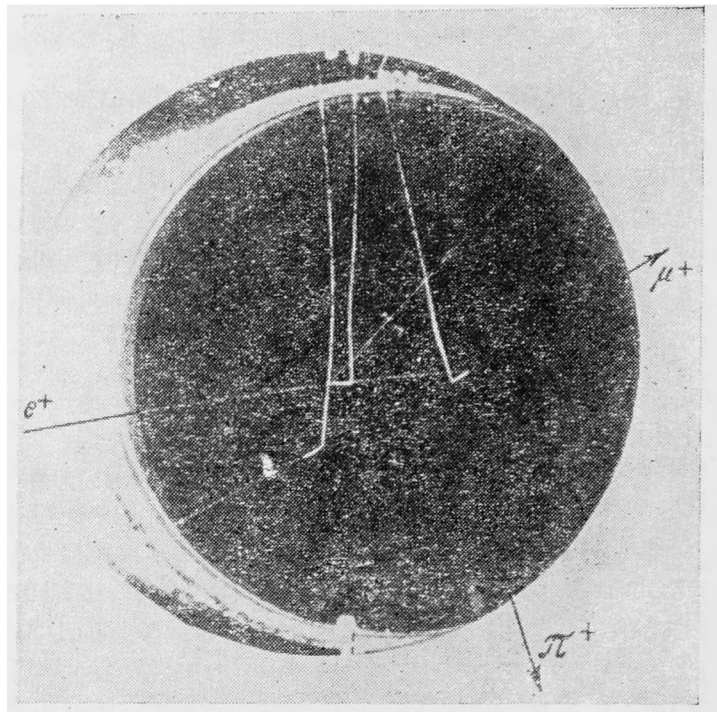


Fig. 1.2 π - μ - e decays in a propane bubble chamber. Positive pions enter the chamber at the top. The short thick tracks are due to positive muons

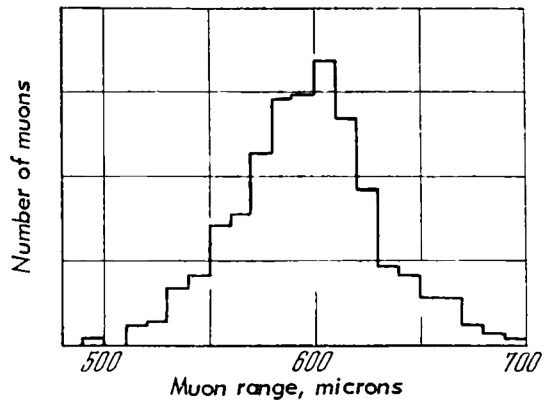


Fig. 1.3 Range spectrum for muons from π - μ decays in Ilford G-S nuclear emulsion (Menon)

1.2 MASSES OF PIONS AND MUONS

In this section we shall consider recent accelerator measurements of the masses of pions and muons.

1.2.1 Deflections in magnetic fields and ranges in emulsions

The most careful measurements of this type were carried out by Barkas et al. [7] on the 184-inch synchrocyclotron at Berkeley. This experiment is illustrated schematically in Fig. 1.4. Pions produced at an internal target T_π by proton bombardment were deflected by the field of the accelerator magnet and were finally intercepted by nuclear emulsions in which they came to rest. From the known geometry of the experiment and from the magnitude and topography of the magnetic field, it was possible to deduce the momentum P_π of the pion, while measurements in the emulsion yielded its range R_π . These two measurements are sufficient to establish the mass of the pion if the range-energy relation is known. To avoid errors associated with errors in this relation, the same emulsions were calibrated using protons from inelastic scatters at a second internal target T_p of the

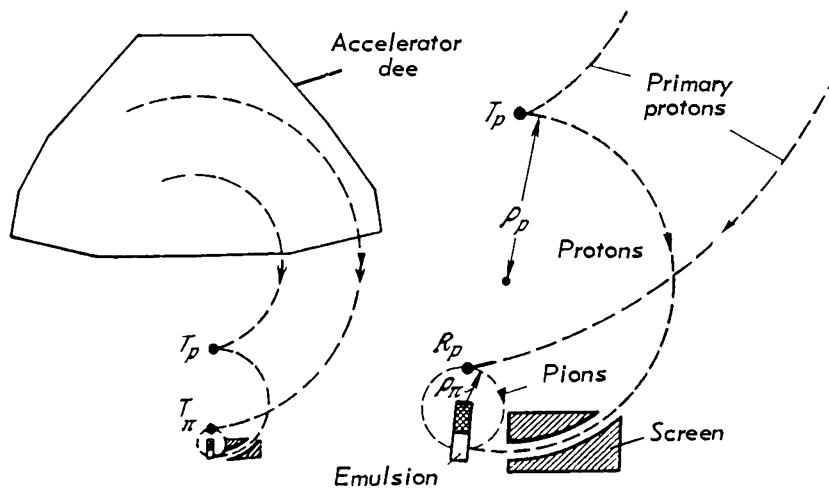


Fig. 1.4 Determination of the masses of light mesons (Barkas et al.). T_p and T_π are targets which are the sources of protons and pions. Nuclear emulsions and trajectories of protons and pions are shown on the right on an enlarged scale. Magnetic rigidities $(Hp)_p$ and $(Hp)_\pi$ are known for each point in the photographic plate and the ranges R_p and R_π can be measured

accelerator. The pion mass obtained in this way (in units of the electron mass m_e) was found to be

$$m_{\pi^+} = (273.34 \pm 0.33) m_e$$

The error is determined by the spread in the ranges of pions (3.7%), the ranges of protons (1.5%) and by the statistical errors of the measurements which were carried out on 368 positive pions and 60 protons.

The mass of the negative pion determined in the same way was found to be

$$m_{\pi^-} = (272.8 \pm 0.45) m_e$$

The π^+ to π^- mass ratio is therefore given by

$$\frac{m_{\pi^+}}{m_{\pi^-}} = 1.0021 \pm 0.0027$$

It may therefore be concluded that the masses of positive and negative muons are the same to within the limits of experimental error.

The ratio of the masses of positive pions and muons was also measured in these experiments and the result was

$$\frac{m_{\pi^+}}{m_{\mu^+}} = 1.321 \pm 0.003$$

and the mass difference was found to be

$$m_{\pi^+} - m_{\mu^+} = (66.41 \pm 0.10) m_e$$

From the above values for the positive-pion mass, we obtain the following result for the mass of the muon

$$m_{\mu^+} = (206.93 \pm 0.35) m_e$$

The mean momentum p_0 of the monochromatic muons from pion decays was also determined in these experiments by comparing the ranges of positive muons from $\pi - \mu - e$ decays in the emulsion with the range of positive muons entering the emulsion from the target. The momentum of the latter was measured by finding the curvature of their trajectories in the magnetic field. The value of p_0 obtained in this way was

$$p_0 = (29.80 \pm 0.04) \text{ MeV}/c$$

The muon energy corresponding to this value of momentum is

$$E_0 = \frac{p_0^2}{2m_\mu} = (4.19 \pm 0.01) \text{ MeV}$$

1.2.2 Negative-pion mass from the reaction $\pi^- + p \rightarrow n + \gamma$

The mass of negative pions can also be determined by measuring the energy of monochromatic γ rays produced when negative pions come to rest in hydrogen. The capture reaction proceeds through the following two channels:



This was shown by Panofsky et al. [8] who measured the γ -ray spectrum due to negative pions stopping in hydrogen. The experiments were carried out on the 184-inch synchrocyclotron and the γ rays were recorded by a spectrometer which measured the energy of electron-positron pairs produced by the γ rays in a lead plate. Such measurements established the presence of a monochromatic γ -ray line due to the reaction (1.2) against a background of uniformly distributed γ rays produced in the decay of neutral pions from the reaction (1.3).

Careful measurements of γ -ray spectra from reactions (1.2) and (1.3) were carried out by Crowe and Phillips [9], who used a γ -ray spectrometer with a resolution of 1.6% and took into account the recoil energy carried off by the neutron, the neutron-proton mass difference and the binding energy of the negative pion in the K shell. The mass of the negative pion obtained in this way was found to be

$$m_{\pi^-} = (272.74 \pm 0.40) m_e$$

1.2.3 Masses of pions and muons deduced from mesonic X rays

Measurement of the energies of characteristic X rays emitted by pionic and muonic atoms has been found to be the most accurate method of determining the masses of light mesons. This method will be discussed in some detail in

Section 4.2.5. Here, we shall only quote the results obtained by Koslov et al. [10] and Stearns et al. [11], and the recent work of Lathrop et al. [12] and Devons et al. [13]. The most accurate masses of pions and muons which follow from these experiments are

$$m_{\pi^-} = (273.34 \pm 0.13) m_e$$

$$m_{\mu^-} = (206.76 \pm 0.02) m$$

Measurements of the masses of charged pions and muons are summarized in Table 1.1. For completeness, this table also shows the values of the $\pi^- - \pi^0$ mass difference obtained by Panofsky and by Chinowsky et al.

1.3 MUON DECAY SCHEME

The decay of a muon leads to the appearance of an electron and two light neutral particles which we can tentatively identify with the neutrino and the antineutrino respectively:

$$\mu^\pm \rightarrow e^\pm + \nu + \bar{\nu}$$

The three-particle decay scheme for the muon was first confirmed by measurements on the decay-electron spectrum in a Wilson cloud chamber, and by the absorption method. Leighton et al. [17] used a cloud chamber exposed to cosmic rays to determine the spectrum of decay electrons. The electron energy distribution obtained in this work is shown in Fig. 1.5, from which it is clear that the spectrum is continuous and extends up to 50-60 MeV. The fact that the electron spectrum is continuous was also confirmed by Zhdanov and Khaidarov [18] and by Steinberger [19] from measurements of the absorption of decay electrons in graphite. The average energy carried off by the decay electrons was found in these experiments to be approximately 35 MeV, i.e. of the order of one-third of the muon rest energy. From

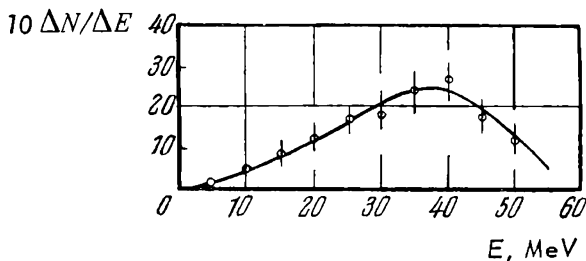


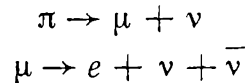
Fig. 1.5 Spectrum of electrons from cosmic-ray $\mu-e$ decays in a Wilson cloud chamber (Leighton et al. [17]). The number of electrons per 10-MeV energy interval is plotted as a function of energy in MeV

Table 1.1 Pion and muon masses

Reference	Method	Mass in units of m_e					
		m_{μ^+}	m_{μ^-}	m_{π^+}	m_{π^-}	$m_{\pi^+} - m_{\mu^+}$	$m_{\pi^-} - m_{\mu^-}$
[7]	Comparison of proton and meson ranges in nuclear emulsion	206.93 ± 0.35	206.30 ± 0.47	273.34 ± 0.33	272.8 ± 0.45	66.41 ± 0.10	
[9]	Energy spectrum of photons from the reaction $\pi^- + p \rightarrow n + \gamma$		206.33 ± 0.41		272.74 ± 0.40		
[10, 11]	X rays from C, P and Si mesonic atoms		206.93 ± 0.13		273.34 ± 0.13		
[14]	Weighted mean (1957)	206.86 ± 0.11		273.27 ± 0.11			
[12, 13]	$3D-2P$ transitions in mesonic phosphorus atoms	206.76 ± 0.02 -0.03					
		206.74 +0.03 -0.04					
		206.78 +0.03 -0.02					
		Mean value: 206.76 ± 0.02 (1960)					
[16]	Spectrum of photons from the reaction $\pi^- + p \rightarrow n + \pi^0$						10.6 ± 3
[16]	Angular correlation of photons from						8.8 ± 0.6

this it was concluded that three light and weakly interacting particles were produced in the decay of muons. The experiments of Hincks and Pontecorvo [20], Sard and Althaus [21] and Piccioni [22] showed that the neutral particles from muon decays were not photons. It was therefore concluded that they were neutrinos which were known to originate in nuclear β decay.

We shall now consider what information about the masses of neutrinos produced in the processes



can be deduced from the measured pion and muon masses given above. Let us begin with the first decay. Conservation of energy and momentum leads to the following expression for the mass of the neutral particle produced in $\pi-\mu$ decay:

$$m_\nu = (m_\pi^2 + m_\mu^2 - 2m_\pi \sqrt{m_\mu^2 + p_\mu^2})^{1/2}$$

Using the most accurate values for m_π , m_μ and p_μ (Table 1.1), i.e.

$$\begin{aligned}m_\pi &= (273.27 \pm 0.11) m_e \\ m_\mu &= (206.76 \pm 0.02) m_e \\ p_\mu &= (29.80 \pm 0.04) \text{ MeV}/c\end{aligned}$$

we find that the upper limit for the mass of the neutrino produced in the decay of pions is given by

$$m_\nu < 9m_e$$

Similarly, the maximum energy received by the electrons in $\mu - e$ decays may be used to estimate the masses of neutral particles produced in the decay of muons. The electron receives maximum energy when both neutral particles are emitted in the opposite direction to the electron. The mass of the neutrino is then given by

$$m_\nu = \frac{1}{2} (m_\mu^2 + m_e^2 - 2m_\mu E_e)^{1/2}$$

where E_e is the maximum energy of the electron in $\mu-e$ decay. Using the most accurate experimental value available at present (cf. Chapter 2), i.e.

$$E_e = (53.00 \pm 0.32) \text{ MeV}$$

and the above value of the mass of the muon, we find that the upper limit for the mass of the neutrino is given by

$$m_\nu < 5m_e$$

The hypothesis that the neutral particles produced in $\pi - \mu$ and $\mu - e$ decays are neutrinos may be regarded as experimentally verified to the accuracy indicated by the above figures.

It is also worth mentioning a direct demonstration of the fact that the charged particle produced in the decay of the muon is in fact an electron. Fig. 1.6 shows a $\pi - \mu - e$ decay recorded in a nuclear emulsion. This photograph is interesting in that it shows a 'fork', due to a collision between the charged product from the decay of the positive muon and an emulsion electron. About ten such forks were

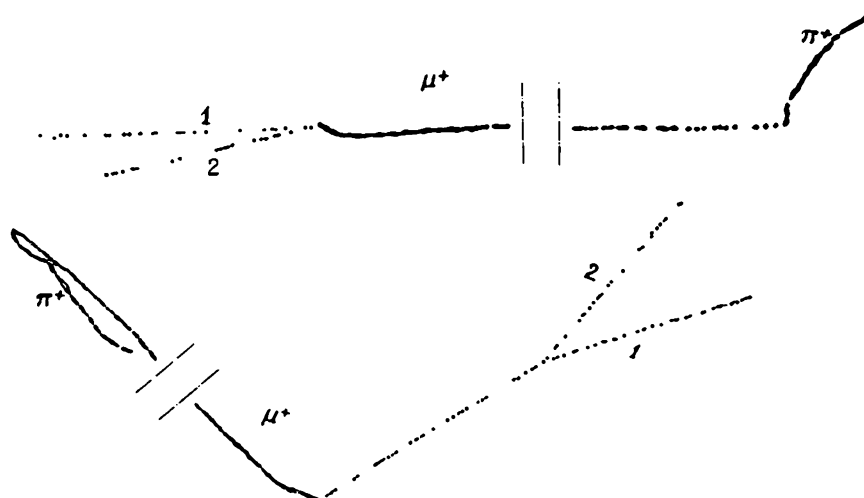


Fig. 1.6 Scattering of a positron from a $\pi - \mu - e$ decay by an electron in a nuclear emulsion. 1 and 2 are respectively positron and electron tracks after scattering

observed by Minervina and Pesotskaya [23]. Energy measurements by the multiple-scattering method and kinematic analysis show that these forks are due to the collision of two particles of equal mass, and that the probability of appearance of such forks is in agreement with the total cross-section of positron-electron scattering which follows from formulae given by Babha.

1.4 SPIN OF THE MUON

There is considerable evidence that the spin of the muon is $1/2$. This conclusion is based both on indirect experiments in which the theory has to be called upon to interpret experimental data, and on very direct experiments in which interpretation of the data requires general quantum-mechanical properties of the angular momentum. Some of these experiments will be discussed here and the remainder will be considered later.

Some evidence about the spin of the muon is provided by its decay scheme: $\mu \rightarrow e + \nu + \bar{\nu}$. If we assume that the two neutral particles in this scheme are identical with the neutrino in β decay, there are only two possibilities for the spin of the muon: $S_\mu = 1/2$ or $3/2$.

The earliest evidence of the fact that the spin of the muon must be less than 1 was obtained as long ago as 1941 from studies of electromagnetic interactions involving the penetrating component of cosmic rays. Studies of 'bursts' in ionization chambers and Wilson cloud chambers screened from the soft component of cosmic rays showed that such bursts are produced as a result of a cascade multiplication of photons or high-energy electrons in the walls of the chamber or in the surrounding medium. The photons and electrons are due to bremsstrahlung or the formation of fast δ rays by high-energy muons in the medium surrounding the chamber. Christy and Kusaka [24] used the Born approximation to show that the probability of such processes for nuclei with large Z increases with the spin of the muon. They then compared the calculated probability of formation of such bursts by the penetrating component of cosmic rays with the measurements of Schein and Gill [25] and concluded that high values for the muon spin, e.g. 1 or $3/2$, had to be rejected, and that the most probable spin was 0, although a spin of $1/2$ was also possible. Subsequent calculations using more recent data on the energy spectrum and mass of the cosmic-ray muons (Belen'kii [26], Hirokawa et al. [27] and others) showed that production cross-sections and the burst-energy spectra were in agreement with a muon spin of $1/2$.

A more direct determination of the spin of the muon is due to Garwin et al. [28] who found that parity was not conserved in $\pi - \mu - e$ decay. They measured the g factor of the muon, i.e. the ratio of its magnetic moment in muonic Bohr magnetons ($eh/2m_\mu c$) to its angular momentum in units

of \hbar . We shall discuss these experiments in detail when we deal with the non-conservation of parity in $\pi - \mu - e$ decays. Here, we shall merely quote the result

$$g = 2.00 \pm 0.10$$

This is in agreement with $g = 2$, which is expected for Dirac particles with spin $1/2$. However, we shall discuss accurate measurements of the g factor of the muon in Chapter 5.

1.5 LIFETIME OF THE MUON

The lifetime of the muon was first estimated as long ago as 1938-1941 by Rossi and others who used the anomalous absorption of the penetrating component of cosmic rays. In this phenomenon muons traversing equal amounts of matter in a dense medium and in the atmosphere are absorbed much more strongly in the latter. Kulenkampf [29] showed that this absorption anomaly might be explained on the assumption that the penetrating component consisted of unstable particles.

The first Geiger-counter measurements of the lifetime of the muon by the delayed-coincidence method were carried out by Rasetti [30]. This method was subsequently greatly improved by Rossi and Nereson [31]. The most accurate measurements of the mean lifetime of cosmic-ray muons appear to be those by Bell and Hincks [32]. Their result was

$$\tau_{\mu} = (2.22 \pm 0.02) \cdot 10^{-6} \text{ sec}$$

Very accurate measurements of the lifetime of the muon have recently been carried out by a number of groups. One such experiment is that performed by Reiter et al. [33] with the accelerator at the Carnegie Institute. The principle of the experiment is illustrated in Fig. 1.7. A beam of positive pions with initial energies of 70 MeV was stopped by a carbon target, 2.5 cm thick. Pions coming to rest were indicated by $123\bar{4}$ coincidences.* Electrons produced from $\mu - e$ decays in the graphite were indicated by $45\bar{6}$ coincidences. The meson beam intensity was high so that the cyclotron

* The symbol $\bar{4}$ represents an anti-coincidence; this notation will be used henceforth.

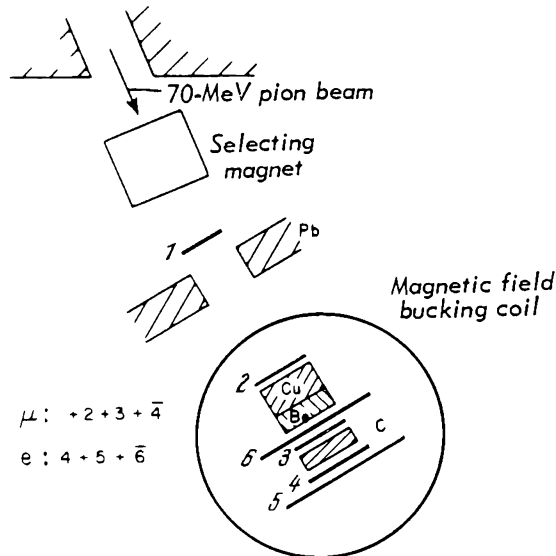


Fig. 1.7 Measurement of muon lifetime (Reiter et al.). The Cu-Be absorber was used to degrade positive muons which finally came to rest in target C

could be run at a low level, thereby reducing the general background in the experimental area. The time interval between the entry of a positive pion into the graphite target and the exit of a decay electron was measured by counting the number of pulses from a 10-Mc/s oscillator. The oscillator was switched on and off by the 1234 and 456 coincidence pulses respectively and the number of oscillator pulses was recorded by a fast scaler. The mean lifetime of the positive muon obtained from these measurements was

$$\tau_{\mu^+} = (2.211 \pm 0.003) \cdot 10^{-6} \text{ sec}$$

Data obtained by other workers are given in Table 1.2.

The most accurate pion lifetimes which are available at present are

$$\tau_{\pi^\pm} = (2.56 \pm 0.05) \cdot 10^{-8} \text{ sec}$$

$$\tau_{\pi^0} = (1.05 \pm 0.18) \cdot 10^{-16} \text{ sec}$$

1.6 INTERACTION OF NEGATIVE MUONS WITH NUCLEI

The basic experimental fact which forms the natural starting point for studies of the interaction of slow muons with nuclei was obtained in the well-known work of Conversi,

Table 1.2 Measurements of the lifetime of the positive muon

Reference	Mean lifetime, μsec	Source	Time measurement
[32]	2.22 ± 0.02	Cosmic rays	Delayed coincidences
[34]	2.20 ± 0.015	Accelerator	CRO
[35]	2.225 ± 0.006	"	Time-to-amplitude conversion
[33]	2.211 ± 0.003	"	Counting of oscillator pulses
[36]	2.208 ± 0.005	"	"
[37]	2.203 ± 0.004	"	"
[57]	2.202 ± 0.002	"	"
[58]	2.198 ± 0.001	"	"
[59]	2.197 ± 0.002	"	"

Pancini and Piccioni [38] who measured the lifetime of both positive and negative muons stopping in various absorbers. The principle of this experiment is illustrated in Fig. 1.8, where F_1 and F_2 are iron blocks each of which consists of two parts magnetized in opposite directions parallel to the axes of the Geiger counters A, B, C. These blocks act as lenses focusing slow muons of either sign on to telescope counters B, depending on the direction of the magnetic field in the blocks. The magnetic lenses were designed to ensure complete removal of muons of opposite sign whose energy was low enough for them to come to rest in the absorber between the counters B and the counter array C. A delayed coincidence system was used to record decay electrons emitted from the absorber in the time interval between 1 and 4.5 μsec after an ABC coincidence, which indicated that a muon had been stopped in the absorber. It was found that decay electrons were not produced when negative cosmic-ray muons came to rest in an iron absorber. This was an expected result, in agreement with the hypothesis that the

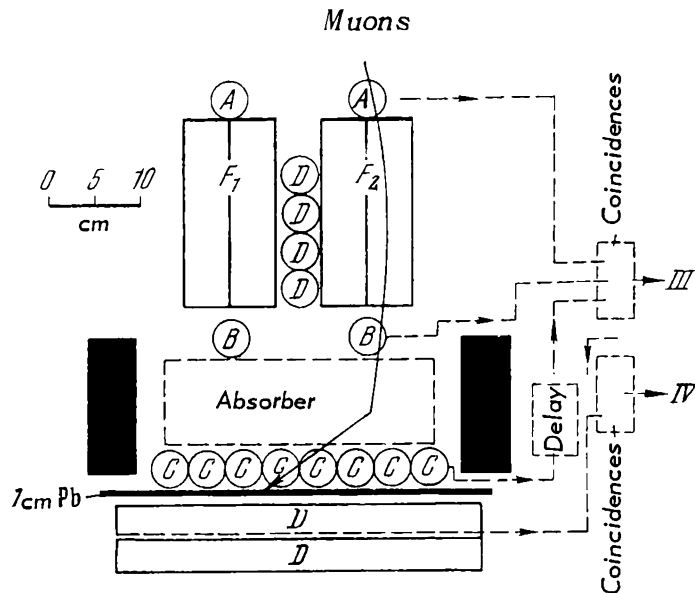


Fig. 1.8 Experiment of Conversi, Pancini and Piccioni. F_1 and F_2 are divided iron blocks with the two halves magnetized in opposite directions ($B = 15$ kgauss). They are used as magnetic lenses for slow muons. Counters A and B are connected in coincidence and pulses from counter C are fed into a delayed coincidence system which records the decay of muons stopping in the absorber. The layer of lead above counters D absorbs decay electrons

negative muons were captured by iron nuclei for a very short period of time. The appearance of decay electrons was, however, detected when negative muons were stopped in a graphite absorber. Their number was comparable with the number of decay electrons from positive muons stopping in graphite. It followed that, at least for light nuclei, the probability of absorption of a negative muon by a nucleus is of the same order as the probability of decay of a positive muon:

$$\Lambda_d = \frac{1}{\tau_{\mu^+}} \approx \frac{1}{2.2 \cdot 10^{-6} \text{ sec}} \approx 4.5 \cdot 10^5 \text{ sec}^{-1}$$

This was a paradoxical result because in 1946 cosmic-ray muons were the only known mesons and were identified with the Yukawa mesons which in turn were thought to be responsible for nuclear forces. Theory showed that such particles should be absorbed by nuclei in a time interval of the order of the 'nuclear time' ($\sim 10^{-23}$ sec). Even if we allow for the fact that a negative muon in the K shell of the mesonic atom

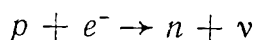
of carbon spends only about 10^{-3} of its life in the nucleus, we find that the probability of its interaction with the nucleus is of the order of

$$\frac{1}{1000} \cdot 10^{23} = 10^{20} \text{ sec}^{-1}$$

while the probability of capture of negative muons by graphite nuclei estimated from the results of Conversi, Pancini and Piccioni turned out to be lower by a factor of 10^{14} . This experiment clearly indicated that the muons could not be the particles in the Yukawa theory.

Following the work of Conversi et al., the interaction between stopping negative muons with the nuclei of various different materials was subjected to intensive study. All the most important results obtained with both cosmic rays and with accelerators will be discussed in Chapter 6. Here we shall simply note that the interaction probability for negative muons in the K shell of a mesonic atom has been very carefully determined right through the periodic table. It has been established that the probability of capture of a negative muon is very small in comparison with the reciprocal nuclear time of 10^{23} sec^{-1} . Existing experimental data are given in Fig. 3.16. It follows from these data that as Z increases from 3 to 82, the probability of capture of a negative muon by the nucleus increases from approximately $0.3 \times 10^5 \text{ sec}^{-1}$ to a number approaching 10^7 sec^{-1} . It is therefore clear that a muon exhibits an exceedingly weak interaction with nuclear matter. The nuclear β decay is another example of an equally weak interaction.

Pontecorvo [39] proposed that the interaction of the negative muon with a nucleus can be described by analogy with K capture in nuclear β decay. The capture of an orbital electron by the nucleus is described by



Similarly, a negative muon in the K shell of the mesonic atom can be captured by a nuclear proton. We therefore have the analogous reaction in which the proton is transformed into a neutron and a neutrino:



It will be found later that all the existing data on nuclear μ^- capture can be explained in terms of this reaction.

1.6.1 Capture of negative muons by protons

The capture reaction (1.1a) has been observed directly in the hydrogen bubble chamber. Neutrons produced in this reaction have energies $E \approx p_\nu^2/2M_n \approx 5.2$ MeV, where p_ν is the momentum of the neutrino and M_n is the neutron mass. Direct observations of reaction (1.1a) in liquid or gaseous hydrogen must involve the detection of such monochromatic neutrons correlated with stopping negative muons. This experiment was carried out by Hildebrand [40]. The negative-muon beam of the Chicago accelerator (99% negative muons; negative pion impurity approximately 0.5%) was stopped in an 8-litre hydrogen bubble chamber placed in a field of 20 kOe. Photographs obtained in this experiment showed stopping muons and recoil protons appearing some distance away from the points at which the muons came to rest. These recoil protons were produced in collisions between neutrons from reaction (1.1a) and protons in the chamber. An example of an event of this type is shown in Fig. 1.9. The energy of the neutron may be found from the range of the recoil proton and the direction of the line joining the

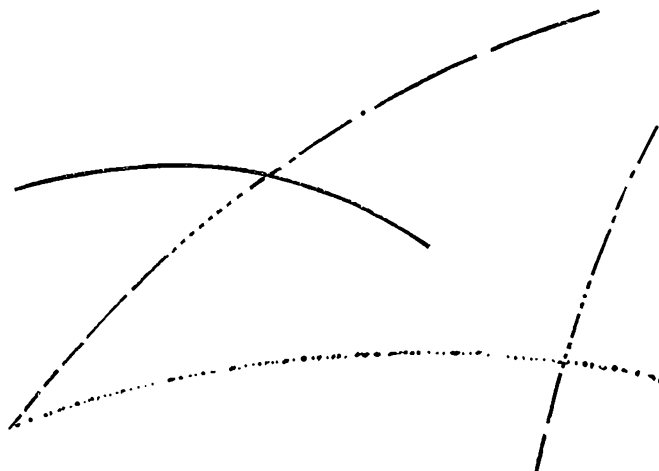


Fig. 1.9 Capture of a muon by a proton in a liquid-hydrogen bubble chamber: the reaction was $\mu^- + p \rightarrow n + \nu$. The short thick track is a recoil proton produced in a collision between a neutron from reaction (1.1a) and a proton in the chamber. The diagram shows a muon decaying at rest (left) and a stopping muon without visible decay, apparently correlated with the appearance of the recoil proton

end of the negative-muon track and the beginning of the proton track. The liquid-hydrogen bubble chamber was in fact used as a fast neutron spectrometer. The efficiency and resolving power of this spectrometer were measured by Pyka [41] who used the π^- -capture reaction



This reaction yields monochromatic neutrons with energies of about 8.9 MeV. The neutron spectrum obtained in Pyka's calibration measurement is shown in Fig. 1.10a. The mean energy of neutrons from reaction (1.2) was found to be $E_n = 8.86 \pm 0.05$ MeV, while the Panofsky ratio was found to be $R = 1.53 \pm 0.10$. Neutron energy spectra obtained by Hildebrand are given in Fig. 1.10b (with the background subtracted) which clearly shows the presence of a 45-particle monochromatic group of neutrons with energies of about 5 MeV. This result is a direct confirmation of the existence of the elementary reaction $p + \mu^- \rightarrow n + \nu$, and can be used to determine the μ^- -capture probability in liquid hydrogen, from the ratio of the number of negative muons captured by

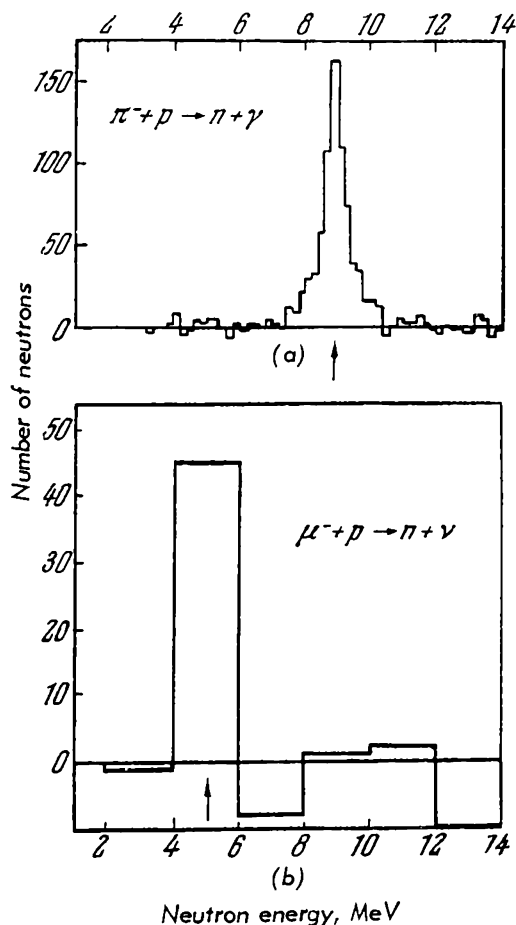


Fig. 1.10 Energy spectrum of neutrons from the reactions $\pi^- + p \rightarrow n + \gamma$ (Pyka) and $\mu^- + p \rightarrow n + \nu$ (Hildebrand)

protons to the total number of negative muons stopping in the chamber:

$$\Lambda_p = \frac{N_{\mu^- \pm p}}{N_{\text{stop}}} \Lambda_d$$

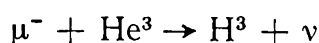
where $\Lambda_d \approx 4.5 \times 10^5 \text{ sec}^{-1}$ is the decay probability of a free muon. In order to determine the number of negative-muon captures by protons it is also necessary to know the efficiency of the bubble chamber for approximately 5.2-MeV neutrons. The efficiency was found to be close to 0.12. The capture probability obtained by this method was $\Lambda_p = 434 \pm 100 \text{ sec}^{-1}$. This probability can also be determined from the ratio of the number of stopping muons which are not accompanied by the appearance of a decay electron to the total number of stopping muons N_{stop} . Owing to the presence of impurities whose nuclei may capture muons, this second method yields only the upper limit for the probability of capture of negative muons by protons:

$$\Lambda_p = 613 \pm 50 \text{ sec}^{-1}$$

The probability of negative-muon capture by protons in the liquid hydrogen filling the bubble chamber is very difficult to relate directly to the probability of capture of a muon by a proton, since the latter may occur either in the mesonic atom (μ^-p) or the mesonic molecule ($p\mu^-p$). In the second case the meson can be captured by either of the two protons and the capture probability is higher by a factor of roughly 2 as compared with the probability of capture of a muon by a proton. However, the μ^- -capture probability for a proton is very dependent on the spin state of the two interacting particles. We shall consider these problems in detail later, but for the moment let us merely note that these mesomolecular complications in the interpretation of the Hildebrand experiment do not affect the estimated probability of capture of a muon by hydrogen which is of the order of 10^3 sec^{-1} .

1.6.2 Capture of negative muons by He^3

Zaymidoroga et al. [42] have investigated the capture of negative muons by He^3 nuclei in the reaction



Helium does not form a molecule, and from the point of view of mesomolecular phenomena there are no difficulties in the interpretation of this reaction. The reaction was observed in a diffusion chamber filled with He^3 to a pressure of 20 atm and placed in a field of 6 kOe. The purity of the He^3 isotope was better than 99.999% and the tritium impurity did not exceed 10^{-15} . Fig. 1.11 shows a characteristic photograph of the capture of a negative muon in He^3 . The curved track is due to the negative muon. A tritium nucleus and neutrino are formed at the point where the negative muon came to rest (the neutrino does not leave a visible track in the chamber). Tritium nuclei produced in this reaction should have energies of approximately 1.90 MeV, which in this experiment corresponded to a range of 2.32 mg/cm². Fig. 1.12 shows the measured range distribution for tritium nuclei in this experiment: most of the tracks form a group with a

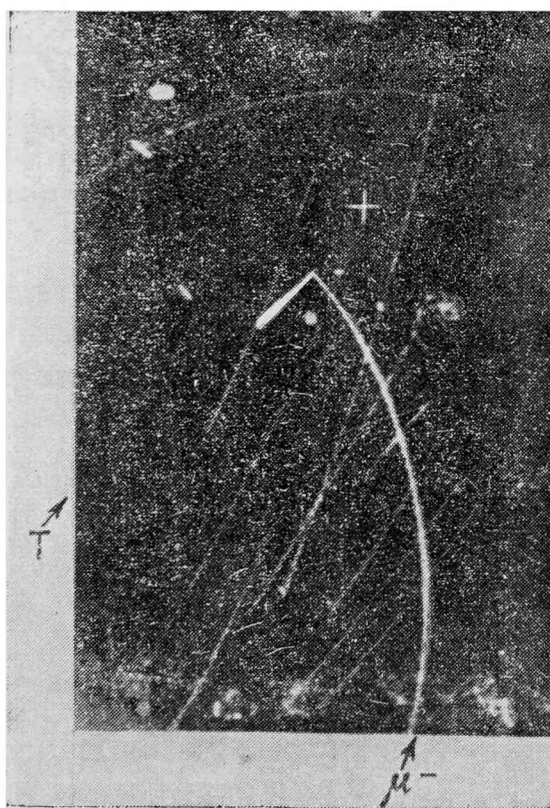


Fig. 1.11 Capture of a negative muon by He^3 nucleus in a diffusion cloud chamber ($\mu^- + \text{He}^3 \rightarrow \text{H}^3 + \nu$). μ^- is the track of the stopping negative muon and T the track of the tritium nucleus H^3 (Zaimidoroga et al.)

maximum at

$$R_{\text{H}^3} = 2.37 \pm 0.02 \text{ mg/cm}^2$$

which is in agreement with the expected range of 2.32 mg/cm². The further group near 5.5 mg/cm² is due to tritium

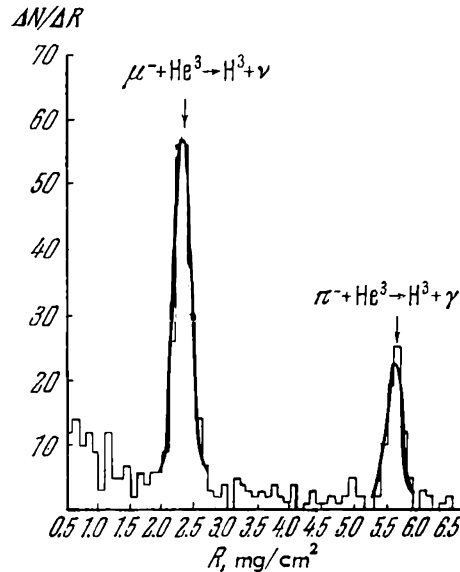


Fig. 1.12 Range spectrum of tritium nuclei from the reaction $\mu^- + \text{He}^3 \rightarrow \text{H}^3 + \nu$

nuclei produced in the radiative capture reaction $\pi^- + \text{He}^3 \rightarrow \text{H}^3 + \gamma$ (the negative-muon impurity of the beam was 2%). The probability of capture of a negative muon by the He^3 nucleus was found to be

$$\Lambda_{\text{He}^3} = (1.41 \pm 0.14) \cdot 10^3 \text{ sec}^{-1}$$

1.7 THE UNIVERSAL FERMI INTERACTION

The universal Fermi interaction was proposed in 1948-1949 by Klein [43], Clementel and Puppi [44], Tiomno and Wheeler [45] and Lee et al. [46]. Evidence for the validity of this hypothesis which was available in 1951 has been discussed by Fermi in his book *Elementary particles*.

Consider the elementary phenomena of β decay, e.g. the decay of the neutron or the capture of an orbital electron by the nucleus



and the elementary reactions involving muons, i.e. their decay

$$\mu^\pm \rightarrow e^\pm + \nu + \bar{\nu} \quad (1.5)$$

and nuclear capture

$$\mu^- + p \rightarrow n + \nu \quad (1.5)$$

The β decay (1.4) and the decay and capture reactions (1.5) have clearly much in common: each involves four fermions (spin 1/2 particles), two of which are neutral.

In Fermi's theory of β decay, which was first proposed by Fermi in 1934, the β -decay process is described by a point interaction between four fermions. The Hamiltonian for this interaction was written down by Fermi by analogy with the Hamiltonian describing the interaction of fermions with the electromagnetic field. Suppose that ψ_i and ψ_f are the wave functions for the initial and final states of a fermion, and that the field is specified by vector and scalar potentials (A, Φ) . In quantum electrodynamics, the amplitude for the transition $\psi_i \rightarrow \psi_f$ is given by

$$M = \int d\tau \{ (\psi_f^* \psi_i) \Phi - (\psi_f^* \alpha \psi_i) A \}$$

where the asterisk indicates the conjugate function, and α is the Dirac spin matrix. The analogy utilized by Fermi to obtain the transition amplitude for the β decay $n \rightarrow p + e^- + \bar{\nu}$ involved the following substitutions:

$$\begin{aligned} \psi_f^* \alpha \psi_i &\rightarrow \psi_p^* \alpha \psi_n \\ A &\rightarrow (\psi_e^* \alpha \psi_\nu) \\ \psi_f^* \psi_i &\rightarrow (\psi_p^* \psi_n) \\ \Phi &\rightarrow (\psi_e^* \psi_\nu) \end{aligned}$$

In this form the transition amplitude for the reaction (1.4) is known to correspond to a pure vector interaction in β -decay theory. For very approximate calculations of the probability of β decay we can confine our attention to the first term in the Hamiltonian, i.e.

$$g_1 (\psi_p^* \psi_n) (\psi_e^* \psi_\nu) \quad (1.6)$$

since terms involving the Dirac matrix α are important only for the description of relativistic effects (g_1 is the

coupling constant for nuclear β decay). By analogy with this interaction, reactions involving the decay of the muon and its capture by a nucleus (1.5) may also be described by a similar Hamiltonian with coupling constants g_2 and g_3 :

$$\begin{aligned} g_2 (\psi_\mu^* \psi_e) (\psi_\nu^* \psi_\nu) \\ g_3 (\psi_n^* \psi_p) (\psi_\nu^* \psi_\mu) \end{aligned} \quad (1.7.)$$

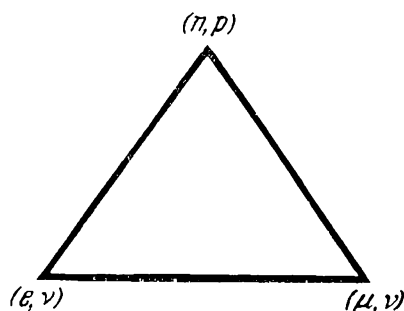
It has been pointed out [43-46] that g_1 , g_2 and g_3 are of the same order of magnitude. The approximate formulae for the reaction probabilities in terms of the coupling constants were derived by Fermi [47] on the basis of (1.6) and (1.7) and are given in Table 1.3, together with the experimental probabilities and coupling constants obtained for comparison between theory and experiment. The fact that the three coupling constants were of the same order of magnitude was regarded as experimental evidence for the existence of a universal Fermi interaction.

Symbolically, the hypothesis of the universal Fermi interaction involving four fermions can be represented by the Puppi triangle (shown in Fig. 1.13) with one pair of strongly

Table 1.3 Orders of magnitude of the weak-interaction constants

Interaction	Neutron decay: $n \rightarrow p + e^- + \bar{\nu}$	Muon decay: $\mu^\pm \rightarrow e^\pm + \nu + \bar{\nu}$	Capture of muon by a proton: $\mu^- + p \rightarrow n + \nu$
Hamiltonian	$g_1 p^* n e^* \nu$	$g_2 \mu^* e \nu^* \nu$	$g_3 n^* p \nu \mu^*$
Calculated probability of interaction	$\frac{1}{\tau} \approx g_1^2 \frac{m_e^5 c^4}{2 \pi^3 \hbar^7}$	$\frac{1}{\tau_{\mu^+}} \approx g_2^2 \frac{1}{1000 \pi^3} \times \frac{m_\mu^5 c^4}{\hbar^7}$	$\Lambda \approx g_3^2 \frac{a^3}{4\pi} \times \frac{m_\mu^5 c^4}{\hbar^7}$
Experimental probability, sec ⁻¹	$\frac{1}{\tau} \approx \frac{1}{1180}$	$\frac{1}{\tau_{\mu^+}} \approx \frac{1}{2.2 \times 10^{-6}}$	$\Lambda \approx 10^3$
Coupling con- stant, erg.cm ³	$\sim 4 \times 10^{-49}$	$\sim 3 \times 10^{-49}$	$\sim 3 \times 10^{-49}$

Fig. 1.13 Weak-interaction triangle (Puppi triangle)



interacting fermions (n, p) and two pairs of weakly interacting fermions (e, ν) and (μ, ν) at the three corners respectively. The last four particles are now referred to as leptons. The interaction between each of these fermion pairs is characterized by the same coupling constant and should be capable of explaining the following weak-interaction phenomena:

1. Decay of the neutron or the capture of a K electron: (np) , $(e\nu)$ side of the triangle.
2. Decay of the muon: $(e\nu)$, $(\mu\nu)$ side of the triangle.
3. Capture of the negative muon by a proton: (np) , $(\mu\nu)$ side of the triangle.

Until 1957 the universal Fermi interaction theory, which was based on the striking fact that the effective coupling constants were of the same order of magnitude, did not lead to an agreement between existing experimental data and quantitative calculations. It is now known that the reason for this failure was a series of inadequate experiments. The discovery of the non-conservation of parity and the subsequent review of all experimental results led to the development of a new weak-interaction theory which has restricted all possible interactions to the vector and axial-vector variants with equal and opposite constants.

In the following chapters we shall discuss in detail experimental data on the weak interactions of muons and the conclusions to which they lead, together with data on nuclear β -decay.

1.8 ELECTRON AND MUON NEUTRINOS

Consider the triangle in Fig. 1.13, which symbolically represents weak interactions. Until recently there were hardly any experimental data which could indicate whether or not the neutrinos at the corners of the triangle were different particles. If they are in fact different particles,

and let us distinguish between the electron neutrino ν_e and the meson neutrino ν_μ . The capture of an electron or a muon by a proton can then be written in the form

$$e^- + p \rightarrow n + \nu_e \quad (1.8)$$

$$\mu^- + p \rightarrow n + \nu_\mu \quad (1.9)$$

These are in fact definitions of the electron and meson neutrinos. When read in the reverse direction these reactions describe the creation of electrons or muons in the interaction of a neutrino and a neutron. The problem of whether or not the two neutrinos are identical can be resolved experimentally by a method put forward by Pontecorvo [48]. If the neutrinos are identical ($\nu_e \equiv \nu_\mu$) collisions between nucleons and neutrinos at energies high enough to produce muons (reaction (1.9)) should result in the creation of both muons and electrons. If, on the other hand, meson neutrinos produce only muons but not electrons, this could be regarded as evidence for the fact that the meson and electron neutrinos are different ($\nu_e \neq \nu_\mu$).

As far as the degree of difficulty is concerned, this experiment may be compared with the well-known experiment of Reines et al. [49] who observed interactions between free antineutrinos and matter. The source of the antineutrinos was a large nuclear reactor and the reaction studied was

$$\bar{\nu}_e + p \rightarrow n + e^+ \quad (1.10)$$

Another experiment with free antineutrinos from a nuclear reactor was carried out by Davis [50] who tried unsuccessfully to observe the reaction

$$\bar{\nu}_e + \text{Cl}^{37} \rightarrow \text{A}^{37} + e^- \quad (1.11)$$

This reaction involves the transformation of a neutron in the Cl^{37} nucleus into a proton, and is therefore reaction (1.8) proceeding in the reverse direction. In order that it could occur, it is sufficient that ν_e and $\bar{\nu}_e$ should be identical particles. The above experiments show that the neutrino and the antineutrino are not identical, i.e. there exist a neutrino ν_e and an antineutrino $\bar{\nu}_e$. Taken in conjunction with the absence of double β -decay, these experiments have been regarded as the experimental foundation for the

hypothesis of the conservation of the number of neutrinos (in general, of leptons) in weak interactions.

The cross-section for the reaction (1.10) is extremely small, so that it is very difficult to observe. Reines et al. measured this cross-section (averaged over the energy spectrum of antineutrinos from the nuclear reactor) and found that

$$\sigma(\bar{\nu} + p \rightarrow n + e^+) = (1.10 \pm 0.25) \cdot 10^{-43} \text{ cm}^2$$

A cross-section of this magnitude precludes the observation of the interaction of muon neutrinos with matter, since the possible sources of such neutrinos have an intensity which is lower by many orders of magnitude than the intensity of an antineutrino beam from a large nuclear reactor.

The theory of the universal Fermi interaction provides a means of calculating the energy dependence of the cross-section for the interaction between neutrinos and antineutrinos on the one hand and protons and neutrons on the other. Consider the reactions



in which electrons and muons are produced by high-energy neutrinos. If the neutrino energy is not too high (less than the proton rest energy $M_p c^2$) the cross-section is given by

$$\sigma \approx \frac{4}{\pi} g^2 p^2 \tag{1.13}$$

where p is the momentum of the neutrino in the centre-of-mass system of the colliding particles and g is the weak-interaction constant. It is evident from this formula that the cross-section increases rapidly with the energy of the neutrino. However, this increase in the cross-section with energy, which was derived on the assumption of a point interaction between the four fermions, cannot continue indefinitely. Lee and Yang [52], Yamaguchi [53], Gabibbo and Gatto [54] and others have shown that if the point interaction between fermions is replaced by an interaction between particles having a finite volume, by the introduction of form factors

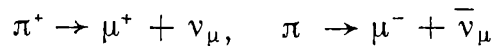
which are determined by the transferred momentum, then in the ultra-relativistic case when the energy of the light particles in (1.12) is much greater than the proton rest energy, the cross-sections for these reactions tend to a definite limit which is approximately given by

$$\sigma = 0.7 \cdot 10^{-38} \text{ cm}^2$$

Although this cross-section is exceedingly small, it is still greater by five orders of magnitude than the cross-section for the interaction of the antineutrino from nuclear β -decay.

Decays of high-energy pions in flight may be used as sources of high-energy muon neutrinos. Pontecorvo [48] and Schwarz [55] have shown that the intensity of neutrino beams produced in this way with the large accelerators which are currently available is sufficient or almost sufficient for such experiments.

The time necessary for an experiment of this kind is only about two years. The experiment has in fact been carried out by Danby et al. [56] on the Brookhaven proton synchrotron which produces 30-GeV protons. Most of the neutrinos used in this experiment were produced in pion decays



and the object was to observe reactions (1.12a) and (1.12b). Both reactions should be observed if the electron and meson neutrinos are identical. If they are not identical, only the muons should appear.

The principle of this experiment is illustrated in Fig. 1.14 which shows part of the Brookhaven proton synchrotron. A beryllium target intercepting 15-GeV protons was located on one of the 3-metre straight segments of the accelerator.

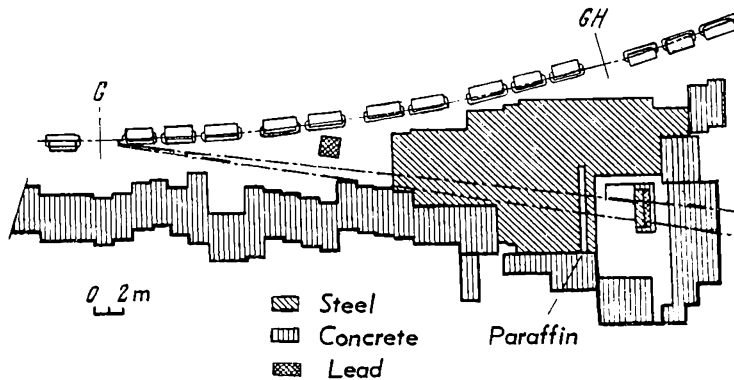


Fig. 1.14 Experiment of Danby et al.

High-energy pions produced in this target were emitted preferentially in the direction of the primary proton beam. The detector recording neutrino interactions was located at a distance of about 34 m from the target and was screened by 13.5 m of iron from the flux of pions and muons from the target. The neutrino-interaction detector consisted of ten identical spark chambers, each of which contained approximately a ton of matter. The detector is illustrated schematically in Fig. 1.15. Each of the ten spark chambers contained nine aluminium plates (area $1.1 \times 1.1 \text{ m}^2$, thickness 2.5 cm) separated by air gaps. The device was screened from the top, from the front and from the rear by the special scintillation counters B, C, D, arranged in anti-coincidence. They cut off the recording system when charged cosmic-ray particles and random muons which had penetrated the screen

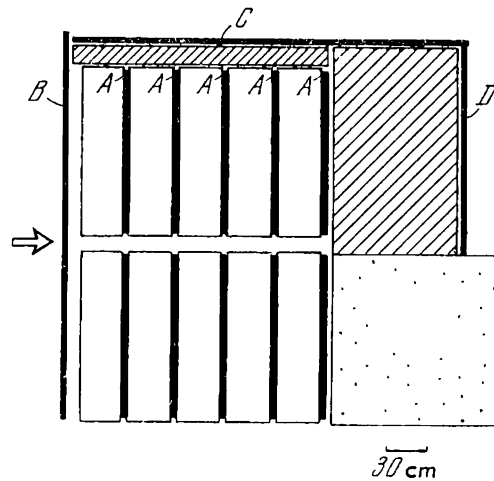


Fig. 1.15 Disposition of spark chambers in the neutrino detector. Arrow shows the direction of the neutrino beam

passed through the detector. The pulse from scintillators A between the spark chambers was used to control the application of the high voltage to the spark chambers. The success of this experiment was largely due to the ingenious way in which the spark chambers were controlled. The control system used the fine time structure of the proton beam which considerably reduced the cosmic-ray and the random coincidence backgrounds.

The neutrino energy spectrum expected under the conditions of this experiment is shown in Fig. 1.16. It falls to zero at about 2 GeV. The figure also shows on an enlarged scale ($\times 10$) the expected spectrum of neutrinos from the decay of kaons in the beam. The ordinates give the number of neutrinos per 1-GeV energy interval per 1 cm^2 of the surface of

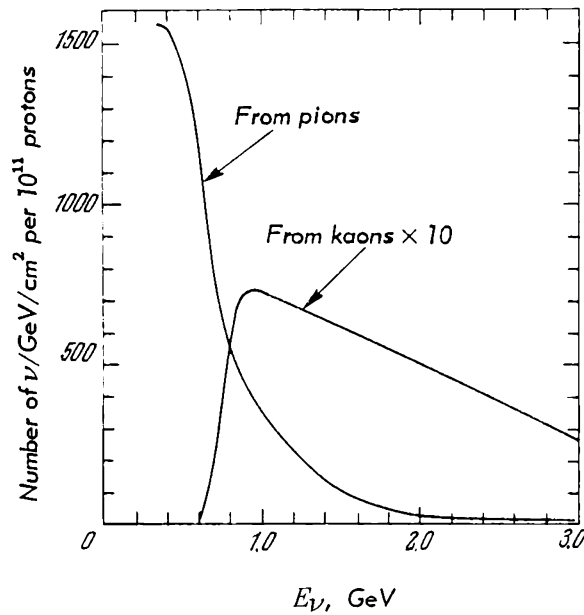


Fig. 1.16 Expected energy spectrum of muon neutrinos in the Brookhaven experiment. The number of neutrinos per GeV per cm^2 of the detector for 10^{11} protons incident upon the target is plotted against the neutrino energy in GeV

the detector for 10^{11} protons entering the target. The total number of protons which passed through the target in this experiment was about 3.5×10^{17} . The muons and electrons produced in reactions (1.12) must have had energies in excess of approximately 100 MeV, since the neutrino energy was shown by the spectrum to be high. Altogether 34 single muons with momenta greater than $300 \text{ MeV}/c$ and without accompanying high-energy electrons were observed in the spark chambers. Fast electrons would have produced showers consisting of a large number of particles. The response of the spark chambers to electrons was tested by exposing them to 400-MeV electrons.

Fig 1.17 shows two typical photographs of muon tracks originating in the plates of one of the spark chambers. Experimental estimates of the expected background due to cosmic-ray muons have shown that the number of such mesons did not exceed 5 out of the 34 observed events. Moreover, the observed number of high-energy muons is of the same order as the effect expected for an interaction cross-section of the order of 10^{-38} cm^2 . This experiment has thus shown that the

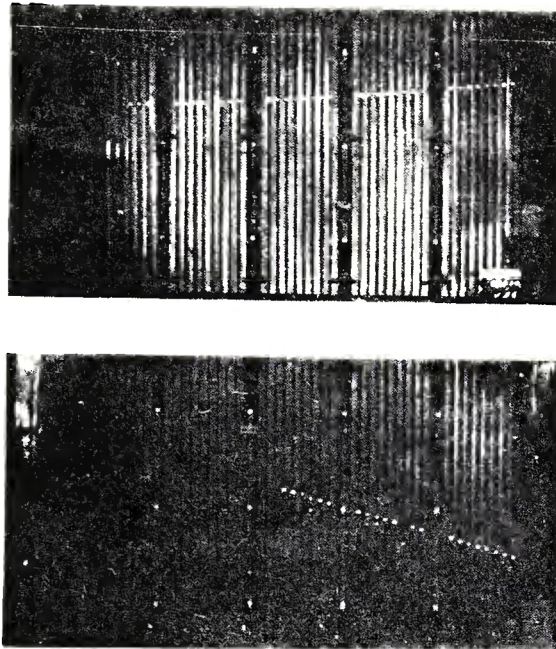


Fig. 1.17 Two typical cases of the appearance of muons in the aluminium plates of the spark chamber

muon neutrinos can produce muons but not electrons. It follows that the muons and electron neutrinos appear to be different particles.

Further studies of this basic problem were performed at CERN. As a result of the neutrino experiment a considerable improvement in the statistics of neutrino interactions was achieved [60, 61].

Let us briefly review the CERN experiment. To begin with, the intensity of the neutrino beam at CERN was higher than the Brookhaven intensity by a factor of about 200. This was due to a number of reasons. First, the CERN experiment was performed with the extracted proton beam so that the muons emitted at 0° to the beam could be used. Second, the CERN workers employed magnetic focusing. Finally, the intensity of the CERN accelerator was higher by a factor of 2-3 as compared with the Brookhaven intensity and the mass of matter in the spark chambers was 100 tons instead of 10. Moreover, the CERN neutrino beam was passed through a freon bubble chamber having a volume of 500 litres and placed in a magnetic field of 27 kgauss. About 500 neutrino interactions were observed in one chamber. The rate of neutrino events in this remarkable experiment was 12-18 per hour in 1963 and up to 40 per hour in 1964. More than

95% of all these events involved a neutrino interaction.

As regards the identity of the muon and electron neutrinos, the result of this experiment may be summarized as follows. Let N_μ be the number of events in which muons were created, and N_e the number of events in which electrons were created. If $\nu_e \equiv \nu_\mu$, then the ratio $R = N_e/N_\mu$ should be equal to unity. The result obtained at CERN was $R = (1.7 \pm 0.5) \times 10^{-2}$, which was less than unity by a factor of more than 50. The difference between the muon and electron neutrinos (see Section 2.14) may thus be regarded as an experimentally established fact.

Chapter 2

PION DECAY

2.1 NON-CONSERVATION OF PARITY IN WEAK INTERACTIONS

In this chapter we shall consider experimental data on pion and muon decays of the form

$$\begin{aligned}\pi &\rightarrow \mu + \nu \\ \mu &\rightarrow e + \nu + \bar{\nu}\end{aligned}$$

and certain other much less probable decay modes. These decays occur with the participation of the neutrino and are typical examples of weak interactions which are characterized by exceptionally small coupling constants (approximately 10^{-49} erg.cm³). An important feature of weak interactions is the fact that they do not conserve spatial parity. This phenomenon was predicted by Lee and Yang [1]. The experimental basis for their theory was the so-called paradox of K_{π_0} and K_{π_3} decays. It is known that all charged kaons have the same mass and the same lifetime and it is therefore natural to expect that there is only one kaon but with a number of decay modes including

$$K_{\pi_2}^+ \rightarrow \pi^+ + \pi^0 \tag{2.1}$$

$$K_{\pi_3}^+ \rightarrow \pi^+ + \pi^- + \pi^+ \quad (2.2)$$

The internal parity of the K_{π_2} meson is $(-1)^S$, where S is its spin. On the other hand, analysis of the energy spectra and angular distributions of pions originating in K_{π_3} decays carried out by Dalitz [2] showed that the probable spin and parity of the K_{π_3} meson is 0^- or 2^- respectively. A K_{π_2} meson with a spin of 0 or 2 should, however, have a positive rather than a negative parity. This problem can be resolved in two ways. It can be assumed that the masses and lifetimes of all the kaons are equal but that the K_{π_2} and K_{π_3} mesons are different particles with different parities. The other possibility, which was considered by Lee and Yang, is that they are identical particles but that parity is not conserved in the decays of kaons, nor, in general, in interactions such as (2.1) and (2.2).

The β decay of polarized Co^{60} nuclei and $\pi - \mu - e$ decay were the first phenomena in which the predicted non-conservation of parity was experimentally verified. These experiments have in fact become the experimental foundation for the two-component theory of the neutrino put forward by Lee and Yang [3], Landau [4] and Salam [5].

2.1.1 Non-conservation of parity in $\pi - \mu - e$ decay

The first experiment in which the non-conservation of parity in $\pi - \mu - e$ decay was observed was performed by Garwin, Lederman and Weinrich [6]. The experiment is illustrated schematically in Fig. 2.1. The beam of 85-MeV positive pions extracted from the accelerator contained about 10% of positive muons, mainly from pions decaying in flight near the cyclotron target and in the deflecting and collimating systems. The separation of pions and muons was achieved in the usual way, using a graphite absorber which stopped pions but transmitted muons with the same initial momentum. The muons finally came to rest in a graphite target. The entry of a muon into the target was indicated by a coincidence between the scintillation counters 1 and 2. The subsequent $\mu - e$ decay in the graphite target was recorded by a positron telescope consisting of two scintillation counters (3, 4).

Coincidence pulses from counters 1 and 2 were delayed by $0.75 \mu \text{ sec}$ and were used to gate the system so that it

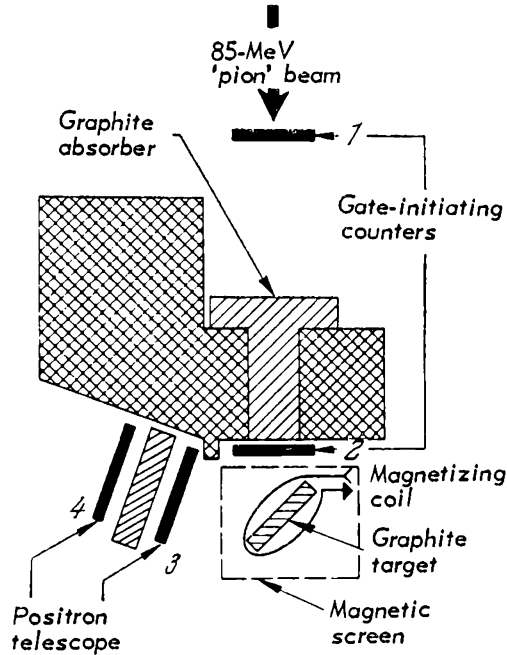


Fig. 2.1 Experiment of Garwin, Lederman and Weinrich in which non-conservation of parity in $\pi-\mu-e$ decay was established

counted positrons leaving the graphite target in the time interval between 0.75 and 2.00 μ sec following the arrival of the muon at the target. Let us suppose that the muons were polarized in the direction of motion. This implies non-conservation of spatial parity in $\pi-\mu$ decay, and the aim of the experiment was to search for any asymmetry in the angular distribution of the emitted positrons relative to the direction of motion. The probability of emission of decay positrons was measured at different angles ϑ to this direction. It is plain from the figure that if there is no magnetic field near the graphite target, the positron telescope will record positrons for which ϑ approached 100° . When a current is passed through the loop shown in Fig. 2.1, the spin of the muon precesses in the constant magnetic field H (which is perpendicular to the plane of the drawing) with an angular frequency

$$\omega = g \frac{eH}{2m_\mu c} \approx 4.28 \cdot 10^4 gH \text{ sec}^{-1} \text{ gauss}^{-1} \quad (2.3)$$

where g is the gyromagnetic ratio (g factor) of the muon, e/m_μ the ratio of its charge to mass, and H the magnetic field. As a result of this precession, the angular distribution

of the decay positrons will rotate about the direction of the magnetic field together with the spin. The angular distribution can therefore be obtained for a constant geometry of the experiment by measuring the 34 coincidence rate as a function of the current in the coil; to each value of the current there corresponds a mean angle of rotation of the spin of the muon. Experimental data corrected for the exponential decay of positive muons are shown in Fig. 2.2 where N is

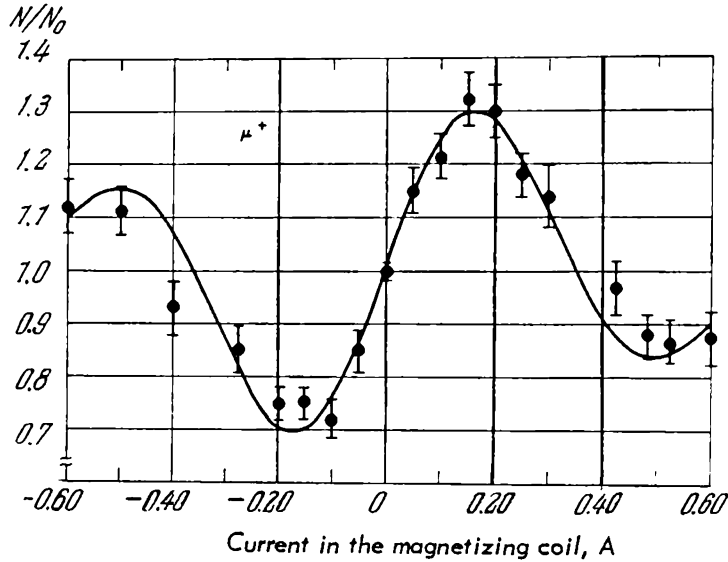


Fig.2.2 Non-conservation of parity in $\pi - \mu - e$ decay (Garwin et al.)

the number of counted positron pulses and N_0 the number of pulses counted in an equal time interval but with the magnetic field reduced to zero. The curve represents the distribution

$$dN \sim [1 + a \cos (\vartheta_0 - \omega t)] dt \quad (2.4)$$

where a is the asymmetry coefficient, ω the meson spin precession frequency, and ϑ_0 the initial phase determined by the geometry of the experiment. In this particular experiment it was found that the asymmetry coefficient was very nearly $a = -1/3$ and the precession frequency ω was found to be in agreement with $g = 2$, which is the value of the g factor for a Dirac particle.

An equally clear demonstration of the non-conservation of spatial parity in $\pi - \mu - e$ decay was obtained from measurements in nuclear emulsions and bubble chambers in which positive pions came to rest, and the complete $\pi - \mu - e$

sequence could be observed. The first measurements of this kind were performed by Friedman and Telegdi [7]. Fig. 2.3 shows distributions obtained by Weissenberg [8]. In this figure the number of decay positrons is plotted as a function of the projected angle in the plane of the emulsion. This distribution is similar to the distribution obtained in the experiments of Garwin et al., and the asymmetry can be described by

$$dN \sim (1 + a \cos \vartheta) d\vartheta \quad (2.5)$$

which is analogous to (2.4). The asymmetry coefficient lies within the range $a \approx -(0.08-0.14)$, depending on the type of emulsion.

Extensive measurements of this kind have shown beyond any doubt that the angular distribution of the decay electron is asymmetric with respect to the momentum of the muon at the instant of decay. However, the $\mu - e$ decay occurs

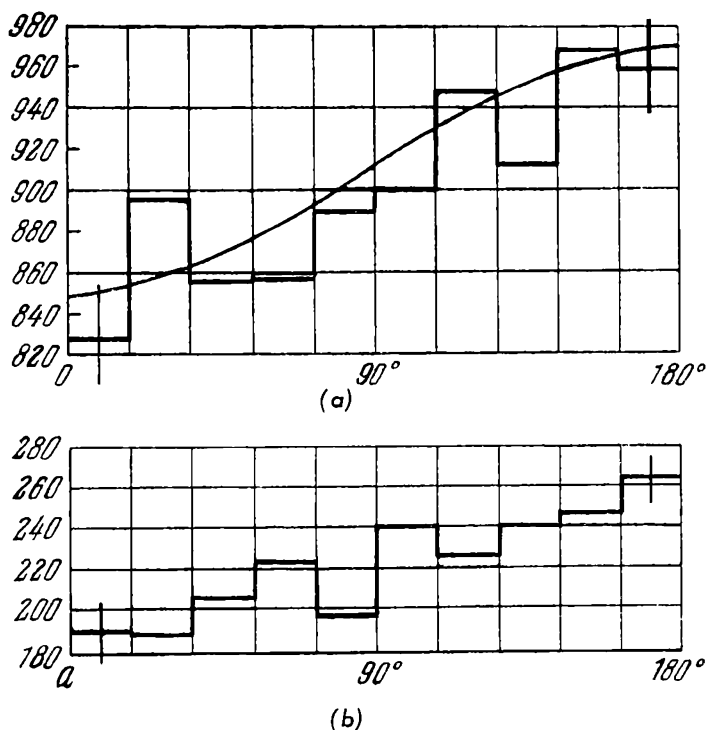


Fig. 2.3 Angular distribution of positrons from the $\pi^+ - \mu^+ - e^+$ decay in normal (a) and diluted (b) NIKFI emulsion. The number of decay positrons in the interval $\Delta\theta = 18^\circ$ is plotted as a function of the angle θ between the momentum of the positive muon at the point where the $\pi - \mu$ decay occurred and the momentum of the electron

after the muon has come to rest, when the only specially defined direction is the direction of its spin. It follows that the direction of the muon spin is related to the direction of emission of the muon from the decay of a pion (longitudinal polarization of the muon), and that the probabilities of emission of electrons in $\mu - e$ decay in the direction of the spin of the muon and in the opposite direction are not equal. It has thus been demonstrated that spatial parity is not conserved in the $\pi - \mu$ and $\mu - e$ decays.

2.1.2 Non-conservation of parity in the β decay of polarized Co^{60} nuclei

The decay of polarized Co^{60} nuclei was the first phenomenon which was found to exhibit non-conservation of parity in weak interactions. Co^{60} nuclei have spin $I = 5$ and positive parity. They are found to decay in accordance with the scheme



Since the Ni^{60} nucleus has the same parity and a spin of $I = 4$, the observed $5^{+} \rightarrow 4^{+}$ transition belongs to the class of $I \rightarrow I - 1$ transitions which occur without change of parity and are known in β -decay theory as pure Gamow-Teller transitions. The experiment of Wu et al. [9] involved the comparison of the intensity of β decays for two opposite polarizations of the initial Co^{60} nucleus. This experiment was analogous to the experiment of Garwin et al. considered above, except that in the Garwin experiment it was the $\pi - \mu$ decay which acted as the polarizer of positive muons while in the Wu experiment the Co^{60} nuclei were polarized by the Rose-Gorter method. We shall not go into the details of this well-known experiment and will confine our attention to a summary of the results. It was found that the counter recording decay electrons emitted approximately in the direction of the magnetic field producing the polarization showed a very large change in the counting rate when the direction of the magnetic field polarizing the Co^{60} nucleus was reversed. The change in the sign of the magnetic field corresponded to a rotation of the spin of the Co^{60} nucleus through 180° , so that this result may be regarded as evidence for considerable asymmetry in the angular distribution of decay electrons relative to the direction of the nuclear spin. This

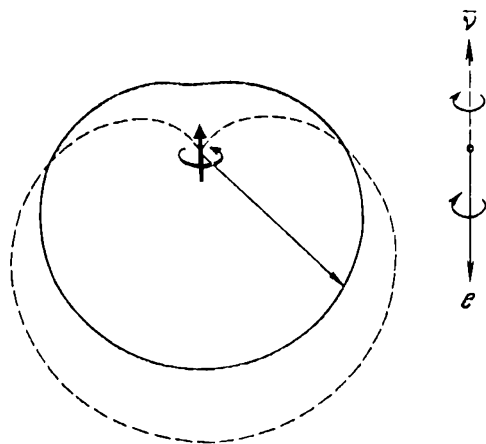
distribution is of the form

$$dN \sim (1 + a \cos \vartheta) d\Omega \quad (2.7)$$

where $d\Omega$ is an element of solid angle, ϑ the angle between the spin direction of the Co^{60} nucleus and the momentum of the β particle, and a the asymmetry coefficient. This coefficient turned out to be negative, i.e. electrons emitted in the decay of polarized Co^{60} nuclei are preferentially emitted in the direction opposite to that of the Co^{60} spin axis.

A characteristic feature of the experiment of Wu et al. was the very large magnitude of the observed effect. For electrons with velocity $\beta = v/c \approx 0.6$, the measured asymmetry coefficient turned out to be of the order of 0.4. Since the polarization of Co^{60} nuclei in this experiment was $p \approx 0.6$ (it was determined from the anisotropy of the γ rays emitted by Co^{60}), the actual value of the asymmetry parameter corresponding to complete polarization of the original nucleus is $0.4/0.6 \approx 0.7$. Theory predicts that the observed asymmetry coefficient should be proportional to the velocity of the β particles emitted by the nucleus, and therefore for relativistic electrons one would expect an asymmetry coefficient of about 1 in this experiment. This corresponds to the maximum possible asymmetry, when there are no decays in which the electron is emitted in the direction of the nuclear spin. This effect can be illustrated by the polar diagram of Fig. 2.4. The solid curve represents approximately the conditions in the experiment of Wu et al. ($\beta \sim 0.6$, $p \sim 0.7$). The broken curve shows the effect expected for a completely polarized nucleus and relativistic electrons ($\beta = 1$).

Fig. 2.4 Polar diagram showing the angular distribution of β particles in the experiment of Wu et al. The distance from the centre of the nucleus to the curve is proportional to $1 + a \cos \theta$. The broken curve shows the situation expected for a completely polarized Co^{60} nuclei. The solid curve corresponds to the experiment of Wu et al. The change in the spin of the nucleus is $\Delta I = -1$; the electron and the antineutrino are emitted in opposite directions, showing that the two particles have opposite helicities



2.1.3 Helicity of the neutrino. Two-component theory

Subsequent experiments performed in many laboratories have extended and improved the data discussed above. All the most important results on $\pi - \mu - e$ decay and some of the basic data on β decay will be discussed later. Here, we shall give a qualitative explanation of the above experiments in terms of a model in which the neutrino is regarded as a particle with spin parallel to momentum. This model is a consequence of the two-component theory of the neutrino put forward by Landau [4], Lee and Yang [3] and Salam [5]. The equations which form the basis of this theory were put forward by Weyl as far back as 1929. Pauli [10] then pointed out that these equations described a particle with spin parallel to its momentum, and rejected them because this was in conflict with the conservation of spatial parity.

In contrast to the usual Dirac theory, in which the neutrino is described by four-component wave functions, the new theory describes the neutrino by two-component functions forming a solution of the Dirac equation for particles of zero rest mass:

$$p\psi_\nu = \mp (\sigma p) \psi_\nu \quad (2.8)$$

where p is the momentum and σ the Pauli spin matrix for the neutrino. The eigenvalues of this equation are $(\sigma p) = \mp p$ and correspond to wave functions for spins parallel or anti-parallel to momentum ($\frac{(\sigma p)}{p} = 1$ or -1 respectively).

The quantity

$$H = \frac{(\sigma p)}{p} = \pm 1 \quad (2.9)$$

is defined in the two-component theory of the neutrino as the helicity of the particle. The neutrino is regarded in this theory as rotating like a right-handed or left-handed screw (positive or negative helicity).

Physically, Equation (2.8) shows that for a given momentum the particle may be found in one of the two possible states with equal and opposite energies. These two states correspond to the particle and the antiparticle, with spin and momentum lying in opposite directions. We shall call the particle with negative helicity the neutrino, and that with positive helicity the antineutrino.

Such two-component neutrinos have the following properties:

1. The neutrino is not invariant under space reflection P of coordinates in which the momentum p changes sign but the spin direction is conserved. This means that space reflection transforms the neutrino into a particle in a non-existent state (Fig. 2.5a).

2. The neutrino is also non-invariant under charge conjugation C . This transformation converts the left-handed

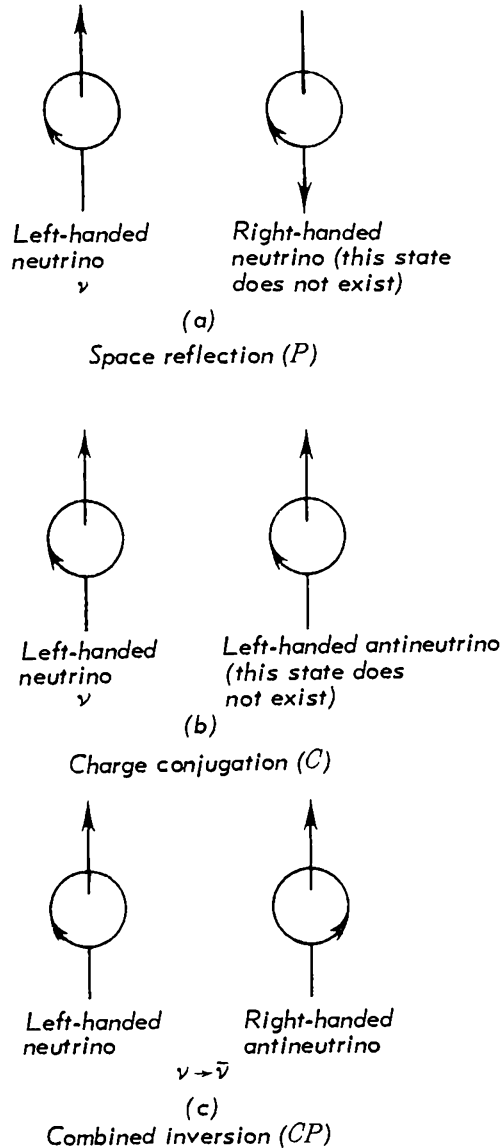


Fig. 2.5 Space reflection, charge conjugation and 'combined inversion' in the two-component theory of the neutrino

neutrino into a left-handed antineutrino. In the two-component theory, the antineutrino must be a right-handed particle and therefore charge conjugation will again transform the neutrino into a particle in a non-existent state (Fig. 2.5b).

3. The two-component neutrino is invariant, however, under successively applied operations of charge conjugation C and space reflection P : these operations (Fig. 2.5c) transform the particle into the antiparticle, e.g. a neutrino into an antineutrino. The existence of this invariance in the two-component theory was pointed out by Landau [4], who referred to it as the conservation of combined parity.

Let us consider now the $\pi - \mu - e$ decay sequence (Fig. 2.6). We shall assume for simplicity that meson and electron neutrinos are identical.

Since the spin of the pion is zero, while the spin of the neutrino is antiparallel to its momentum, it follows from the law of conservation of spin that the muon and the neutrino, which are emitted in opposite directions, should have the same helicities, i.e. $H_\mu = H_\nu = 1$ or $H_\mu = H_\nu = -1$. The two possibilities are indicated in the upper part of Fig. 2.6.

In the decay of the muon

$$\mu \rightarrow e + \nu + \bar{\nu}$$

we shall consider only the limiting case where the electron receives its maximum energy. This occurs when the neutrino and the antineutrino have equal momenta which are opposite to the momentum of the electron. The total angular momentum carried off by the neutrino and the antineutrino emitted

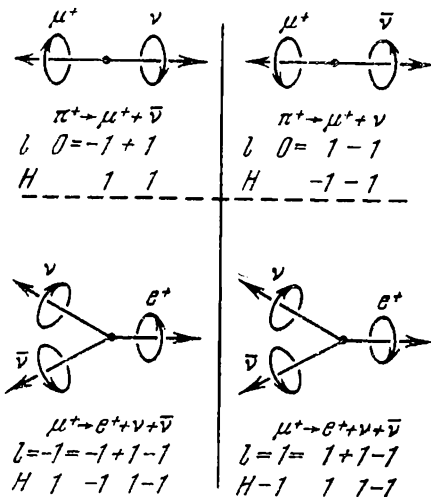


Fig. 2.6 Helicity of particles in $\pi - \mu - e$ decay on the two-component theory of the neutrino. This scheme shows that if the electrons emitted in the $\mu - e$ decay emerge preferentially in the direction opposite to that of the muon spin, then the helicities of the muon and of the electron are opposite. Comparison of the left- and right-hand parts of the diagram show that experiments in which the asymmetry of $\pi - \mu - e$ decay is investigated cannot distinguish the two possibilities $\pi \rightarrow \mu + \nu$ and $\pi \rightarrow \mu + \bar{\nu}$, i.e. they cannot establish the helicity of the neutrino

in the same direction is zero (the neutrino and the antineutrino have opposite helicities) so that the entire spin of the muon becomes available for the electron. If we assume that the electron is longitudinally polarized, i.e. it has definite helicity, then the direction in which it is emitted can only be parallel to the direction in which the muon is emitted in the $\pi - \mu$ decay. The two directions will be the same if the helicity of the muon and of the electron is the same, or they will be opposite if the helicity of the electron is opposite to that of the muon. Since the second possibility is indicated by experiment, we may conclude that the muon and its decay electron have opposite helicities. However, studies of the asymmetry in $\pi - \mu - e$ decay cannot yield the absolute helicities of both particles, i.e. one cannot distinguish in this way between the right- and left-hand sides of Fig. 2.6. The experiment of Wu et al. may be explained in a similar way (cf. Fig. 2.4). The $5^+ - 4^+$ transition occurs during the decay of Co^{60} and the total momentum carried off by the antineutrino and the electron should be equal to 1. Consider an electron emitted in the direction of spin of the Co^{60} nucleus, and suppose that its energy approaches the maximum energy. Since in this case the recoil momentum of the nucleus is negligible, the electron and the antineutrino are emitted in opposite directions. Suppose now that the momentum of the antineutrino is parallel to its spin. In this case, if the total transferred momentum is to be 1, the electron should be emitted in the backward direction and its spin should be opposite to its momentum. It follows that the representation in which the antineutrino has a spin parallel to its momentum explains the observed asymmetry in the angular distribution of the decay electrons and their longitudinal polarization.

2.1.4 Non-conservation of parity in K_{μ_2} decay

The longitudinal polarization of the muon at the instant of $\pi - \mu$ decay is due to the fact that the neutrino emitted in the decay of the spinless pion is longitudinally polarized. This situation is also found to occur in the decay of the K_{μ_2} meson whose spin is also zero:

$$K_{\mu_2} \rightarrow \mu + \nu \quad (2.10)$$

It follows that if the same type of neutrino is produced in both decays, the muons from the $\pi - \mu$ and $K - \mu$ decays

should have the same polarizations. The conservation of leptons and the longitudinal polarization of the neutrino can thus be investigated by measuring the polarization of the muon from K_{μ_2} decay.

We shall now consider the experiment of Combes et al. [11] who succeeded in measuring this polarization. The principle of this experiment is illustrated in Fig. 2.7. A beam of positive kaons with momenta of about 480 MeV/c was

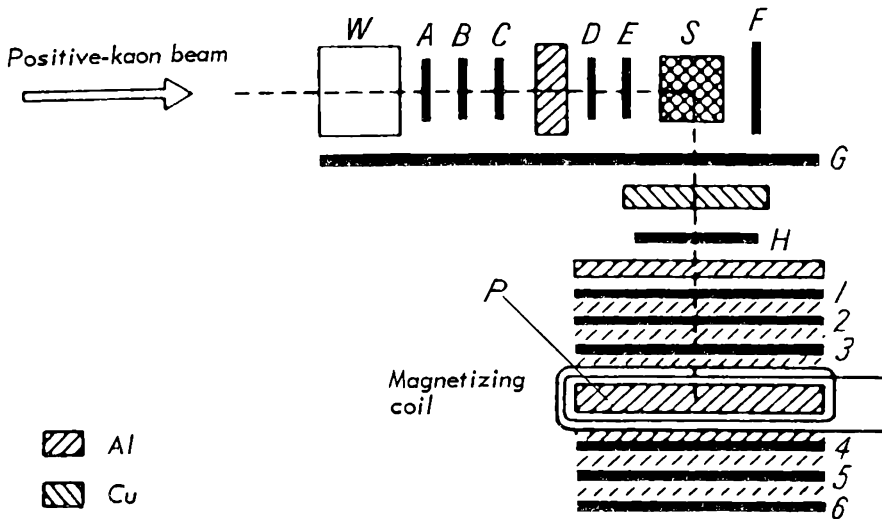


Fig. 2.7 Measurement of the polarization of muons produced in $K \rightarrow \mu + \nu$ decay (Coombes et al.)

stopped in a polystyrene target S. Monochromatic positive muons from K_{μ_2} decays in this target lost their energy in the absorbers and finally came to rest in target P, which was placed in a solenoid producing a horizontal magnetic field. Under these conditions the spin of the positive muon will precess in the plane of the drawing. The water-filled Cerenkov counter W stopped protons having the same incident momentum as the positive kaons, and was connected in an anti-coincidence system thus ensuring that pions which were present in large numbers in the positive kaon beam were eliminated. The arrival of a positive kaon in the target S and of a muon from K^+ decay in the aluminium target P was indicated by $\bar{W}ABCDEF\bar{G}H$ coincidences, whilst the appearance of decay electrons was indicated by $32\bar{1}\bar{4}\bar{G}$ (or $456\bar{3}\bar{G}$) coincidences. A special electronic circuit was used to determine the time interval between these coincidence pulses. A definite angle of rotation of the muon spin in the constant magnetic field of the solenoid corresponded to each

such time interval, and the decay curve determined in this way was expected to be modulated in accordance with the law $1 + a \cos(\vartheta_0 - \omega t)$, where a is the asymmetry coefficient for the K_{μ_2} decay and ω the muon spin precession frequency. Fig. 2.8 shows the results obtained in this experiment with

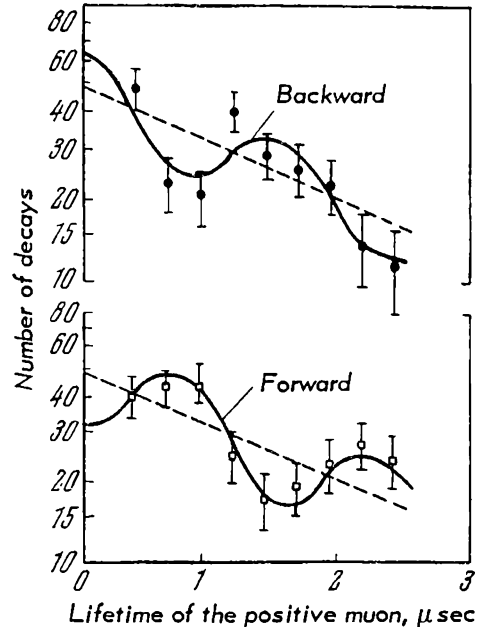


Fig. 2.8 Decay curve for positrons from $K \rightarrow \mu + \nu$ decays; the decay exponential $\exp(-t/\tau)$ is modulated by the sinusoid

with a field of 50 gauss. The number of $\mu - e$ decays per unit interval of time is plotted as a function of the spin precession time (equal to the lifetime). It is evident that the exponential decay curve was in fact modulated by a sinusoid with a period determined by the muon spin precession frequency ω (cf. Equations (2.3) and (2.4)):

$$N(t) \sim e^{-t/\tau} [1 + a \cos(\vartheta_0 - \omega t)]$$

The asymmetry coefficient was found to be

$$a = -0.31 \pm 0.04$$

which is in agreement with the result

$$a = -0.305 \pm 0.033$$

obtained by Coffin et al. [12] who measured the asymmetry in $\pi - \mu - e$ decays when muons came to rest in an aluminium target under approximately the same electron detection conditions (in both cases the range of recorded electrons was in excess of 9.3 g/cm^2). This experiment therefore showed

that muons produced in the decay of pions and K_{μ_2} mesons, i.e.

$$\pi \rightarrow \mu + \nu \text{ and } K_{\mu_2} \rightarrow \mu + \nu$$

have the same longitudinal polarizations. It follows that the helicities of both neutrinos are the same, and therefore the neutrinos which appear together with the muons have the same properties in both decays. The identity of the two neutrinos is also necessary for the validity of the law of conservation of leptons.

2.2 ELEMENTS OF π - μ - e DECAY THEORY

Before we proceed to the basic experimental facts about $\pi - \mu - e$ decay, let us consider the elements of $\mu - e$ decay theory. In accordance with the hypothesis of a universal Fermi interaction, this theory is constructed by analogy with the theory of nuclear β decay. Consider the basic process of nuclear β decay, i.e. the decay of the neutron

$$n \rightarrow p + e^- + \bar{\nu} \quad (2.11)$$

The Hamiltonian for this process will also describe all processes which are obtained from (2.11) by transposing one of the particles in the equation and changing it into the anti-particle, e.g. the capture of an orbital electron

$$p + e^- \rightarrow n + \nu \quad (2.11a)$$

or the inverse β decay

$$p + \bar{\nu} \rightarrow n + e^+ \quad (2.11b)$$

The most general form of this Hamiltonian [1], which takes into account the non-conservation of spatial, charge and temporal parity, is

$$H = \sum_i g_i \bar{(\psi_p)} \Gamma_i \psi_n \bar{(\psi_e)} \Gamma_i \psi_\nu + g'_i \bar{(\psi_p)} \Gamma_i \psi_n \bar{(\psi_e)} \Gamma_i \gamma_5 \psi_\nu \quad (2.12)$$

+ Hermitian conjugates

This expression consists of two parts characterized by the coupling constants g_i and g'_i . The constants g'_i determine effects which occur with non-conservation of parity. Each of the operators $\bar{\psi}_k$ corresponds to the creation of a particle,

indicated by the subscript k , or the annihilation of the anti-particle, while the operator ψ_k corresponds to the annihilation of a particle k (or the creation of the antiparticle). The operators ψ are four-component Dirac spinors and each pair of such spinors is separated by the operator Γ_i or the operator $\Gamma_i\gamma_5$ in those terms of the Hamiltonian which are responsible for the non-conservation of parity. The requirement of relativistic invariance of the interaction leads to the fact that the Hamiltonian may in the most general case consist of the sum of five terms corresponding to the scalar (S), pseudoscalar (P), tensor (T), vector (V) and axial-vector (A) parts of the interaction. The operators Γ_i which correspond to the five types of interaction are

$$\begin{aligned}\Gamma_S &= 1, & \Gamma_P &= -i\gamma_5 \\ (\Gamma_V)_\rho &= \gamma_\rho, & (\Gamma_A)_\rho &= -i\gamma_\rho\gamma_5 \\ (\Gamma_T)_{\mu\nu} &= \frac{i}{2\sqrt{2}} (\gamma_\mu\gamma_\nu - \gamma_\nu\gamma_\mu)\end{aligned}\quad (2.13)$$

where γ_i are the usual Dirac γ matrices and $\gamma_5 = \gamma_1\gamma_2\gamma_3\gamma_4$.

By analogy with nuclear β decay, the decay of the muon

$$\mu^\pm \rightarrow e^\pm + \bar{\nu} + \nu$$

is described by the Hamiltonian

$$H = \sum_i g_i (\bar{\psi}_e \Gamma_i \psi_\mu) (\bar{\psi}_\nu \Gamma_i \psi_\nu) + g'_i (\bar{\psi}_e \Gamma_i \psi_\mu) (\bar{\psi}_\nu \Gamma_i \gamma_5 \psi_\nu) \quad (2.14)$$

in which the operators Γ_i are defined as above, $\bar{\psi}_e$ is the electron creation operator, ψ_ν and $\bar{\psi}_\nu$ are the antineutrino and the neutrino creation operators respectively, and ψ_μ is the muon annihilation operator. Larsen et al. [13], Okun' et al. [14, 16], Kinoshita and Sirlin [15], Sharp and Bach [17] and others have discussed the various consequences which follow from the non-conservation of parity in $\mu - e$ decay. In particular, the above Hamiltonian leads to the following expression for the decay probability of the free muon (in sec^{-1}) in the process $\mu^\pm \rightarrow e^\pm + \nu + \bar{\nu}$:

$$\begin{aligned}dN(x, \vartheta) &= \frac{1}{\pi\tau} \left\{ 3(1-x) + 2\varrho \left(\frac{4}{3}x - 1 \right) \right. \\ &\quad \left. \mp \xi \cos\vartheta \left[(1-x) + 2\delta \left(\frac{4}{3}x - 1 \right) \right] \right\} x^2 dx d\Omega\end{aligned}\quad (2.15)$$

(This formula is obtained if one neglects the rest energy of the electron in comparison with its kinetic energy.) In this expression, $dN(x, \vartheta)$ is the number of decay electrons with energies between x and $x + dx$, which are emitted in the solid element $d\Omega$ at an angle ϑ to the direction of the muon spin at the instant of the $\pi - \mu$ decay. The signs - and + in front of the term including $\cos \vartheta$, which arise as a result of non-conservation of parity, refer to negative and positive muons respectively. The electron energy x in this formula is given as a fraction of the maximum energy which the electron can receive in the decay process ($x = E/E_{\max}$; $E_{\max} \approx 52.8$ MeV). Therefore

$$0 \leq x \leq 1$$

The parameter τ in (2.15) represents the mean lifetime of the muon which is equal to the reciprocal of the total decay probability:

$$\int dN(x, \vartheta) = \frac{1}{\tau}$$

It is evident from the above formula that the shape of the energy spectrum of decay electrons and their angular distribution are determined by the three parameters ϱ , ξ and δ . The first of these is usually called the Michel parameter [18] and characterizes the form of the isotropic part of the electron spectrum. The second parameter δ determines the form of the term in (2.15) which is asymmetric in ϑ , and is analogous to the Michel parameter ϱ in the isotropic part of the spectrum. It is clear that the parameter ξ represents the asymmetry in the angular distribution averaged over the entire spectrum. In fact, on integrating Equation (2.15) with respect to the electron energy between 0 and 1, we find that the angular distribution of the electrons is of the form

$$dN(\vartheta) = \frac{1}{\tau} \left(1 \pm \frac{1}{3} \xi \cos \vartheta \right) \frac{d\Omega}{4\pi} \quad (2.15a)$$

In this expression, $\xi/3 = a$ is called the asymmetry coefficient of the angular distribution; the parameter ξ determines the degree of longitudinal polarization of the muon at the instant of $\pi - \mu$ decay.

The three parameters ϱ , δ and ξ , together with the mean lifetime of the muon, τ , depend on the five pairs of weak-

interaction constants g_i in the Hamiltonian H (Equation (2.14)). We shall not reproduce this dependence here and will only note that the four parameters τ , ϱ , ξ and δ can be measured experimentally. They represent only four relationships between the ten complex (twenty real) constants. It is evident that an experimental determination of τ , ϱ , ξ and δ is insufficient to fix the interaction constants. The situation is not much improved even by the introduction of more complicated experiments, e.g. studies of the polarization of electrons from $\mu - e$ decays.

The Hamiltonian is considerably simplified by the fact that weak interactions are invariant under time reversal. The strongest experimental evidence for this is the decay of polarized neutrons for which there is an experimental correlation between the plane of emission of the electron and the antineutrino, and the spin of the proton. The invariance of weak interactions under time reversal is a consequence of the conservation of combined parity and the so-called CPT-theorem of Pauli and Luders. Invariance under time reversal ensures that the constants g and g' in the Hamiltonian (2.14) are real, and therefore instead of twenty real constants there are only ten

Studies of non-conservation of parity in the β decay of Co^{60} , and in $\pi - \mu - e$ decay which we described above, show that there is a maximum degree of non-conservation of parity in these phenomena. This means that the coupling constants g_i and g'_i in the interaction Hamiltonian, which correspond to terms conserving and not conserving parity, are approximately equal. This is most easily seen, for example, in the experiment of Wu et al. which involved a pure Gamow-Teller transition determined by the axial-vector interaction. Theory [1] shows that the asymmetry of the emitted decay electrons is

$$dN(\vartheta) \sim (1 + A\beta p \cos \vartheta) d\Omega$$

where $\beta = v/c$ is the electron velocity, p the degree of polarization of the Co^{60} nuclei, ϑ the angle between the direction of the spin of the original nucleus and the momentum of the decay electron, and A a coefficient describing the degree of asymmetry which is given by (in the absence of a tensor term in the Hamiltonian)

$$A_{G-T} = \mp \frac{2g_A g'_A}{g_A^2 + g'_A{}^2}$$

Experiment yields $A = 1 \pm 0.05$ from which it follows that the two axial-vector constants are equal. If this result is extended to all the remaining constants, their number is reduced by a factor of 2 and the expression for the interaction Hamiltonian in nuclear β decay (Equation (2.12)) and in muon decay (Equation (2.14)) can be described by five real constants:

$$H_\beta = \sum_i g_i \bar{(\psi_p \Gamma_i \psi_n)} \bar{(\psi_e \Gamma_i (1 + \gamma_5) \psi_\nu)} \quad (2.16)$$

$$H_\mu = \sum_i g_i \bar{(\psi_e \Gamma_i \psi_\mu)} \bar{(\psi_\nu \Gamma_i (1 + \gamma_5) \psi_\nu)} \quad (2.16a)$$

The form of the interaction Hamiltonian is simplified still further in the two-component theory of the neutrino, with the result that out of five constants only two remain.

In this theory the neutrino wave function (we are assuming that the neutrino has negative helicity) satisfies the transformation

$$\gamma_5 \psi_\nu = -\psi_\nu$$

It is readily seen that if we introduce this neutrino into the Hamiltonian (2.16a), which describes the decay of the muon, the terms in the Hamiltonian corresponding to S , T and P interactions will vanish and the only remaining terms will be those corresponding to vector and axial-vector interactions:

$$H_\mu = \sum_{i=V,A} g_i \bar{(\psi_e \Gamma_i \psi_\mu)} \bar{(\psi_\nu \Gamma_i (1 + \gamma_5) \psi_\nu)} \quad (2.17)$$

where

$$(\Gamma_V)_\rho = \gamma_\rho, \quad (\Gamma_A)_\rho = i\gamma_\rho \gamma_5$$

Similarly, the Hamiltonian for the β -decay interaction involving this neutrino will be of the form

$$H_e = \sum_{V,A} g_i \bar{(\psi_n \Gamma_i \psi_p)} \bar{(\psi_\nu \Gamma_i (1 + \gamma_5) \psi_e)} \quad (2.17a)$$

If the helicity of the neutrino is positive, then

$$\gamma_5 \psi_\nu = \psi_\nu$$

The vector and axial-vector interactions are thus removed and the S , P and T interactions remain.

In the two-component theory, the four parameters of

$\pi - \mu - e$ decay (see Equation (2.15)) are given by

$$\frac{1}{\tau} = \frac{\mu^5}{3 \times 2^7 \pi^3} (g_A^2 + g_V^2) \quad (2.18)$$

$$\xi = \frac{g_V g_A^* + g_A g_V^*}{|g_A|^2 + |g_V|^2}, \quad \varrho = \frac{3}{4}, \quad \delta = \frac{3}{4}$$

Moreover, the energy spectrum of the decay electrons and their angular distribution in the two-component theory assume the form

$$dN \sim 2x^2 [(3-2x) + \xi \cos \vartheta (1-2x)] dx d\Omega \quad (2.19)$$

Further simplification of the interaction Hamiltonian is introduced in the $V - A$ theory (Sudarshan and Marshak [20], Feynman and Gell-Mann [21], Sakurai [19]) in which it is assumed that the vector and axial-vector interaction constants are equal and opposite, i.e.

$$g_V = -g_A = g$$

It can readily be shown that in this case the Hamiltonian for the $\mu - e$ decay (2.17) is of the form

$$g (\bar{\Psi}_\mu \gamma_\rho (1 + \gamma_5) \Psi_\nu) (\Psi_\nu \gamma_\rho (1 + \gamma_5) \Psi_e) \quad (2.20)$$

while the Hamiltonian for β decay is

$$g (\bar{\Psi}_n \gamma_\rho (1 + \gamma_5) \Psi_p) (\bar{\Psi}_\nu \gamma_\rho (1 + \gamma_5) \Psi_e) \quad (2.20a)$$

The $\mu - e$ decay parameters given by (2.18) are then

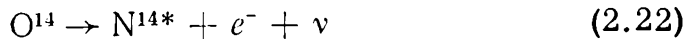
$$\frac{1}{\tau} = \frac{m_\mu^5 g^2}{3 \times 2^6 \times \pi^3} \quad (2.21)$$

$$\xi = 1, \quad \varrho = \delta = \frac{3}{4}$$

Experimental data on $\mu - e$ decay will be discussed in detail below. We shall compare them with the predictions resulting from the adopted form of the Hamiltonian and will see that none of the experiments which have been performed so far are in good agreement with the predictions which follow from the $V - A$ interaction Hamiltonian (2.20). We shall then briefly consider β -decay data in order to establish an agreement, if any, with the Hamiltonian (2.20a).

2.3 LIFETIME OF THE FREE MUON

If the β decay of the neutron and the decay of the muon are described by the same coupling constant, then the coupling constant determined from nuclear β decay should, after substitution into the expression for the lifetime of the muon (Equation (2.21)), yield the correct value for this parameter. We can use for this purpose the value of the coupling constant obtained from the β decay of O^{14} :



This decay involves the pure Fermi transition $0^{+} \rightarrow 0^{+}$ which is described by a Hamiltonian with a unique vector coupling constant. Experimental studies of the electron spectrum and of the lifetime in this decay have been carried out by Bardin et al. [23] who obtained the following result:

$$ft = (3060 \pm 13) \text{ sec}$$

where t is the mean lifetime of the β -active O^{14} nucleus and f the usual dimensionless quantity in the theory of β decay, representing an integral over the β -particle spectrum. In this case, the theory of β decay yields the following expression for the vector constant [24]

$$g_V^2 = 2\pi^3 \frac{\ln 2}{M_F^2} \left(\frac{\hbar}{m_e c} \right)^6 \frac{\hbar}{(ft)_{O^{14}}} m_e c^2 \quad (2.23)$$

where M_F^2 is the matrix element for the decay of O^{14} . Since this matrix element can be computed exactly and is equal to 2, it follows from (2.23) that

$$g_V = (1.416 \pm 0.003) \cdot 10^{-49} \text{ erg cm}^3 \quad (2.24)$$

or, in the system of units in which $\hbar = c = 1$

$$g_V = (1.014 \pm 0.002) \cdot 10^{-5} M^{-2}$$

where M is the proton mass. Using this value for the constant g , we obtain from Equation (2.21)

$$\tau = (2.25 \pm 0.01) \cdot 10^{-6} \text{ sec}$$

This value for the lifetime which is predicted by the $V - A$ theory may be compared with the most accurate measurements of the lifetime of the positive muon given in

Table 2 (Section 1.5). The weighted mean of the four recent most accurate values in this table yields $\tau = (2.2000 \pm 0.0015) \times 10^{-6}$ sec.

The discrepancy between the predicted and measured values of the lifetime of the positive muon does not exceed 2%. This is the most satisfactory evidence at present for the fact that the vector interaction constants in nuclear β decay and in $\mu - e$ decay are equal. From the point of view of the theory of weak interactions, however, this good agreement between the vector interaction constants is a source of worry rather than satisfaction. The point is that the decay of the muon differs from β decay in that the latter involves the participation of strongly interacting particles which are not present in the process $\mu \rightarrow e + \nu + \bar{\nu}$. It will be shown later that this leads to a modification of the axial-vector interaction constant in β decay. Nevertheless the problem arises as to why strong interactions do not affect the vector interaction constant.

An attempt to resolve this problem was made by Feynman and Gell-Mann [21], who introduced the hypothesis of 'conserved vector current'. This hypothesis was based on an idea of Gershteyn and Zel'dovich [25] who pointed out the analogy between electromagnetic interactions which conserve electric charge and the vector interaction in β decay.

The above agreement deteriorates somewhat after the introduction of radiative corrections into the value of $f\tau$ for O^{14} (these corrections change the vector interaction constant for β decay by approximately 0.8%) and into the theoretical value of the muon decay probability. These corrections were calculated by Berman [87] and Kinoshita and Sirlin [96]. The corrected value of the lifetime of the free muon is then

$$\tau = (2.30 \pm 0.05) \cdot 10^{-6} \text{ sec}$$

and the discrepancy with experiment increases to 4%.

Owing to uncertainties in the calculated radiative corrections, this discrepancy can hardly be regarded as significant at the present time.

2.4 ENERGY SPECTRUM OF ELECTRONS FROM $\mu - e$ DECAY. MEASUREMENT OF THE MICHEL PARAMETER ρ

It is important to remember that the only parameter depending on the interaction constants which can be deduced

from studies of the energy spectrum of decay electrons is the Michel parameter ρ . The family of curves shown in Fig. 2.9 represents the spectrum of decay positrons for different values of ρ . All these curves pass through the point $x = 0.75$ and lead to a mean electron energy \bar{x} in the range $x = 0.6-0.7$. As can be seen from Fig. 2.9, the Michel parameter ρ characterizes the 'hardness' of the spectrum: the proportion of slow electrons in the spectrum increases with decreasing ρ . The magnitude of the Michel parameter ρ may be determined by comparing experimental and theoretical spectra. We have seen, however, that this parameter

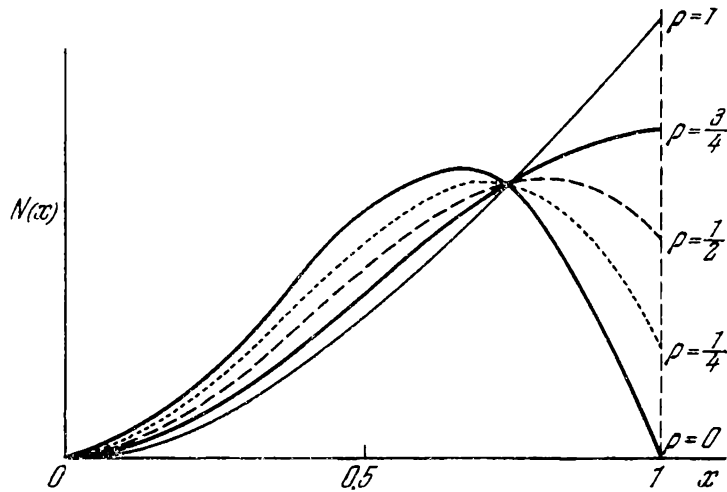


Fig. 2.9 Spectrum of positrons from $\mu-e$ decays for different values of the Michel parameter ρ

represents only one relationship between the ten unknown interaction constants describing $\mu - e$ decay, and therefore the magnitude of ρ provides very little information about the coupling constants. Thus, for example, in the general case, if the decay $\mu \rightarrow e + \nu + \bar{\nu}$ involves all five parts of the interaction, the magnitude of ρ lies between 0 and 1, and if two identical neutrinos are emitted, ρ may lie between 0 and $3/4$.

The situation is considerably simpler in the two-component theory of the neutrino, where, in the case of the $\mu \rightarrow e + \nu + \bar{\nu}$ decay, these ten parameters reduce to the two parameters g_V and g_A . In this theory the Michel parameter ρ should be equal to $3/4$ if the neutrino and antineutrino exist, or 0 if these two particles are indistinguishable, i.e. if $\mu \rightarrow e + 2\nu$ or $\mu \rightarrow e + 2\bar{\nu}$.

This difference in the form of the spectrum in the decays

$$\mu \rightarrow e + 2\nu \quad (2.25)$$

and

$$\mu \rightarrow e + \nu + \bar{\nu} \quad (2.26)$$

has a simple explanation from the point of view of Pauli's principle. At the end of the spectrum, where the electron energy is a maximum, both neutrinos are emitted in the opposite direction to the electron. In the case of (2.25), the emission of two longitudinally polarized neutrinos is forbidden by the Pauli principle and the spectrum of (2.25) falls to 0 as $x \rightarrow 1$. In the case of (2.26), on the other hand, this decay mode is possible since the neutrino and anti-neutrino are different particles. It follows that the shape of the spectrum provides crucial information for the two-component theory: if the neutrino is a two-component particle it is necessary that $\rho = 0$ ($\nu = \bar{\nu}$) or $3/4$ ($\nu \neq \bar{\nu}$).

The shape of the spectrum of decay positrons has been investigated by many workers. However, most of the early work suffered from poor energy resolution and low statistical accuracy. There was also a considerable systematic error in the magnitude of ρ deduced from the shape of the spectrum because the mass of the muon, and hence the upper limit of the spectrum, were not known accurately enough at the time. We shall consider only the most accurate recent measurements of electron spectra. The classical instrument for such measurements is the Wilson cloud chamber or the bubble chamber. We have already seen in Chapter 1 that one of the first spectra of decay electrons was obtained by Leighton et al. By placing a chamber of this kind in a magnetic field of a few kilogauss and selecting for measurements tracks of decay electrons having a total length of a few centimetres, it is possible to achieve a precision of 3-5% in the measured momentum. Rosenson [26] has described an experiment of this kind.

Plano [27] has investigated the spectrum of decay electrons using a 30-cm liquid-hydrogen bubble chamber in a magnetic field of 8800 gauss. The electron momenta were measured to within 1.5% and the spectrum obtained from 9213 $\pi - \mu - e$ decays is indicated by the histogram in Fig. 2.10. The three solid curves represent the calculated spectra for $\rho = 0.85, 0.75$ and 0.65 . The 'best' value of ρ deduced from these data is

$$\rho = 0.780 \pm 0.025$$

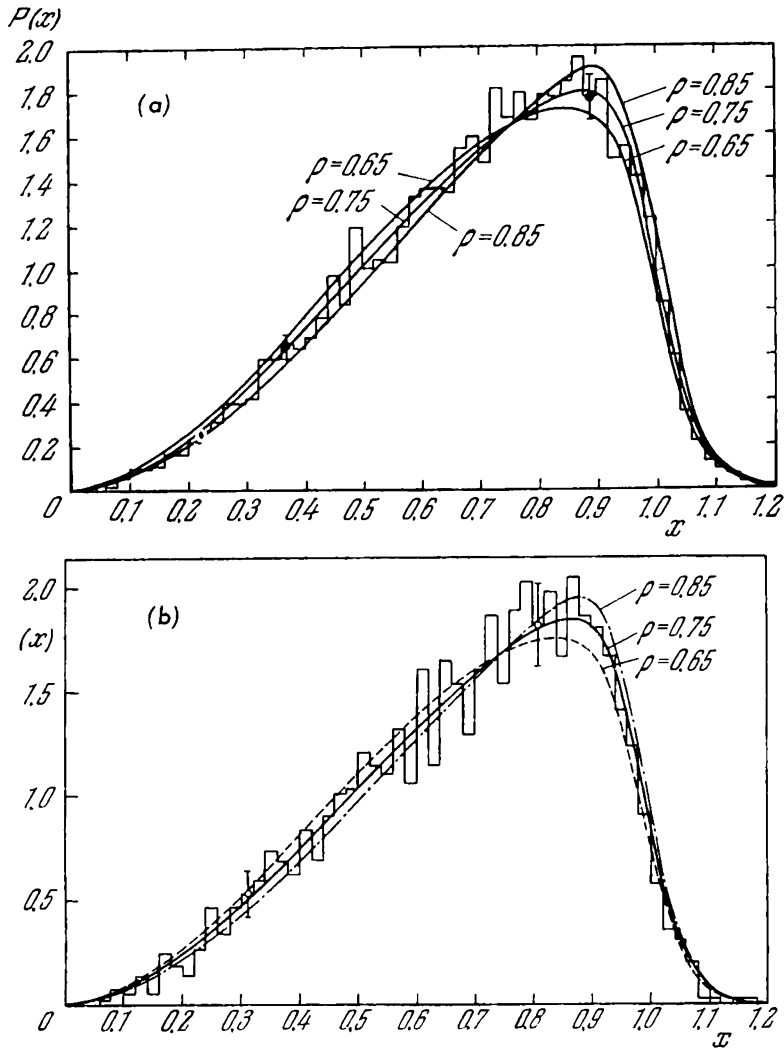


Fig. 2.10 Spectra of positrons from $\mu^+ - e^+$ decays (Plano et al., upper figure) and of electrons from $\mu^- - e^-$ decays (lower figure). The solid and broken curves represent calculated spectra for $\rho = 0.65$, 0.75 and 0.85

Similar measurements on the electron spectrum from μ^- decays were performed by Block et al. [132] using a helium bubble chamber in a field of 14 000 gauss. The resulting spectrum is shown in Fig. 2.10, together with the positron spectrum obtained by Plano et al. As can be seen, the two spectra are identical in shape. The Michel parameter found from the electron spectrum was

$$\rho = 0.751 \pm 0.034$$

The magnitudes of ρ for the electron and positron spectra

must be equal if the positive and negative muons form a particle-antiparticle pair.

Very accurate measurements of the shape of the spectrum, the Michel parameter ρ and the end-point energy were carried out by Anderson et al. [28] with the Chicago synchrocyclotron by investigating the decay of positive pions into electrons and neutrinos. Electrons from $\mu - e$ or $\pi - e$ decays were recorded by a double-focusing magnetic spectrometer (Fig. 2.11). The 62.9-MeV positive-pion beam was absorbed in scintillator 3 after passing through counters 2 and 1. This scintillator served as the source of the decay electrons. After passing through the spectrometer channels, these electrons were focused on counters 4a, 4b, 4c, which defined three adjacent energy ranges. The internal spectrometer channels are illustrated in greater detail in Fig. 2.12 which shows the electron counters 5, 4a, 4b, 4c and the counter source 3 in which the positive pions came to rest. The transmission of the spectrometer was about 1.3% for each of the channels 4a, 4b, and 4c, and the total line width at half-height measured for α particles from a Pu^{239} source was 3.4%. We shall not discuss here the electronic devices which were employed in conjunction with this apparatus, and shall consider only the energy spectrum of electrons

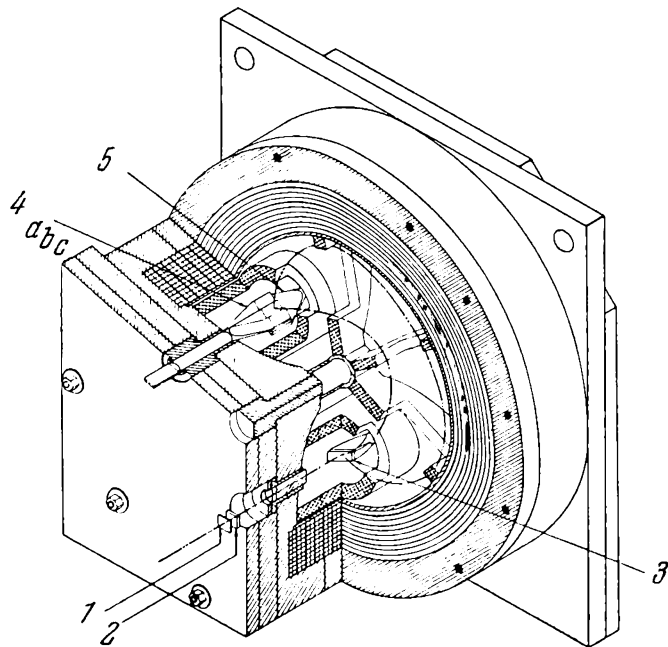


Fig. 2.11 The spectrometer of Anderson et al.

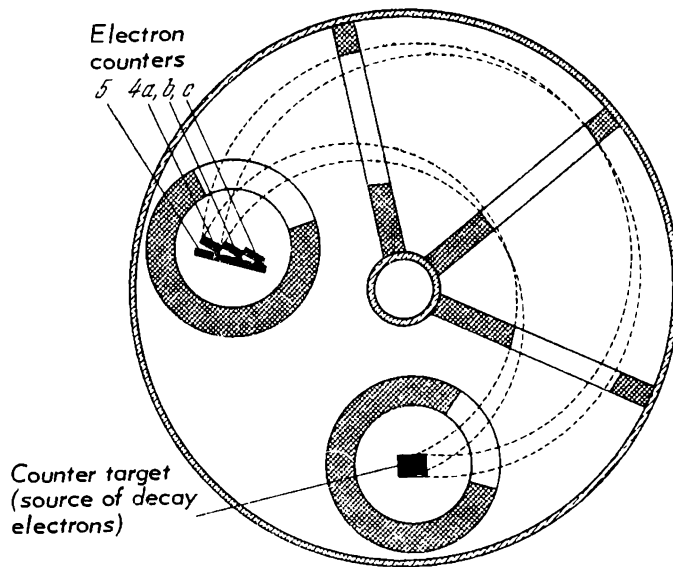


Fig. 2.12 Arrangement of internal channels in the Anderson spectrometer

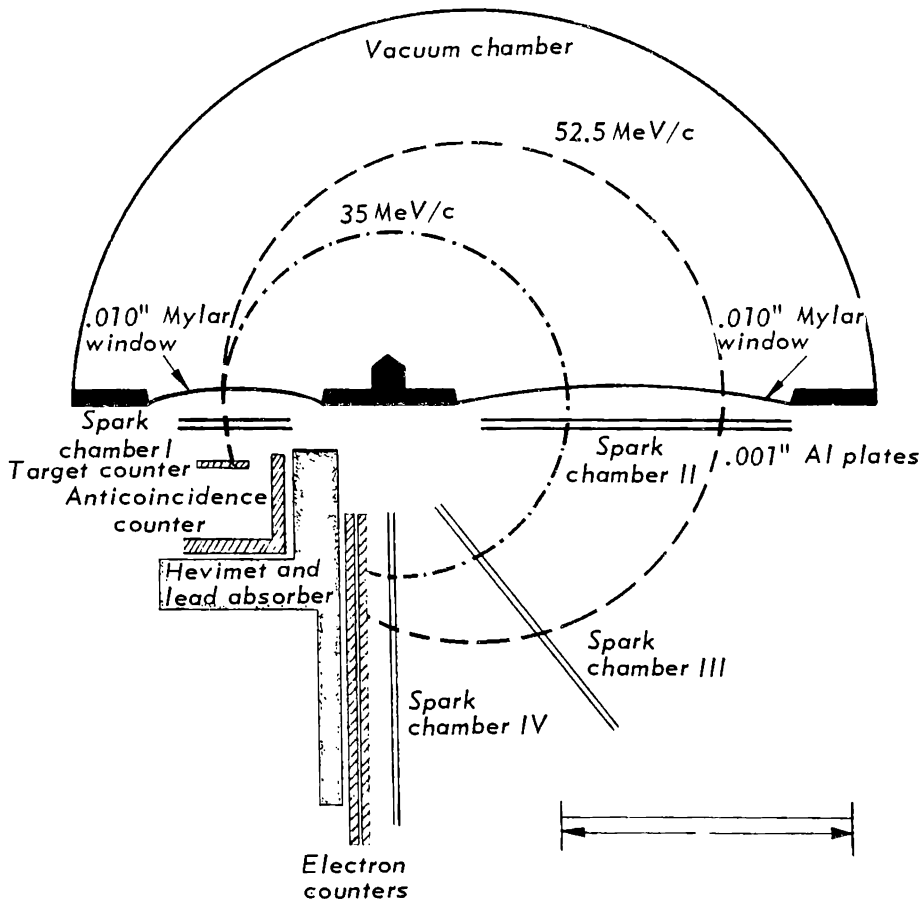


Fig. 2.13 Magnetic spectrometer of Bardon et al. [133] for determination of the positron spectrum from μ -e decays. The broken curve shows positron trajectories for momenta of 35 and 52.5 MeV/c

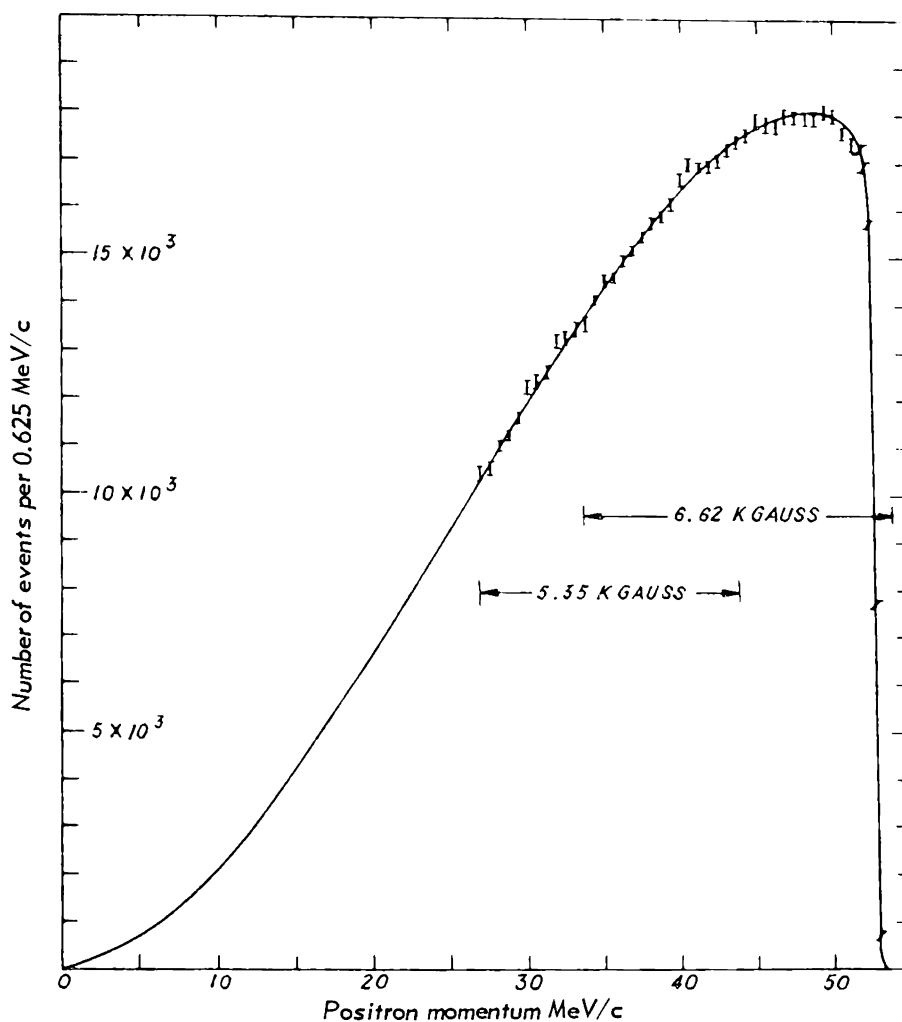


Fig. 2.14 Positron spectrum measured with the Bardon spectrometer. The solid curve corresponds to $\rho = 0.75$ (with corrections)

from $\mu - e$ decays obtained with this instrument. The spectrum from channel 4c is shown in Fig. 2.36, in which the number of electrons per 10^6 coincidences between counters 2 and 3 is plotted as a function of the electron energy in MeV.

The values of the Michel parameter ρ and the maximum electron energy E_{\max} obtained in the three channels 4a, 4b, 4c are given below.

Channel	ρ	E_{\max} , MeV
a	0.76 ± 0.01	53.00 ± 0.32
b	0.77 ± 0.01	52.99 ± 0.32
c	0.77 ± 0.01	53.02 ± 0.32

The most accurate measurements of the shape of the spectrum and of the Michel parameter ρ appear to have been performed by Bardon et al. [133], using a magnetic spectrometer in conjunction with a spark chamber. This experiment

Table 2.1 Summary of data on the measured values of the Michel parameter ρ

Reference	Method	Value of ρ	Particle
[26]	Diffusion chamber in magnetic field	0.67 ± 0.05	μ^+
[27]	Hydrogen bubble chamber in magnetic field	0.780 ± 0.025	μ^+
[132]	Helium bubble chamber in magnetic field	0.751 ± 0.034	μ^+
[28]	Magnetic spectrometer	0.77 ± 0.01	μ^+
[30]	"	0.74 ± 0.02	μ^+
[31]	"	0.68 ± 0.02	μ^+
[133]	Magnetic spectrometer and spark chamber	0.747 ± 0.005	μ^+

is illustrated in Fig. 2.13. The spectrometer vacuum chamber was placed in a magnetic field (5.35 or 6.62 kgauss) and four spark gaps were used to establish the particle trajectory. The coordinates of the spark in each of these gaps were determined with the aid of four microphones located at appropriate points. The microphone signals were fed directly into a computer. The spectrum obtained in this way is shown in Fig. 2.14. Analysis of this spectrum yielded the following values for the Michel parameter and the limiting energy: $\rho = 0.747 \pm 0.005$; $E_{\max} = 52.81 \pm 0.02$ MeV.

The spectrum of electrons from $\mu - e$ decays has also been determined from the multiple scattering of decay electrons in nuclear emulsions. These results [29, 32, 33] are in agreement with the results obtained with magnetic spectrometers but their accuracy is considerably lower. The values of the Michel parameter deduced from the most accurate measurements are summarized in Table 2.1. It is clear from this data that the magnitude of ρ determined experimentally is very close to the value $\rho = 3/4$, which is predicted by the two-component theory of the neutrino for the decay of the muon into an electron, a neutrino and an antineutrino, in accordance with the scheme $\mu \rightarrow e + \nu + \bar{\nu}$.

2.5 MEASUREMENTS OF ASYMMETRY IN THE ELECTRON ANGULAR DISTRIBUTION

We have seen (cf. Equation (2.15)) that the angular distribution of decay electrons averaged over all energies

is of the form

$$dN_{\pm} \sim (1 \pm a \cos \vartheta) d\Omega \quad (2.27)$$

where the asymmetry coefficient $a = \xi/3$. ξ is the degree of longitudinal polarization of the muons at the instant of decay and ϑ is the angle between the spin of the muon and the electron momentum. According to the two-component theory,

$$\xi = -\frac{g_V g_A^* + g_A g_V^*}{|g_V|^2 + |g_A|^2} \quad (2.28)$$

whilst according to $V - A$ theory, where $g_V = g_A = g$, the longitudinal polarization of the muon is unity, and

$$\xi = -1$$

It follows that the prediction of the $V - A$ theory of the Fermi interaction, which demands that

$$|\xi| = 3|a| = 1$$

can be verified by measuring the asymmetry coefficient.

In the first experiment of Garwin et al., it was found that $|\xi|$ was close to unity for muons stopping in the graphite target. Subsequent experiments were performed with the aim of establishing whether $|\xi|$ could in fact be assumed equal to unity. Since the positive muon is partially depolarized prior to decay, the measured asymmetry coefficient may be appreciably less than 1. In the case of depolarization, Equation (2.27) must be replaced by

$$dN \sim (1 + a\kappa \cos \vartheta) d\Omega$$

where κ is a coefficient representing the depolarization of the muon. The nature of the depolarizing interaction will be discussed in detail in Chapter 6. For the moment we shall merely note that there are two main types of depolarization of positive muons. The first of these is the kinematic depolarization. Suppose that the positive muons produced at the instant of decay are completely polarized in the pion's system. The positive muons which come to rest in, for example, the graphite target in the experiment of Garwin et al., originate in $\pi - \mu$ decays in flight, and consist of forward and backward emitted mesons in the pion's system.

Since the Lorentz transformation does not affect the direction of spin, it follows that the spin of muons originating in 'backward' decays is opposite to that of muons originating in 'forward' decays. This is the reason for the kinematic depolarization. Calculations given in Chapter 6 show that kinematic depolarization produced under conditions existing in accelerators may reduce the polarization in the pion's system by 10-20%.

Kinematic depolarization does not occur in the decay of pions coming to rest in emulsions or chambers, and if there were no other reasons for changes in spin direction, the muon would at the end of its 600-micron range have the same polarization as at the beginning. In reality, there is one further depolarization mechanism. At the end of its range the positive muon is slow and capable of capturing an electron, forming a hydrogen-like atom known as muonium. It will be shown in Chapter 6 that the interaction between the magnetic moments of the positive muon and the orbital electron in the muonium atom is the most effective mechanism for the depolarization of positive muons after slowing down in matter.

Having made these preliminary remarks, we will now consider experiments in which the asymmetry coefficient of the angular distribution of electrons was measured under conditions for which the depolarization effects discussed above were reduced to a minimum. In the experiment of Bardon et al. [133], the limiting value of the asymmetry coefficient was determined using positive muons emitted in flight at the maximum possible angle (threshold angle). The muons originated from a 60-MeV positive-pion beam. It is evident that the maximum angle of emission to the pion beam corresponds to the emission of a muon at right angles to the beam direction in the rest system of the pion. For 60-MeV pions the threshold angle is 16.5° . It can readily be seen that positive muons emitted at this angle are transversely polarized. The experiment is illustrated schematically in Fig. 2.15. Counters 2 and 3 (the latter was placed in front of the target) identify positive muons emitted at angles within the range $16.5^\circ \pm 0.75^\circ$ to the pion beam. The circle indicates the position of Helmholtz coils which were used to compensate the fringing magnetic field of the cyclotron. The rotation of the spin of the muon was achieved with the aid of a solenoid wound directly on to the bromoform target in which the muons were brought to rest. Scintillation counters were

used to record decay electrons emitted in the backward ($36\bar{5}$) and forward ($45\bar{6}$) directions between 1.5 and 4.5 μ sec after a positive muon had been stopped in the bromoform target. The pulse produced by a muon stopping in the target ($123\bar{5}$ coincidence) was used to produce a magnetic field in the solenoid for 1 μ sec, and this rotated the spin of the muon

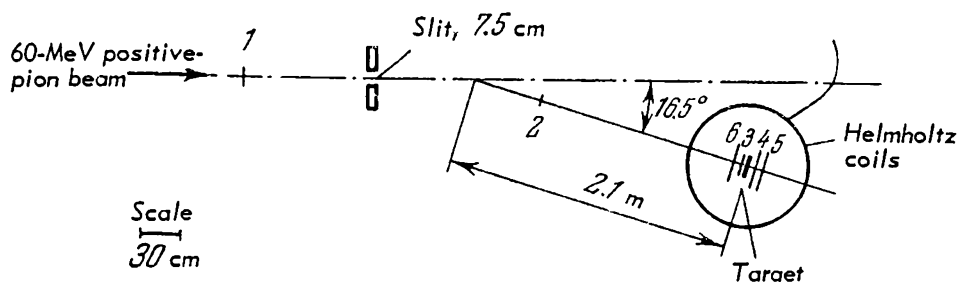


Fig. 2.15 The experiment of Bardon et al. (1–6 are scintillation counters)

through $\pm 90^\circ$ so that the spin pointed towards one of the electron telescopes.

After introducing corrections for the small kinematic-depolarization produced by the finite aperture of the telescope recording the positive muons, and for the angular resolutions and efficiencies of the two electron telescopes, Bardon et al. obtained the following value for the asymmetry parameter:

$$a \geq -0.325 \pm 0.015$$

This agrees to within experimental error with the limiting value $a = -1/3$ predicted by the $V - A$ theory.

Let us consider now the results of experiments in which the depolarization due to the formation of muonium atoms was eliminated. This can be achieved by placing the target in which the $\pi^+ - \mu^+$ decays occur in a strong magnetic field. In fact, the field, H_0 , produced by the positive muon at the electron orbit of the muonium atom is about 1500 gauss. By placing the target in a field $H \gg H_0$ one can decouple the magnetic moments of the nucleus (positive muon) and of the electron, and preserve the polarization of the muon (Paschen-Back effect).

The electron asymmetry in $\mu - e$ decays from positive pions stopping in a hydrogen bubble chamber placed in a field of 8800 gauss was investigated by Plano in the experiments

described earlier. The result was

$$a = -0.31 \pm 0.03$$

It is clear that the results obtained in all of these experiments are very close to the value $a = -1/3$.

2.6 ENERGY DEPENDENCE OF ASYMMETRY IN THE ELECTRON ANGULAR DISTRIBUTION

It is evident from (2.15) that, in addition to the Michel parameter g which determines the form of the isotropic part of the spectrum, the shape of the spectrum is also characterized by the asymmetry parameter δ . The latter parameter determines the dependence of the asymmetry on energy: if the asymmetry is independent of the electron energy, then $\delta = 0$. In the two-component neutrino theory $\delta = 3/4$, which corresponds to maximum asymmetry $x = 1$, at the end of the spectrum.

Moreover, it is evident from (2.15) that the angular distribution of decay electrons is

$$I(\vartheta) d\Omega \sim (1 \pm a \cos \vartheta) d\Omega = \left[1 \mp \xi \frac{1-2x}{3-2x} \cos \vartheta \right] d\Omega$$

It follows from this expression that the asymmetry should be very dependent on energy: it should be zero at the midpoint of the spectrum $[(1-2x)/(3-2x) = 0 \text{ when } x = 1/2]$ and maximum at the end of the spectrum $[(1-2x)/(3-2x) = -1 \text{ when } x = 1]$. At energies smaller than $x = 1/2$ the asymmetry should have a different sign and should increase with decreasing energy. At the beginning of the spectrum the modulus of the asymmetry coefficient is equal to one-third of its value at the end. The dependence of the asymmetry on energy, which is predicted by the two-component neutrino theory, is indicated by the solid curve in Fig. 2.21.

We shall now consider experiments in which the energy dependence of the asymmetry and the magnitude of the asymmetry parameter δ were measured.

In the nuclear-emulsion method, the determination of δ requires a knowledge of both the energy of decay electrons

and their angular distribution relative to the direction of emission of positive muons at the time of pion decay. It is evident from Equation (2.15) that the difference in the energy spectrum of forward and backward emitted particles is independent of ϱ and is determined exclusively by δ . Fig. 2.16 shows the results of such measurements obtained by Weissenberg et al. [29]. The difference in the number of particles emitted in the backward and forward directions for

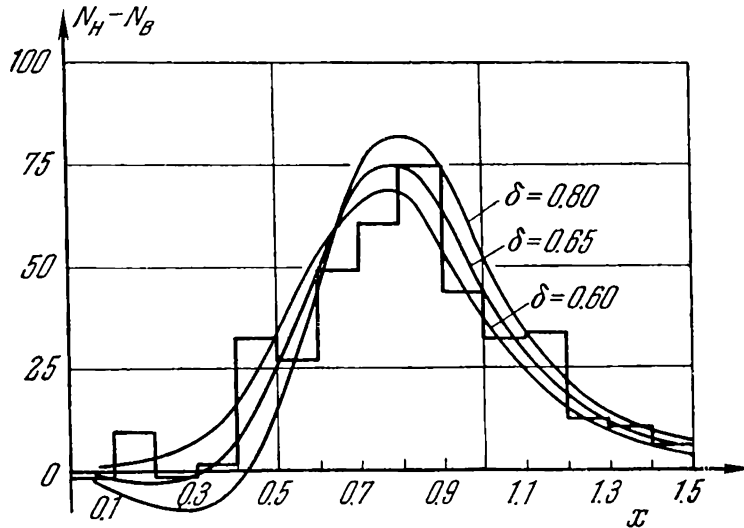


Fig. 2.16 Asymmetry spectrum for $\pi^+ \rightarrow \mu^+ - e^+$ decays in nuclear emulsions. The difference between the number of particles emitted in the backward and forward directions is indicated by the histogram. The solid curves show the expected asymmetry spectra for different values of the asymmetry parameter δ

a momentum interval corresponding to $\Delta x = 0.05$ is plotted as a function of the energy of the decay electrons. The curves indicate the expected difference spectra for $\delta = 0.50, 0.65$ and 0.80 . The 'best' value of δ deduced from these data is

$$\delta = 0.63 \pm 0.12$$

where the uncertainty includes both the statistical and systematic experimental errors. The electron asymmetry in $\mu - e$ decays in nuclear emulsions has also been measured by Babayan et al. [37], Castagnoli et al. [38] and Besson et al. [33]. These workers confirmed the rapid increase in the asymmetry with the electron energy predicted by the two-component neutrino theory.

Bubble-chamber measurements of the asymmetry in the angular distribution of electrons from $\pi - \mu - e$ decays have been carried out by Barmin et al. [39], Alikhanyan et al. [40], Balandin et al. [41], Pless et al. [42] and Alston et al. [43]. All these measurements have shown that the observed asymmetry and its dependence on the electron energy are in agreement with the predictions of the two-component neutrino theory, which requires a rapid increase with increasing energy of the decay electrons.

The most accurate measurements of the energy dependence of the asymmetry appear to have been carried out by Plano with the liquid-hydrogen bubble chamber placed in a magnetic field. We have already discussed this experiment in connection with the determination of the Michel parameter g ; the electron spectrum obtained in this work is shown in Fig. 2.10.

Fig. 2.17 shows the asymmetry spectrum obtained by Plano, i.e. the spectrum of the forward-backward difference.

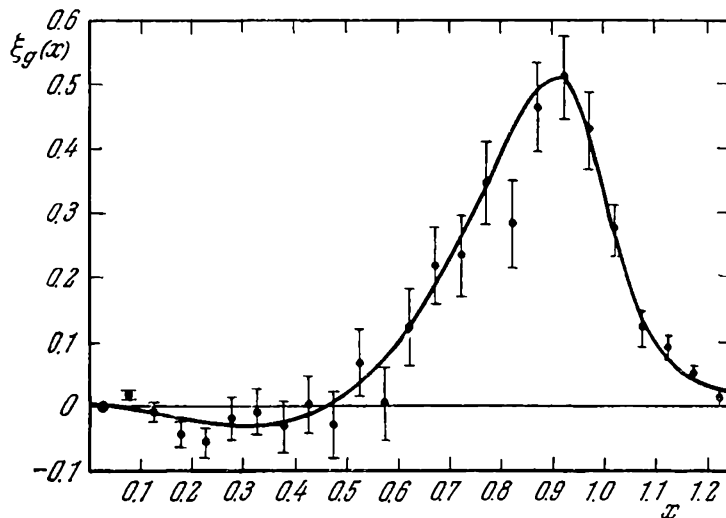


Fig. 2.17 Asymmetry spectrum for $\pi^+ - \mu - e$ decays in a hydrogen bubble chamber (Plano). The solid curve is theoretical and is corrected for instrumental resolution ($\xi = 1$, $\delta = \rho = 3/4$)

It is similar to the corresponding spectrum obtained with nuclear emulsions (Fig. 2.16). The higher precision in the measurement of electron energy and the small statistical errors revealed the presence of details in the spectrum which are predicted by the two-component theory, including the change in the sign of the asymmetry in the low-energy region $x < 0.5$. The magnitude of the asymmetry parameter

was found to be

$$\delta = 0.78 \pm 0.05$$

We shall now consider counter measurements of the dependence of the asymmetry on energy. The first experiment of Garwin et al. [6] did not confirm the rapid increase in the asymmetry coefficient with energy, which was predicted by the theory. They placed absorbers between the counters of the electron telescope 3, 4 (Fig. 2.4) with a thickness of 8 g/cm^2 ($E_e > 25 \text{ MeV}$) and 16 g/cm^2 ($E_e > 35 \text{ MeV}$), and found that there was practically no increase in the maximum-to-minimum ratio. In the first case, the ratio was equal to 1.86 ± 0.20 , and in the second 1.92 ± 0.19 , instead of the expected 2.5. This very small increase in the asymmetry coefficient was due to the emission of γ rays by electrons traversing the absorber. The γ rays were recorded by the counters through secondary phenomena, mainly Compton scattering, and produced an apparent increase in the range of slow electrons, thus masking the increase in the asymmetry coefficient. In the second paper by the Columbia group [44], special precautions were taken to prevent the detection of electrons via their bremsstrahlung; the number of scintillation counters in the electron telescope was increased to three (cf. Fig. 2.1) and the graphite absorber was divided into two parts. In the apparatus of Mukhin et al. [45] the electron telescope consisted of five arrays of scintillation counters with four layers of polyethylene absorber between them. Their results are shown in Figs. 2.18 and 2.19 in which the measured asymmetry is plotted as a function of absorber thickness in g/cm^2 and the corresponding minimum electron energies.

The solid curves represent the variation of the asymmetry with energy predicted by the two-component neutrino theory, corrected for the energy and angular efficiency of the detection system. The experimental data are clearly in agreement with the two-component theory. A similar conclusion was drawn by Cassels et al. [46] who determined the electron energy with a large sodium-iodide crystal (diameter 15 cm, length 12.5 cm) which absorbed the electrons and almost all of their secondary emission.

Kruger and Crowe [47] have used magnetic spectrometers to determine the dependence of the asymmetry coefficient on the electron energy. Their experiment is illustrated schematically in Fig. 2.20. A beam of positive muons, from

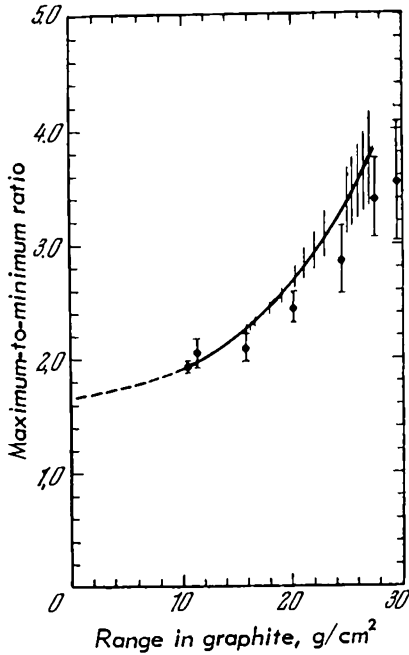


Fig. 2.18 Asymmetry spectrum for $\pi^+-\mu-e$ decays (Weinrich)

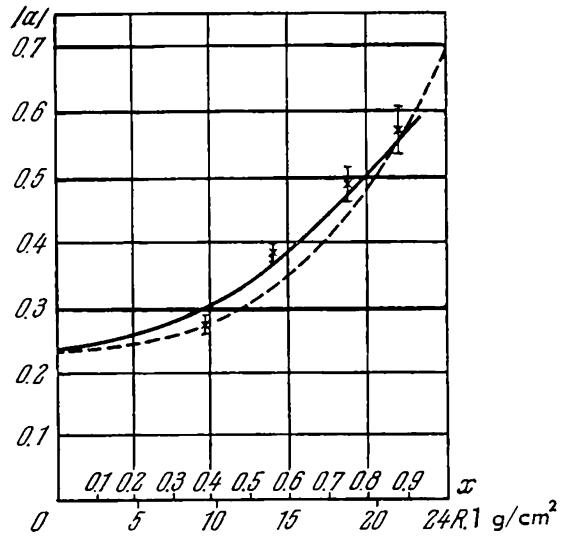


Fig. 2.19 Asymmetry spectrum for the $\pi^+-\mu-e$ decay (Mukhin et al.)

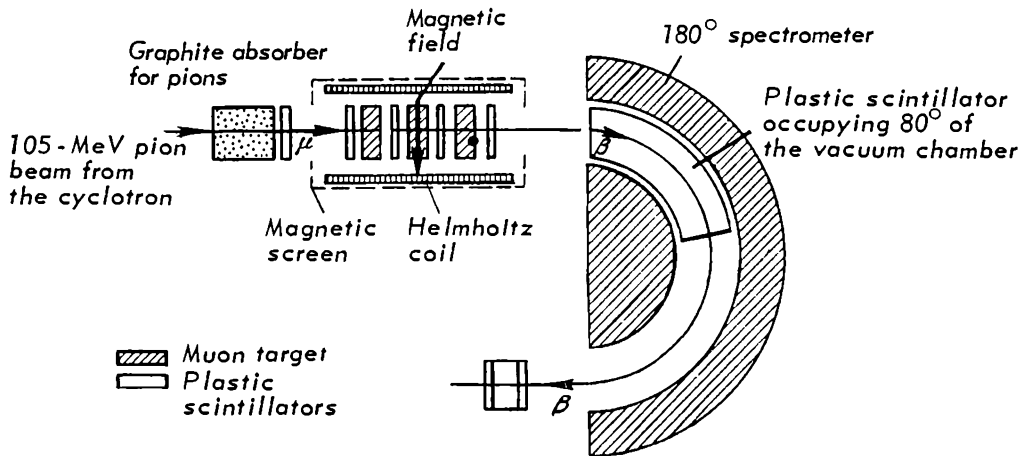


Fig. 2.20 The magnetic spectrometer of Kruger and Crowe

which the pion impurity was removed by an absorber, was stopped in a target surrounded by a magnetic screen. In the absence of a current in the Helmholtz coils, the muons retained their polarization and electrons entering the magnetic spectrometer were the forward electrons, having an intensity $I(0)$. When the Helmholtz coils were energized they produced a field of 55 gauss which caused the muons to precess

at a constant frequency, and therefore the average intensity of decay positrons, $I(H)$, in the presence of the field H was essentially equal to the unpolarized yield, i.e. the symmetric term in (2.19). Knowing $I(0)$ and $I(H)$, and the angular and energy resolution of the instrument, it was possible to calculate the asymmetry coefficient at a particular energy recorded by the spectrometer. The energy dependence of the asymmetry coefficient $a(x)$ which was obtained in this work is shown in Fig. 2.21. It is in good agreement with the two-component neutrino theory.

It may thus be concluded that all the above measurements of kinematic parameters characterizing $\pi - \mu - e$ decay are

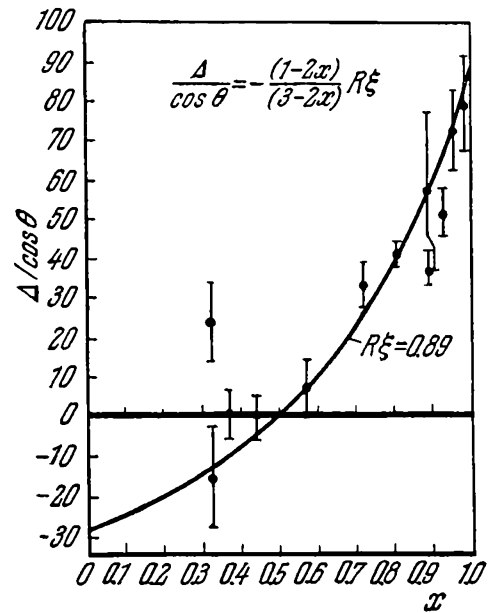


Fig. 2.21 Asymmetry spectrum obtained with the magnetic spectrometer of Krüger and Crowe. The asymmetry coefficient (in %) is plotted as a function of the positron energy. The solid curve shows the asymmetry expected from the two-component theory of the neutrino for $\xi = 0.89$ (11%) depolarization

in good quantitative agreement with the predictions of the weak-interaction theory of the two-component neutrino, with equal and opposite coupling constants for the vector and axial-vector part of the interaction. As experimental accuracy increases, the degree of agreement appears to improve.

2.7 HELICITY OF THE ELECTRON NEUTRINO

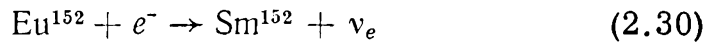
Let us proceed now to the helicity of the particles participating in $\pi - \mu - e$ decay. The experiments which we discussed in Chapter 1, suggest that there are two types of neutrino. If we assume the law of conservation of neutrinos of both types, the decay of pions and muons must

be written in the form

$$\begin{aligned} \pi^+ &\rightarrow \mu^+ + \bar{\nu}_\mu, & \mu^+ &\rightarrow e^+ + \bar{\nu}_e + \bar{\nu}_\mu \\ \pi^- &\rightarrow \mu^- + \bar{\nu}_\mu, & \mu^- &\rightarrow e^- + \bar{\nu}_e + \nu_\mu \end{aligned} \quad (2.29)$$

It follows that both types of neutrino are produced in the decay of the muon.

We shall begin our review of experimental data with measurements of the helicity of the electron neutrino. The most direct determination of the helicity of the electron neutrino was carried out by Goldhaber et al. [48]. This is one of the basic experiments which enables one to distinguish between the possible variants of β decay. The helicity of the neutrino was determined by studying K capture in europium:



The isotope Eu^{152} has a metastable state with zero spin and negative parity (0^-). The capture of a K electron leads to the formation of the Sm^{152*} isotope in the excited state 1^- ; the emission of a γ ray from this state brings Sm^{152} to its ground state (cf. Fig. 2.22). The lifetime of the intermediate state is short enough (approximately 10^{-14} sec) to ensure that recoil nuclei in the solid Eu^{152} source do not lose their momenta before γ -ray emission takes place. Resonance scattering of the emitted γ rays is then possible because of the Doppler effect: it occurs when the moving nucleus emits a photon in the direction of its motion. It is evident that the momentum of the neutrino is then opposite to the direction

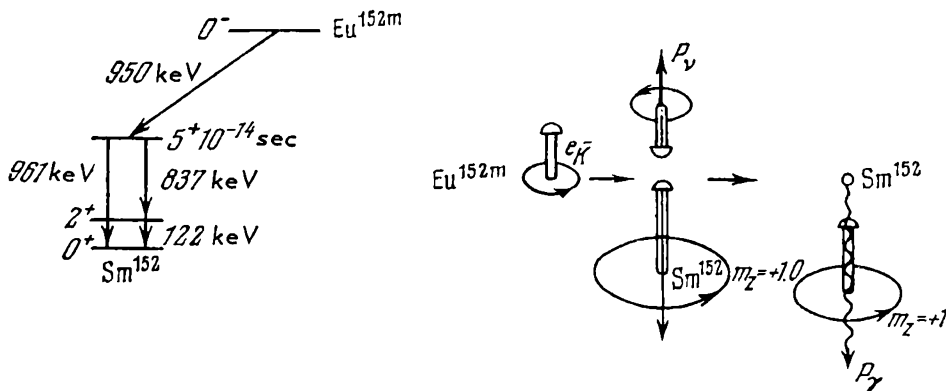


Fig. 2.22 Transition scheme for $\text{Eu}^{152} \rightarrow \text{Sm}^{152}$. The sketch on the right shows the helicities in the case of the emission of a left-handed neutrino in the reaction $\text{Eu}^{152m} + e^- \rightarrow \text{Sm}^{152} + \nu$ and the subsequent emission of a γ ray

of emission of the γ rays. Since orbital electrons captured by the nucleus are S electrons, the sub-states of the intermediate nucleus Sm^{152*} will be described by the following quantum numbers:

$$m = \begin{matrix} -1 \\ +1 \\ 0 \end{matrix}$$

if the neutrino emitted in the z direction has a spin parallel to its momentum (the antineutrino is emitted), and

$$m = \begin{matrix} +1 \\ -1 \\ 0 \end{matrix}$$

if the neutrino is emitted.

The helicity diagram corresponding to the second of these possibilities is shown in Fig. 2.22. In both cases the γ rays (emitted in the $+z$ direction) are circularly polarized. In the first case, their polarization is right-handed, whilst in the second case it is left-handed. The experiment was designed to investigate the passage of these γ rays through magnetized iron. Since the Compton cross-section is different for left-handed and right-handed photons, the number of photons transmitted through the magnetized iron absorber will be different in the two cases.

The experiment is illustrated schematically in Fig. 2.23. The Eu^{152} source was placed immediately in front of the magnetized iron blocks. The γ -ray detector was shielded from the direct γ -ray beam by a lead absorber and was surrounded by a circular scatterer consisting of Sm_2O_3 . γ rays from the source passed through the magnetized iron, underwent resonance scattering in the circular Sm_2O_3 scatterer and then entered the detector. The experiment consisted of measuring the difference in the γ -ray counting rate of the detector for opposite directions of magnetic field in the iron absorber.

The results of this experiment show that the helicity of the γ rays undergoing resonance scattering is negative. It follows that the neutral particle emitted in the K -capture reaction (2.30) is polarized in the direction opposite to the direction of its momentum. The neutrino therefore has negative helicity.

We recall that the two-component neutrino theory predicts

two possibilities for nuclear β decay:

1. Both V and A interactions are present in β decay and the neutrino has negative helicity.
2. The neutrino has positive helicity and only S , P and T interactions occur.

It follows from the above experiment and from the electron-neutrino angular correlation measurements that the first of these two possibilities occurs in β decay.

2.8 THE HELICITY OF ELECTRONS FROM $\mu - e$ DECAY

We shall now consider the experimental determinations of the helicity of electrons from muon decays. These experiments are based on the principle that the bremsstrahlung emitted by longitudinally polarized electrons retains the helicity of the electrons, i.e. is circularly polarized, the direction of polarization being unambiguously related to the helicity of the electrons. The direction of the circular polarization of the bremsstrahlung can be determined from Compton scattering in magnetized iron just as in the experiment of Goldhaber et al. discussed in Section 2.7.

The degree of longitudinal polarization of electrons from $\mu - e$ decays has been calculated by many workers. We

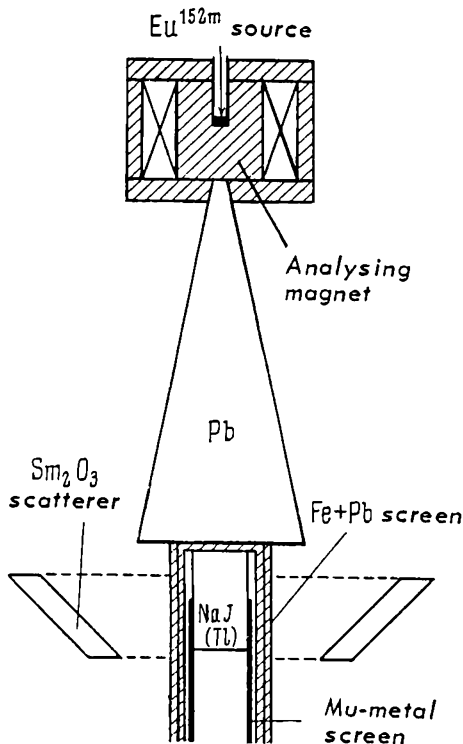


Fig. 2.23 Determination of the helicity of the neutrino (Goldhaber et al.)

shall use the result obtained by Uberall [49] from the two-component neutrino theory:

$$P = \frac{\{[\xi(3 - 2x) + (1 - 2x) \cos \vartheta]^2 + (1 - \xi^2) \sin^2 \vartheta\}^{\frac{1}{2}}}{3 - 2x + \xi(1 - 2x) \cos \vartheta} \quad (2.31)$$

where ξ is the longitudinal polarization of the muon and ϑ the angle between the spin of the muon and the direction of emission of the electron. It follows from this formula that if $\xi = 1$, the electrons are 100% polarized and the polarization is independent of ϑ . Fully polarized muons therefore give rise to fully polarized electrons.

The helicity of electrons from $\mu - e$ decays has been measured by Culligan et al. [50] on the Liverpool accelerator and by Macq et al. [51] at Berkeley. Fig. 2.24 illustrates the experiment of Culligan et al. The $\pi \rightarrow \mu \rightarrow e$ decay took place in the carbon target C. Electrons leaving the target were absorbed in the lead plate and the polarization of the resulting bremsstrahlung was investigated with an analyser consisting of a block of iron magnetized by a special coil and an NaI(Tl) scintillation counter which measured the transmission of the iron absorber with the magnetization parallel and antiparallel to the direction of propagation of the γ rays. One of the main difficulties in this experiment was the shielding of the scintillation counters from the magnetic field. To achieve this, all the photomultipliers were carefully screened with soft iron and mu-metal, and the fringing field of the

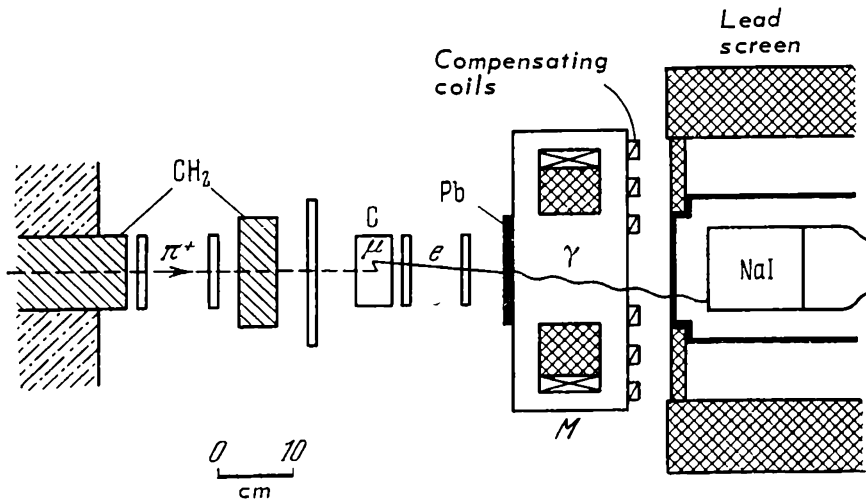


Fig. 2.24 Measurement of the helicity of electrons from $\mu - e$ decay (Liverpool experiment)

magnet near the bremsstrahlung counters was compensated by the special coils indicated in Fig. 2.24. Special checks showed that the effect of the residual field on the operation of the photomultipliers could be neglected.

The system was calibrated with bremsstrahlung from Y^{90} β particles which are known to be highly polarized. The carbon target was replaced by a $150\text{-}\mu\text{C}$ Y^{90} capsule, and the pulse-height spectrum of the NaI(Tl) counter was measured for the two directions of the magnetic field. The result is shown in Fig. 2.25 in which the difference in the counting rates for the two opposite directions of the magnetic field is plotted as a function of energy in MeV. The curve shows clearly the expected increase in analysing power with energy. Experimental results for positive and negative muons are shown in Fig. 2.26 in which the same quantities are plotted along the two axes as in Fig. 2.25. It is evident that there is an effect due to the magnetic field, and that it is opposite in sign for positive and negative muons. The integral effect

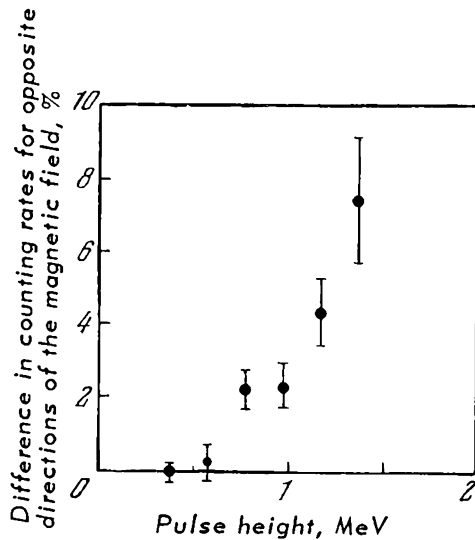


Fig. 2.25 Calibration of the helicity analyser using bremsstrahlung photons due to β rays from a Y^{90} source

for γ rays with energies in excess of 12 MeV is $+4.7 \pm 1.2\%$ and $-5.6 \pm 2.3\%$ for positive and negative muons, respectively. For γ rays with energies greater than 8 MeV the results were $+6.1 \pm 0.7\%$ and $-4.9 \pm 1.5\%$, respectively, which is in agreement with the theoretically expected value for 100%-polarized electrons. The transmission of the magnet for γ rays from positive muons was greater when its north pole faced the γ -ray source. Since the Compton cross-section is a minimum when the photon and electron spins are parallel, this means that the photons, and therefore the original

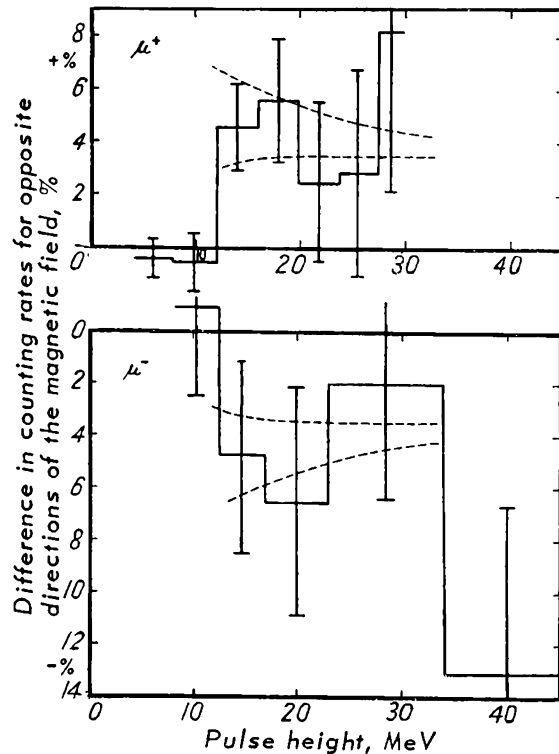


Fig. 2.26 Experimental data on helicity

electrons, had positive helicity. Consequently, electrons from μ -decays have negative helicity.

It is important to note that the above experiments provide direct evidence for the fact that both spatial and charge parity is not conserved in these decays. Consider, for example, the sequence of events in the above experiments. It begins with a meson and ends with bremsstrahlung photons:

$$\pi^+ \rightarrow \mu^+ + \bar{\nu} \rightarrow e^+ + \bar{\nu} + \bar{\nu} \rightarrow \text{right-handed photons}$$

$$\pi^- \rightarrow \mu^- + \bar{\nu} \rightarrow e^- + \bar{\nu} + \nu \rightarrow \text{left-handed photons.}$$

Transition from the first line to the second corresponds to charge conjugation since the charge of all the particles is changed. Charge conjugation therefore results in a change in the polarization of the emitted photons, whereas in the case of charge invariance the polarization should remain constant.

2.9 HELICITY OF MUONS

2.9.1 Helicity of muons from δ -ray showers in magnetized iron

Alikhanov et al. [52] have measured the helicity of muons directly by observing δ -ray showers produced by fast cosmic-ray muons in magnetized iron. Alikhanov and Lyubimov

pointed out that the cross-section for the production of δ rays by positive muons should include both an isotropic term σ_0 and a term σ_S depending on the mutual orientation of the muon and electron polarizations, \mathbf{P}_μ and \mathbf{P}_e . This effect was examined by Berestetskii who obtained the following formula for the cross-section:

$$\sigma(E, \mathbf{P}_e, \mathbf{P}_\mu) dE = (\sigma_0 + \mathbf{P}_e \cdot \mathbf{P}_\mu \sigma_S) dE$$

$$\sigma_0 = \frac{2\pi r_e^2 m_e c^2}{\beta_\mu^2 E^2} \left\{ 1 - \beta_\mu^2 \left(\frac{E}{E_m} \right) + \frac{1}{2} \left(\frac{E}{E_\mu} \right)^2 \right\} \quad (2.32)$$

$$\sigma_S = - \frac{2\pi r_e^2 m_e c^2}{\beta_\mu^2 E^2} \left(1 - \frac{E}{E_m} + \frac{E}{2E_\mu} \right)$$

where E is the kinetic energy of a δ ray. E_m is the maximum energy which may be transferred to the electron and is given by

$$E_m = \frac{E_\mu^2}{E_\mu + \frac{m_\mu^2 c^2}{2m_e}}$$

E_μ is the total energy of the muon.

When the energy of such δ rays is high enough, they can give rise to electron-photon showers in the material in which they are produced. When the energy of the δ ray approaches E_m , the ratio $\sigma_S/\sigma_0 \rightarrow 1$ and the effect of the non-conservation of parity in δ -ray production by muons interacting with polarized electrons is very high. However, in reality, this effect is 'diluted' by the presence of a large number of unpolarized electrons in the magnetized iron, by δ rays with less than the maximum energy and, in the case of cosmic-ray muons, by considerable depolarization of the muons.

The experiment of Alikhanov et al. is illustrated in Fig. 2.27, where I, II, III are counter hodoscopes which could be used to reconstruct the muon trajectory and to determine its sign from the direction of its deflection in the magnetic induction (10^4 gauss) inside the iron core of the permanent magnet A. The δ -ray showers were produced in the iron core B of the closed electromagnet with triangular cross-section in which the magnetic induction was 14 400 gauss. Counter row S recorded showers originating in the lateral

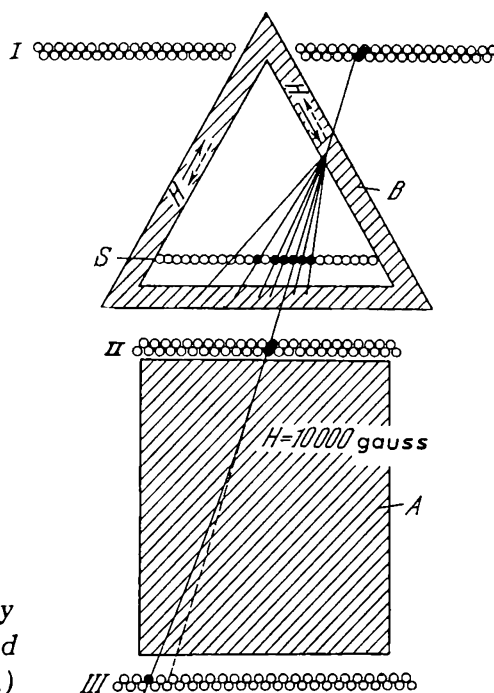


Fig. 2.27 Measurement of the helicity of the muon using δ showers and magnetized iron (Alikhanov et al.)

sides of the triangle. The direction of the magnetic field in the triangle was reversed after each recorded shower. Events were indicated by a coincidence between I, II, and III, and at least three counters in row S. The number of mesons passing through the apparatus was about 500 per minute, of which between one and two generated showers with more than two δ rays; the energies of muons producing these showers lay in the range 3-6.5 GeV.

The final results, expressed in terms of the difference in the number of showers recorded with forward and reverse fields, were as follows:

$$S_+ = -0.37 \pm 0.41 \quad (\text{positive muons})$$

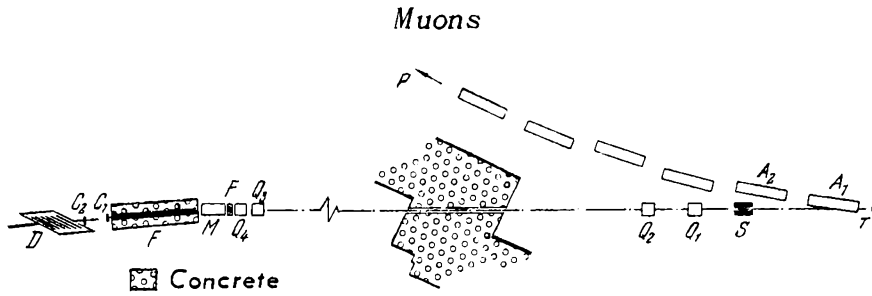
$$S_- = +0.82 \pm 0.42 \quad (\text{negative muons}).$$

It follows that the effect has a sign corresponding to negative helicity of the positive muon. The average value of S is

$$S_{\pm} = 0.58 \pm 0.29$$

while the expected result assuming about 30% polarization of the cosmic-ray muons was approximately 0.3.

A similar experiment was performed on the CERN proton synchrotron by Backenstoss et al. [54] using an 8-GeV negative-muon beam (Fig. 2.28). Negative pions with momenta



P - circulating - proton beam; A - synchrotron magnets;
 s - Pb collimator; Q - quadrupoles; M - dispersing magnet;
 F - graphite filter embedded in concrete; C - counters; D -
 detector

Fig. 2.28 Experimental arrangement

of 12.1 ± 0.3 GeV/c leaving the internal target T were focused by the magnet A₁ on to a 2-cm-wide slot in an 80-cm-long lead collimator. The beam contained about 8×10^5 particles per pulse and was focused by the quadrupoles Q₁ and Q₂. Muons with momenta of 11 GeV/c, which originated from forward pion decays in the 45-m decay path, were focused by the second pair of quadrupoles Q₃, Q₄ through a 760-cm graphite filter F which absorbed about 3 GeV of the meson energy. On leaving the filter the negative-muon beam had an energy of 8 GeV with a spread of about 15%. Counters C₁ and C₂ (7×7 cm²) recorded a muon flux of 2000 particles per pulse. The pion impurity passing through C₁ and C₂ was about 3×10^{-5} of the muon flux. The figure also shows the electron-shower detector D which was in the form of a total absorption counter consisting of twenty interleaved layers of iron and plastic scintillator sheets ($1 \times 30 \times 40$ cm³). Each of the plastic scintillators was viewed by a photomultiplier. The induction in the iron was 20 000 gauss. The shower detector D was calibrated against electrons with energies between 1 and 10 GeV, and was found to be linear with a resolution $\Delta E/E$ varying between 30 and 12% in this energy range. The results obtained are shown in Fig. 2.29 in which the difference in the number of δ -ray showers produced for the two opposite directions of the magnetic field, i.e. the quantity

$$(N_a - N_p)/(N_a + N_p)$$

is plotted as a function of the shower energy. About 1.2×10^7 muons with a longitudinal polarization of about 85% were recorded in 12.5 hours.

The solid curve gives the expected effect for negative

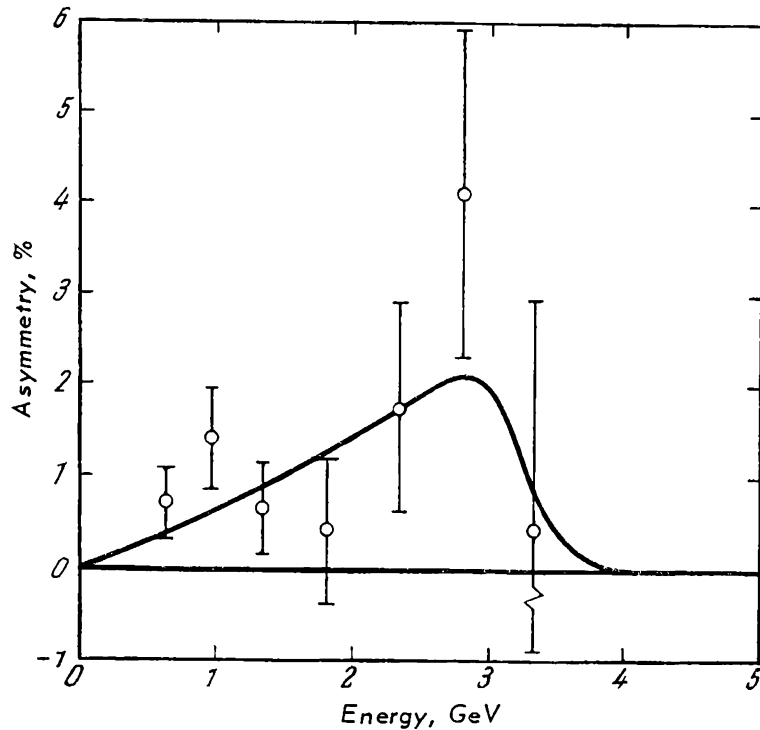


Fig. 2.29 Measurement of the helicity of the negative muon (Backenstoss et al.). The relative difference in the number of showers for the two opposite directions of the field is plotted as a function of the shower energy

muons with positive helicity. The helicity of the negative muon obtained in this experiment was

$$H(\mu) = +1.17 \pm 0.32$$

and is in agreement with the prediction

$$H_{\mu^-} = +1$$

2.9.2 Helicity of muons from the azimuthal asymmetry in Mott scattering

Another important method of determining the helicity of the muon is the determination of the left-right asymmetry in Coulomb scattering of transversely polarized muons by nuclei. This asymmetry was predicted for electrons and positrons by Mott and is due to the interaction between the magnetic moment of the scattered particle and the magnetic moment due to its motion around the scattering nucleus, i.e.

the spin-orbit interaction. The Mott scattering cross-section may be written in the form

$$\frac{d\sigma(\vartheta, \varphi)}{d\Omega} = \sigma(\vartheta) \left[1 + S(\vartheta) \frac{\sigma(\mathbf{p}_1 \times \mathbf{p}_2)}{\sin \vartheta} \right] \quad (2.33)$$

where ϑ is the angle of scattering, \mathbf{p}_1 and \mathbf{p}_2 are unit vectors in the direction of the momentum of the particle before and after scattering, respectively, σ is the direction of the spin of the scattered particle and $S(\vartheta)$ is a parameter representing the asymmetry in Mott scattering. Suppose that the target nucleus (Fig. 2.30) is at the origin of coordinates, and let a transversely polarized muon with spin parallel to

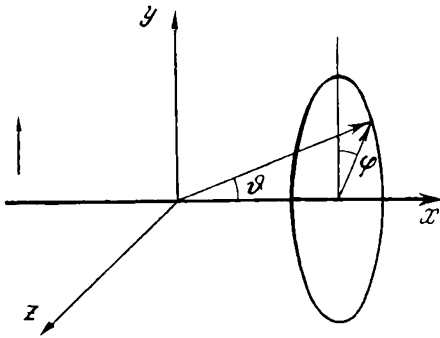


Fig. 2.30 Left-right asymmetry in Mott scattering. The scattering centre is at the origin and the particle approaches along the x axis with spin parallel to the y axis. The cross-section for scattering to the left ($\varphi = -\pi/2$) is $\sigma(\vartheta) [1 + S(\vartheta)]$, while the cross-section for scattering to the right ($\varphi = \pi/2$) is $\sigma(\vartheta) [1 - S(\vartheta)]$

the y axis be incident upon it along the x axis. Suppose further that the circle shown in the drawing represents the locus of the possible end points of \mathbf{p}_2 for scattering at an angle ϑ .

The azimuthal angle φ will be measured from the y axis. It is evident from the formula shown above for the differential cross-section that the number of scatters to the right ($\varphi = \pi/2$) is then given by

$$N \sim [1 + S(\vartheta)]$$

and the number of scatters to the left ($\varphi = -\pi/2$) is

$$N \sim [1 - S(\vartheta)]$$

It follows that $S(\vartheta)$ determines the ratio of the difference in the number of particles scattered to the right and to the left to the total number of scattered particles:

$$S(\vartheta) = \frac{N\left(\varphi = \frac{\pi}{2}\right) - N\left(\varphi = -\frac{\pi}{2}\right)}{N\left(\varphi = \frac{\pi}{2}\right) + N\left(\varphi = -\frac{\pi}{2}\right)} \quad (2.34)$$

Table 2.2

Energy, MeV		Scattering angle θ°			
		15	60	105	150
2.1	δ barn	6200	38	2.8	0.64
	100 $S(\theta)$	0.3	0.2	-5	-17
9.6	δ barn		1.1	0.032	0.0065
	100 $S(\theta)$	340 0.2	-2	-8	-22

Theoretical calculations of the asymmetry in the scattering of polarized muons by nuclei, similar to those performed by Sherman for polarized electrons, have been carried out by Bincer [55], Moroz [56], Frolov [57], Rawitscher [58] and Franklin et al. [59].

As an example illustrating the magnitude of the expected effect, consider the calculated magnitude of $S(\theta)$ for a target nucleus with $Z = 80$ [59] and negative muons with energies of 2.1 MeV ($v/c \approx 0.2$) and 9.6 MeV ($v/c = 0.4$). These calculations were performed for an extended nucleus in the form of a uniformly charged sphere of radius $R = 1.2 A^{1/3} \times 10^{-13}$ cm.

Measurements of the asymmetry in Mott scattering have been carried out for muons by Bardon et al. who used transversely polarized negative muons from negative-pion decays in flight at the threshold angle (as in the experiments on the determination of the polarization of muons, cf. Section 2.4).

The experiment is illustrated in Fig. 2.31. A beam of 43-MeV pions was passed through a system of quadrupole lenses and focused on to a 7.5-cm thick lithium degrader. Pions lost a proportion of their energy in this degrader and entered the region of useful decays with an angular divergence of $\pm 2^\circ$ and an energy of 28 ± 2.5 MeV. Muons selected by the decay angle had a mean transverse polarization of 90% in the plane of decay ($p_y = 0.9$) and a uniform energy distribution in the range 9-33 MeV, which was chosen as a compromise between the maximum back-scattered intensity and the magnitude of asymmetry.

The muons were scattered by lead sheets, 3 having an areal density of 2 g/cm^2 , which were placed on plastic scintillators (Fig. 2.31). The counters 4 were placed to the left and right of each lead plate and detected muons scattered in the lead

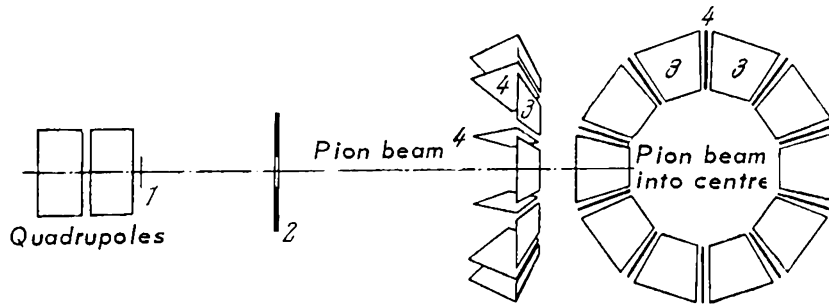


Fig. 2.31 Determination of the helicity of muons from Mott scattering (Bardon et al.)

plate through angles between 105° and 165° . The entire device was repeated cyclically ten times, forming a ring with the pion beam passing through its centre. The entry of a muon into a scatterer was indicated by 123 coincidences (counter 2 was in the form of a ring) and scattering events were detected by $\bar{1}234$ coincidences, followed within 3μ sec by a second count in 4 produced by the decay electron from the scattered muon. This procedure enabled the background of muonic X rays from muons stopping in the lead to be considerably reduced.

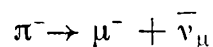
The experiment was carried out for about 100 hours and approximately 3×10^8 muons transits through the scatterers were recorded. The total number of left and right scatters was 515 and 618, respectively, yielding

$$\frac{L-R}{L+R} = -0.090 \pm 0.031$$

The expected asymmetry for $p_y = \pm 1$ was

$$\frac{L-R}{L+R} = \pm 0.09$$

and the experiment demonstrates clearly that the negative muon produced in the decay



has positive helicity (right-handed polarization).

The experimental data on the helicity of particles involved in nuclear β decay and $\pi - \mu - e$ decay which have been considered above are summarized in Table 2.3. This table gives the measured helicities of the following particles: electron neutrinos, electrons and positrons produced in μ decay, and

Table 2.3

	Measurement				Conclusion from conservation of leptons			
Particle	ν_e	e^-	e^+	μ^-	μ^+	ν_μ	$\bar{\nu}_\mu$	$\bar{\nu}_e$
Helicity	-1	-1	+1	+1	-1	-1	+1	+1

negative muons. The helicity of the remaining particles, including the muon neutrino, can be determined by assuming conservation of leptons. For example, consider

$$\pi^- \rightarrow \mu^- + \nu_\mu$$

Since the spin of the negative pion is zero, and the negative muon and the muon antineutrino are emitted in opposite directions, the helicity of the muon antineutrino should be the same as the helicity of the negative muon, i.e. positive. Consequently, muon neutrinos should have negative helicity. It follows that the meson and electron neutrinos (antineutrinos) have the same helicity. We have seen that such neutrinos with negative helicity are necessary for the validity of the V and A interactions in nuclear β -decay and in meson decays. We may therefore conclude that the above measurements of the helicities of leptons confirm the universal nature of weak interactions.

2.10 COMPARISON OF EXPERIMENTAL DATA ON WEAK-INTERACTION CONSTANTS IN β AND μ - e DECAY

It was shown that all experimental data on the decay of the muon are in agreement with the predictions of the $V-A$ theory of $\mu-e$ decay with real, equal and opposite coupling constants:

$$g_V = -g_A = g$$

The hypothesis of the universal Fermi interaction requires that all β -decay phenomena should be explicable by this interaction. In this section we shall consider to what extent experimental data on β decay do in fact satisfy this requirement.

Studies of the angular correlation between electrons and neutrinos in allowed β decays have been an important source of information about the possible interactions governing

nuclear β decay. β -decay theory predicts that this correlation should be of the form

$$1 + a\beta \cdot \cos \vartheta \quad (2.35)$$

where β is the velocity of the electron, ϑ the angle between the direction of emission of the electron and the neutrino respectively, and a a correlation coefficient which depends on the ratio r between the Fermi and Gamow-Teller constants g_F and g_{G-T} :

$$r = \frac{g_F^2 M_F^2}{g_F^2 M_F^2 + g_{G-T}^2 M_{G-T}^2} \quad (2.36)$$

where M_F^2 and M_{G-T}^2 are the squares of the corresponding matrix elements. For a pure Fermi interaction ($0 \rightarrow 0$ transition without parity change), the correlation coefficient is determined exclusively by the vector and scalar interaction constants:

$$a_F = \frac{g_V^2 + g_V'^2 - g_S^2 - g_S'^2}{g_V^2 + g_V'^2 + g_S^2 + g_S'^2} \quad (2.37)$$

and when $g_S = g_S' = 0$ we have $a_F = 1$.

For a pure Gamow-Teller transition the correlation coefficient depends only on the axial-vector and tensor constants:

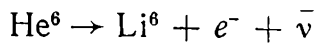
$$a_{G-T} = \frac{1}{3} \frac{g_T^2 + g_T'^2 - g_A^2 - g_A'^2}{|g_T|^2 + |g_T'|^2 + |g_A|^2 + |g_A'|^2} \quad (2.38)$$

If the decay is governed exclusively by the axial-vector constant ($g_T = g_T' = 0$) then $a_{G-T} = -1/3$. In intermediate cases the correlation coefficient is given by

$$a = a_F r + a_{G-T} (r - 1)$$

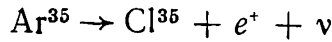
Results of recent experiments are shown in Fig. 2.32 where the electron-neutrino correlation coefficient a is plotted as a function of r . The straight line in this figure represents the expected correlation coefficient when only V and A interaction constants are involved. The rectangles represent experimental data; their width gives the errors in r and their height errors in the correlation coefficient a .

The decay



is a pure Gamow-Teller transition. The expected correlation coefficient for this case is $a = -1/3$, while the experimental result obtained by Herrmannsfeldt et al. [61] is $a = -0.39 \pm 0.2$.

In the case of



we have a pure Fermi transition for which the expected correlation coefficient is $a = 1$. The experimental values obtained by Allen et al. [62] and Herrmannsfeldt et al. [63] respectively are

$$a = +0.85 \pm 0.12$$

$$a = +0.93 \pm 0.14$$

These data imply therefore that only axial-vector and vector interactions participate in nuclear β decay. This conclusion is also confirmed by the other results shown in the graph, i.e. the decay of Li^8 (Lauterjung et al. [64]), Ne^{19} (Alford and Hamilton [65], Maxson et al. [66], Good and Lauer [67]), Ne^{23} (Ridley [68]) and by the data of Burgov and Terekhov [69] who investigated the angular correlation of cascade γ rays in the decay of Na^{24} . In this case, the

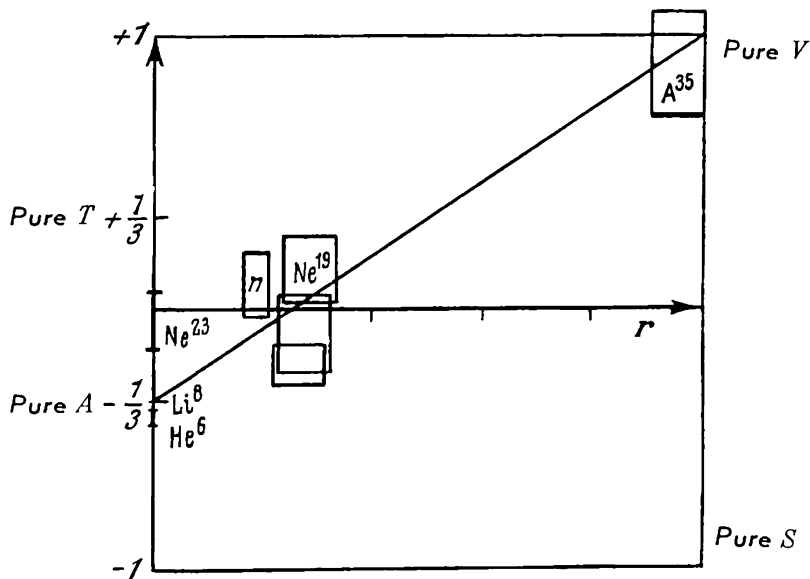


Fig. 2.32 Electron-neutrino correlation in β decay

contribution of the Fermi interaction was small and the correlation coefficient was expected to be $-1/3$. By placing a resonance absorber in the path of the γ rays, these workers observed Doppler broadening of the angular distribution of the γ rays due to the motion of recoil nuclei. The result obtained by Burgov and Terekhov was $a = -0.15 \pm 0.22$.

Let us consider now the experimental data on the angular distribution of electrons from the decay of polarized neutrons. This experiment was carried out by Burgy et al. [70] who used a polarized neutron beam produced by reflecting neutrons from a magnetized cobalt mirror [71].

The theory of β decay yields the following expression for the angular distribution of electrons from the decay of polarized neutrons:

$$dN \sim (1 + A\beta\rho \cos \vartheta) d\Omega \quad (2.39)$$

where ρ is the polarization of the neutron beam, $\beta = v/c$ is the velocity of the decay electrons and A is given by

$$A = -\frac{2(R^2 + R)}{3R^2 + 1}$$

where

$$R = \frac{g_A}{g_V}$$

For $g_A = -g_V$ the asymmetry coefficient should be zero, and hence $A = 0$. The experiment of Burgy et al. yielded $A = -0.11 \pm 0.02$. If we assume the $V - A$ interaction, and that the neutrino has negative helicity, we have

$$R = \frac{g_A}{g_V} = -1.25 \pm 0.03$$

The square of the ratio of these constants can also be obtained from data on the energy spectrum and lifetime of neutrons and certain nuclei undergoing $0^+ \rightarrow 0^+$ transitions. The most accurate determination of the lifetime of the neutron is due to Sosnovskii et al. [72] who found that

$$\tau = 11.7 \pm 0.3 \text{ min}$$

The quantity R^2 deduced from these measurements is 1.42 ± 0.08 . The mean value of R^2 is therefore 1.49 ± 0.06 , which

corresponds to

$$R = \frac{g_A}{g_V} = -1.22 \pm 0.03 \quad (2.40)$$

It follows from these experiments that the ratio $\frac{g_A}{g_V}$ is not equal to -1 as predicted by the $V - A$ theory. This increase of approximately 20% in g_A in nuclear β decay is explained in the theory by the renormalization of the axial-vector constant which is due to the fact that strongly interacting particles participate in nuclear β decay. This renormalization of g_A does not occur in $\mu - e$ decay

$$\mu \rightarrow e + \nu + \bar{\nu}$$

which involves only weakly interacting particles. We have already seen in our discussion of the muon lifetime data that the vector interaction constant g_V is unaffected by strong interactions. In view of the above results, the Hamiltonian for β decay (see Equation (2.20)) should be written in the form

$$H = g(\bar{\Psi}_n \gamma_\rho (1 - R \gamma_5) \Psi_p) (\bar{\Psi}_\nu \gamma_\rho (1 + \gamma_5) \Psi_e) \quad (2.41)$$

with $R \approx -1.22$.

2.11 DECAY OF THE PION INTO AN ELECTRON AND A NEUTRINO

It follows from the existence of the universal Fermi interaction that in addition to the usual decay of the pion into a muon and a neutrino, one should also be able to observe the decay of the pion into an electron and a neutrino:

$$\pi \rightarrow e + \nu$$

Theoretical estimates of the relative probability of this decay mode have been based on the assumption that the pion may be regarded as an intermediate state of a virtual pair of particles consisting of a nucleon and an antinucleon. Thus, for example, the positive pion has been regarded as a state of the proton-antineutron pair ($p\bar{n}$), the negative pion as a state of the neutron-antiproton pair ($n\bar{p}$), and so on. The decay of the pion is then described as the annihilation of this pair into a muon and a neutrino, which occurs via the weak

interaction

$$\pi \rightarrow N + \bar{N} \rightarrow \mu + \nu$$

The universal nature of the weak interaction also means that the pion can decay into an electron and neutrino:

$$\pi \rightarrow N + \bar{N} \rightarrow e + \nu$$

Fig. 2.33 shows the Feynman diagram for such processes.

No information is available at present about the absolute probability of these processes. It is possible, however, to predict the probability ratio for muon and β -decay modes of the pion. In particular, since the pion is a pseudoscalar particle, this transition is only possible in weak-interaction theory with pseudoscalar or axial-vector coupling. Calculations of this kind were carried out as long ago as 1949 by Ruderman and Finkelstein [73] and Steinberger [74] who showed that for pseudoscalar coupling, the decay probability ratio for the $\pi \rightarrow e + \nu$ and $\pi \rightarrow \mu + \nu$ decay modes is

$$R = \frac{\omega(\pi \rightarrow e + \nu)}{\omega(\pi \rightarrow \mu + \nu)} \approx \frac{M_\pi^2 - M_e^2}{M_\pi^2 - M_\mu^2} = 5.4 \quad (2.42)$$

i.e. the case of pseudoscalar coupling may be rejected. For the axial-vector interaction

$$R = \frac{\omega(\pi \rightarrow e + \nu)}{\omega(\pi \rightarrow \mu + \nu)} \approx \frac{M_\pi^2 - M_e^2}{M_\pi^2 - M_\mu^2} \cdot \frac{M_e^2}{M_\mu^2} = 1.36 \cdot 10^{-4} \quad (2.43)$$

This result became particularly important after the discovery of the non-conservation of parity which led to a $V - A$ theory restricting all possible interactions in β decay to the vector and axial-vector variants. Practically all experimental data on β decay were eventually found to be in agreement

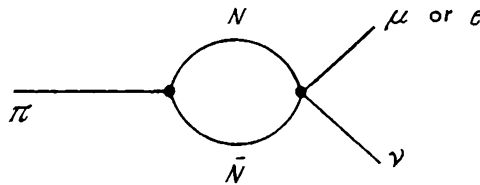


Fig. 2.33 Feynman diagram for the process $\pi \rightarrow \mu + \nu$ or $e + \nu$ when the pion is regarded as an intermediate state of a nucleon-antinucleon pair

with this theory, and only the absence of $\pi \rightarrow e + \nu$ decay could become critical for the theory.

The search for the electron decay of the pion was a difficult experimental problem. The early work by Friedman and Rainwater [75], Lokanathan and Steinberger [76] and Anderson and Lattes [77] did not lead to the discovery of this decay mode, since the sensitivity and reliability of the experimental methods were either inadequate or only just within the necessary range. It was not until 1958 that the existence of this decay mode was demonstrated with adequate reliability.

Experimentally, the problem was to isolate a monochromatic β line with energy of about 70 MeV originating in $\pi \rightarrow e$ decays against a background of a much larger number of betas from $\mu - e$ decays having a continuous energy spectrum with a cut off at about 53 MeV. In the experiment of Lokanathan and Steinberger [76], the separation of monochromatic electrons from $\pi \rightarrow e$ decays from electrons belonging to the continuous $\mu \rightarrow e$ spectrum was carried out by the absorption method with appropriate filters in the electron telescope. An additional criterion was the time distribution of the electron pulses: since the $\pi \rightarrow e$ decay occurs with the lifetime of the pion, events due to $\pi \rightarrow e$ decays should be recorded mainly in 'fast' coincidences, while the slow coincidences should be mainly due to $\mu \rightarrow e$ electrons.

No $\pi \rightarrow e$ decays were recorded in this experiment, and after an analysis of the sensitivity of the apparatus, Lokanathan and Steinberger concluded that the probability of the $\pi \rightarrow e$ decay was not more than 1 in 17 000. In view of the fact that many of the estimates in their experiments were very approximate, in particular, the estimated efficiency of the electron telescope may have been too high, it may be concluded that their result is not in sharp conflict with the theory which requires the ratio to be 1:9000.

Fazzini et al. [78] and Ashkin, Fazzini et al. [79] used the same basic principle as Lokanathan and Steinberger. However, they improved the method with the result that the apparatus became more sensitive to $\pi \rightarrow e$ decays. The main improvement was a considerable increase in the efficiency of the electron telescope, and the improvement in the time resolution of pulses from $\pi \rightarrow \mu \rightarrow e$ and $\pi \rightarrow e$ decays. The experiment is illustrated in Fig. 2.34. The electron telescope consisted of eight scintillation counters (5.12) separated by seven graphite absorbers. Coincidences 1234

(counter 3 served as the target in which the pion came to rest) signalled pions stopping in counter 3. Coincidences 5-12 indicated decay electrons. A fast coincidence circuit recorded all coincidences between counters 1, 2, 3, $\bar{4}$ and counters 5-12 in the time interval between 60 and 160 nsec after the arrival of a pion ($123\bar{4}$). In the presence of such coincidences, pulses from counters 3 and 12 were fed into a 'fast' oscilloscope and the wave-form was photographed. The pulse from the large NaI counter at the end of the electron telescope was also displayed on this oscilloscope.

A typical oscilloscope trace for the usual $\pi \rightarrow \mu \rightarrow e$ decay is shown in Fig. 2.34 (top left). The π and μ pulses originated in counter 3 as a result of the arrival of a pion and its decay into a muon. Pulse e (3) from counter 3 is produced by a decay electron. The same electron produced coincidences 5-12 and the pulse from counter 12, which can also be seen on the trace.

The second trace from which the muon pulse is absent may have been due to the $\pi \rightarrow e$ mode, but it may also have been due to the usual $\pi \rightarrow \mu \rightarrow e$ decay in which the muon pulse was not resolved by the scintillation counter, or a random coincidence between pulses ($123\bar{4}$) and (5-12). To separate true $\pi \rightarrow e$ decays from the background of unresolved $\pi \rightarrow \mu \rightarrow e$ decays and random coincidences, Fazzini et al. investigated the number of $\pi \rightarrow \mu \rightarrow e$ and $\pi \rightarrow e$ decays as a function of the thickness of the absorber in the electron

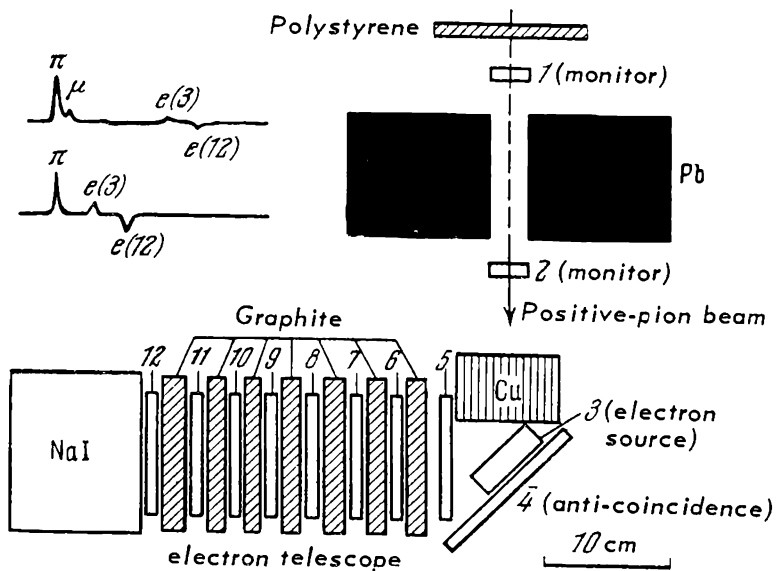


Fig. 2.34 The search for π - e decay mode (Fazzini et al.)

telescope, and the distribution of these decays in time. Total absorption of electrons from $\mu \rightarrow e$ decays requires 30 g/cm^2 of carbon. Forty $\pi \rightarrow e$ decays were observed at thicknesses of about 30, 31, 32 and 34 g/cm^2 in which pulses from the pion and electron were separated by more than 8.3 nsec. The time distribution of these forty decays was in agreement with the lifetime of the positive pion ($\tau_{\pi^+} = (22 \pm 4) \text{ nsec}$). These data therefore provide a very definite indication of the existence of the $\pi \rightarrow e$ decay mode.

Ashkin, Fazzini et al. estimated the probability of the $\pi \rightarrow e + \nu$ decay mode, using the efficiency of the electron telescope calculated by the Monte Carlo method. The result was

$$R = \frac{\omega(\pi \rightarrow e + \nu)}{\omega(\pi \rightarrow \mu + \nu)} = (1.22 \pm 0.30) \cdot 10^{-4}$$

The electron decay of the pion has also been detected in bubble-chamber photographs by Impeduglia et al. at Columbia University [80]. A liquid-hydrogen bubble chamber of diameter 30 cm and depth 15 cm was placed in a field of 8800 gauss and was exposed to a beam of slow positive pions. On the average, the chamber recorded about ten stopping pions per picture. In most cases the observed decay electrons were due to the decay of muons originating from pion decays, and the complete $\pi \rightarrow \mu \rightarrow e$ sequence was clearly seen on the photographs. In approximately one case out of forty, the intermediate slow muon was not observed. Such electrons originated either from the decay of stopping muons produced in the decay of pions in flight, or (this is less likely) as a result of $\pi \rightarrow e + \nu$ decays. To isolate the exceedingly rare cases of $\pi \rightarrow e + \nu$ from $\mu \rightarrow e$ decays, the momentum of the decay electrons was determined from their deflection in the magnetic field (the maximum momentum of electrons from $\mu \rightarrow e$ decays is $53 \text{ MeV}/c$, while $\pi \rightarrow e$ decays yield monochromatic electrons with momentum of about $70 \text{ MeV}/c$).

Out of a total number of 65 000 $\pi \rightarrow \mu \rightarrow e$ decays, there were 1766 events in which the slow intermediate muon could not be seen. Moreover, the positron spectrum for 2983 $\pi \rightarrow \mu \rightarrow e$ decays was carefully determined and it was seen that in none of these cases did the energy of the electrons exceed 62 MeV, while in the spectrum of the $\mu \rightarrow e$ decays shown in Fig. 2.35 there are six values of energy near 70 MeV. They therefore had to be ascribed to $\pi \rightarrow e$ decays. The mean

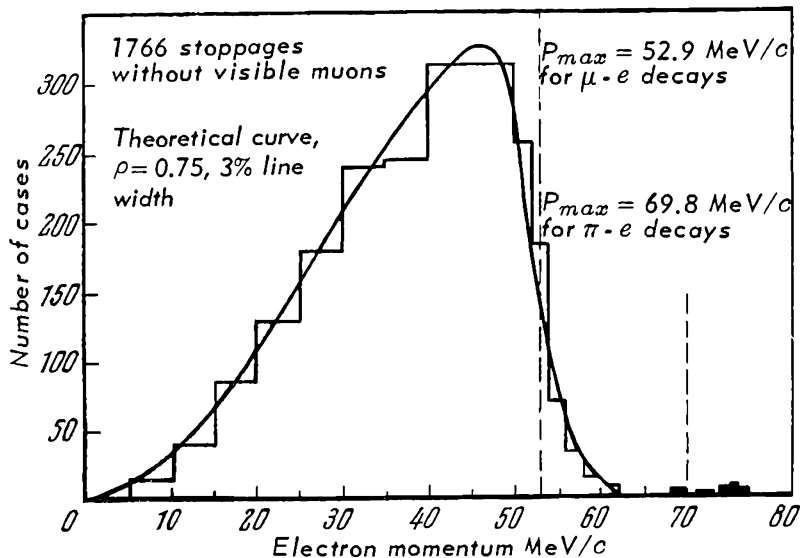


Fig. 2.35 The spectrum of positrons from $\mu \rightarrow e$ decays obtained with a hydrogen bubble chamber. Histogram—experimental data, solid curve—expected spectrum for $\rho=0.75$. The spectrum of $\mu \rightarrow e$ decays cuts off at about 55 MeV. The six particles from $\pi \rightarrow e$ decays have energies of about 70 MeV

energy for these six cases was 72.9 ± 1.5 MeV, which is higher than the expected value of 69.8 MeV. The discrepancy may be due to systematic calibration errors.

Let us consider now the experiments of Anderson and Lattes [77] and Anderson et al. [81], the latter being a continuation of the former. In these experiments, the group of monochromatic 70-MeV electrons from $\pi \rightarrow e$ decays was separated from electrons due to $\mu \rightarrow e$ decays by means of the magnetic spectrometer described in Section 2.4. In the first experiment [77], the electron decay mode was not detected, and it was deduced from the estimated sensitivity of the apparatus that the relative probability of $\pi \rightarrow e$ decays could not be greater than 2×10^{-5} . After the electron decay was detected in the experiments described above, Anderson et al. [81] repeated the experiment with improved electronic equipment. The magnetic spectrometer which they employed has already been discussed (cf. Figs. 2.15 and 2.16). Instead of the single detector of decay electrons used in [77], the new instrument incorporated the three scintillators 4a, b, c at the exit of the spectrometer which recorded electrons in three adjacent energy intervals. We shall not discuss here the relatively complicated electronic equipment employed in this experiment, and will merely note that the $\pi \rightarrow e$

decays were indicated on the screen of an oscilloscope by a large positive pulse produced by a pion stopping in counter 3, a smaller positive pulse produced by the electron leaving counter 3 and a negative pulse produced by the electron entering counter 5. The time interval between the first two positive pulses was equal to the lifetime of the pion in the target counter 3. As a control experiment, the mean lifetime of the positive pion was estimated from the distance between pulses from counters 2 and 3. The result was

$$\tau_{\pi} = (25.6 \pm 0.8) \cdot 10^{-9} \text{ sec}$$

Electron energy spectra from $\pi - \mu - e$ decays obtained with this spectrometer have been discussed earlier in connection with the Michel parameter ρ .

Fig. 2.36 shows spectra of electrons from $\pi - \mu - e$ and $\pi - e$ decays obtained with this instrument. The number of $\mu - e$ and $\pi - e$ coincidences per 10^7 coincidences between counters 2 and 3 is plotted as a function of electron energy in MeV. It should be noted that the scale for the $\pi - \mu - e$ decay is greater by a factor of 200.

The relative probability of $\pi - e$ decay

$$R = \frac{\omega(\pi \rightarrow e + \nu)}{\omega(\pi \rightarrow \mu + \nu)}$$

was found to be $R = (1.21 \pm 0.07) \times 10^{-4}$. Theory, including radiative corrections to $\pi - e$ decay, yields 1.23×10^{-4} .

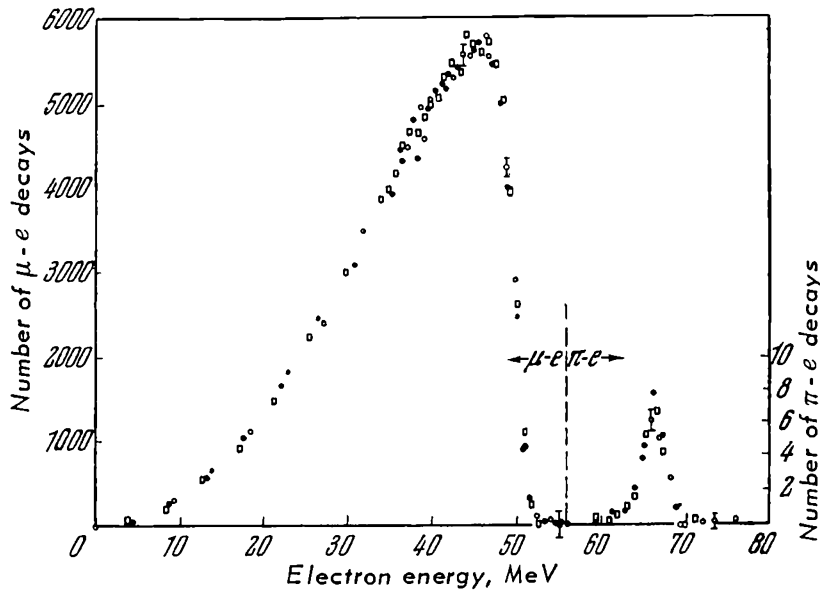


Fig. 2.36 The spectrum of electrons from $\pi - e$ and $\mu - e$ decays (Anderson et al.)

It may therefore be concluded that the existence of the $\pi \rightarrow e + \nu$ decay mode and the agreement of the measured decay probability with the theory of the universal Fermi interaction with vector and axial-vector variants have now been demonstrated.

2.12 β DECAY OF THE PION

In this section we shall consider experimental data on the decay of charged pions into electrons, neutral pions and neutrinos in accordance with the scheme

$$\pi^\pm \rightarrow e^\pm + \pi^0 + \nu \quad (2.44)$$

By analogy with the β decay of nucleons, this decay mode may be referred to as the β decay of the charged pion. Zel'dovich [82] has estimated the probability of this process by analogy with the Fermi β transition $I = 0 \rightarrow I = 0$. He showed that the probability of the β decay of charged pions should be of the order of 10^{-8} of the probability of the normal $\pi \rightarrow \mu + \nu$ decay mode. The decay mode indicated by (2.44) is of interest in connection with the success of the universal Fermi interaction theory which predicts that the vector constant in weak interactions is unaffected by the presence of strong interactions. We have already indicated that this prediction is a consequence of the hypothesis involving the conservation of the vector current.

If this hypothesis is valid, then the probability of process (2.44) will be

$$\omega(\pi^+ \rightarrow \pi^0 + e^+ + \nu) \approx \frac{g^2 \Delta^5}{30\pi^3} \quad (2.45)$$

where g is the vector weak-interaction constant given by (cf. Equation (2.24)) $g \approx 1.00 \times 10^{-5} M^{-2}$, M the proton mass and Δ the mass difference of charged and neutral pions, which is equal to 8.8 ± 0.6 electron masses (Table 1, Chapter 1). Using Equation (2.45) and the known mean lifetime of charged pions ($\tau = 2.56 \times 10^{-8}$ sec), it can easily be verified that the relative probability of the β decay of charged pions should be

$$R = \frac{\omega(\pi \rightarrow \pi^0 + e + \nu)}{\omega(\pi \rightarrow \mu + \nu)} \approx 1 \cdot 10^{-8} \quad (2.46)$$

Several theoretical calculations have been performed to obtain a more accurate result for (2.46). The most rigorous derivation of the possible corrections to (2.45) was carried out by Terent'ev, who found that $R = (1.03 \pm 0.03) \times 10^{-8}$. The error indicated in this result includes theoretical uncertainties and uncertainties connected with errors in the values of the constants.

We thus see that a determination of the probability of the β decay of charged pions should, at least in principle, lead to the verification of the conservation of vector current.

Fig. 2.37 illustrates an experiment in which the probability of β decay of charged pions was measured by Dunaitsev et al. [83, 135] using the synchrocyclotron at the Joint Institute for Nuclear Research in the USSR. Coincidences due to the two γ rays produced in the decay of the neutral pion in

1, 2, 3 - scintillation counters identifying the positive pion beam; 4 - counter in which positive pions came to rest; 5, 6 - Cerenkov spectrometers for γ rays from neutral-pion decays; CH_2 - Polyethylene absorber, M - magnetic lens

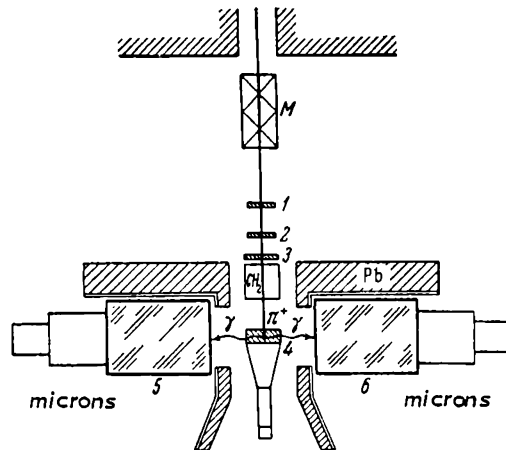


Fig. 2.37 Detection of β decay of pions ($\pi^+ \rightarrow \pi^0 + e^+ + \nu$)

(2.44) were recorded. The positive pions were stopped in the scintillator of counter 4 and γ rays from neutral-pion decays were recorded by total absorption Cerenkov counters. The most important source of background in this difficult experiment was charge exchange of positive pions in the scintillator. This gave rise to neutral pions whose decay simulated the required effect.

Similar studies have been carried out by Depommier et al. [84], Bacstrow [85] and Bartlett et al. [137] who recorded both the γ rays from decaying neutral pions, and decay positrons with energies of about 4 MeV. In addition, the annihilation radiation due to positronium produced after the deceleration of the positron in the scintillator was recorded. Decay probability data obtained in these experiments are summarized in Table 2.4.

It follows from this table that the probability of the β

Table 2.4 Measured decay probability for the $\pi^+ \rightarrow \pi^0 + e^+ + \nu$ decay mode

Reference	Number of $\pi^+ \rightarrow \pi^0 + e^+ + \nu$ decays	Relative decay probability R
[135]	43	$(1.1 \pm 0.2) \times 10^{-8}$
[136]	38	$(1.0 \pm 0.2) \times 10^{-8}$
[85]	10	$(2.0 \pm 0.6) \times 10^{-8}$
[137]	36	$(0.97 \pm 0.2) \times 10^{-8}$

decay of the pion does in fact approach the theoretical result. This means that the 'weak vector charge' of pions is the same as the 'weak vector charges' of nucleons and leptons to within 20%.

2.13 RADIATIVE CORRECTIONS TO $\pi - \mu - e$ DECAY

2.13.1 Radiative corrections to the energy spectrum and asymmetry in $\mu - e$ decay

The predictions of the four-fermion interaction theory, discussed earlier in connection with the parameters characterizing $\pi - \mu - e$ decays, were obtained without taking into account the interaction between the four fermions participating in the decay $\mu \rightarrow e + \nu + \bar{\nu}$ and the electromagnetic field. Radiative corrections to $\mu - e$ decay have been calculated by Behrends [86], Berman [87], Kinoshita and Sirlin [88], Kuznetsov [89], Gatto and Luders [91], Tzoar and Klein [92], Pratt [93], Fronsdal and Uberall [94] and others. These corrections are proportional in first-order perturbation theory to the product of the square of the weak-interaction constant and the square of the charge of the electron, i.e. proportional to $G^2\alpha$ where $\alpha = e^2/hc$ is the fine-structure constant.

To find the correct energy spectrum and decay probability, the interaction Hamiltonian H' of the two-component neutrino theory must be replaced by

$$H = H' + H''$$

where

$$H'' = e\bar{\psi}_\mu\gamma_\rho\psi_\mu A_\rho + e\bar{\psi}_e\gamma_\rho\psi_e A_\rho$$

represents the interaction with the electromagnetic field A_ρ . Restriction to first-order perturbation theory corresponds to Feynman diagrams 2-6 in Fig. 2.38.

Diagrams 2-4 represent virtual processes in which the emitted photons are absorbed by one of the four particles, while the last two diagrams represent the emission of real photons in the form of internal bremsstrahlung from the $\mu - e$ decay:

$$\mu \rightarrow e + \nu + \bar{\nu} + \gamma \quad (2.47)$$

This phenomenon is called the radiative decay of the muon. Radiative corrections soften the spectrum by removing high-energy electrons and transferring them to the low-energy part of the spectrum. Since the intensity of the decay electrons falls off very rapidly at low energies, small radiative



Fig. 2.38 Feynman diagrams for radiative corrections to $\mu - e$ decay

corrections will alter the shape of the low-energy end of the spectrum considerably. The magnitude of this effect is illustrated in Fig. 2.39, which shows the electron spectrum predicted by the two-component theory ($\rho = 3/4$) and the corrected spectrum. The corrections reduce the Michel parameter ρ by approximately 6%. In the experimental determinations of ρ discussed above, the spectrum was compared with the theoretical spectrum corrected for radiative effects, and therefore Table 2.1 gives the 'true' value of ρ .

Another consequence of the radiative corrections is a modification of the asymmetry in the electron spectrum at low energies. This effect has been discussed by Kinoshita and Sirlin [96] and Kuznetsov [89], who have shown that the change in the asymmetry coefficient is quite substantial for electron energies below 5-10 MeV (10-20%). It has no effect on the accuracy of the measured asymmetry parameter ρ , however, because the number of such electrons is small. The effect of radiative corrections on the magnitude of the asymmetry coefficient averaged over the entire spectrum

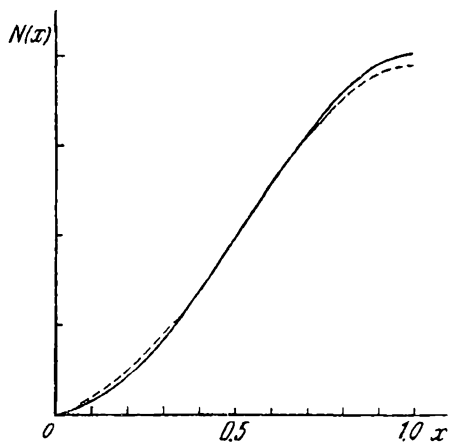


Fig. 2.39 The spectrum of electrons from $\mu - e$ decays with and without radiative corrections (broken and solid curves respectively)

is therefore also very small. The corrections reduce the absolute magnitude of this coefficient by less than 1%, making it equal to -0.330 instead of $-1/3$ as predicted by the $V - A$ theory. Radiative corrections will also affect the total decay probability for muons, increasing it by approximately 0.5% (cf. Section 2.3).

2.13.2 Internal bremsstrahlung in $\mu - e$ decay

$\mu - e$ decay results in the appearance of a fast charged particle. We have already indicated that the appearance of the charge is accompanied by the emission of photons which are usually referred to as internal bremsstrahlung, while the decay itself (cf. Equation (2.47)) is called radiative decay. The probability of radiative decay, in accordance with the scheme given by (2.47), and the energy spectrum of the resulting photons have been calculated by many workers beginning with Lenard [98]. He obtained the spectrum and the angular distribution of photons from $\mu - e$ decays, which he described by the sum of scalar, vector and tensor interactions. It should be noted that if the form of the Hamiltonian for the $\mu - e$ decay is known then the radiative decay is unambiguously determined. However, the form of the photon spectrum is determined mainly by the electromagnetic nature of the process and is not very sensitive to the precise form of the weak interaction.

In the first approximation the photon spectrum produced in the radiative decay is proportional to

$$E_{\gamma}^{-1} dE_{\gamma}$$

i.e. it has the form of the bremsstrahlung spectrum, diverging in the infrared.

The photon spectrum integrated over the electron spectrum and angles of emission has been calculated by Kinoshita and Sirlin [96] for the two-component neutrino, neglecting the electron mass in comparison with its energy. The result is

$$R(y) dy = \frac{\alpha}{3\pi} (1-y) dy \left\{ \left[2 \ln \frac{m_\mu}{m_e} - \frac{17}{6} + \ln(1-y) \right] \right. \\ \left. \times \left[\frac{3}{y} - 2(1-y)^2 \right] - \frac{1}{12} (1-y)(22-13y) \right\} dy \quad (2.48)$$

where $R dy$ is the ratio of the radiative decay probability of the muon to the total probability of its decay in accordance with the scheme $\mu \rightarrow e + \nu + \bar{\nu}$; $y = \frac{2E_\gamma}{m_\mu c^2}$ is the ratio of the photon energy to the maximum energy of the decay electrons. A similar expression for this spectrum has been reported by Eckstein and Pratt [95]. The energy spectrum of the internal bremsstrahlung is shown in Fig. 2.40, where $R(y)$ is plotted as a function of the photon energy y . It can readily be shown by integrating this spectrum that about 4.9% of all $\mu - e$ decays are accompanied by the emission of photons with energies greater than $2m_e$, which corresponds to the threshold for the formation of electron-positron pairs. Even when the photon energy is greater than $20 m_e \approx 10$ MeV, the number of such decays is still 1.2%. We thus see that internal bremsstrahlung is a very appreciable effect. It may be noted that the magnitude of this effect is independent of the relative magnitude of the V and A interaction constants.

Direct observation of radiative decays in particle-track detecting devices is not possible because photons do not

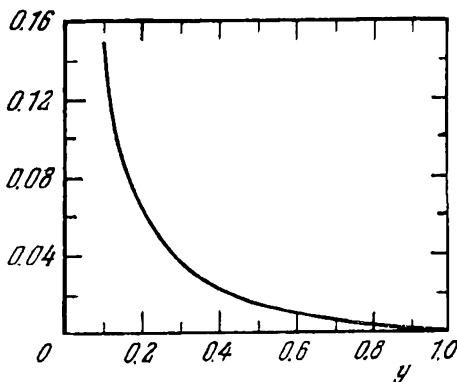


Fig. 2.40 Internal bremsstrahlung spectrum (Eckstein and Pratt). Radiative decay probability is plotted as a function of photon energy y

produce tracks. However, internal conversion of photons into electron-positron pairs at the time of decay can be noted from the appearance of the characteristic three-particle decay, in which three electrons are found to originate at the point at which the muon comes to rest:

$$\mu \rightarrow e + \nu + \bar{\nu} + (e^+ + e^-)$$

Eckstein and Pratt have shown that the probability of this phenomenon is lower by approximately three orders of magnitude than the process

$$\mu \rightarrow e + \nu + \bar{\nu} + \gamma$$

Fig. 2.41 shows an example of a three-electron decay of a positive muon recorded in a nuclear emulsion of Gurevich et al. [99].

A search for such decays was also conducted by Lee and Samios [100], who looked at 2.2×10^5 $\pi - \mu - e$ decays

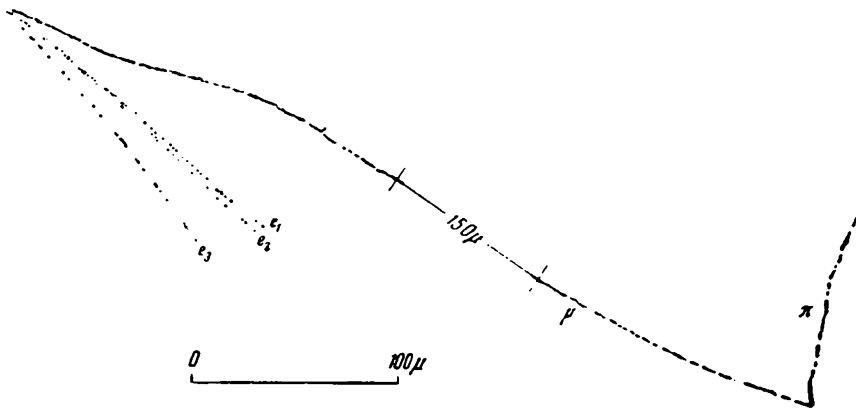


Fig. 2.41 Decay of the pion in accordance with the scheme $\mu \rightarrow e + \nu + \bar{\nu} + e^+ + e^-$. The electron-positron pair (e_1, e_2) occurs at the point of decay of the muon (Gurevich et al.)

obtained with a hydrogen bubble chamber in a field of 8800 gauss. They detected three decays into three electrons similar to those found by Gurevich et al. The radiative decay of the muon has also been investigated with a 5-inch freon bubble chamber by Crittenden et al. [101], who looked at approximately 3.3×10^5 stopping positive muons. They detected about ten muon decays with the emission of three electrons. From these data, and from the known scanning efficiency, the relative probability of this decay mode has

been found to be

$$R = \frac{\omega(\mu^+ \rightarrow e^+ + \nu + \bar{\nu} + (e^+ + e^-))}{\omega(\mu^+ \rightarrow e^+ + \nu + \bar{\nu})} = (2.2 \pm 1.5) \cdot 10^{-5}$$

which is in qualitative agreement with the theoretical estimates of Eckstein and Pratt.

In the same paper, Crittenden et al. [101] reported measurements of the probability of the radiative decay process $\mu \rightarrow e + \nu + \bar{\nu} + \gamma$ and of the photon spectrum produced in this decay. The basic idea was to look for electron-positron pairs which were spatially correlated with the point at which the muon decayed. Fig. 2.42 shows the photon spectrum determined from the range and scattering of electron-positron

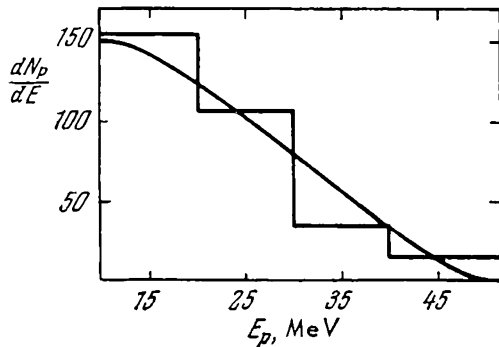


Fig. 2.42 The spectrum of internal bremsstrahlung obtained from measurements of the energy of conversion pairs in a bubble chamber. The number of pairs in a 10-MeV interval is plotted as a function of the pair energy E_p in MeV (histogram); the solid curve is the expected spectrum based on Equation (2.48)

pairs. It is based on 313 such decays. The solid curve shows the expected spectrum (Equation (2.48)). It is clear that the agreement is excellent. Theory shows that the probability of decay accompanied by photons with energies in excess of 10 MeV ($y \gtrsim 0.2$) is

$$R(\gtrsim 0.2) = \frac{\omega(\mu \rightarrow e + \nu + \bar{\nu} + \gamma)}{\omega(\mu \rightarrow e + \bar{\nu})} = 1.3 \cdot 10^{-2}$$

whilst the experimental result was $R(\gtrsim 0.2) = (1.4 \pm 0.4) \times 10^{-2}$.

One of the first attempts to observe radiative $\mu - e$ decay using counter techniques was reported by Ashkin et al. [102]. A more detailed experimental study was carried out by Kim et al. [103], who recorded the photons with a large NaI(Tl) crystal used as a total absorption spectrometer (Fig. 2.43). The positive-pion beam was brought to rest in a graphite target which was viewed by a telescope consisting of annular

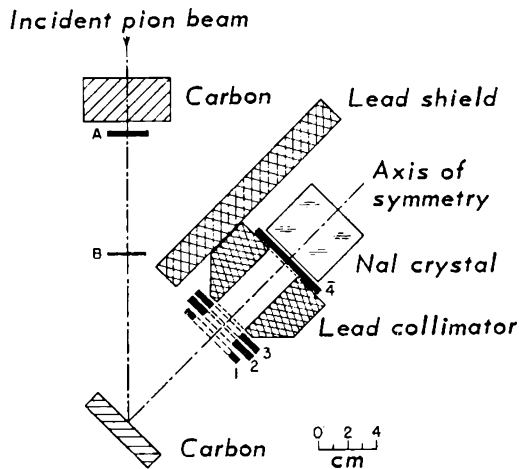


Fig. 2.43 Determination of the spectrum of internal bremsstrahlung in $\mu - e$ decay (Kim et al.)

scintillators 1, 2, 3, an anti-coincidence counter $\bar{4}$ and a large NaI crystal surrounded by a lead converter. Unpolarized muons were produced as a result of $\pi - \mu$ decays in the graphite target and the radiative decay of these muons was signalled by coincidences between decay electrons in the three annular counters 1, 2, 3 and photons in the NaI counter. The coincidence pulse was used as a gating pulse, allowing the pulse from the NaI counter to enter a 50-channel pulse-height analyser. The amplitude of the pulse from the NaI counter was a measure of the photon energy in the $\mu \rightarrow e + \bar{\nu} + \bar{\nu} + \gamma$ decay.

The experimental data are compared with the theoretical predictions in Fig. 2.44, in which y' is the energy of photons recorded by the NaI counter, and $R(y') \Delta y'$ the ratio of the

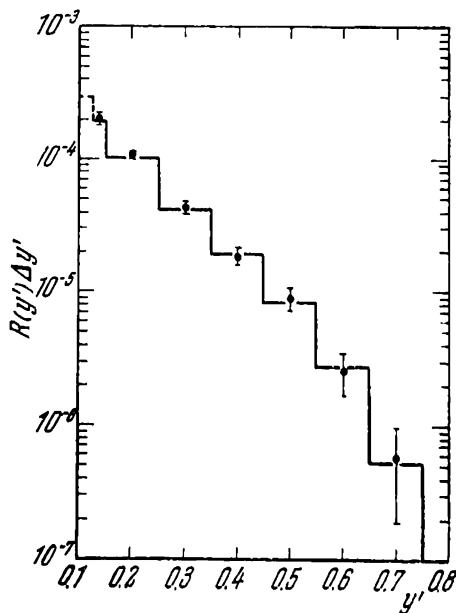


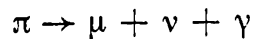
Fig. 2.44 The experimental spectrum of internal bremsstrahlung from $\mu - e$ decay (Kim et al.). The histogram represents the expected spectrum in accordance with Equation (2.48)

probability of radiative decay to the total probability of the usual $\mu \rightarrow e + \nu + \bar{\nu}$ decay mode. The histogram shows theoretical values of $R(y') dy'$ calculated on the basis of $V - A$ theory with a two-component neutrino ($\rho = 3/4$), corrected for the resolution of the apparatus. The experimental data are indicated by the points.

The above review of experimental data on the internal bremsstrahlung from $\mu - e$ decays shows that they are in good agreement with predictions based on the assumption that the muon interacts with the electromagnetic field in a way which is analogous to the interaction of an electron with this field.

2.13.3 Internal bremsstrahlung from pion decays ($\pi - \mu + \nu + \gamma$)

$\pi \rightarrow \mu$ decays result in the appearance of monochromatic muons, and the distribution of secondary-muon ranges shown in Fig. 1.3 (Chapter 1) can be accounted for by fluctuations in ionization losses. There are, however, rare cases in which muons with anomalously large and anomalously small ranges are observed. These are due to two causes. Some of the $\pi \rightarrow \mu$ decays occur in flight, mainly near the end of the pion range, and these are sources of muons with both anomalously large and anomalously small ranges, depending on the angle between the directions of motion of the muon and of the pion at the instant of decay. Another source of anomalous ranges is the radiative decay of the pion. This effect is characterized by the appearance of a photon at the instant of decay and is analogous to the internal bremsstrahlung in $\mu \rightarrow e$ decay (cf. Section 2.13.2). In this process, the decay is accompanied by the appearance of a photon in accordance with the scheme



and the energy of the muon is reduced accordingly. Since radiative decays can lead only to a reduction in the muon range, they can easily be separated from decays in flight if the muon is emitted in the forward direction. A muon emitted in the forward direction with an anomalously short range can only have been produced in the radiative decay of a pion.

An interesting example of the radiative decay of a pion has been published by Fry et al. [104] and is shown in Fig. 2.45. A muon and an electron-positron pair originate at the point

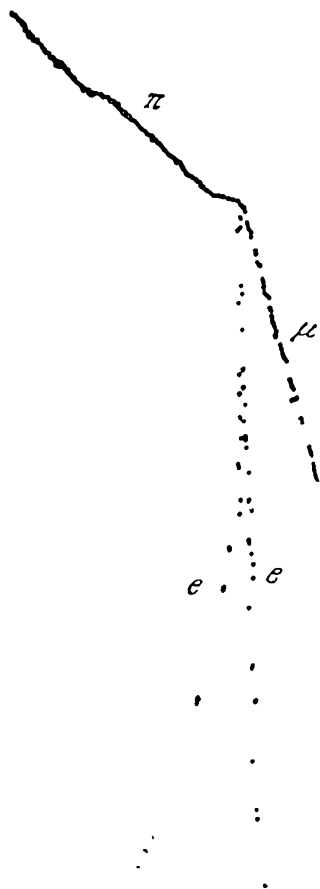
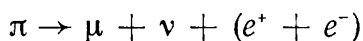


Fig. 2.45 Radiative decay $\pi \rightarrow \mu + \nu + (e^+ + e^-)$

at which the pion decays. The pair was produced as a result of internal conversion of the photon at the time of decay according to the scheme



A similar conversion process was discussed previously in connection with radiative $\mu - e$ decay (Fig. 2.41).

Fry [105] found six decays in flight and an equal number of radiative decays among 11 841 $\pi - \mu$ decays in photographic emulsions. He used this result to calculate the ratio of the probability of radiative decay to the probability of the usual decay mode. The result was

$$R = \frac{\omega(\pi \rightarrow \mu + \nu + \gamma)}{\omega(\pi \rightarrow \mu + \nu)} = (3.3 \pm 1.3) \cdot 10^{-4}$$

Detailed studies of radiative pion decay were carried out by Castagnoli and Muchnik [106] in photographic emulsions. These workers used Ilford G-5 emulsions and found 87 muon tracks with anomalously short ranges (less than 500 microns)

among 93 045 $\pi - \mu$ decays. Analysis of the possible distribution of ranges shows that, with these statistics, fluctuations in ionization losses could not have led to the appearance of short-range muons with ranges less than 475 microns. After excluding a small number of decays in flight and a few doubtful short tracks for which the $\pi - \mu$ decay point could not be unambiguously determined, or for which ionization and multiple-scattering measurements gave contradictory results, there was a residue of 25 ranges between 340 and 475 microns. The experimental data are compared with theoretical predictions in Fig. 2.46. The probability $F(R)$ of emission of a muon with a range less than a given value R was

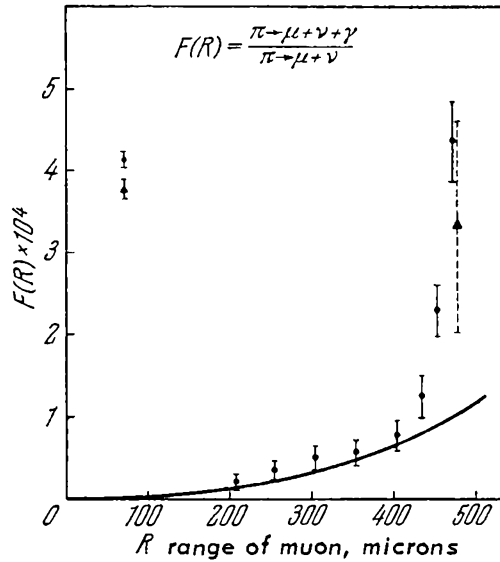


Fig. 2.46 Radiative decay of the pion (Castagnoli and Muchnik). The solid curve represents the theoretical decay probability given by Equation (2.49)

obtained by integrating the differential photon spectrum from $\pi \rightarrow \mu + \nu + \gamma$ decays, calculated by Ioffe and Rudik [107] and by Fialho and Tiomno [108], who showed that

$$R dE = \frac{e^2}{2\pi} \frac{p}{p_0^2} \left[\frac{4p_0}{E_0 - E} \frac{E}{p} \left(\ln \frac{E + p}{\mu} - \frac{p}{E} \right) + \frac{E_0 - E}{p} \ln \frac{(E + p)M - \mu^2}{(E - p)M - \mu^2} \right] dE \quad (2.49)$$

where $R dE$ is the ratio of the probability of radiative decay ($\pi \rightarrow \mu + \nu + \gamma$) to the usual decay ($\pi \rightarrow \mu + \nu$) mode, E and p are the energy and momentum of the muon, and E_0 and p_0 are the maximum values of these parameters corresponding to the normal decay.

The figure also shows Fry's results; the indicated uncertainties are the statistical errors. For ranges $r \leq 435$ microns, these data are in agreement with the theory which yields $R(r \leq 435 \text{ microns}) = 0.79 \times 10^{-4}$. The experimentally observed probability of radiative decay with the muon energy in the range 1.85-3.35 MeV is

$$R = \frac{\omega(\pi \rightarrow \mu + \nu + \gamma)}{\omega(\pi \rightarrow \mu + \nu)} = (1.24 \pm 0.25) \cdot 10^{-4}$$

It is evident from Fig. 2.46 that the agreement between experiment and theory deteriorates as R increases, but this discrepancy need not be regarded as decisive because it may be due to underestimates of straggling, inadequate geometrical corrections, and so on.

Binnie et al. [109], working on the Liverpool synchrocyclotron, recorded photons from radiative pion decays using counter techniques. After subtracting a substantial background, there were twenty residual cases of radiative decay. The number expected under the conditions of the experiment was twelve. The results of this work are therefore in qualitative agreement with (2.49) and with the results obtained with nuclear emulsions.

Theoretical aspects of radiative $\pi - \mu$ decay have been considered by a number of workers. Ioffe and Rudik and Fialho and Tiomno assumed that $\pi - \mu$ decay can be described by gradient or non-gradient point interaction. The radiative decay probability has also been estimated by Huang and Low [110], who postulated that the pion decays into a virtual proton-antinucleon pair which then undergoes annihilation. Assuming that

$$\frac{G_V}{G_A} \approx 1, \quad \frac{G_p}{G_A} \approx \frac{m_e}{M}$$

where m_e and M are the masses of the electron and of the nucleon respectively, they found that the relative probability of the radiative mode was

$$R = \frac{\omega(\pi \rightarrow \mu + \nu + \gamma)}{\omega(\pi \rightarrow \mu + \nu)} \approx 1.1 \cdot 10^{-4} \ln \frac{\omega_{\max}}{\omega_{\min}}$$

where ω_{\max} and ω_{\min} are the maximum and minimum energies of the recorded photons respectively. By recording all photons between 1 MeV and the maximum possible energy of 28 MeV, we obtain $R = 3.7 \times 10^{-4}$, which is in agreement with the experimental values of R given above.

2.14 SEARCHES FOR RARE MUON DECAY MODES

2.14.1 The $\mu \rightarrow e + \gamma$ mode

The decay of the muon into an electron and a photon has attracted considerable attention and has been investigated with gradually increasing sensitivity. This decay mode is a necessary consequence of theories requiring the existence of an intermediate particle responsible for the weak interaction. Feynman and Gell-Mann [21] proposed that the interaction of four fermions occurs non-locally and hence the two currents forming the four-fermion interaction (e.g. $\mu\nu$ and $e\bar{\nu}$) exchange a particle between them. This particle should be charged and its spin should be 1 (charged vector boson) in order to ensure that vector and axial-vector forms of the weak interaction are possible. Moreover, in order to explain the absence of the process

$$K \rightarrow W + \gamma$$

the mass of the intermediate boson W should be greater than the mass of the kaon. The existence of this boson leads to a number of consequences for $\mu - e$ decay. For example, Lee and Yang have shown that the Michel parameter ρ which determines the shape of the spectrum of electrons from muon decays ($\mu \rightarrow e + \nu + \bar{\nu}$), increases from $\rho = 3/4$ in the two-component neutrino theory to

$$\rho = \frac{3}{4} \approx \frac{1}{3} \left(\frac{m_\mu}{m_W} \right)^2$$

while the lifetime of the muon decreases in the ratio

$$1 : \left[1 + \frac{3}{5} \left(\frac{m_\mu}{m_W} \right)^2 \right]$$

as compared with the value predicted by $V - A$ weak-interaction theory. Thus, if the mass of the intermediate boson is equal to the mass of the kaon, the magnitude of ρ should

increase to approximately 0.76, whilst the lifetime should decrease by 2-3%. However, we saw at the beginning of this chapter that the Michel parameter ρ cannot be measured at present to an accuracy which would allow us to distinguish between 0.75 and 0.76, and the uncertainties in the lifetime of the muon associated with radiative corrections are also of the order of a few per cent. There is, however, another consequence of the existence of the intermediate boson which can be tested experimentally, namely, the muon can decay into an electron and a γ ray:

$$\mu \rightarrow e + \gamma$$

If the intermediate boson W exists, this is a second-order process in which the γ ray is produced as a result of the following virtual interactions.

1. Transformation of the muon into an intermediate boson and a neutrino

$$\mu \rightarrow W + \nu \quad (2.50)$$

2. Emission of a photon by the intermediate boson:

$$W \rightarrow \gamma + W \quad (2.51)$$

3. Conversion of the intermediate boson into an electron through the absorption of a neutrino:

$$W + \nu \rightarrow e \quad (2.52)$$

These processes can be described by the Feynman diagram shown in Fig. 2.47. The net result of these processes is the creation of an electron and a photon:

$$\mu \rightarrow e + \gamma$$

This effect requires that the neutrino emitted in (2.50) should be absorbed in the process described by (2.52).

The first of these neutrinos is connected with the muon in the muon weak-interaction current, and the second with the

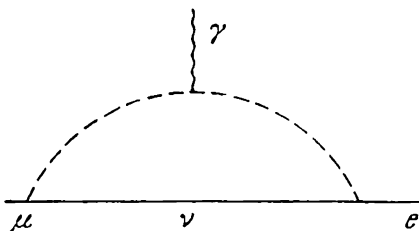


Fig. 2.47 Feynman diagram for the $\mu \rightarrow e + \gamma$ decay with an intermediate vector boson

electron in the electron current. Hence in order that the reactions (2.51)-(2.53) should be possible, it is necessary that muon and electron neutrinos be identical ($\nu_\mu \equiv \nu_e$).

The probability of the above three processes should be of the order of the product of the weak- and electromagnetic-interaction constants $G^2\alpha$, i.e. it should be large enough for an experimental test. Gell-Mann et al. [117] have estimated the relative probability of $\mu \rightarrow e + \gamma$ and $\mu \rightarrow e + \nu + \bar{\nu}$ decays as

$$R = \frac{\omega(\mu \rightarrow e + \gamma)}{\omega(\mu \rightarrow e + \nu + \bar{\nu})} \approx \frac{3}{8\pi} \frac{1}{137} \left(\ln \frac{\Lambda^2}{m_W^2} \right)^2$$

This formula is valid for $\Lambda \gg m_W$, where m_W is the mass of the intermediate vector boson Λ the cut-off parameter. For reasonable values of this parameter, $R \sim 10^{-3} - 10^{-4}$.

Let us consider now the various experimental searches for this decay mode.

a. Bubble-chamber experiments.

The detection of $\mu \rightarrow e + \gamma$ decays in the bubble chamber reduces to a search for $\mu - e$ decays accompanied by the appearance at some distance from the decay point of an electron-positron pair due to conversion of the γ ray. The pair energy should approach 53 MeV and the γ ray should be emitted in the opposite direction to the electron. Krestnikov et al. [118] have looked for such decays in a freon-filled bubble chamber. They analysed 91 000 stopping positive muons in the chamber and with a γ -ray recording efficiency of about 25% at 53 MeV they did not find a single decay which could be reliably identified as the $\mu \rightarrow e + \gamma$ decay. It follows that the probability of this decay, R , is less than 4×10^{-5} . Crittenden et al. [101] used a similar method and were also unable to find a single $\mu \rightarrow e + \gamma$ decay among 220 000 μ^+ decays and hence estimated that $R < 2.5 \times 10^{-5}$.

b. Counter experiments.

In these experiments the target in which the positive pions are brought to rest and the $\mu - e$ decay can occur is surrounded by positron and γ -ray counters capable of recording particles with energies of about 55 MeV. The efficiency and resolution of the γ -ray and electron counters have gradually been increased, and backgrounds due to random coincidences and to radiative decays ($\mu \rightarrow e + \nu + \bar{\nu} + \gamma$)

have been reduced. Another improvement has been the development of faster oscilloscopes for recording the events. The first experiments of this kind were carried out by Lokanathan and Steinberger [119], who did not detect the $\mu \rightarrow e + \gamma$ mode and concluded that $R < 2 \times 10^{-5}$.

Davis et al. [120] recorded γ rays and electrons with two telescopes consisting of scintillation and water-filled Cerenkov counters and concluded that $R < 10^{-5}$.

As an example of such experiments, let us consider the work of Frankel et al. [121] (Fig. 2.48). A beam of 250-MeV/ c positive muons was brought to rest in a lucite target.

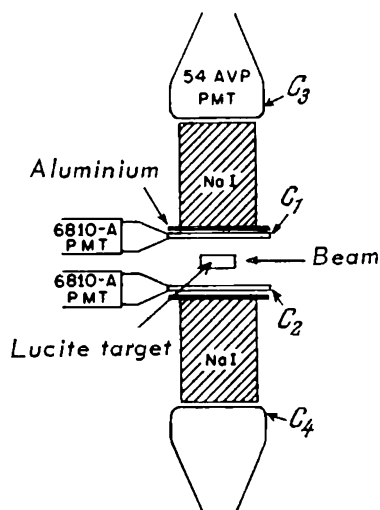


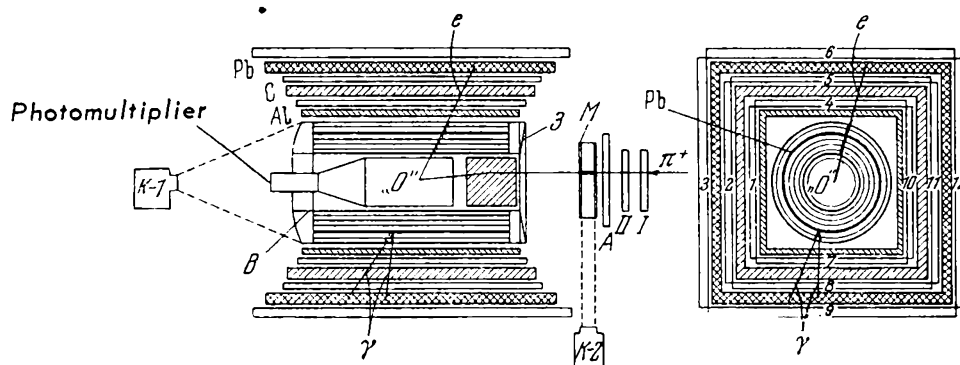
Fig. 2.48 Search for the $\mu \rightarrow e + \gamma$ decay mode (Frankel et al.)

C_1 and C_2 were plastic scintillators, and C_3 and C_4 large NaI(Tl) crystals (12.5-cm diameter, 15-cm long). Monochromatic positrons and γ rays produced in possible $\mu \rightarrow e + \gamma$ decays would have been reliably observed in these crystals. Counters C_1 and C_2 were used in an anti-coincidence system: the absence of pulses from them indicated that the operation of C_3 and C_4 was due to γ rays. $C_3 C_4 C_1 \bar{C}_2$ or $C_3 C_4 \bar{C}_1 C_2$ coincidences signalled the required decays when the total energy dissipated in C_3 and C_4 was about 53 MeV.

In a fortnight's run, about 9×10^6 $\mu \rightarrow e + \nu + \bar{\nu}$ decays were recorded, in which the positron energy was about 53 MeV, but the number of coincidences between these positrons and pulses due to γ rays of equal energy did not exceed the expected random coincidence rate. Analysis of these data leads to the conclusion that $R < 1.2 \times 10^{-6}$ with a 90% confidence level. The absence of $\mu \rightarrow e + \gamma$ decays has also been confirmed by O'Keefe et al. [122], using the Liverpool accelerator, by Berley et al. [123], and by Ashkin et al. [102], working with the CERN synchrocyclotron.

In all these papers the upper limit for the relative probability of this decay mode was reported to lie in the range $R = (1.5-6.0) \times 10^{-6}$. These results are summarized in Table 2.5. A further increase in the sensitivity of such measurements was achieved by placing spark chambers in front of the positron and γ -ray counters. This procedure has led to a considerable increase in the angular resolution of the apparatus, and to an increase in the efficiency and reliability of the experiments.

Fig. 2.49 shows the apparatus used by Alikhanov et al. [123a]. In this figure, O is a cylindrical counter target in which the positive pions were brought to rest (2300 per sec).



B – six-layer cylindrical spark chamber; M – single-layer plane spark chamber; K-1, K-2 – cameras; S – mirror used to obtain stereoscopic image; I, II, A, 1-12 – scintillation counters

Fig. 2.49 The experiment of Alikhanov et al.

Coincidences in counters O, A (4,5,6) or (7,8,9) or (1,2,3) or (10,11,12) fix the number of $\mu - e$ decays in the counter target O. Fast O,4,5,7,8,6,9,A and O,1,2,10,11,3,12,A coincidences were used to produce a pulse which operated the spark chambers. The tracks left by charged particles in the gaps between the spark-chamber electrodes were photographed in two directions by cameras K-1 and K-2. A third camera photographed the screen of an oscilloscope, which was used to measure the time between the I,II,O and O,4,5,7,8,6,9,A or O,1,2,10,11,3,12,A coincidence signals.

The six-layer, cylindrical spark chamber, which was coaxial with the counter target O, was designed for the detection of the electron and γ ray in the muon decay. One of the cylinders was made of lead and the others of aluminium. In this way, electron-positron pairs produced by γ rays were recorded in the last two gaps of the chamber, while electrons were recorded in all six gaps.

The plane, single-gap spark chamber M was used to determine the coordinates of the point of entry of positive pions into the counter O in the plane perpendicular to the beam. The following selection criteria were used to separate possible $\mu \rightarrow e + \gamma$ decays from the background of normal $\mu - e$ decay modes accompanied by the detection of γ rays in the cylindrical spark chamber.

1. The time between the arrival of a positive pion and the e, γ , event measured on the oscilloscope must lie in the range $0 < t < 5 \mu \text{ sec}$.
2. There must be no other tracks in the cylindrical spark chamber apart from the electron track and the tracks of the electron pairs produced by the γ .
3. The point of entry of the positive pion, measured with the aid of the spark chamber M, must be within 2 cm of the extension of the electron track into the cylindrical spark chamber.
4. The angle between the electron and the γ ray must be within the range $180 \pm 6^\circ$ in the plane perpendicular to the beam, and in the range $180 \pm 40^\circ$ in the other projection.

In 66 hours of operation, 5.5×10^8 stopping positive pions were recorded in counter O, and there were six events for which the angles between the electron and γ ray lay in the range $174\text{-}144^\circ$ in the first projection. These were most probably $\mu \rightarrow e + \nu + \bar{\nu} + \gamma$ decays. Calculations predicted six radiative decays in the range $180\text{-}144^\circ$. This experiment yielded the following upper limit for the probability of $\mu \rightarrow e + \gamma$ decays with a 90% confidence level:

$$R \leq 5 \cdot 10^{-7}$$

A further reduction in the upper limit of the experimental value for the $\mu \rightarrow e + \gamma$ decay probability has been obtained with spark chambers by Frankel et al. [124, 126] and Bartlett et al. [125, 126]. In both cases large spark chambers were placed before electron and γ -ray counters. Despite the greatly increased sensitivity, no $\mu \rightarrow e + \gamma$ decays were detected, and the upper limits for the relative decay probability were found to be

$$R \leq 1.9 \cdot 10^{-7}, \quad R \leq 6 \cdot 10^{-8}$$

with a 90% confidence level. A complete summary of the various experimental data is given in Table 2.5.

It is clear that experiments with progressively increased

Table 2.5

Reference	Method of recording of the electron and photon from $\mu \rightarrow e + \gamma$ decays	$R = \frac{\omega(\mu \rightarrow e + \gamma)}{\omega(\mu \rightarrow e + \nu + \bar{\nu})}$
[118]	Freon bubble chamber	$< 4 \times 10^{-5}$
[119]	Scintillation counters	$< 2 \times 10^{-5}$
[101]	Freon bubble chamber	$< 2.5 \times 10^{-5}$
[120]	Cerenkov counters	$< 10^{-5}$
[123]	Scintillation counters	$< 2 \times 10^{-6}$
[121]	Large crystals for e and γ counting	$< 1.2 \times 10^{-6}$
[122]	NaI(Tl) crystal for electrons and telescope with lead converter for γ 's	$< 6 \times 10^{-6}$
[102]	Range telescope for electrons and large NaI(Tl) crystal for γ 's	$< 10^{-6}$
[123]	Spark chambers and scintillation counters	$< 5 \times 10^{-7}$
[138]	Spark chambers and large crystals for e 's and γ 's	$< 4 \times 10^{-8}$
[125]	Spark chambers and scintillation counters	$< 6 \times 10^{-8}$
[139]	"	$< 10^{-8}$

sensitivity and reliability have not succeeded in detecting the expected $\mu \rightarrow e + \gamma$ decay mode, and that the relative probability of this mode is less than 10^{-7} - 10^{-8} . It is thus considerably lower than the probability $R \sim 10^{-3}$ - 10^{-4} predicted by $V - A$ theory, assuming the presence of the intermediate vector boson.

2.14.2 The $\mu \rightarrow 3e$ mode

The Fermi interaction theory involving a pair of charged and a pair of neutral particles forbids the process

$$\mu^\pm \rightarrow e^\pm + e^+ + e^- \quad (2.53)$$

However, if the decay

$$\mu \rightarrow e + \gamma \quad (2.54)$$

exists, then the decay of the muon into three electrons could occur as a result of the internal conversion of the γ ray. The probability for this process would be lower by two or three orders of magnitude than the probability of (2.54).

The decay mode (2.53) should be accompanied by the appearance at the decay point of three coplanar relativistic electron tracks. These events can be recorded in nuclear emulsions and bubble chambers with almost 100% efficiency, but have not been observed so far. Table 2.6 shows the result of searches for the $\mu \rightarrow 3e$ decay mode using bubble chambers and nuclear emulsions.

The total number of $\pi \rightarrow \mu - e$ decays which have been observed in various laboratories is now considerably greater than 10^6 and it may therefore be concluded that the relative probability of $\mu \rightarrow 3e$ decays must be less than 10^{-6} , i.e.

$$R = \frac{\omega(\mu \rightarrow e + e + e)}{\omega(\mu \rightarrow e + \nu + \bar{\nu})} \ll 10^{-6}$$

A search for the $\mu^+ \rightarrow 3e$ decay mode has been carried out using counter techniques by Parker and Penman [127] and by Babaev et al. [128, 140]. The former experiment is illustrated in Fig. 2.50, which shows the scintillation-counter target in which the positive-pion beam came to rest (the beam is incident at right angles to the plane of the figure), and three identical electron telescopes for detecting the three decay electrons from $\mu^+ \rightarrow e^+ + e^- + e^+$ decays. Each electron

Table 2.6 Search for the $\mu \rightarrow 3e$ mode

Reference	Number of $\pi \rightarrow \mu - e$ decays	Method
[100]	2.2×10^5	Hydrogen bubble chamber
[101]	3.3×10^5	Freon bubble chamber
[126]	4.0×10^5	Nuclear emulsion
[99]	2.0×10^5	"

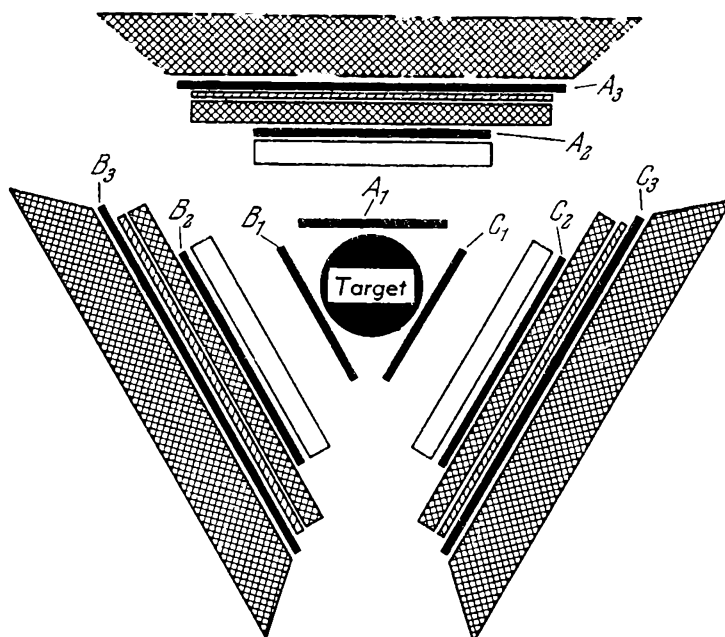


Fig. 2.50 Search for the $\mu^+ \rightarrow 3e$ mode (Parker and Penman). The cylindrical target (scintillation counter) is surrounded by three identical electron telescopes (A_1, A_2, A_3), (B_1, B_2, B_3) and (C_1, C_2, C_3)

telescope consists of two scintillation counters with graphite absorbers between them and a large anti-coincidence counter. About 10^9 mesons were brought to rest in the cylindrical counter target. When the efficiency of the entire apparatus for the simultaneous detection of the three electrons is taken into account, the number of stopping pions is calculated to be 1.7×10^7 . Altogether five cases were found of the simultaneous appearance of three electrons which were time-correlated with the $\pi^+ - \mu$ decay. It was estimated that all five cases could be explained by the decay scheme

$$\mu^+ \rightarrow e^+ + e^- + e^+ + \nu + \bar{\nu}$$

i.e. a radiative decay in which, instead of the photon, an electron-positron pair is produced.

The upper limit for the three-electron decay probability

$$R = \frac{w(\mu \rightarrow e + e + e)}{w(\mu \rightarrow e + \nu + \bar{\nu})}$$

was estimated to be 5×10^{-7} , which is less than the result obtained with bubble chambers and nuclear emulsions. Babaev et al. [128] have used spark chambers in conjunction with

scintillation counters in an apparatus similar to that employed by Alikhanov et al. Again, the three-electron decay of the muon was not detected and the upper limit of the relative decay probability was found to be $R < 2.6 \times 10^{-7}$.

Frankel et al. have found that $R < 1.5 \times 10^{-7}$.

2.14.3 The neutrino-less conversion of a muon into an electron

The neutrino-less conversion of a muon into an electron refers to the transformation occurring in the Coulomb field of the nucleus N of a mesonic atom. This process can be described by the scheme



where N is a nucleon or nucleus. In this process, the nucleus recoils and the electron energy is approximately equal to

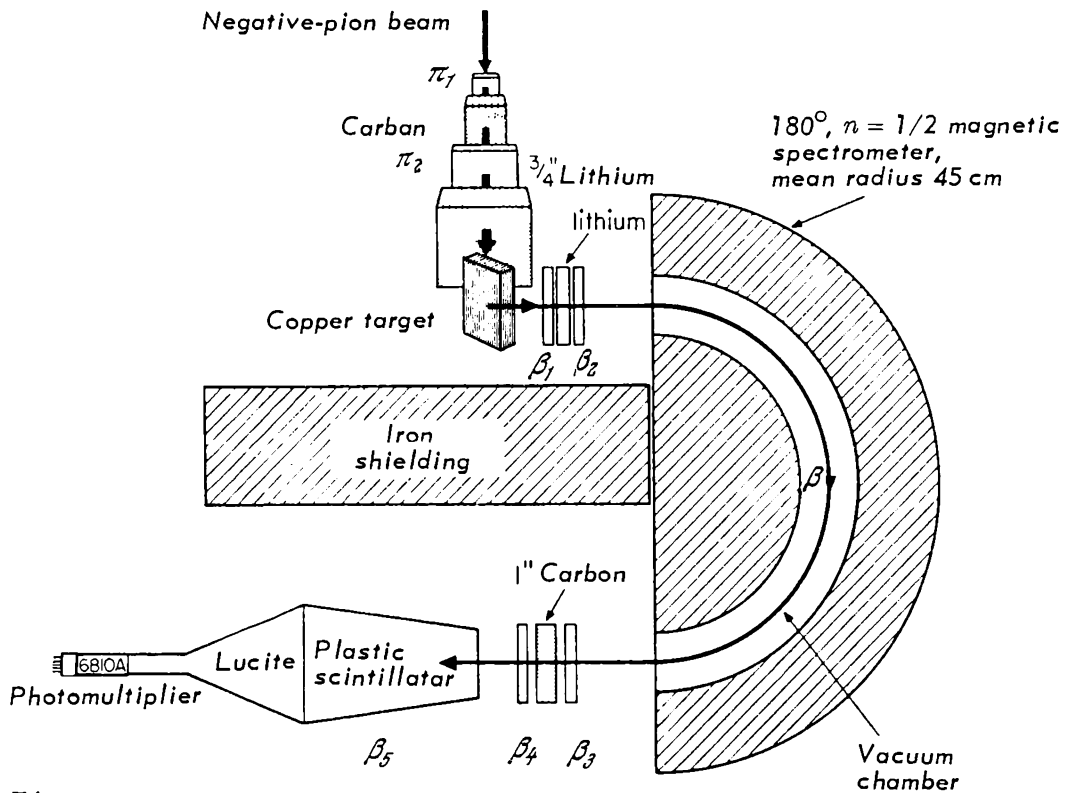


Fig. 2.51 Search for the transformation of the negative muon into an electron without the emission of a neutrino (Sard, Crowe and Krüger). The meson beam is horizontal and the particles leaving the meson target at right-angles to the muon beam enter the magnetic spectrometer. The energy of these particles is measured with a long scintillator at the spectrometer exit

the muon rest energy $m_\mu c^2 = 100$ MeV or a little less if the nucleus is left in an excited state. The possibility of this process is also connected with the $\mu \rightarrow e + \gamma$ decay mode. The negative muon absorbs a virtual photon in the nuclear Coulomb field, transforming into an electron, while the nucleus N^* absorbs the excess momentum of the interaction.

Until recently, the only search for this reaction was the work by Steinberger et al. [129], who looked for μ - e conversion by recording particles with ranges greater than 24.5 g/cm² of polyethylene, leaving a 3.2-mm copper plate in which negative muons came to rest. The neutrino-less reaction in this case is

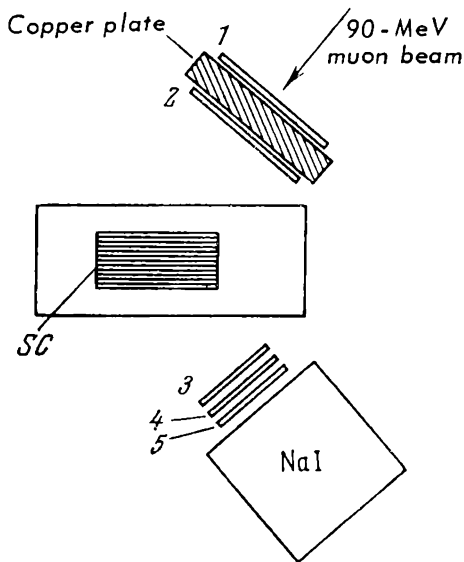


The result was negative and it was estimated that the ratio R of the probability of the reactions described by (2.56) to the probability of absorption of the negative muon by the copper nucleus was

$$R = \frac{\omega(\mu^- + \text{Cu} \rightarrow e^- + \text{Cu})}{\omega(\mu^- + \text{Cu} \rightarrow \nu + \text{Fe})} < 10^{-3}$$

Sard et al. [130] used a magnetic spectrometer to select electrons with energies of approximately 95 MeV, as shown in Fig. 2.51. This led to a considerable reduction in the background and to an improvement in resolution. These workers found an upper limit for R of $(4_{-2}^{+3}) \times 10^{-6}$.

Conversi et al. [131] have studied the decay mode (2.55) in a series of experiments of progressively increasing sensitivity. The last experiment of this group is illustrated in Fig. 2.52. Negative muons were brought to rest in the copper plates of a spark chamber so that it was possible to observe the trajectories of electrons whose energy was measured by a large NaI scintillator counter. The use of the spark chamber together with the oscilloscope technique for displaying counter pulses led to a considerable improvement in resolution. Among 2×10^9 mesons coming to rest in the copper plates of the spark chamber, four electrons with energies between 95 and 100 MeV were recorded, but they could have been due to the background. Conversi concluded from this that the relative probability of the neutrino-less conversion of the negative muon into an electron is not more than 2×10^{-7} .



SC – spark chamber in whose copper plates the negative muons were observed; NaI – totally absorbing crystal recording electrons with energy of ≈ 100 MeV; 1, 2 – scintillator counters for recording the negative muon beam; 3, 4, 5, NaI form an electron telescope

Fig. 2.52 Experiment of Conversi et al.

It may be concluded that measurements to date do not show the existence of the neutrino-less conversion of the negative muon into an electron. However, as the sensitivity of the methods increases and the background is reduced, the upper limit of the probability R continues to fall. The various published experimental results are summarized in Table 2.7.

2.14.4 Discussion of data on rare decay schemes

The data reviewed above indicate that none of the following decay modes have so far been observed:

$$\mu \rightarrow 3e \quad (2.53)$$

$$\mu \rightarrow e + \gamma \quad (2.54)$$

$$\mu^- + N \rightarrow N + e \quad (2.55)$$

This may be regarded as strong evidence against the existence of the intermediate vector boson if the analysis is confined to the single-neutrino theory. Consider, for example, the decay $\mu \rightarrow e + \gamma$. If the boson responsible for weak interactions exists, and if the two neutrinos are identical, this decay should occur with a relative probability of about 10^{-3} - 10^{-4} , whereas experiment yields $R < 10^{-7}$ - 10^{-8} .

The simplest hypothesis which would explain the absence of these reactions is that there exist two types of neutrino,

i.e. the muon neutrino originating in $\pi - \mu$ decay:

$$\pi \rightarrow \mu + \nu_{\mu}$$

and the electron neutrino which appears, for example, in β decay:

$$n \rightarrow p + e + \bar{\nu}_e$$

If these neutrinos are different, then reactions (2.53)-(2.55) are forbidden absolutely by the law of conservation of leptonic charge, since the right and left sides of these reactions contain different leptons.

In Chapter 1 we considered the neutrino experiments performed at Brookhaven and CERN. These experiments showed that the neutrinos produced in $\pi - \mu + \nu$ decays can produce muons in accordance with the schemes

$$\begin{aligned}\bar{\nu}_{\mu} + p &\rightarrow n + \mu^{+} \\ \nu_{\mu} + n &\rightarrow p + \mu^{-}\end{aligned}$$

but do not produce electrons and positrons, i.e.

$$\begin{aligned}\bar{\nu}_{\mu} + p &\not\rightarrow n + e^{+} \\ \nu_{\mu} + n &\not\rightarrow p + e^{-}\end{aligned}$$

One would expect that such electrons would be produced if $\nu_e \equiv \nu_{\mu}$. Results of such experiments thus indicate why the search for the rare decay schemes has been unsuccessful.

It must also be noted that there are as yet no direct experimental data indicating the existence of the intermediate

Table 2.7

Reference	Method of recording of electrons with energies ~ 100 MeV	Range in polyethylene
[129]	Magnetic spectrometer	$< 10^{-3}$
[130]	Differential range spectrum	$< (4^{+3}_{-2}) \times 10^{-6}$
[131]	Spark chamber	$< 5.9 \times 10^{-6}$
[131]	Totally absorbing NaI crystal	$< 2 \times 10^{-7}$

boson responsible for weak interactions. Experiments with high-energy neutrinos which were considered in Chapter 1 did not provide any evidence for the existence of such a particle. Analysis of these experiments leads to the conclusion that if such a particle does exist, its mass must be very large ($M_W \geq 2$ GeV with a 99% confidence level).

NEGATIVE-MUON CAPTURE

3.1 NEUTRONS FROM NUCLEAR μ^- CAPTURE

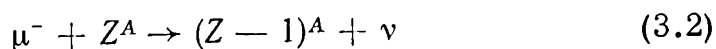
In Chapter 1 we summarized the results of experimental studies of the interaction of muons with the simplest nuclei, i.e. protons and He^3 . It was shown that the interaction of the negative muon with nuclear matter can be explained by postulating the reaction



in which the proton captures the negative muon and is transformed into a neutron and a neutrino. Practically the entire energy liberated in this process, which is close to the rest energy of the negative muon, is carried off by the neutrino. A detailed analysis was given in Chapter 1 of the experimental data on the interaction of negative muons with nuclei, together with a discussion of the conclusions which may be drawn from these data relating to the nature of the Fermi interaction (3.1).

The secondary particles produced in this reaction are the neutron and the neutrino. We will begin our review of phenomena which occur during the capture of negative muons by nuclei, with experiments in which the neutrons emitted

in this process have been observed. It follows from the elementary reaction (3.1) that the capture of a negative muon by a proton reduces the nuclear charge by 1:



If the muon is captured by a proton at rest, the energy of the neutron in reaction (3.1) is approximately 5.2 MeV. Since, however, the nucleons in the nucleus are in constant motion, the neutron energy is found to be appreciably greater, and may reach a few tens of MeV. The fast neutron either leaves the nucleus, or ejects a particle through a direct interaction, or transfers its energy to other nucleons, thus 'exciting' the nucleus. In the 'evaporation' which follows this excitation, the emission of protons and other charged particles is impeded by the Coulomb barrier, and therefore the particles emitted during this process are mainly neutrons and γ rays.

The first experiments with neutrons from nuclear μ^- capture were those of Sard et al. [1] and Groetzinger [2], who established the existence of a correlation between the absorption of a negative muon and the emission of a neutron, and estimated the mean number of neutrons per μ^- capture (the so-called 'multiplicity' \bar{n}). In some experiments performed after 1952-1953, it was possible to increase the neutron detection efficiency, and this led to a considerable improvement in the statistical accuracy (Widgoff [3], Jones [4], Kaplan [5]). Experiments carried out prior to 1953 have been reviewed by Sard and Crouch [6].

The first apparatus for the detection of neutrons from nuclear μ^- capture was built by Sard at Washington University (Fig. 3.1). Coincidences between two rows of Geiger counters, A and B, which were not accompanied by counts in the row C, i.e. events of the type $ABC\bar{C}$, identified cosmic-ray mesons which passed through 12.7 cm of lead and came to rest in the 7-cm-thick lead target. Neutrons emitted by the lead nuclei were detected by the thermal neutron counters N located in a large block of paraffin which slowed them down to thermal energies. The neutron counters were proportional counters filled with B^{10} -enriched boron trifluoride. Neutrons emitted in μ capture were identified by delayed coincidences in N, using the fact that the moderation of fast neutrons to thermal energies occurs in a time of the order of 1 μ sec, whereas the drift of time before B^{10}

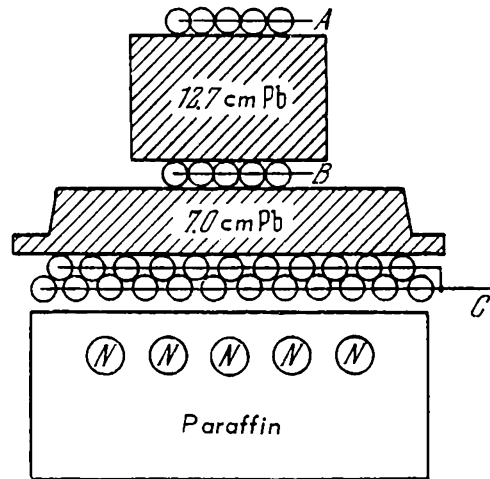


Fig. 3.1 Detection of neutrons resulting from the capture of slow cosmic-ray negative muons in lead (Sard et al.)

capture is of the order of $10\text{--}100\mu\text{sec}$. After each $ABC\bar{C}$ event, the circuit produced an $80\text{-}\mu\text{sec}$ gating pulse which was delayed by $4\mu\text{sec}$ relative to the $ABC\bar{C}$ pulse. This delay was necessary to reduce the background due to prompt counts in N. $ABC\bar{C}N$ coincidences selected neutrons which were time-correlated with the capture of negative muons in the lead absorber. For control purposes, the neutron counters were covered by a cadmium shield. The efficiency of the apparatus and the significance of the final results may be judged from the following figures. In 181 hours of operation at sea level, there were 61 $ABC\bar{C}N$ coincidences, whilst the estimated number of random coincidences was 0.2. When the boron counters were placed behind the cadmium shield there were no $ABC\bar{C}N$ coincidences in 51 hours of operation. In addition to showing the correlation between stopping negative muons and the emission of neutrons, the experiment was also the first direct demonstration of the fact that negative muons captured by nuclei were capable of producing nuclear disintegrations.

An interesting modification of this method was reported by Althaus [7], who combined a multiplate Wilson cloud chamber with boron neutron counters sunk in a paraffin block. This method was used to obtain photographs of muons stopping in the lead plates of the cloud chamber accompanied by counts in the boron counters.

Similar methods of recording neutrons with boron counters surrounded by paraffin were used by Groetzinger et al. [2, 8], who deflected negative muons on to an absorber with a magnetic field. The number of neutrons per muon capture in the lead absorber was estimated from these experiments to be $\bar{n} = 1.96 \pm 0.72$.

Quantitative experiments of the kind described above are very difficult because of the absolute neutron detection efficiency and the number of muon captures must be determined. Moreover, the effect of particles which can also generate neutrons, e.g. protons and pions must be eliminated. This was achieved by performing some of the measurements underground (a real density of the absorber up to 2000 g/cm²).

The neutron detection efficiency in the above experiments was quite small. For example, even in the experiments of Widgoff [3], who achieved the highest efficiency, it only amounted to about 7%.

In the experiments of Kaplan [5], however, the neutrons were detected with an efficiency approaching 60% by a liquid scintillator containing cadmium (Fig. 3.2). The volume of the detector was so large that the efficiency was practically independent of the neutron energy. The neutron counter was in the form of a cylinder (75-cm long, 75-cm diameter) with reflecting walls, and filled with a toluene solution of terphenyl. Of the neutrons slowed down in this medium 95% were captured by the cadmium in the solution, giving rise to γ -ray cascades with total energies of 9.2 MeV. The remaining 5% of neutrons were captured by protons with the appearance of 2.2-MeV γ rays. Most of these were converted into electrons producing scintillations in the counter. The scintillator was viewed by 44 photomultipliers in two independent groups. Pulses from the neutron counter and from counters I, II, III, IV, which defined the negative-muon beam were fed into two oscilloscopes whose screens were photographed on the same frame.

The following neutron multiplicities were obtained:

1. silver $\bar{n} = 1.55 \pm 0.06$;
2. iodine $\bar{n} = 1.49 \pm 0.06$;
3. gold $\bar{n} = 1.63 \pm 0.06$;
4. lead $\bar{n} = 1.64 \pm 0.07$.

Table 3.1 gives the neutron distributions obtained in these experiments ($f(n)$ represents the probability of emission of n neutrons).

It is evident from Table 3.1. that the probability of emission of no neutrons at all in the capture of negative muons by heavy nuclei is comparatively high: it approaches 0.4 and is nearly equal to the probability of emission of a single neutron. The data are not accurate enough to establish the existence of emission of four or more neutrons.

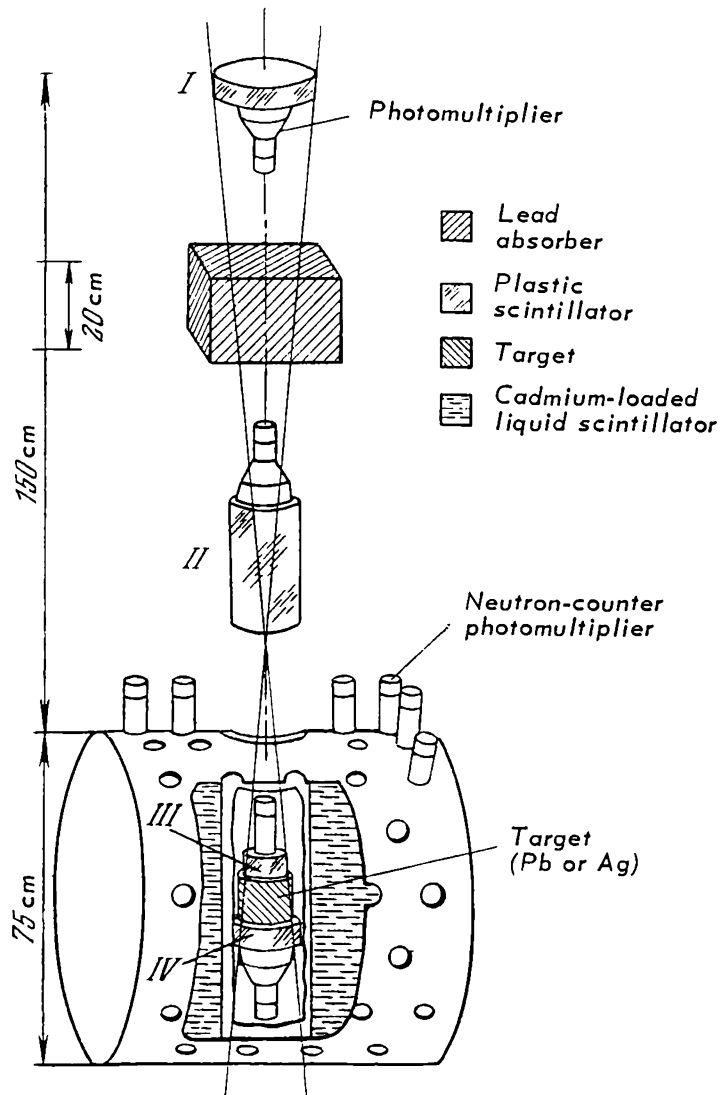


Fig. 3.2 Detection of neutrons from negative-muon capture in lead, iodine, gold, and silver (Kaplan et al.)

Table 3.2 summarizes most of the available data on the mean number of neutrons produced in nuclear μ^- capture.

Analyses of the emission of neutrons in μ^- capture based upon evaporation theory have been carried out by Tiomno and Wheeler [11], Rosenbluth [12], Lubkin [15], Kaplan [5] and Singer [16]. The problem was to find the nuclear excitation function from a postulated model, and hence, to use the evaporation theory to determine parameters such as the mean number of neutrons per capture, the number distribution of emitted neutrons and the neutron energy spectrum. Some of the results of such estimates are

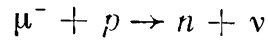
Table 3.1 Distribution of neutrons from negative-muon captures in Ag, I, Au and Pb

Element	$f(0)$	$f(1)$	$f(2)$
Ag	0.383 ± 0.025	0.455 ± 0.025	0.124 ± 0.015
I	0.393 ± 0.026	0.463 ± 0.026	0.107 ± 0.014
Au	0.368 ± 0.022	0.447 ± 0.023	0.144 ± 0.014
Pb	0.376 ± 0.027	0.446 ± 0.028	0.121 ± 0.016
Element	$f(3)$	$f(4)$	$f(> 4)$
Ag	0.033 ± 0.007	0.002 ± 0.003	0.002 ± 0.002
I	0.029 ± 0.007	0.007 ± 0.004	0.000 ± 0.002
Au	0.027 ± 0.006	0.011 ± 0.003	0.002 ± 0.002
Pb	0.049 ± 0.010	0.007 ± 0.004	0.002 ± 0.002

Table 3.2 Mean number \bar{n} of neutrons (multiplicity) in nuclear negative-muon capture

Nucleus	Z	\bar{n}	Method	Reference
Na	11	1.0 ± 0.4	Boron counters for slow neutrons, magnetic determination of the sign of the sign of the muons	[4]
Mg	12	0.6 ± 0.2	Boron counters for slow neutrons	[9]
Al	13	0.95 ± 0.17	Boron counters for slow neutrons	[4]
Ca	20	0.40 ± 0.4	"	[9]
Ag	47	1.55 ± 0.06	Liquid scintillator with Cd for neutron counting	[5]
Sn	50	1.54 ± 0.12	Boron counters for slow neutrons	[3]
I	57	1.7 ± 0.4	Radiochemical method: search for Te isotopes, accelerator	[10]
Pb	82	1.49 ± 0.06		[5]
		2.14 ± 0.13		[3]
		1.64 ± 0.07		
		1.70 ± 0.30	Boron counters for slow neutrons	[6]
		1.50 ± 0.40	"	[4]
Au	79	1.96 ± 0.72	Boron counters for slow neutrons	[8]
		2.32 ± 0.17		[3]
		1.63 ± 0.06		[5]

given by Kaplan [5], who used two nuclear models, namely, the Fermi gas model with two values of the reduced nucleon mass ($M_r = M$ and $M_r = M/2$), and the α -particle model in which negative muons are assumed to be absorbed by an α particle in a nucleus. Both models are capable of accounting for the experimental data on neutron multiplicities for lead and silver in terms of the elementary reaction



A more sensitive verification of evaporation theory would be achieved by studying the neutron energy spectrum and by improving the accuracy of data on the probability of emission of several neutrons, but experiments of this kind have not been performed to date.

3.2 EMISSION OF CHARGED PARTICLES IN NUCLEAR μ^- CAPTURE

For twelve years following the discovery of the muon in 1936, no experimental evidence was forthcoming for the existence of specifically nuclear interactions in nuclear μ^- capture. One of the first experiments indicating the presence of such interactions was performed by Camerini [17], who exposed nuclear emulsions at mountain altitudes. The emulsions were surrounded by a lateral lead screen but were exposed at the top and bottom to cosmic radiation. By following meson tracks in the emulsion from the capture of σ stars back to the points of entry into the photographic plate, Camerini showed that multi-prong σ stars were produced as a result of the capture of mesons leaving the lead screen, whilst mesons producing single-prong stars usually entered emulsions from above, i.e. from air. Such stars were due mainly to negative muons produced at moderate altitudes by primary cosmic radiation.

George and Evans [18], exposed nuclear emulsions under a depth equivalent to 40 m of water. The emulsions were prepared and developed underground to reduce the background, and a total of about 30 σ stars due to negative muons was observed.

A detailed study of stars produced as a result of nuclear μ^- capture became possible when pure negative-muon beams produced by accelerators became available. The

experiments have now been carried out both with nuclear emulsions and with bubble chambers. A characteristic feature of negative muons stopping in emulsions or bubble chambers is that most of the stopping tracks are not accompanied by the appearance of secondary charged particles in the detecting medium. We have seen above that about 40% of μ^- captures by heavy nuclei are not accompanied even by the emission of neutrons. It is evident that the emission of charged particles is impeded to an even greater extent by the presence of the Coulomb barrier. According to [18, 19], 97.6% of negative muons stopping in the emulsion do not form visible stars, 2.2% give rise to single-prong stars and only about 0.2% are accompanied by stars with two or more prongs.

These data are summarized in Table 3.3, together with the corresponding prong distribution for stars produced by stopping negative pions in nuclear emulsions (Menon et al. [23]). Less than 3% of stopping negative muons produce visible stars, compared with 72% of stopping negative pions.

A similar result was obtained by Stanard [20], who studied the probability of μ^- capture in carbon, using a propane bubble chamber. He found only three one-prong stars among 190 negative muons stopping in the chamber. The energy of the secondary particles in these stars was found to be less than 15 MeV when they were assumed to be protons.

Secondary charged particles emitted as a result of μ^- capture by the emulsion nuclei have short ranges which only in rare cases exceed 2-3 mm. The singly charged particles (protons, deuterons and tritons) have not therefore been individually identified so far, but the identification of α particles is relatively easy. If it is assumed that all singly charged particles in stars are protons, then it follows from the data of Morinaga and Fry [19] that the number of such 'protons' per μ^- capture in emulsion nuclei is 2.2%,

Table 3.3 Track-number distribution (in %) for σ_μ and σ_π stars in nuclear emulsions

Number of tracks Stars	0 (muon stopping without visible secondary track)	1	2	3	4	5	6
	σ_μ	97.6	2.2	~ 0.2	15	8	2
σ_π	28	23	23				

whilst the number of α particles is 0.5%. The energy spectra of these 'protons' and α particles for single-prong σ_μ stars in emulsions are shown in Figs. 3.3 and 3.4, in which the number of particles per 1-MeV energy range is plotted as a function of their energy in MeV. It is evident from

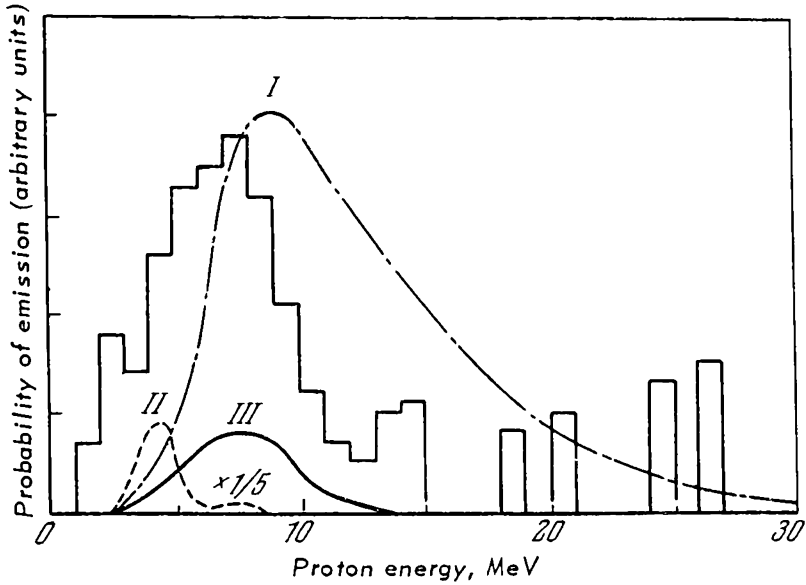


Fig. 3.3 Spectrum of protons emitted in σ_{μ^-} stars in nuclear emulsions. The histogram is based on the data of Fry. Curves I, II, and III are calculated from models I, II, III (see text)

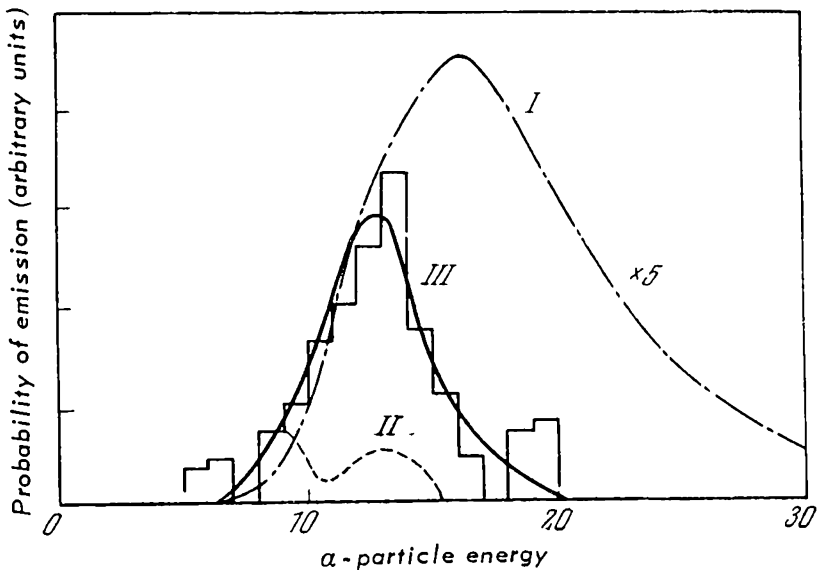
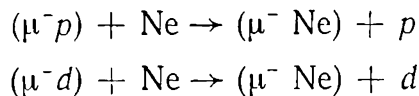


Fig. 3.4 Spectrum of α particles emitted in σ stars in emulsions. The histogram is based on the data of Fry. Curves I, II, and III are calculated from models I, II, III (see text)

these distributions that the energy of charged particles in σ_μ stars does not exceed about 25 MeV.

The introduction of the liquid-nitrogen bubble chamber and of the diffusion chamber has opened up new possibilities for the investigation of σ_μ stars. Alvarez et al. (cf. Chapter 5), who discovered the muon catalysis of the fusion of a proton and a deuteron into the He^3 nucleus, showed that the transfer of the negative muon occurred very efficiently between the proton and the deuteron. As a result of collisions between the mesonic atom (μ^-p) and deuterium nuclei, the negative muon leaves the mesonic atom (μ^-p) and forms (μ^-d). This process reaches saturation when the deuterium concentration is about 1%. Schiff [21] and Dzhelepov et al. [22] have shown that the negative muons in (μ^-p) and (μ^-d) mesonic atoms have a high probability of transfer to impurity nuclei introduced artificially into the chamber.

Schiff introduced neon in relative amounts of 15×10^{-6} and 260×10^{-6} into a liquid-hydrogen bubble chamber (cf. Chapter 5) and observed the transfer reactions



As a result of these reactions, the negative muon is captured by the neon atom where it either decays or is captured by the nucleus.

Fig 3.5 shows an unusual photograph obtained by Schiff in this experiment. The primary negative muon enters at left, forming a visible track. Near the point of interaction a 'rejuvenated' negative muon track is produced showing the characteristic X gap.

The energy of the 'rejuvenated' muon is about 5.4 MeV so that the usual sequence $(\mu^-p) + d \rightarrow (\mu^-d) + p$ and $(\mu^-d) + p \rightarrow \text{He}^3 + \mu^-$ must have taken place. An unusual feature of this photograph is that the 'rejuvenated' negative muon is slowed down in hydrogen, forms the mesonic atom (μ^-p) and is again captured by a deuteron, which is indicated by the second X gap at the end of its range. Finally it is transferred from the deuteron to a neon nucleus and its capture results in the appearance of a single-prong star at the end of the sequence.

Schiff observed 136 σ_μ stars produced as a result of negative-muon capture by neon nuclei. Fig. 3.6 shows the range spectrum of charged particles emitted in these stars. Only

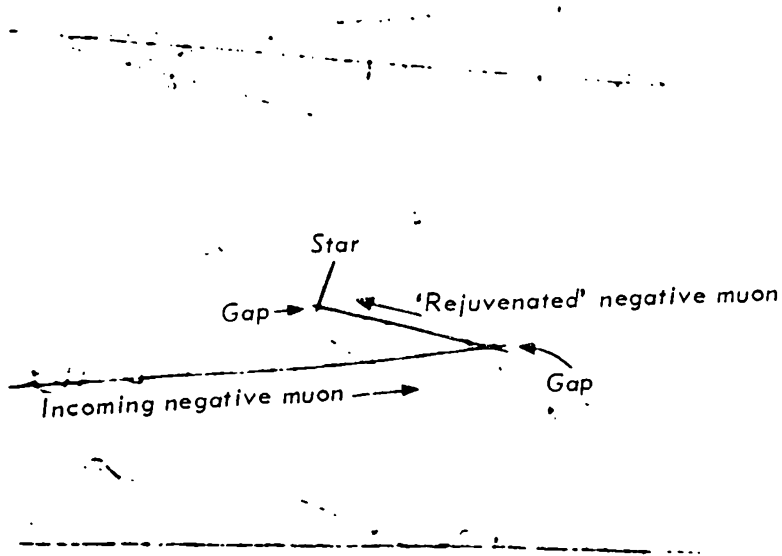


Fig. 3.5 Unusual photograph of a negative muon stopping in a liquid-hydrogen bubble chamber containing deuterium and neon impurities

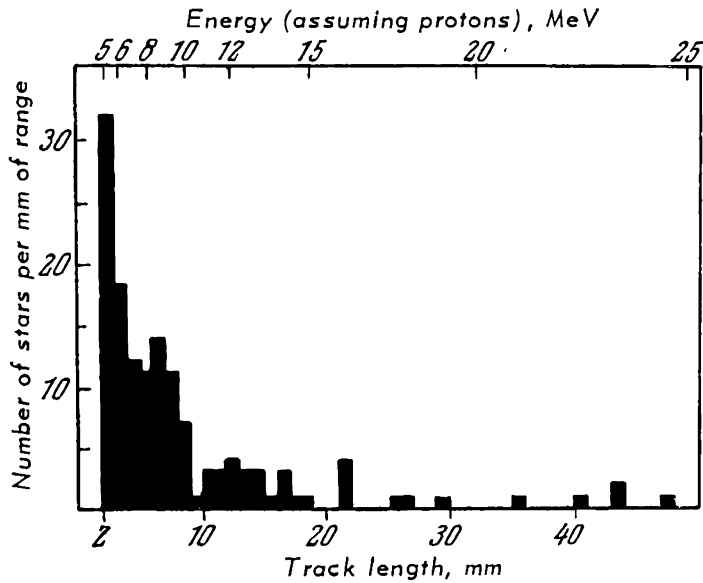


Fig. 3.6 Spectrum of protons from σ_{μ^-} stars produced as a result of negative-muon capture by neon

those secondary particles whose ranges were greater than 2 mm were selected. This cut-off explains the absence from the histogram of short-range particles. The energy of the secondary particles determined from the range-energy relation on the assumption that all the particles were protons

is indicated along the upper scale. As can be seen, the maximum proton energy does not exceed 25 MeV. In one case (not indicated in the histogram), a proton from a single-prong star had an energy of 29 MeV. Most of these stars have a single secondary charged particle and only five stars out of the 136 observed had two prongs. Schiff estimated that the probability that a negative muon captured by a neon nucleus would produce a visible star was $3.2 \pm 0.5\%$. All these data are in agreement with the results obtained from the study of σ_μ stars in nuclear emulsions.

Analysis of Fry's data on the nature and spectrum of particles in σ_μ stars in emulsions, in terms of various possible nuclear models, has been performed by Ishii [24], who calculated the spectrum of α particles and protons evaporated as a result of μ^- capture in AgBr emulsion crystals. In order to obtain the nuclear excitation function, it is necessary to know the momentum spectrum of nucleons in the nucleus. Ishii used the following models: Fermi gas model with $kT = 0$ and $kT = 9$ MeV, and the Chew-Goldberg distribution

$$F(p) = \frac{A}{(B + p^2)^2},$$

where A and B are constants. Comparisons of these estimates with theory are given in Table 3.4.

It is evident that none of these models is capable of explaining the predominance of protons among secondary particles in σ_μ stars. It may be noted that the number of α particles obtained from the Fermi gas model with $kT = 9$ MeV is in good agreement with experiment. Fig. 3.4 shows the spectrum of α particles calculated by Ishii. It is evident that the spectrum obtained using the Fermi gas model with $kT = 9$ MeV (curve III) is in good agreement

Table 3.4

Nucleon momentum distribution in the nucleus	Number of emitted particles, %	
	α particles	Protons
Chew-Goldberger	7.9	2.3
Fermi gas ($kT = 0$)	~ 0.1	~ 0.02
Fermi gas ($kT = 9$ MeV)	0.45	0.23
Experiment	0.5	2.2

with the experimental $\bar{\alpha}$ -particle spectrum, but there is a considerable discrepancy in the case of the proton spectrum. Singer [25] has attempted to explain the experimental data on the number of protons in σ_μ stars by postulating the existence of nucleon clusters on the nuclear surface.

3.3 NUCLEAR γ RAYS FROM μ^- CAPTURE

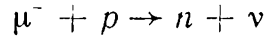
There is a lack of experimental data on γ rays from negative-muon capture. They appear to have been observed for the first time by Chang [26], who studied cosmic-ray negative muons stopping in thin lead plates placed in a Wilson cloud chamber. He showed that about three γ rays with energies between 1 and 3 MeV were emitted per negative-muon capture in lead. Part of this radiation was due to X rays produced as a result of cascade μ^- transitions in the mesonic lead atom, but the remainder was due to the relaxation of the excited nucleus after μ^- capture. The same conclusion was reached by Harris and Shanley [27], who performed a similar experiment using a Wilson cloud chamber containing thin lead foils situated in a magnetic field. Sens [28] separated the mesonic-atom emission of lead from nuclear γ rays by measuring their time distribution: mesonic-atom X rays are produced immediately after μ^- capture, whereas γ rays from the excited nucleus exhibit an exponential distribution which is determined by the μ^- -capture probability in lead nuclei. Sens obtained the distribution in Fig. 3.7, which clearly shows the 'prompt' emission of the mesonic atom and the nuclear γ -ray emission for which the mean lifetime was found to be $\tau = 72 \pm 10$ nsec. This result is in agreement to within the experimental error with data on decay electrons from stopping negative muons in lead. Sens' data show that the γ rays constitute about 50% of the mesonic X rays. There are 6-7 mesonic photons with energies greater than or approximately equal to 350 keV per μ^- -capture in lead, and this estimate therefore yields about three γ rays of this energy per μ^- -capture in lead.

We note that γ rays and neutrons emitted by nuclei excited as a result of μ^- capture may be used as indicators of the disappearance of negative muons. This method is particularly convenient for heavy elements where the μ^- -capture probability is much greater than the μ^- -decay probability (see Section 3.6).

3.4 THEORETICAL CONCLUSIONS

3.4.1 Hamiltonian for the four-fermion process $\mu + p \rightarrow n + \nu$

In the preceding sections of this chapter we have reviewed data on the nature of nuclear reactions occurring as a result of μ^- capture. These data were found to be in qualitative agreement with the hypothesis that the primary interaction of the negative muon with nuclear matter is



In the succeeding sections we shall be concerned with many phenomena resulting from nuclear μ^- capture. It is important, however, to note that currently available data on μ^- capture by protons and complex nuclei are insufficient to enable the Hamiltonian for the basic process (3.1) to be deduced from them. The reason for this is that the phenomena occurring within the nucleus are very complicated. It is, however, possible to carry out a more modest programme: starting with the universal Fermi interaction, we can write

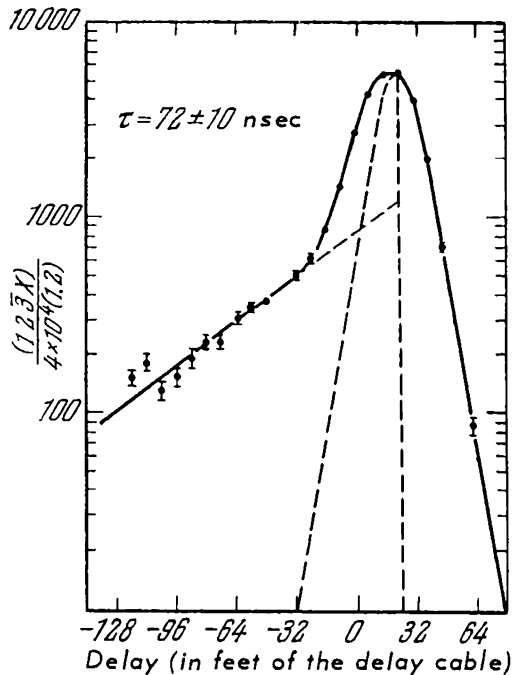


Fig. 3.7 Integral decay curve (Sens). The number of photons is plotted as a function of the delay between the stoppage of the negative muon in the absorber and the appearance of the photons

down the Hamiltonian for this process by analogy with the Hamiltonian for nuclear β decay, and then consider all the possible consequences of this Hamiltonian. Comparison with experimental data can then be used to verify the assumed interaction.

It was shown in the chapter on muon decay that the decay process could be described by the Hamiltonian

$$H = g (\bar{\psi}_\mu \gamma_\rho (1 + \gamma_5) \psi_\nu) (\bar{\psi}_\nu \gamma_\rho (1 + \gamma_5) \psi_e) \quad (3.3)$$

which is a mixture of the vector and axial-vector interactions with equal and opposite real coupling constants ($g_V = -g_A = g$). The same interaction was found to be capable of describing all the experimental data on nuclear β decay for which the prototype is the decay of the neutron

$$n \rightarrow p + e^- + \bar{\nu} \quad (3.4)$$

or the K -capture process

$$p + e^- \rightarrow n + \nu \quad (3.4a)$$

The Hamiltonian for these interactions is

$$iH = g (\bar{\psi}_n \gamma_\rho (1 - x\gamma_5) \psi_p) \cdot (\bar{\psi}_\nu \gamma_\rho (1 + \gamma_5) \psi_e)$$

where $x = g_A/g_V$ is the ratio of the coupling constants. In the case of the Hamiltonian for $\mu - e$ decay written above this ratio is $x = -1$. Nuclear β decay involves a complication connected with the fact that only the vector coupling constant retains the value which it had in the muon decay, whilst the effective axial-vector constant is greater so that $g_A = xg_V$, where $x \approx -1.21$.

This change in the axial-vector coupling constant is connected with the renormalization of the weak interaction (3.4), which is due to the fact that strongly interacting particles participate in nuclear β decay. This is distinct from muon decay, in which strongly interacting particles do not participate, and there are no effects connected with strong interactions.

If the four-fermion interaction is in fact universal, then negative-muon capture by a proton should be described by the same Hamiltonian as (3.4a), except that the wave function for the electron should be replaced by the muon wave function. We then have

$$H = g (\bar{\psi}_n \gamma_\rho (1 - x\gamma_5) \psi_p) (\bar{\psi}_\nu \gamma_\rho (1 + \gamma_5) \psi_\mu) \quad (3.5)$$

The energy released in nuclear β decay is of the order of 1 MeV. For example, the energy liberated in the decay of the neutron



is only 0.79 MeV, whilst the maximum energy released in nuclear β decay does not exceed 10-11 MeV. The energy liberated in μ^- capture by a proton is about 100 MeV. In these circumstances, strong-interaction effects such as virtual-pion exchange between proton and neutron in the reaction (3.1) become important. These effects have been estimated by Harris and Shanley [27] and by Wolfenstein [30]. They showed that when virtual-pion exchange is taken into account, the change in the vector and axial-vector coupling constants in the reaction $\mu^- + p \rightarrow n + \nu$, is small by comparison with β decay and may be neglected. However, virtual-pion exchange leads to the appearance of a large pseudoscalar interaction constant which is given by

$$g_P^\mu \approx 8g_A \quad (3.6)$$

The Hamiltonian is further complicated by the hypothesis of the conservation of vector current suggested by Gershtein and Zel'dovich [31] and by Feynman et al. [32]. Gell-Mann has shown that this hypothesis gives rise to the appearance of an additional 'weak-magnetism' constant which is proportional to the difference between the anomalous magnetic moments of the proton and the neutron ($\mu_p - \mu_n = 3.7$ nuclear magnetons):

$$g_M = g_V (\mu_p - \mu_n) \quad (3.7)$$

The appearance of these additional constants means that the Hamiltonian for the reaction $\mu^- + p \rightarrow n + \nu$ is determined by the following effective coupling constants:

effective vector constant

$$G_V \approx g_V (1 + \nu/2M)$$

effective pseudoscalar constant

$$G_A \approx g_A - g_V (1 + \mu_p - \mu_n) \frac{\nu}{2M} \quad (3.8)$$

effective pseudoscalar constant

$$G_P \approx [g_P - g_A - g_V (1 + \mu_p - \mu_n)] \frac{\nu}{2M}$$

where ν is the energy carried off by the neutrino and M the nucleon mass. The effective coupling constant determining the probability of the Fermi ($0 \rightarrow 0$) transition is given by

$$G_F^2 = G_V^2 \quad (3.9)$$

Finally, the effective Gamow-Teller constant determining the probability of $|\Delta I| = \pm 1$ or 0 transitions (but not $0 \rightarrow 0$ transitions) is given by

$$G_{G-T}^2 = G_A^2 + \frac{1}{3} G_P^2 - \frac{2}{3} G_P G_A \quad (3.10)$$

3.4.2 Probability of μ^- capture by a proton

Let us now consider Primakoff's calculations [33] of the probability of μ^- capture by a proton in the reaction $\mu^- + p \rightarrow n + \nu$ using a Hamiltonian with the above coupling constants, and then compare these results with experiment. In the μ^- -capture reaction, the proton with spin 1/2 is transformed into a neutron with the same spin, and we have an instance of the transition $|\Delta I| = 0$, which is a mixed Fermi and Gamow-Teller transition. Its analogue in nuclear β decay is electron capture ($p + e^- \rightarrow n + \nu$) and neutron decay ($n \rightarrow p + e^- + \bar{\nu}$). The probability of the latter processes is determined by the effective weak-interaction constant for the mixed Fermi and Gamow-Teller transitions in β decay: $g^2 = g_V^2 + 3g_A^2$.

Primakoff obtained the following expression for the probability of negative-muon capture from the K shell of a mesonic atom:

$$\Lambda(H_1^1) = \Lambda(1,1) v^2 \left(1 + \frac{m_\mu}{m_p} \right)^{-4} \quad (3.11)$$

where m_μ and m_p are the masses of the negative muon and proton respectively, and $v = 0.94$ is the momentum communicated to the neutrino in the reaction $\mu^- + p \rightarrow n + \nu$ in units of $m_\mu c$. The coefficient of $\Lambda(1,1)$ is therefore

$$v^2 \left(1 + \frac{m_\mu}{m_p} \right)^{-4} = 0.58 \quad (3.12)$$

The quantity $\Lambda(1,1)$ itself was shown by Primakoff to be given by

$$\Lambda(1,1) = \frac{1}{2\pi^2} \frac{m_\mu^5 g^2 c^4}{137^3 h^7} R \quad (3.13)$$

where g^2 is the effective weak-interaction coupling constant for the reaction $n \rightarrow p + e^- + \nu$ as given above, and R the ratio of the effective coupling constant for the reaction $\mu^- + p \rightarrow n + \nu$, i.e. $G^2 = G_F^2 + 3G_{G-T}^2$, to g^2 :

$$R = \frac{G_F^2 + 3G_{G-T}^2}{g_V^2 + 3g_A^2} \quad (3.14)$$

The ratio R determines the correction due to the replacement of the ordinary weak-interaction constants obtained from neutron-decay data by the meson weak-interaction constants (3.8). This correction does not exceed 10%. For example, if $\mu^- + p \rightarrow n + \nu$ is described by all the coupling constants in (3.8), then $R = 1.06$. If terms corresponding to 'weak magnetism' are absent, then $R = 0.9$, whilst in the absence of both additional terms $R = 1$.

These three hypotheses which we have denoted by A, B, and C yield the following values for $\Lambda(H_1^1)$:

Table 3.5

Hamiltonian (cf. Equation (3.8))	sec ⁻¹
A 'weak magnetism' + pseudo-scalar constant	169
B 'weak magnetism' absent	141
C 'weak magnetism' and pseudo-scalar constant absent	158

3.4.3 Spin dependence of the V-A interaction

A characteristic feature of the $V - A$ interaction is the fact that it is very dependent on the mutual orientation of the spins of the interacting particles. Consider, for example, μ^- capture by the proton in the hydrogen mesonic atom. This can occur from the two hyperfine-structure states of the mesonic atom corresponding to the singlet and triplet spin states in which the proton and muon spins S_p and S_μ are

either antiparallel or parallel. In the former case, the resultant spin is zero and in the latter it is one. In the $V - A$ theory, where $g_V = -g_A$, the capture probability in the triplet state for which $S_p + S_\mu = 1$ is zero ($\Lambda_+ = 0$), but the capture probability in the singlet state is finite. When the additional terms in the interaction Hamiltonian (3.8) are taken into account, the capture probability from the triplet state is found to be finite but is still much less than Λ_- . Thus, Primakoff's calculations yield

$$\Lambda_+ = 13 \text{ sec}^{-1}, \quad \Lambda_- = 636 \text{ sec}^{-1} \quad (3.15)$$

i.e. for hypothesis A in Table 3.5, the capture probability from the singlet state is approximately 50 times greater than that from the triplet state. We note that the quantity $\Lambda(H_i^1)$, which is the μ^- -capture probability for a proton, is equal to the weighted mean of Λ_+ and Λ_- :

$$\Lambda(H_i^1) = \frac{1}{4}\Lambda_- + \frac{3}{4}\Lambda_+ = 169 \text{ sec}^{-1}$$

3.5 μ^- CAPTURE IN HYDROGEN

In the experiment considered in Chapter 1, Hildebrand found the following value for the μ^- -capture probability in hydrogen

$$\Lambda = 434 \pm 100 \text{ sec}^{-1}$$

A similar experiment has been carried out by Bertolini et al. [34]. at CERN. They found that

$$\Lambda = 420 \pm 75 \text{ sec}^{-1}$$

If we combine these two results which are clearly in good agreement, we obtain

$$\Lambda = 425 \pm 60 \text{ sec}^{-1}$$

Another method of studying μ^- capture in liquid hydrogen has been used by Bleser et al. [35], who employed counter techniques and detected neutrons emitted more than $1 \mu \text{ sec}$ after the muon came to rest. This experiment will be discussed in detail in Chapter 5. With this method of measurement, neutrons are recorded from μ^- captures occurring

mainly in the mesonic molecule ($p\mu p$). The probability of this capture was found to be

$$\Lambda = (515 \pm 85) \text{ sec}^{-1}$$

Direct comparison of experimental results on μ^- capture in liquid hydrogen with theoretical predictions is difficult because the negative muon may exist following capture in hydrogen either in the form of the ($p\mu$) mesonic atom or in the form of the ($p\mu p$) molecule. The μ^- -capture probability for the mesonic atom is quite different from that for the mesonic molecule, since in the mesonic atom the negative muon may be captured by only one proton whereas in the mesonic molecule it may be captured by either of the two protons. In both cases, the capture probability is very dependent on the spin states of the interacting particles. The results described above can only be interpreted if the following information is available:

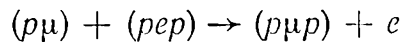
1. The relative proportion of time which the muon stopping in liquid hydrogen spends in the mesonic atom ($p\mu$) and in the mesonic molecule ($p\mu p$).
2. The population of the different spin orientations of the muon and the proton ($S = S_\mu + S_p = 0$ or 1) in the mesonic atom and the mesonic molecule.
3. The probability of finding the negative muon at the point occupied by a proton in the two systems under consideration.

These problems have been subjected to detailed theoretical analysis by Zel'dovich and Gershtein [36], Gershtein [37], Weinberg [38], Cohen et al. [39], Skyrme [40], Jackson [41] and others, and their results may be summarized briefly as follows. The negative muon in the mesonic atom (μ^-p) can exist in two hyperfine-structure states ($S = S_p + S_\mu = 0$ or 1) which differ in energy by 0.04 eV. However, owing to the Gershtein-Zel'dovich mechanism, the triplet state, in which the μ^- -capture probability is small will convert rapidly to the singlet state in which the probability is high. The reason for this conversion is that a neutral (μ^-p) atom in the triplet state may exchange its proton for another with opposite spin direction as a result of collisions with hydrogen atoms and molecules, and may thus find itself in a lower energy state. The probability of this conversion depends on the concentration of protons participating in these collisions. In liquid hydrogen, the half-life of the triplet

state does not exceed approximately 0.01% of the negative-muon half-life and, owing to this conversion, practically all (μ^-p) atoms produced in μ^- capture are found to be in the singlet state. The ratio of the number of mesonic molecules to the number of mesonic atoms has been considered by Cohen et al. [39], who showed that

$$\frac{N(p\mu p)}{N(p\mu)} \gg 1$$

which is explained by the fact that the reaction



in which the liberated energy is about 124 eV, occurs with high probability. For example, in chemically and isotopically pure liquid hydrogen, about 95% of the captured muons are in the $(p\mu p)$ molecule [39]. This molecule can exist either in the ortho-state, in which the proton spins are all parallel, or in the para-state, in which they are antiparallel. Calculations show that, as a result of collisions, the para-mesonic molecules are converted into ortho-molecules in a time of about one-tenth of the muon half-life. Owing to this rapid para-ortho conversion, it is the ortho-state which is important for the ultimate fate of the negative muon captured in liquid hydrogen. We thus see that the singlet state ($S_p + S_\mu = 0$) is important in the mesonic atom, whilst in the mesonic molecule the important state is the ortho-state of the two protons ($S_{p1} + S_{p2} = 1$). The μ -capture probability in these two states of the mesonic atom and mesonic molecule does not differ by more than a factor of 2, and since the relative number of mesonic atoms is small, the number of $(p\mu)$ atoms may not be of great practical importance.

In the ortho-mesonic molecule in which the spins of the two protons are parallel, the negative muon can be either in the $S = 1 - 1/2 = 1/2$ state or the $S = 1 + 1/2 = 3/2$ state, and it is necessary to know the μ^- -capture probability for both of these states. Primakoff has shown that in the $S = 1/2$ state the capture probability is

$$\Lambda\left(\frac{1}{2}\right) = 2\gamma_0 \left(\frac{3}{4} \Lambda_- + \frac{1}{4} \Lambda_+ \right) \quad (3.16)$$

whilst in the $S = 3/2$ state it is

$$\Lambda_1 \left(\frac{3}{2} \right) = 2\gamma_0 \Lambda_+ \quad (3.17)$$

where Λ_- and Λ_+ are the μ^- -capture probabilities in the singlet and triplet states of the mesonic atom respectively, and γ_0 is the ratio of the probabilities of finding the negative muon at the point occupied by the proton of the ortho-mesonic molecule and the mesonic atom.

In the para-mesonic molecule

$$\Lambda_{p\mu p}^{\text{para}} = 2\gamma_p \left(\frac{1}{4} \Lambda_- + \frac{3}{4} \Lambda_+ \right) \quad (3.18)$$

where γ_p is defined as above, except that here it refers to the para-molecule. Weinberg's calculations [38] yield

$$\gamma_0 = 1.165, \quad \gamma_p = 1.308$$

If we neglect the probability of finding the negative muon in the para-molecule, we find that the total μ^- -capture probability is

$$\Lambda \approx \Lambda_{p\mu p}^{\text{ortho}} = \xi \Lambda \left(\frac{1}{2} \right) + (1 - \xi) \Lambda \left(\frac{3}{2} \right) \quad (3.19)$$

where ξ determines the probability of finding the negative muon in the $S = 1/2$ state, whilst $(1 - \xi)$ determines the probability of finding it in the $S = 3/2$ state. Since $\Lambda_+ \ll \Lambda_-$ we have

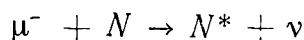
$$\Lambda \approx 2\xi \frac{3}{4} \Lambda_- \gamma \quad (3.20)$$

The parameter ξ is determined by the populations of the various μ^- spin states in the mesonic molecule. Weinberg has shown that it must lie within the range $1/2 \leq \xi \leq 1$, so that, subject to the above simplifications, the expected value of the μ^- -capture probability in liquid hydrogen lies within the range $3/4 \Lambda_- \gamma < \Lambda < 2 \times 3/4 \Lambda_- \gamma$. When this is referred to a single proton it is found that the μ^- -capture probability lies within the range $\Lambda = (300-600) \text{ sec}^{-1}$. The above experimental data for the μ^- -capture probability in liquid hydrogen are in agreement with this estimate. Meso-molecular phenomena are too complex to enable us, at

present, to extract from experimental data all the information about the interaction between the negative muon and the proton which they contain. It may be expected that with increasing experimental accuracy it will be possible to determine the effective Fermi weak-interaction constant for the capture reaction $\mu^- + p \rightarrow n + \nu$ directly from experiment.

3.6 TRANSITION OF NUCLEI TO DEFINITE STATES ON μ^- CAPTURE

In the μ^- -capture reaction



the final nucleus N^* may be in one of a large number of excited states, and in order to compare experimental data and theory it is necessary to know the matrix elements for transitions from the ground state of the original nucleus N to all the energetically accessible states of the nucleus N^* . This problem can only be solved for a particular nuclear model. Therefore capture reactions in which the nucleus N^* is found in a definite state, from which it then returns to the ground state through β decay, are of particular interest. The matrix element for the β transition is usually known and, when this is so, the experimental problem of comparing the interaction constants in muon capture and in β decay can be reduced to the comparison of the direct and reverse transition probabilities. This situation occurs, for example, in μ^- capture by He^3 , Li^6 and C^{12} nuclei, leading to the formation of H^3 , He^6 and B^{12} respectively, in the ground state. These nuclei return to the ground states of the original nuclei through β decay. These reactions are summarized in Table 3.6.

All these transitions occur without change of parity and the last two are pure Gamow-Teller transitions. The He^3 and H^3 nuclei do not have excited states. The nuclear-level schemes for the $\text{Li}^6 \xrightarrow{\mu^-} \text{He}^6$ and $\text{C}^{12} \xrightarrow{\mu^-} \text{B}^{12}$ transitions are shown in Figs. 3.8 and 3.9, from which it is evident that the first excited states of He^6 and B^{12} lie at a considerable distance from the ground state (1.7 MeV and 0.95 MeV in He^6 and B^{12} respectively). Since the excitation energy received by the nucleus in muon capture is small and of the order of 5 MeV, the probability of μ^- capture to the ground

Table 3.6

Negative-muon capture reaction	β -decay reaction	Spin and parity		ΔJ	Transition
		N	N^*		
$\mu^- + \text{He}_2^3 \rightarrow \text{H}_1^3 + \nu$	$\text{H}_1^3 \rightarrow \text{H}_2^3 + e^- + \bar{\nu}$	$\frac{1}{2}$	$\frac{1}{2}$	0	Mixed
$\mu^- + \text{Li}_3^6 \rightarrow \text{He}_2^6 + \nu$	$\text{He}_2^6 \rightarrow \text{Li}_3^6 + e^- + \bar{\nu}$	1^+	0^+	-1	Gamow-Teller
$\mu^- + \text{C}_6^{12} \rightarrow \text{B}_6^{12} + \nu$	$\text{B}_6^{12} \rightarrow \text{C}_6^{12} + e^- + \bar{\nu}$	0^+	1^+	1	Gamow-Teller

state of the product nucleus is appreciably greater than the probability of capture to excited states.

The first calculations of the transition probability of μ^- capture from the ground state of C^{12} to the ground state of B^{12} were carried out by Godfrey [42]. Fujii and Primakoff [43] found that the ratio of the transition probability from the state $N(a)$ to the state $N^*(b)$ in μ^- capture

$$\mu^- + N(a) \rightarrow N^*(b) + \nu$$

to the probability of the reverse transition in β decay.

$$N^*(b) \rightarrow N(a) + e^- + \bar{\nu}$$

is given by

$$\frac{\Lambda^\mu(a \rightarrow b)}{\Lambda^\beta(b \rightarrow a)} = \left[\pi(\eta_{ba})^2 \frac{Z^3 m_\mu^5}{(137)^3 f_{ba}} \right] \cdot \frac{2I_b + 1}{2I_a + 1} \cdot \left| \frac{\text{ME}_{\text{nucl}}^\mu(a \rightarrow b)}{\text{ME}_{\text{nucl}}^\beta(b \rightarrow a)} \right|^2 \quad (3.21)$$

In this formula $\eta_{ba} \approx v_{ba}/m_\mu$ is the ratio of the energy of the neutrino from the μ^- -capture reaction to the rest energy of the negative muon, Z is the nuclear charge of a , I_a and I_b are the spins of nuclei a and b , and the function f_{ba} is defined by

$$f_{ba} = \int_1^{(E_e)_{\text{max}}} F_{ba}(Z, E_e) (E_{e\text{max}} - E_e)^2 E_e (E_e^2 - 1)^{1/2} dE_e$$

where E_e is the total energy of the decay electron in the $b \rightarrow a$ transition and F_{ba} is the Fermi function for this transition. The quantities denoted by ME in Equation (3.21) are

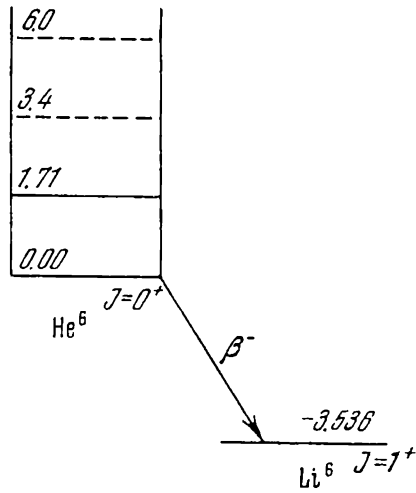


Fig. 3.8 Lower levels of He⁶

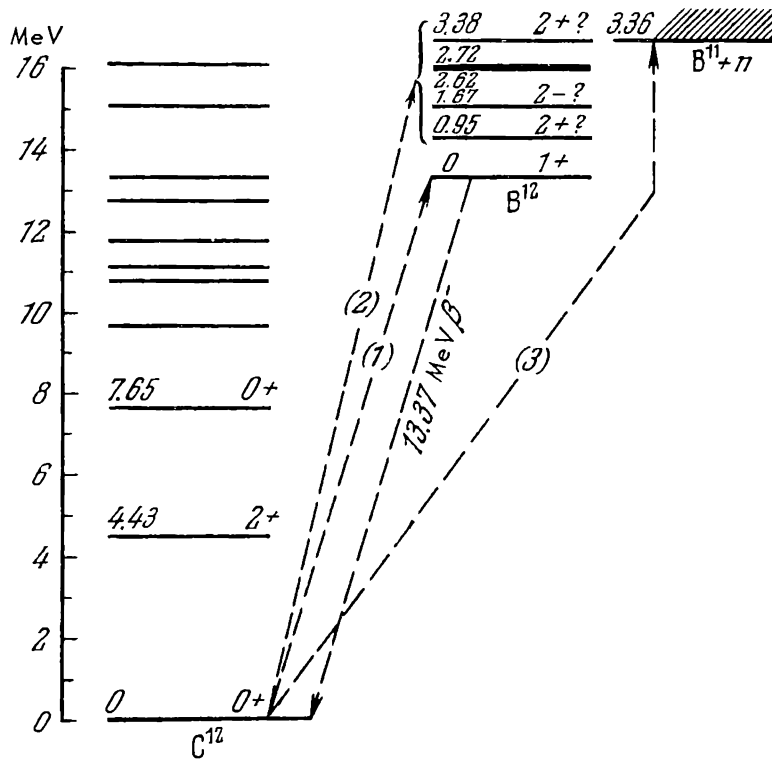


Fig. 3.9 Nuclear levels of B¹² and C¹²

the matrix elements for nuclear transitions. The matrix element

$$|M_{\text{nucl}}^{\mu}(a \rightarrow b)|^2$$

is proportional to the square of the effective muon weak-interaction constant G_{μ}^2 for the $a \rightarrow b$ transition, whilst the

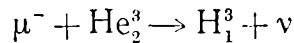
matrix element for the reverse transition in β decay

$$|M^\beta(b \rightarrow a)|^2$$

is proportional to the square of the effective β -decay weak-interaction constant g_β^2 . Comparison of these constants can be made by comparing the direct and reverse transition probabilities $\Lambda^\mu(a \rightarrow b)$ and $\Lambda^\beta(b \rightarrow a)$.

3.7 MEASUREMENTS OF THE EFFECTIVE CONSTANT FOR THE MIXED TRANSITION ($\frac{1}{2}^+ \rightarrow \frac{1}{2}^+$) IN μ^- CAPTURE

The reaction (cf. Table 3.6)



involves a mixed transition whose probability is determined by the sum of squares of the Fermi and Gamow-Teller constants

$$G^2 = G_F^2 + 3G_{G-T}^2 \quad (3.22)$$

In Chapter 1 we considered the experiment of Zaimidoroga et al. [42], who measured the μ^- -capture probability for He^3 nuclei. He found that the capture probability was

$$\Lambda = (1.41 \pm 0.14) \cdot 10^3 \text{ sec}^{-1}$$

This experiment is of particular interest for two reasons. Firstly, there is no ambiguity in the interpretation of the results since all captures occur from the two hyperfine-structure states of the helium mesonic atom. Secondly, the capture probability can in this case be calculated accurately if the coupling constants are known. The accuracy of these calculations appears to be in the region of 5%. They have been performed by Fujii and Primakoff [43], Werntz [44] and Fujii [45]. Their results are summarized in Table 3.7, from which it is evident that the μ^- -capture probability in He^3 is a function of the nuclear radius R . The experiments of Hoffstadter et al. have shown that the largest of the three nuclear radii is the most probable. It follows that the experimental data are in good agreement with the expected capture probability given in Table 3.7. It may therefore be concluded that experiment confirms the magnitude of the square of the

effective coupling constant

$$G^2 = G_F^2 + 3 G_{G-T}^2$$

obtained from the assumed interaction Hamiltonian (3.8) to within 10%. This experiment does not, of course, yield separately the values of the squares of the two coupling constants G_F^2 and G_{G-T}^2 .

3.8 DETERMINATION OF THE EFFECTIVE CONSTANT FOR THE GAMOW-TELLER TRANSITION IN μ^- CAPTURE

The last two transitions in Table 3.6, in which the spin changes by 1 and there is no change of parity, are pure Gamow-Teller transitions, whose probability is determined by the effective coupling constant

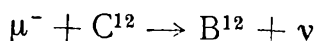
$$G_{G-T}^2 = G_A^2 + \frac{1}{3} G_P^2 - \frac{2}{3} G_P G_A \quad (3.23)$$

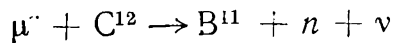
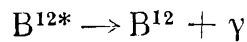
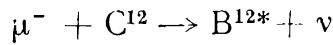
This probability is independent, to within terms of order $(v/M)^2$, of the axial-vector coupling constant and a comparison of the probability of these transitions with the probabilities of the reverse β transitions enables us to compare the axial-vector coupling constants in muon capture and β decay. An experiment with Li^6 has not been performed as yet because of considerable experimental difficulties. Negative-muon capture by C^{12} nuclei was first investigated by

Table 3.7

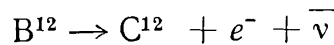
Reference	Assumed nuclear radius $\times 10^{13}$ cm	Muon absorption probability
[45]	1.5	$1.66 \times 10^3 \text{ sec}^{-1}$
[44]	1.56	$1.56 \times 10^{13} \text{ sec}^{-1}$
[43]	1.78	$1.46 \times 10^3 \text{ sec}^{-1}$

Godfrey [42]. μ^- capture by C^{12} (cf. Fig. 3.9) leads to the formation of a B^{12} nucleus in either the ground or an excited state in accordance with the schemes





and so on. Captures to the ground or excited states of B^{12} can be identified experimentally by the subsequent decay of B^{12} to the ground state of C^{12} :

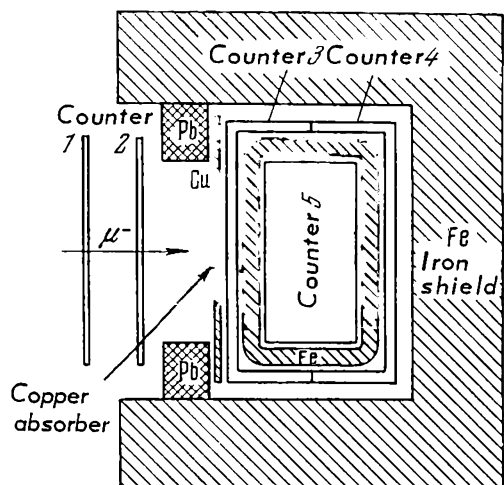


In Godfrey's experiment, slow cosmic-ray negative muons were brought to rest in an organic liquid scintillator having a volume of about 1.3 litres, and an oscilloscope was used to display two types of pulses following the arrival of stopping negative muons: pulses from electrons originating in $\mu - e$ decays characterized by a mean life of $2 \mu\text{sec}$, and pulses from the β decay of B^{12} whose half-life is about $39 \mu\text{sec}$. This experiment has been repeated by a number of groups using counter techniques with muon beams from accelerators (Burgman et al. [46], Love et al. [47], Bloch [48] and Maier et al. [49]). Fetkovich et al. [50] have determined the probability of the reaction $\mu^- + \text{C}^{12} \rightarrow \text{B}^{12} + \nu$ using a propane bubble chamber. The experiment was improved and repeated by Argo et al. [51] using cosmic radiation as a source of slow negative muons.

Argo et al. also estimated the number of negative-muon captures leading to the formation of B^{12} by measuring the number of γ rays with energies greater than 0.5 MeV which accompanied μ^- capture. It was found that only about 10% of all interactions led to the formation of an excited B^{12} nucleus (arrow 2 in Fig. 3.9).

Among accelerator experiments, we shall consider the measurements of Maier et al. [49]. The apparatus is illustrated in Fig. 3.10. The 45-MeV negative-muon beam, which had a pion contamination of about 1/3%, was brought to rest in the scintillation counter 5 ($10 \times 10 \times 5 \text{ cm}^3$). The number of negative muons decaying in 5 was determined by counting the number of decay electrons, and the number of μ^- captures in carbon leading to the formation of excited B^{12} nuclei was found by detecting the β -decay electrons from these nuclei (also in counter 5). Counters 3 and 4 which completely surrounded counter 5 were used as a cosmic-ray shield and

Fig. 3.10 The experiment of Maier [49]. Stopping negative muons are indicated by 1,2,5,4 coincidences, electrons from $\mu-e$ decays by counter 5, electrons from B^{12} decays by 5,3,4 coincidences; counters 3 and 4 surround counter 5 in which the negative muons come to rest and B^{12} nuclei are formed



were connected in anti-coincidence with counter 5. The iron screen around counter 5 was 7-mm thick and shielded the anti-coincidence counters $\bar{3}$, $\bar{4}$ from electrons originating in counter 5 from β decays of B^{12} . The principal aim of this experiment was to determine the decay curves $\mu-e$ decay and the β decay of B^{12} , and to verify experimentally the absence of other β activity induced by the meson beam. The transition probability $\Lambda (C^{12} \rightarrow B^{12})$ was found to be

$$\Lambda = (7.01 \pm 0.27) \cdot 10^3 \text{ sec}^{-1}$$

After the introduction of a 10% correction to allow for the fact that some of the transitions occurred to excited states of B^{12} , the final transition probability was found to be

$$\Lambda (C^{12} \rightarrow B^{12}) = (6.31 \pm 0.24) \cdot 10^3 \text{ sec}^{-1}$$

It is also interesting to consider the experiments of Fetkovich et al. [50], in which the reaction $\mu^- + C^{12} \rightarrow B^{12} + \nu$ and the subsequent decay of B^{12} nuclei were recorded by an ingenious method involving time-delayed photography of tracks in a propane bubble chamber exposed to a negative-muon beam. The sensitive time of the chamber was about 20 msec and the pressure was released immediately after the accelerator pulse. The bubble chamber was photographed twice: immediately after the pulse in order to determine whether or not the negative muon stopping in the chamber decayed, and again after 15 msec in order to record the slow electron from the decay of B^{12} . The volume was displaced slightly during the 15-msec interval so that in the case of the decay of B^{12} the photographs showed two identical and parallel negative-muon tracks and the track of the

decay electron between the ends of these tracks. The numbers of μ^- and B^{12} decays were counted simultaneously. In all, 46 B^{12} decays were observed and the transition probability $\Lambda (C^{12} \rightarrow B^{12})$ was calculated to be $(7.6 \pm 1.2) \times 10^3 \text{ sec}^{-1}$.

The probabilities $\Lambda (C^{12} \rightarrow B^{12})$ obtained by different workers are summarized in Table 3.8.

The capture probabilities given in Table 3.8 have been reduced by 10% in order to correct for transitions to the excited states of B^{12} . It is evident that the results of Burgman et al. and Argo et al. are much higher than the other data, and may have been subject to some systematic error. This is quite possible in view of difficulties associated with absolute measurements of this kind, especially when they are carried out with cosmic rays. The other results are in good agreement with each other.

Let us now consider the theoretical estimates of the probability of the reaction $\mu^- + C^{12} \rightarrow B^{12} + \nu$ which have been performed by Wolfenstein [52], Morita and Fujii [53] and Fujii and Primakoff [54]. All of these calculations were based on the interaction Hamiltonian considered above, i.e. it was assumed that the Hamiltonian consisted of three parts - the first representing the $V - A$ interaction, the second the induced pseudoscalar interaction and the third the interaction due to the 'weak magnetism' of Gell-Mann and Feynman. The results of these calculations are summarized in Table 3.9. The shell model with $J - J$ coupling was assumed to obtain the matrix elements for the $B^{12} \rightarrow C^{12}$ transitions.

Wolfenstein has estimated that the uncertainties in these calculations are about 20%, and the estimates given in the table are virtually indistinguishable to within this accuracy.

It is evident from the transition probabilities estimated above that it is impossible to decide experimentally between

Table 3.8

Reference	$\Lambda \times 10^3 \text{ sec}^{-1}$	Source of mesons
[42]	5.9 ± 1.5	Cosmic rays
[46]	9.18 ± 0.5	Accelerator
[42]	9.05 ± 0.95	Cosmic rays
[47]	6.8 ± 1.5	Accelerator
[50]	6.8 ± 1.1	"
[49]	6.31 ± 0.24	"
[48]	5.8 ± 1.3	"

Table 3.9

	Assumed interaction Hamiltonian		Calculated probability for the $C^{12} + \mu \rightarrow B^{12} + \nu$ transition ($\Lambda \times 10^3 \text{ sec}^{-1}$)		
	C_P/C_A	'Weak magnetism'	I	II	III
<i>A</i>	8	Present	7.4 ± 1.6	7.12	7.86
<i>B</i>	8	Absent	5.9 ± 1.2	5.68	6.34
<i>C</i>	0	Absent	7.3 ± 1.5	7.0	—

I – Wolfenstein [52] – including relativistic corrections for the neutrino wave function, d wave included; II – Morita and Fujii [53] – including relativistic corrections; III – Fujii and Primakoff [54] – without relativistic terms in the Hamiltonian

hypotheses A and C, since the calculated transition probabilities for these two variants do not differ by more than 1.5%. We shall therefore confine our attention to the comparison of the most accurate experimental result

$$\Lambda = (6.31 \pm 0.24) \cdot 10^3 \text{ sec}^{-1}$$

with the expected probability for hypothesis A

$$\Lambda = (7.4 \pm 1.6) \cdot 10^3 \text{ sec}^{-1}$$

As can be seen, these data agree to within the estimated errors. It may therefore be considered that the above experiments confirm the equality of the effective axial-vector interaction constants for β decay and negative-muon capture, i.e.

$$|G_{G-T}^\mu|^2 = |g_A^\beta|^2$$

but only to within 20%. The accuracy of theoretical and experimental estimates of capture probabilities is insufficient to indicate the influence of the additional interaction constants.

Knowing the constant $G^2 = G_F^2 + 3G_{G-T}^2$ from μ^- capture in He^3 , and the constant G_{G-T}^2 from μ^- capture in C^{12} , it is possible to estimate the magnitude of the Fermi constant, G_F , in negative-muon capture. Using Maier's data for the μ^- -capture probability in C^{12} (Table 3.8), it is found that $|G_F| \approx 0.8_{-0.3}^{+0.4} |G_{G-T}|$. The two coupling constants are therefore equal, as predicted by the Hamiltonian (3.8), but the experimental accuracy is not high.

3.9 MEASUREMENTS OF THE TOTAL μ^- -CAPTURE PROBABILITY

3.9.1 Capture time for negative muons

The principal method of determining the μ^- -capture probability for stopping muons is to compare the mean lifetimes of negative and positive muons. A negative muon in the K shell of a mesonic atom can either decay or be captured by the nucleus, and the total probability that it will disappear as a result of the two processes is equal to the sum of the decay and capture probabilities, Λ_d and Λ_c :

$$\Lambda = \Lambda_d + \Lambda_c \quad (3.24)$$

If τ is the mean negative-muon lifetime in the K shell and Λ_d is the muon-decay probability we have

$$\frac{1}{\tau} = \Lambda_d + \Lambda_c \quad (3.25)$$

and the determination of the total capture probability Λ_c from the K shell reduces to the measurement of negative-muon lifetime τ in this shell and the decay probability Λ_d . It is usually assumed that the decay probability for a muon in the K shell of the mesonic atom is the same as the decay probability for a free positive muon, i.e. $\Lambda_d = \frac{1}{\tau_0}$, where τ_0 is the lifetime of a free muon. In reality the decay probabilities are not equal (cf. Section 3.11), but the difference is small and has very little effect on Λ_c :

$$\Lambda_c = \frac{1}{\tau} - \frac{1}{\tau_0} \quad (3.26)$$

which is obtained on the assumption that $\Lambda_d(Z) = \frac{1}{\tau_0}$.

To identify $1/\tau$ with the total probability for the disappearance of the muon through decay and capture processes, it is necessary that the time spent by the negative muon in cascade transitions from distant orbits to the K orbit of the mesonic atom should be small in comparison with τ , which lies between approximately 2 μsec (light mesonic atoms) and 0.08 μsec (heavy mesonic atoms). A calculation of the time necessary for the negative muon to approach the nucleus was first performed by Fermi and Teller [55] in connection with the experiments of Conversi, Pancini and

Piccioni. This calculation shows that the total time for the muon to be slowed down from a velocity of the order of the velocity valence electrons (muon energy ~ 2 keV) until it reaches the mesonic K shell is 9×10^{-14} sec for carbon and 6×10^{-14} sec for iron. The negative muon therefore spends most of its lifetime in the K shell of the mesonic atom, and therefore the μ^- -capture probability from the K shell can be accurately identified with the reciprocal of the muon lifetime.

Calculations such as these have been verified for negative pions, and there are no reasons to suppose that the result will be substantially different for negative muons. For example, Fry and White [56] and Fields et al. [57] observed $\pi^- - \mu^-$ decays in flight in an emulsion and a liquid-hydrogen bubble chamber respectively. Since the time of interaction between a nucleus and a negative pion in the K shell of the mesonic atom is smaller by many orders of magnitude than the mean lifetime of the free pion, all the $\pi^- - \mu^-$ decays occur in flight during the slowing-down process, and the ratio of the number of such decays to the total number of observed stopping tracks is determined by the ratio of the slowing-down time to the mean negative-pion lifetime. The velocity of the pion at the instant of decay is determined by the kinematics of the decay: the angle between the muon and the pion tracks, and the μ^- range. The results obtained by Fields et al. [57] may be summarized by saying that a 175-keV negative pion, which is being slowed down in liquid hydrogen is captured by a nucleus within 3×10^{-12} sec. This result confirms the above conclusion that in all experiments in which the negative-muon lifetime has been measured, the time taken in cascade transitions to the K shell is negligible.

3.9.2 *Methods of measuring the negative-muon lifetime*

First let us consider the experimental methods used with cosmic rays. Here, the slow-muon flux consists of particles of both signs, and therefore the measured negative-muon lifetime is subject to a 'background' due to positive-muon decays. This background is particularly important in the determination of the lifetime of negative muons captured in light atoms, when it is comparable to the positive-muon lifetime.

A number of methods have been devised to eliminate this effect. Negative and positive muons can be roughly separated

with the aid of magnetized iron blocks, by determining the sign of the charge with a counter hodoscope system in a magnetic field, or by recording the interactions of negative muons not by means of decay electrons but by means of neutrons and γ rays emitted by excited nuclei on μ^- capture.

a. Separation of negative muons by magnetic analysis.

This method has been used by the Rome group [58, 59]. In the first experiments the muons were roughly separated by magnetized iron blocks as in the experiments of Conversi et al. In later experiments [60] the sign of the muons was determined with a counter hodoscope system (Fig. 3.11). Decay electrons from the target were recorded by scintillation counters S_2 , S_3 and special electronic circuits were used to determine, with the aid of an oscilloscope, the time interval between the pulses from counters S_1 and S_2 or S_2 and S_3 , which indicated the stopping of a muon and the appearance of a decay electron. Apparatus of this kind, incorporating iron blocks of total weight 13 kg, recorded about 1.3 decays per hour with a signal-to-background ratio of 4.

b. Separation of negative muons using γ rays and neutrons from excited nuclei.

The nuclear μ^- -capture probability increases rapidly with the nuclear charge Z , and for $Z \sim 11$ it is approximately equal to the μ^- -decay probability, i.e. it approaches $4.5 \times 10^5 \text{ sec}^{-1}$. As Z increases further, the probability is found to be proportional to Z^4 . For example, when $Z = 15$ the negative-muon lifetime is approximately three times smaller than the positive-muon lifetime, whilst for $Z = 20$ the factor is approximately 7. It follows that even for moderate values of Z there is a large reduction in the electron yield, and it is experimentally more convenient to record the rate of interaction of negative muons by recording γ rays and neutrons emitted by nuclei on μ^- capture. This method completely avoids the background due to positive-muon decays, since positively charged particles cannot be absorbed by the nuclei. First measurements of the negative-muon lifetime by this method were carried out by the Princeton group (Keuffel et al. [61], Meier and Keuffel [62]).

These workers measured the lifetime for eight elements with atomic numbers between 29 and 82. Fig. 3.12 illustrates

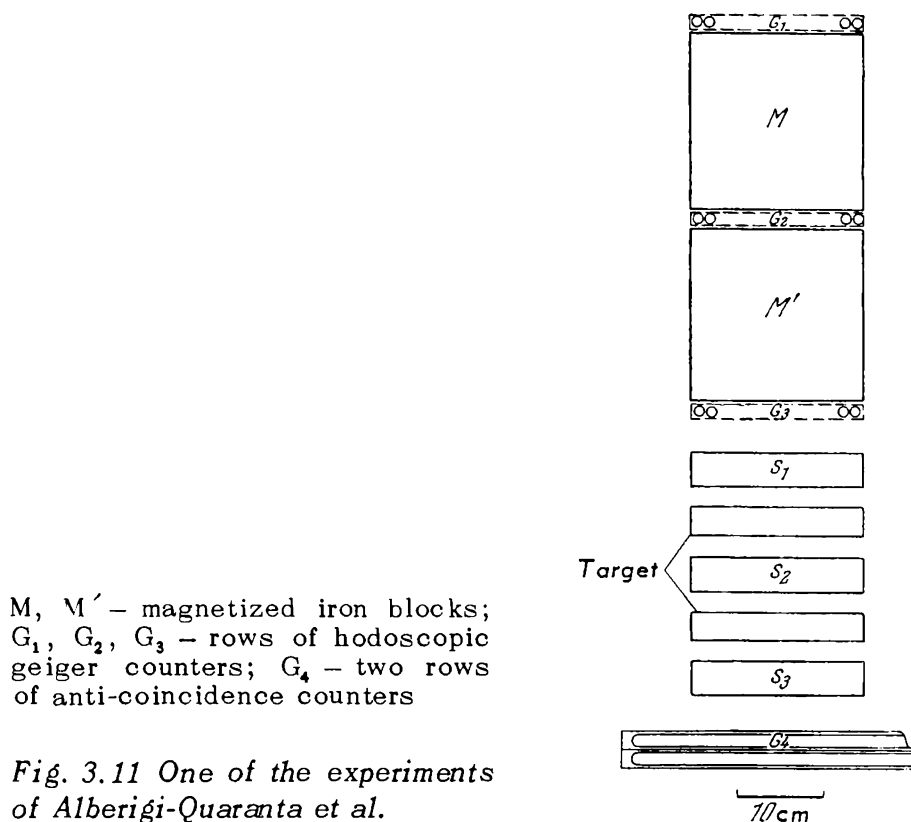


Fig. 3.11 One of the experiments of Alberigi-Quaranta et al.

the experiment of Meyer and Keuffel [62]. The background of correlated particles, which had a considerable effect on the early measurements reported in [61], was substantially reduced by means of the counter hodoscope systems G_2 and G_3 . In Fig. 3.12, S_1 and S_2 are liquid scintillation counters. Singly charged particles stopping in the target were detected by $G_1 S_1 \bar{G}_4$ coincidences and $S_2 \bar{G}_4$ coincidences were produced by neutral particles (neutrons or γ rays) which gave rise to recoil protons or electrons in the scintillator S_2 . The time interval between the pulses in S_1 and S_2 was measured with the aid of a chronotron similar to that described by Neddermeyer et al. [63].

In the experiments by the Leeds group (Hillas et al. [64], Gilboy and Tennent [65]) the negative-muon lifetime was also determined by recording neutrons and γ rays from excited nuclei. To reduce the background of correlated particles, which is particularly high in the initial channels of the time-measuring system, these measurements were performed 10^{-7} sec after the first pulse. In this way it was possible to avoid the use of counter hodoscopes above the apparatus, and the thick lead filter employed by the Princeton group. The experiment of Hillas et al. [64] is shown in Fig. 3.13

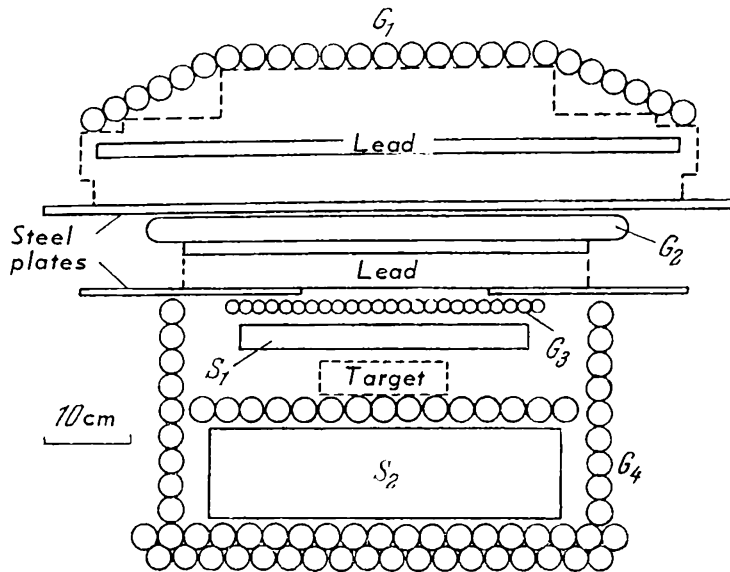


Fig. 3.12 The experiment of Meyer and Keuffel. S_1 and S_2 are liquid scintillators. The broken line indicates the position of lead scintillators in the second version of the experiment

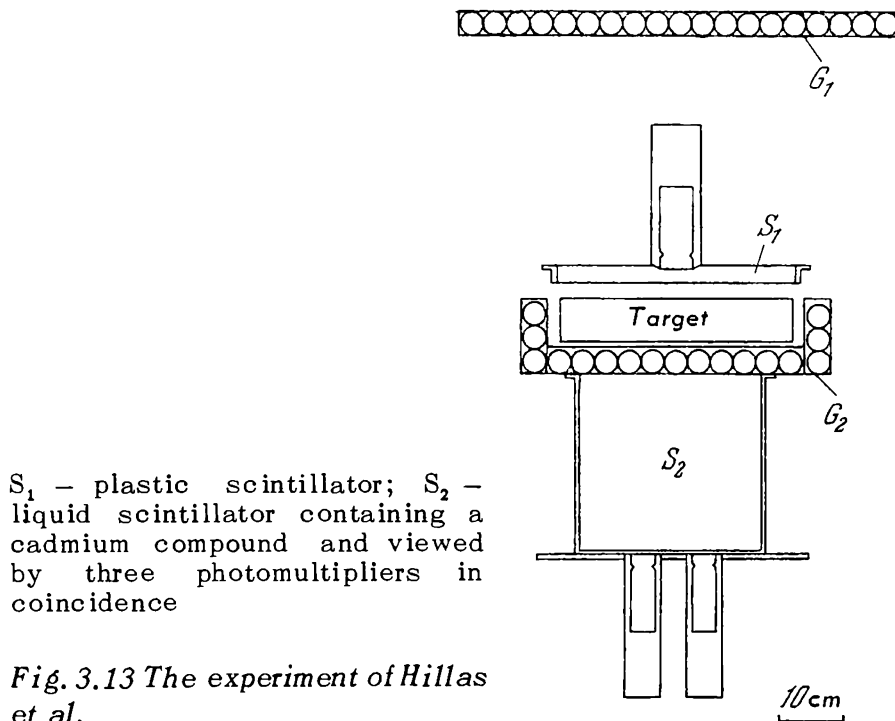
The pulse from the scintillator S_1 was used to produce a gating pulse, whilst the pulse from S_2 was used to cut it off. The length of the gating pulse was determined by using the leading edge to turn on, and the trailing edge to turn off a stabilized oscillator of known frequency connected to a scaler. The lifetime was measured to within 5-6% for elements with Z between 24 and 30 (chromium to zinc). This apparatus recorded about 25 negative-muon captures per hour with a signal-to-noise ratio of 5 and a three-week run was necessary to obtain a statistical error of 5%.

It is also worth recalling the recent experiments of Barrett et al. [66] in which the interaction of negative muons was detected by recording γ rays or neutrons from excited nuclei. This apparatus recorded about seven μ^- -captures per hour. Barrett et al. measured the negative-muon lifetime and decay probability in iron (see Section 3.11). It is interesting to note that a total of 500-hours running time was required in this experiment to measure the lifetime of the negative muon with an accuracy of 4% ($\tau = (196 \pm 8)$ nsec). Holmstrom and Keuffel [67] developed similar apparatus with a considerably greater relative aperture, and determined the ratio of the decay probability in copper and iron. In this apparatus a 6% accuracy in the mean lifetime was achieved in 85 hours, a remarkably short time for cosmic-ray measurements.

c. Accelerator measurements of negative-muon lifetime.

The most accurate measurements of the negative-muon lifetime throughout the periodic table were carried out by Sens [68], Sens et al. [69], Yovanovitch et al. [70], Lundy et al. [71], Lathrop et al. [72] (Chicago group) and Astbury et al. [73, 74] (Liverpool group).

Fig. 3.14 illustrates some experiments of the Chicago group. The negative-muon beam had an initial momentum of 145 MeV/c, and the composition of the beam as it left the synchrocyclotron was: 70% negative pions, 10% negative muons and 20% electrons. The muon-to-pion ratio was later



improved from 1:7 to 7:1, i.e. by a factor of nearly 50. The negative pions still remaining in the beam were attenuated in 28.2 g/cm² of copper. Fig. 3.15 shows the differential range spectrum for negative pions and muons in the beam. The negative-muon beam prepared in this way was brought to rest in a target of the substance under investigation. Stopping negative muons were indicated by 1234 coincidences, and the escape of a decay electron from the target by 345 coincidences. A time-to-amplitude converter was used to determine the time interval between the 1234 and 345 pulses. This produced an output pulse whose amplitude was propor-

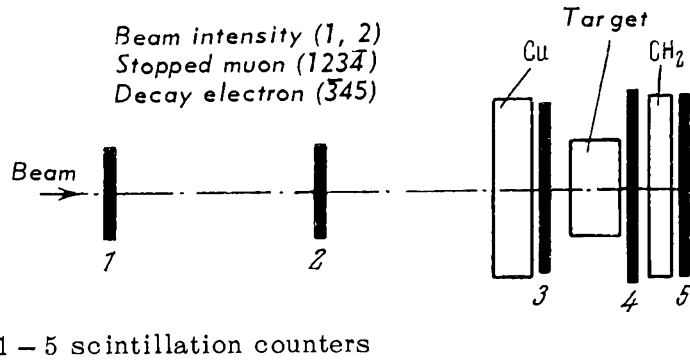


Fig. 3.14 Measurement of the lifetime of negative muons (Sens et al.)

tional to the time interval between the start and stop pulses. The output-pulse amplitudes were measured by a 100-channel pulse-height analyser. A similar system was used by the Liverpool group.

3.9.3 Main experimental data

Table 3.10 summarizes recent accelerator data on negative-muon lifetimes, and is partly based on Tennent's review. The table also includes the most accurate results obtained with cosmic rays. The first columns give the atomic number Z of the target in which the negative muons came to rest, the mass number A and the isotopic excess $\frac{A-Z}{2A}$. Column 9 gives the measured lifetime in nanoseconds, column 7 gives the

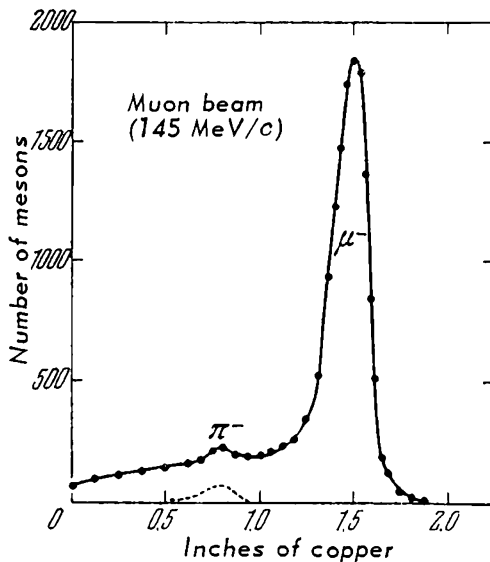


Fig. 3.15 Differential range spectrum for pions and muons in the negative-muon beam used by the Chicago group

μ^- -capture probability $\Lambda_c(Z)$ calculated from

$$\Lambda(Z) = \Lambda_d(Z) + \Lambda_c(Z)$$

where the μ^- -decay probability was assumed to be

$$\Lambda_d(Z) = \frac{1}{\tau_0}$$

where τ_0 is the mean positive-muon lifetime. In calculations of $\Lambda_c(Z)$ it was assumed that $\Lambda_d(Z) = (4.52 \pm 0.03) \times 10^5 \text{ sec}^{-1}$, corresponding to $\tau_0 = 2.22 \pm 0.02 \mu \text{ sec}$ as reported by Bell and Hinks (see Chapter 1).

Fig. 3.16 shows some of the results of Table 3.10 where the μ^- -capture probability $\Lambda_c(Z)$ is plotted as a function

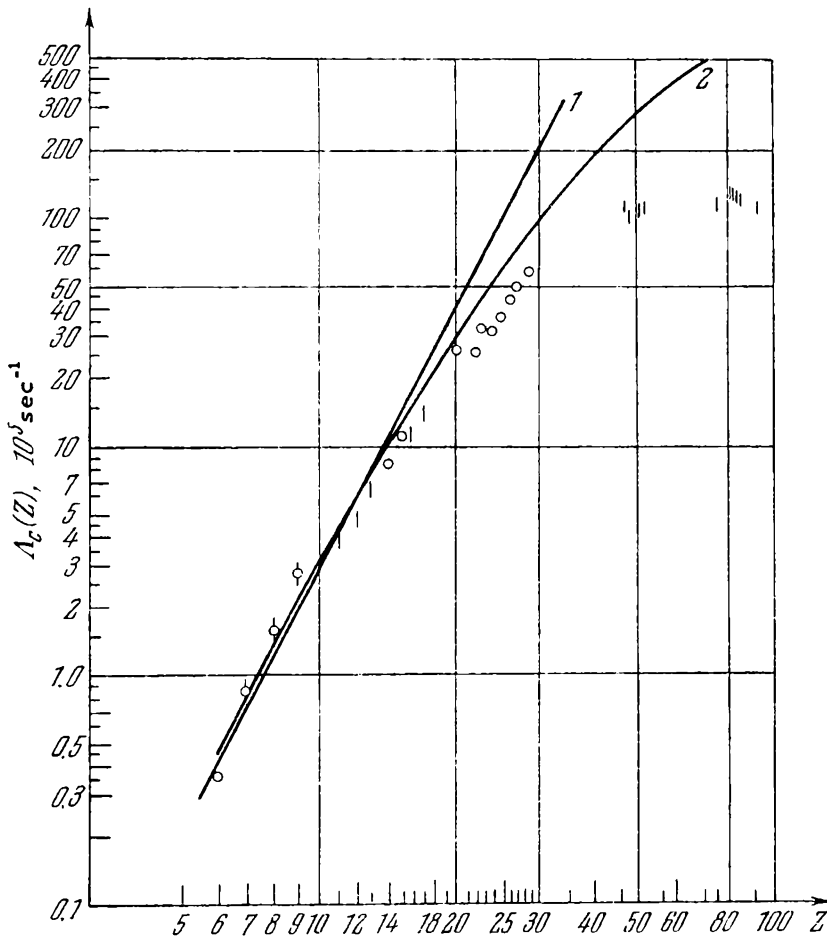


Fig. 3.16 Probability of capture of negative muons by different nuclei. Curve 1 shows $\Lambda_c(Z) \approx Z$, and curve 2 shows $\Lambda_c(Z) \approx Z_{eff}^4$. Open circles represent experimental data for which the error was less than the diameter of the circles

Na	11	23	0.261	10.1 (9.99)	3.44	2.50 ± 0.40	8.40 ± 0.14	1190 ± 20	[74]
Mg	12	24	0.250	10.9 (10.7)	5.28	4.80 ± 0.02 5.07 ± 0.20 5.0 ± 0.2	9.62 ± 0.2	1071 ± 2 1040 ± 20	[72] [68] [74]
Al	13	27	0.259	11.6 11.5	6.33	6.91 ± 0.20	11.4 ± 0.13	880 ± 10	[68]
Si	14	28	0.250	12.4 (12.3)	9.29	6.88 ± 0.16 6.62 ± 0.03 7.77 ± 0.25	11.4 ± 0.16 12.3 ± 0.15	877 ± 12 864 ± 2 810 ± 10	[73] [72] [68]
P	15	31	0.258	13.1 (13.0)		8.50 ± 0.03 11.21 ± 0.05		767 ± 2 635 ± 2	[72]
S	16	32	0.250	13.8 (13.7)	14.4	13.9 ± 0.9	18.5 ± 0.68	540 ± 20	[68]
Cl	17		0.260	14.5 (14.3)	14.9	13.5 ± 0.5 13.9 ± 0.9	18.5 ± 0.68	540 ± 20	[74] [68]

Table 3.10 (continued)

Element	Z	A	A - Z 2A	Z _{eff}	Λ_p	$\Lambda_c(Z)$ (10^5 sec^{-1})		$\Lambda(Z)$	$\tau(Z)$ 10^{-9} sec^{-1}	Reference
						7	8			
1	2	3	4	5	6	7	8	9	10	
Cl	17	35				18.02 ± 0.49	22.54 ± 0.52		[76]	
Cl	17	37				12.51 ± 0.52	17.03 ± 10.49		[76]	
K	19	39	0.257	15.8 (15.6)	22.3	19.9 ± 1.2	24.4 ± 1.2	410 ± 1.2	[68]	
Ca	20	40	0.250	16.4 (16.2)	28.8	26.8 ± 0.4	31.3 ± 0.4	319 ± 4	[73]	
Ca	44					25.5 ± 0.5 24.44 ± 0.23	30.0 ± 0.6	333 ± 7	[68] [77]	
Ti	22	48	0.270	17.6 (17.4)	26.9	17.93 ± 0.40	22.74 ± 0.40	330 ± 7	[77]	
V	23	51	0.274	18.2 (18.1)	27.9	26.3 ± 0.6	30.3 ± 0.6	279 ± 5	[68]	
						31.3 ± 0.7	35.8 ± 0.7	264 ± 4	[73]	
						33.7 ± 0.6	37.9 ± 0.6		[68]	

Cr	24	52	0.269	18.7 (18.5)	35.1	32.4 ± 0.8	36.2 ± 0.8	276 ± 6	[68]
Mn	25	55	0.257	19.3 (19.1)	36.7	32.8 ± 2.3	37.3 ± 2.3	268 ± 16	[65]
									[73]
Fe	26	56	0.267	19.8 (19.9)	46.6	45.3 ± 1.0	49.8 ± 1.0	201 ± 4	[68]
									[66]
Co	27	59	0.271	20.3	46.6	46.5 ± 2.1	51.0 ± 2.1	196 ± 8	[66]
									[67]
Ni	28	59	0.261	20.8 (20.7)	61.7	44.2 ± 3.3	48.7 ± 3.3	205 ± 12	[65]
									[73]
Cu	29	64	0.272	21.2 (21.2)	54.9	50.6 ± 0.9	55.1 ± 0.9	181 ± 3	[73]
									[65]
						46.4 ± 3.0	50.9 ± 3.0	196 ± 11	[65]
						61.6 ± 1.2	66.1 ± 1.2	151 ± 3	[73]
						60.3 ± 1.4	64.9 ± 1.4	154 ± 3	[68]
						60.0 ± 0.8	64.5 ± 0.8	155 ± 4	[73]
						57.9 ± 1.6	62.5 ± 1.6	160 ± 4	[68]

Table 3.10 (continued)

Element	Z	A	$\frac{Z-A}{2A}$	Z_{eff}	Λ_p	$\Lambda_c(Z)$	$\Lambda(Z)$		$\tau(Z)$ 10^{-9} sec^{-1}	Reference
					(10^5 sec^{-1})					
1	2	3	4	5	6	7	8	9	10	
Zn	30	65	0.271	21.7 (21.7)	61.6	56.8 ± 2.3	61.3 ± 2.3	163 ± 6	[67]	
						54.9 ± 2.5	59.4 ± 2.5	168 ± 7	[65]	
						53.6 ± 2.7	58.1 ± 2.7	172 ± 8	[62]	
Mo	42	96	0.281	26.2 (26.4)	102	57.6 ± 1.7	62.1 ± 1.5	161 ± 4	[68]	
						61.7 ± 5.7	66.2 ± 5.7	151 ± 13	[65]	
						90.9 ± 1.8	95.2 ± 1.8	105 ± 2	[68]	
Ag	47	108	0.282	27.7 (28.0)	122	99.5 ± 6.5	104 ± 6.5	96 ± 6	[62]	
						112.5 ± 5.0	118 ± 4.2	85 ± 3	[68]	
						114.5 ± 5.7	119 ± 5.7	84 ± 4	[61]	
Cd	48	112	0.286	27.9 (28.2)	112	100.5 ± 5.0	105.3 ± 5.5	95 ± 5	[68]	
						94.5 ± 5.9	99.0 ± 5.9	101 ± 6	[62]	
						112 ± 7	116 ± 7	86 ± 5	[62]	
Sn	50	119	0.289	28.5	109					

Sb	51	122	0.291	28.7	108	116 ± 10	120 ± 10	83 ± 7	[62]
W	74	184	0.299 (32.8)	32.9 (32.8)	129	119.2 ± 3.0	123.5 ± 3.0	81 ± 2	[68]
Hg	80	201	0.301	33.6	127	134 ± 8	139 ± 8	58 ± 4	[62]
Tl	81	204	0.302	33.7 (34.2)	119	129.0 ± 7.5	133 ± 7.1	72 ± 4	[68]
Pb	82	207	0.301	33.8 (34.2)	119	129 ± 5	133 ± 5.8	75 ± 3	[62]
						117.0 ± 7.5	122 ± 7.4	82 ± 5	[68]
						132 ± 11	137 ± 11	73 ± 6	[60]
Bi	83	209	0.301	33.9 (34.0)	126	122 ± 7.5	127 ± 8	79 ± 5	[68]
U	92	238	0.307	34.8 (34.9)	93.8	109.0 ± 5.0	114 ± 5	68 ± 5	[61]
								88 ± 4	[68]

Note. The magnitude of $\Lambda_0(Z)$ in column 7 was calculated from the formula $\Lambda(Z) = 1/\tau - 1/\tau_0$ where $1/\tau_0 = (4.52 \pm 0.03) \times 10^{-5} \text{ sec}^{-1}$. The values of Z_{eff} in column 5 were calculated from (3.30). The values of Z_{eff} calculated by Sens et al. [69] are given in brackets. Column 6 gives the values of Λ_p calculated by Primakoff's formula (3.28) with $\gamma\Lambda(1,1) = 188 \text{ sec}^{-1}$ and $\delta = 3.15$

tion of Z on a double logarithmic scale. $\Lambda_c(Z)$ was taken from Table 3.10, and whenever there were a number of values of $\Lambda_c(Z)$ measured with comparable accuracy, the final $\Lambda_c(Z)$ was taken to be the weighted mean of these values.

3.9.4 μ^- -Meson capture probability in carbon

For elements with low atomic numbers, the nuclear μ^- -capture probability is much smaller than the decay probability, and the negative-muon lifetime τ_{μ^-} is very nearly equal to the lifetime of a free positive muon. The capture probability Λ_c is then given by the difference of two nearly equal numbers:

$$\Lambda_c = \frac{1}{\tau_{\mu^-}} - \frac{1}{\tau_0}$$

and hence it is difficult to measure accurately. In such cases one can use a method involving counting the number of stopping negative muons which are not accompanied by the appearance of decay electrons as in the work of Hildebrand, who measured the μ^- -capture probability in hydrogen and tritium (see Chapter 1). Stenard has carried out such measurements for carbon, using a propane chamber. Among 2334 $\mu^- - e^-$ decays he found (after correcting for the π^- impurity) 185 stopping negative muons which were not accompanied by decay electrons. This result yields

$$\Lambda_c = \frac{N_i}{N_d \tau_d} = \frac{185}{2334 \cdot 2.22 \cdot 10^{-6}} = (0.36 \pm 0.04) \cdot 10^5 \text{ sec}^{-1}$$

which is in good agreement with the most accurate measurement of Λ_c from the negative-muon lifetime which was performed by Reiter et al. [75] who found $\Lambda_c = (0.373 \pm 0.011) \times 10^5 \text{ sec}^{-1}$ for carbon.

Similar measurements based on an analysis of 1000 stopping negative muons in a propane bubble chamber was performed by Fields et al. [78]. They found that $\Lambda_c = 0.45 \times 10^5 \text{ sec}^{-1}$, which agrees with the μ^- -capture probabilities for carbon given in Table 3.10 to within the limits of the experimental error.

3.10 THE Z^4 LAW. PRIMAKOFF'S FORMULA

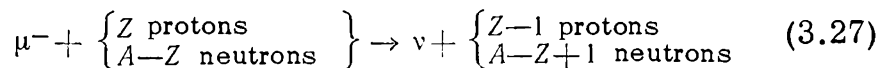
It is evident from Table 3.10 and Fig. 3.16 that near $Z = 11-12$ the capture probability is approximately equal to the decay probability for a free muon:

$$\Lambda_c (Z \sim 11) \approx \Lambda_d$$

Moreover, for low Z , the capture probability is approximately proportional to Z^4 and decreases very rapidly (indicated by the straight line in Fig. 3.16) As Z increases, the measured capture probability departs from this simple law, and for heavy nuclei with $Z \gtrsim 40$, the capture probability reaches saturation with a value of about $(110-120) \times 10^5 \text{ sec}^{-1}$.

The Z^4 law, which is approximately valid for low Z , is a consequence of the fact that the capture probability is proportional to the number of protons in the nucleus and to the density of the negative-muon wave function in the volume occupied by the nucleus which is proportional to Z^3 .

We shall now consider Primakoff's calculations of the μ^- -capture probability for different nuclei. Primakoff used the Hamiltonian based on the $V - A$ interaction with the additional constants due to virtual-pion exchange and 'weak magnetism' given in (3.8), and assumed a homogeneous nuclear matter consisting of Z protons and $A - Z$ neutrons. The analysis was based upon the following approximation. The capture reaction involving a nucleus consisting of Z protons and $A - Z$ neutrons, i.e.



leads to some final state of the nucleus ($Z - 1, A - Z + 1$) and the total interaction probability Λ_c is obtained by adding the squares of the matrix elements of all the energetically possible final states. By replacing this summation by a summation over all final states without restriction, Primakoff obtained the following formula which is valid provided Z is not too low:

$$\Lambda_c (Z) = Z_{\text{eff}}^4 \cdot \Lambda (H_i^1) \cdot \gamma \left(1 - \frac{\delta(A-Z)}{2A} \right) \quad (3.28)$$

This result relates the nuclear μ^- -capture probability $\Lambda_c (Z)$

and the μ^- -capture probability $\Lambda(H_1^1)$ of a proton. The quantity Z_{eff} is the effective nuclear charge and the parameter γ is defined by (see Equation (3.12))

$$\gamma = \frac{\langle \eta \rangle_{Z,A}^2}{0.58}$$

where $\langle \eta \rangle_{Z,A}$ is the momentum of the neutrino (in units of $\sqrt{m_\mu c}$) produced in the nuclear μ^- capture, averaged over all the possible states of the final nucleus. The parameter γ represents the change in phase space for the neutrino in μ^- capture by a complex nucleus in comparison with the phase space accessible in μ^- capture by a proton. This reduction in phase space is mainly due to the presence of bound states which are occupied by neutrons after the negative-muon capture, and to a lesser extent by the effect of nuclear recoil. Primakoff has estimated that $\langle \eta \rangle_{Z,A} \approx 0.75$. The quantity $(1 - \delta(A-Z)/2A)$ is proportional to the neutron excess $A - Z$ and represents the reduction in the total muon-capture probability by the Pauli principle: the presence of final states occupied by neutrons reduces the probability of the reaction (3.27). The physical significance of the correlation coefficient δ is that it represents the rate of decrease of the probability of finding two nucleons with parallel spins near each other as they approach. The calculated value of δ is not very different from 3, and therefore Pauli's principle has an appreciable effect: for nuclei with $A \sim 2Z$ it reduces the capture cross-section by a factor of approximately 4, and the effect is even greater for heavier nuclei.

The μ^- -capture probability $\Lambda(H_1^1)$ is an average over the spin states and its dependence on the weak-interaction constants was discussed in detail in 3.4.2, where it was shown that

$$\Lambda(H_1^1) \sim (G_F^2 + 3G_{G-T}^2)$$

where

$$G_F = G_V$$

and

$$G_{G-T} = G_A^2 + \frac{1}{3}G_P^2 - \frac{2}{3}G_P G_A$$

The remaining point which we must consider is the physical meaning of Z_{eff} , the effective charge of the nucleus. This parameter was first introduced by Wheeler [79] who

estimated the nuclear μ^- -capture probability by analogy with K capture. The appearance of Z_{eff} is connected with the finite linear dimensions of the nucleus. As the nuclear charge increases, the K shell of the mesonic atom becomes closer to the nucleus, and from $Z \sim 30$ onwards, the meson spends an increasing amount of its time actually inside the nucleus. It is then no longer possible to represent the nucleus as a point charge. Even for relatively low values of the charge, the linear dimensions of the nucleus, as well as the charge distribution within it, must be taken into account in calculating the capture probability. This leads to the appearance of the effective charge

$$Z_{\text{eff}} = \pi a_\mu^3 \frac{\int \rho(x) |\psi_\mu(x)|^2 d^3x}{\int |\psi_\mu(x)|^2 d^3x} = \pi a_0^3 \langle \rho \rangle \quad (3.29)$$

where a_μ is the Bohr radius of the muon orbit, $(\hbar^2/m_\mu e^2)$, $\rho(x)$ the nuclear charge density, ψ_μ the muon wave function and $\langle \rho \rangle$ represents the mean density of proton charge within the volume bounded by the K shell of the mesonic atom. These calculations can only be carried out on the basis of a definite model. It is clear, however, that for low Z , where the linear dimensions of the nucleus are smaller than the radius of the K shell, we have $Z_{\text{eff}} \rightarrow Z$, whilst for heavy nuclei, where the entire muon orbit lies inside the nucleus, the latter tends to behave as an infinite medium, and an increase in Z should not lead to a further increase in the capture probability. It follows that for high nuclear charges, the effective charge Z_{eff} should tend to a constant limit. Wheeler took the harmonic oscillator functions for ψ_μ and assumed that the nuclear radius was $R = (e^2/2m_e c^2) A^{1/3}$ and $m_\mu = 210m_e$. Assuming modern values for the muon mass and the 'electromagnetic' values for the nuclear radius, as was done by Hillas [80], the expression for Z_{eff} becomes

$$Z_{\text{eff}} = Z \left[1 + \left(\frac{Z}{42} \right)^{1.47} \right]^{-\frac{1}{1.47}} \quad (3.30)$$

i.e. for low Z , $Z_{\text{eff}} \sim Z$ and for high Z , $Z_{\text{eff}} \rightarrow 42$.

The values of Z_{eff} calculated from this formula are given in column 5 of Table 3.10. They were improved somewhat by Sens [68] who used electron-scattering data and $2P - 1S$ transition energies in muonic atoms to determine nuclear radii and nuclear-charge distributions. Sens' data for the effect-

ive charge are given in brackets in column 5 of Table 3.10. They are not very different from those obtained from Hillas' formula.

We thus see that the effective charge Z_{eff} in Primakoff's formula (3.28) represents the dependence of the capture probability on the atomic properties of the mesonic atom; the coefficients $\langle \eta \rangle$ and δ represent the dependence on the nuclear properties, whilst $\Lambda (H_1^1)$ is determined by the nature of the weak interaction itself.

Comparison of experimental data on μ^- -capture probabilities in different nuclei with Primakoff's formula has been carried out by Sens [68] and Telegdi [81]. The former based his analysis on his own measurements for 29 elements, whilst Telegdi performed a similar analysis but included more accurate recent data on capture probabilities. Fig. 3.17 shows a comparison of Primakoff's formula with experimental data; the quantity $\Lambda_c / \langle \varrho \rangle$ is plotted as a function of the neutron excess $(A-Z)/2A$, where Λ_c is the experimental

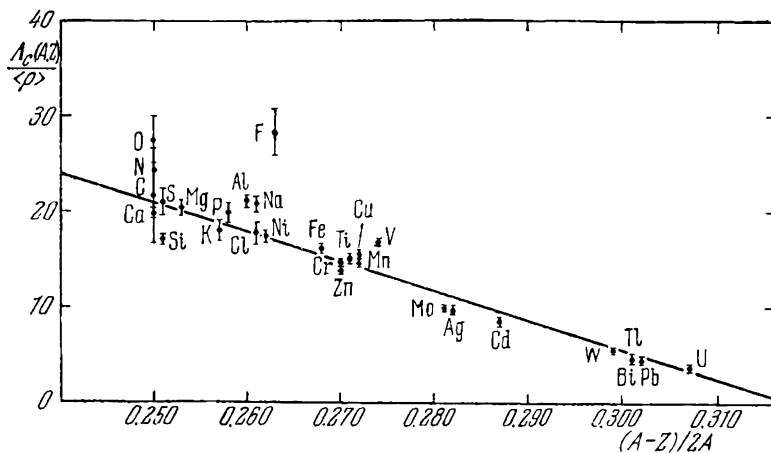


Fig. 3.17 Negative-muon capture probability as a function of neutron excess (Sens' diagram). The straight line was found by the method of least squares

value of the capture probability and $\langle \varrho \rangle$ is given by (3.29). We see that with a few exceptions, the experimental points lie on the straight line. The slope of this line yields the correlation coefficient δ in Primakoff's formula, and the value of Λ_c extrapolated to $A = Z = 1$ gives $\gamma \Lambda (H_1^1)$. Sens' analysis yielded

$$\delta = 3.15, \quad \gamma \Lambda (H_1^1) = 188 \text{ sec}^{-1} \quad (3.31)$$

whilst Telegdi found that

$$\delta = 3.13, \quad \gamma \Lambda (H_1^!) = 183 \text{ sec}^{-1} \quad (3.31a)$$

These two results are practically identical and, since according to Primakoff's estimate (see above) $\gamma \approx 0.75^2/0.58 \times 1$, it follows that

$$\Lambda (H_1^!) \approx 188 \text{ sec}^{-1}$$

Since the theoretically calculated γ was only determined to within 20-30%, the result obtained for $\Lambda (H_1^!)$ is not inconsistent with the three values of this quantity given in Table 3.5, obtained for the three different assumptions about the form of the Hamiltonian. These experimental data cannot therefore be used to distinguish between hypotheses A, B and C, but they do confirm the presence of the Fermi constant in the interaction Hamiltonian. This follows, for example, from the analysis given by Telegdi.

3.11 μ^- -DECAY PROBABILITY IN A BOUND STATE

It is usually assumed in the determination of the nuclear μ^- -capture probability from measurements of the mean negative-muon lifetime that the decay probability in the K shell of the mesonic atom is equal to the decay probability for a free muon, i.e. the positive muon in matter.

In reality there is a difference between the capture probability for a free muon and a muon in the K shell of a mesonic atom. Firstly, the total energy of the bound negative muon is less than the total energy of the free positive muon by the binding energy of the negative muon in the K shell of the mesonic atom. Consequently, the phase space accessible to the decay particles is reduced, and hence the total decay probability is decreased. Secondly, the motion of the negative muon in the K orbit gives rise to a relativistic change in the time scale, so that its lifetime in the laboratory system increases (decay probability decreases), just as for a fast cosmic-ray muon whose lifetime is measured by an observer at rest. Finally, the effect of the nuclear Coulomb field on the decay electron may influence the decay probability.

The above facts modify not only the total decay probability but also the form of the electron energy spectrum produced in $\mu^- - e^-$ decays. For example, the orbital motion of

the muon in the K shell of the mesonic atom leads to a Doppler shift in the spectrum of decay electrons. The spectrum therefore contains electron energies in excess of the limiting energy, which in the decay of the free positive muon is equal to 52.8 MeV. The nuclear Coulomb field also has an effect on the form of the spectrum and impedes the emission of electrons at very low energies.

Changes in the decay probability and in the shape of the electron energy spectrum in $\mu^- - e^-$ decay have been calculated by Porter and Primakoff [82], and in greater detail by Muto [83]. Following the discovery of non-conservation parity, such calculations were carried out for the $V - A$ interaction by Gilinsky and Mathews [84], Überall [85], Terent'ev [86], Huff [87], Krueger et al. [88] and others.

The reduction in the decay probability due to the change in phase space can be readily estimated because the free-muon decay probability is proportional to the fifth power of the muon rest energy (cf. Chapter 2):

$$\Lambda_d(0) \sim (m_\mu c^2)^5 = E_0^5 \quad (3.32)$$

For a bound negative muon this expression may be replaced by

$$\Lambda_d(Z) \sim (E_0 - |B|)^5 \quad (3.33)$$

where $B = m_\mu c^2 (Z\alpha)^2/2$ is the binding energy of the negative muon in the K shell. For small Z we have, on expanding and retaining the first power of B/E_0 ,

$$R = \frac{\Lambda_d(Z)}{\Lambda_d(0)} \approx 1 - \beta \left(\frac{Z}{137} \right)^2 \quad (3.34)$$

where $\beta = 2.5$. When time dilatation is taken into account, β increases to about 3.

More accurate estimates of the reduction in the decay probability led to the same result: the ratio R falls off monotonically with increasing Z and contains only a term of order Z^2 . Fig. 3.18 shows the form of $R(Z)$ obtained by the workers mentioned above.

From the experimental point of view, the determination of the decay probability for a negative muon in the K shell requires the separation of the second component $\Lambda_d(Z)$ from the total probability $\Lambda(Z) = \Lambda_c(Z) + \Lambda_d(Z)$. This can be done

if we know the ratio

$$f(Z) = \frac{\Lambda_d(Z)}{\Lambda(Z)}$$

which is equal to the ratio of the number of $\mu^- - e$ decays and the total number of negative muons stopping in the target Z . To obtain $f(Z)$ one must measure the number of decay electrons N_e leaving the target, the number of negative muons N_μ stopping in the target and the detection efficiency ε for decay electrons:

$$f(Z) = \frac{\Lambda_d(Z)}{\Lambda(Z)} = \frac{N_e^-}{N_\mu^- \varepsilon} \quad (3.35)$$

The efficiency ε can be determined by the 'calibrated efficiency' method used by Lederman and Weinrich [89] and Yovanovitch [70]. They used the same target Z to stop negative- and positive-muon beams with the same range spectrum, and determined the electron detection efficiency from the positron yield in $\mu^+ - e$ decays in the target, assuming that the detection efficiency was the same for electrons and positrons. In this case $\varepsilon = N_e^+ / N_\mu^+$, and substituting into (3.35) we have

$$\Lambda_d(Z) = \Lambda(Z) \frac{N_e^- / N_\mu^-}{N_e^+ / N_\mu^+} \quad (3.36)$$

In reality, the electron and positron spectra from $\mu - e$ decays are different, and therefore the above assumption that the detection efficiency is the same for positrons and electrons is not really valid. However, the error introduced by this is not more than a few per cent, provided the nuclei are not too heavy. Yovanovitch used this method to determine $\Lambda_d(Z)$ for $Z = 6, 20, 22, 23, 26, 27, 28, 30, 53$ and 82 , and Lederman and Weinrich used it to determine $\Lambda_d(Z)$ for $Z = 4, 8, 13, 20, 22, 26, 29, 42$, and 48 .

Another method of determining $\Lambda_d(Z)$ is to use a multilayer target consisting of a large number of alternating thin plates with atomic numbers Z_1 and Z_2 respectively, where Z_1 is a material of low atomic number, e.g. carbon, polyethylene or aluminium. When the number of thin plates is sufficiently high, the electron detection efficiency is the same for both high and low Z plates, and

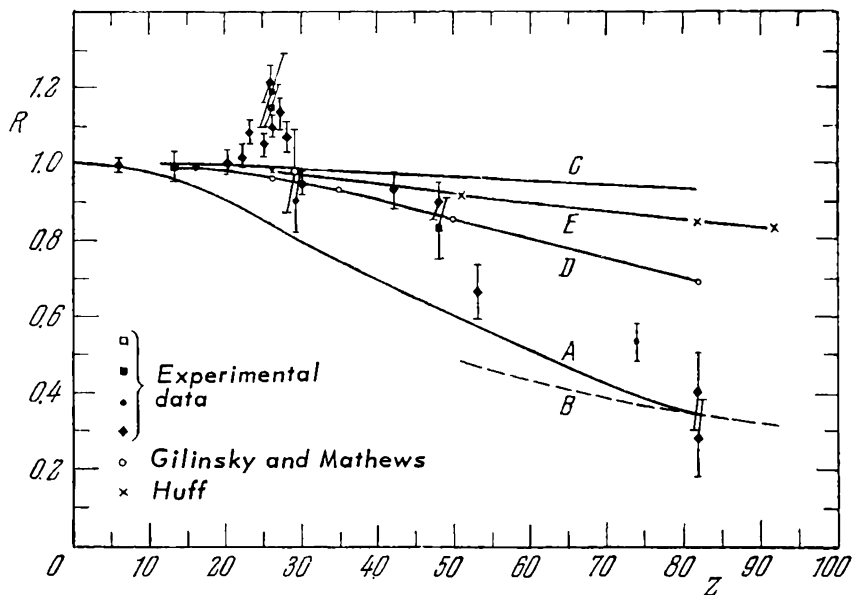
$$\frac{\Lambda_d(Z_2)}{\Lambda_d(Z_1)} = \frac{N_e(Z_2)}{N_e(Z_1)} \cdot \frac{N_\mu(Z_1)}{N_\mu(Z_2)} \frac{\Lambda(Z_2)}{\Lambda(Z_1)} \quad (3.37)$$

The ratio $R = \Lambda_d(Z_2)/\Lambda_d(Z_1)$, which is not very different from $R = \Lambda_d(Z_2)/\Lambda_d(0)$, can be determined if the ratio of stopping muons in the two target materials, $N_\mu(Z_2)/N_\mu(Z_1)$, and the ratio of decays, $N_e(Z_2)/N_e(Z_1)$, are known. The former can be determined either from the range-energy relation [74], or by direct measurement [70]. The ratio $N_e(Z_2)/N_e(Z_1)$ may be found by extrapolation to $t = 0$ of the integral decay curves, which consist of two time components and are given by

$$f(t) = N_e(Z_1) \exp[-\Lambda_t(Z_1)t] + N_e(Z_2) \exp[-\Lambda_t(Z_2)t] + B$$

where B is the constant background. The most accurate results obtained for R by the above methods are shown in Fig. 3.18.

Comparison of experimental data with the calculated values of R (Fig. 3.18) shows that instead of the monotonic decrease in the decay probability for the bound negative muon with



A – semi-classical calculations taking into account the change in the phase volume and time dilatation for an exponential meson wave function; B – same for Gaussian wave function; C – calculations allowing only for time dilatation with an exponential meson wave function; D – calculation of Gilinsky and Mathews; E – Huff's calculations

Fig. 3.18 A plot of the ratio of the decay probability for a bound negative muon and a free muon as a function of the nuclear charge Z

increasing Z , which follows from (3.34), there is in fact a maximum near $Z = 26$ (iron).

Possible reasons for this anomaly have recently been discussed by Keuffel [90] and Chilton [91], who proposed that it is connected with the emission of γ rays as a result of the nuclear excitation during negative-muon capture. If the excitation energy is greater than the neutron binding energy, the emission of a neutron is more probable than the emission of γ rays. Analysis shows that the emission of γ rays with energies in excess of 10 MeV has a very low probability, but at lower excitation energies, when the emission of a neutron is not possible, γ -ray emission predominates and several γ rays may be emitted per capture. It is very difficult to calculate the spectrum of γ rays produced after negative-muon capture, but approximate results may be obtained by considering the spectrum of γ rays from the nuclear capture of thermal neutrons. The mean number of γ rays per thermal-neutron capture is 2.5-4 for nuclei with intermediate atomic weight. This may be regarded as the lower limit for the mean number of γ rays per negative-muon capture. It may therefore be supposed that the observed anomaly near $Z = 26$ may be explained by the detection of γ rays from excited nuclei instead of decay electrons. Yovanovitch used a thick target and an electron telescope consisting of three plastic scintillators separated by two aluminium plates. The minimum electron energy detected by this telescope was 4 MeV. A similar arrangement was used by Lederman and Weinrich. γ rays with energies of 5-10 MeV producing Compton electrons or pairs either in the target or in the first absorber could be recorded as electrons, with an overall detection probability of about 1%. Allaby et al. [92], working on the Liverpool synchrocyclotron, used a large NaI crystal to determine the γ -ray spectrum and yield from negative muons stopping in iron and zinc targets. They found that to within the statistical error, the γ -ray spectra and yields from the two targets were identical: 0.320 ± 0.005 for Fe and 0.285 ± 0.010 for Zn (per negative-muon capture). These results are inconsistent with Chilton's assumption. However, Culligan et al. [93] and Ignatenko [94] have recently performed new measurements of R for iron with special precautions to reduce the γ -ray background. The experiments of Culligan et al. are illustrated in Fig. 3.19a. The counter telescope 5,6 was used to detect electrons from $\mu - e$ decays in the iron target located in a field of 10 000 gauss. A sodium-iodide

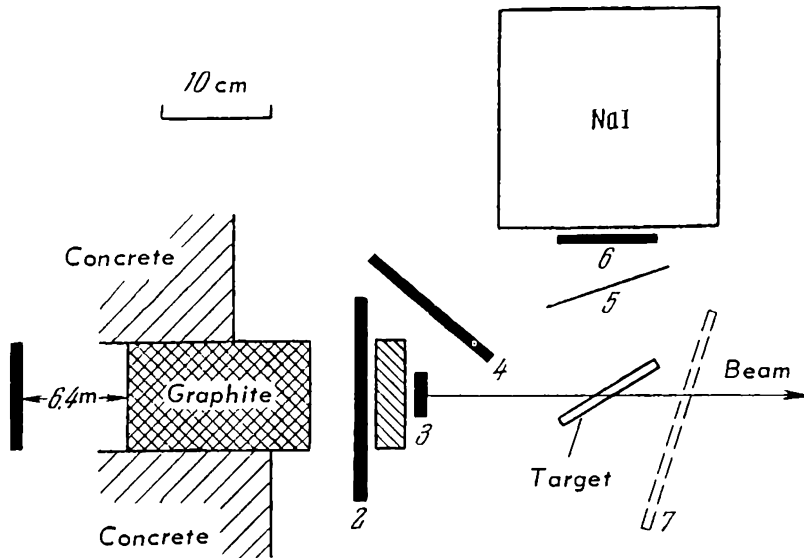


Fig. 3.19a Determination of the decay probability for negative muons stopping in iron and of the spectrum of decay electrons (Culligan et al.)

scintillation spectrometer placed behind the electron telescope was used to measure the energy of the decay electrons. The distance between counters 1 and 2 was about 7 m, so that negative muons stopping in the target could be identified from the time of flight measured with the aid of the telescope 1,2,3. Fig. 3.19b shows the energy spectrum of decay electrons obtained with this apparatus. The broken curve indicates the spectrum expected for $\mu^+ - e^+$ decays with a Michel parameter $\rho = 3/4$.

Clearly, the electron spectrum is substantially different from the expected positron spectrum. The reasons for the difference have been discussed above. The solid curve which is a moderately good representation of the experimental points was calculated by Überall for $\mu^- - e^-$ decays in iron.

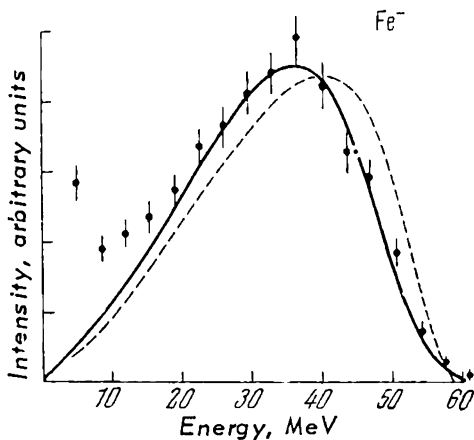


Fig. 1.19b Spectrum of decay electrons from negative muons stopping in iron. The solid curve gives the theoretical spectrum (Überall) showing the experimental 'spread', while the broken curve gives the electron spectrum from the decay of free muons ($\rho = 3/4$), again subject to experimental spread

The ratio R obtained in this experiment was

$$R = 0.972 \pm 0.042$$

A similar result has been reported by Ignatenko et al.

It therefore seems probable that the anomaly at $Z=26$ is purely experimental and is connected with the detection of γ rays from excited iron nuclei.

3.12 ISOTOPIC EFFECT IN NUCLEAR μ^- CAPTURE

Primakoff's formula for the μ^- -capture probability by complex nuclei (3.25) predicts a considerable isotopic effect. For example, it predicts that for the chlorine isotopes

$$\frac{\Lambda_c(\text{Cl}^{37})}{\Lambda_c(\text{Cl}^{35})} = 0.78 \quad \text{for } \delta = 3.15$$

Physically, this is due to the fact that each extra neutron reduces the number of negative-muon states which are accessible after capture, and therefore that an increase in the number of neutrons should reduce the μ^- -capture probability. A search for the isotopic effect was made by Bertram et al. [76] who used silver chloride. Natural chlorine is a mixture of Cl^{35} (75.43%) and Cl^{37} (24.57%). Bertram et al. used two targets, one enriched with Cl^{35} (96.8%) and the other enriched with Cl^{37} (76%). The experiment is shown in Fig. 3.20.

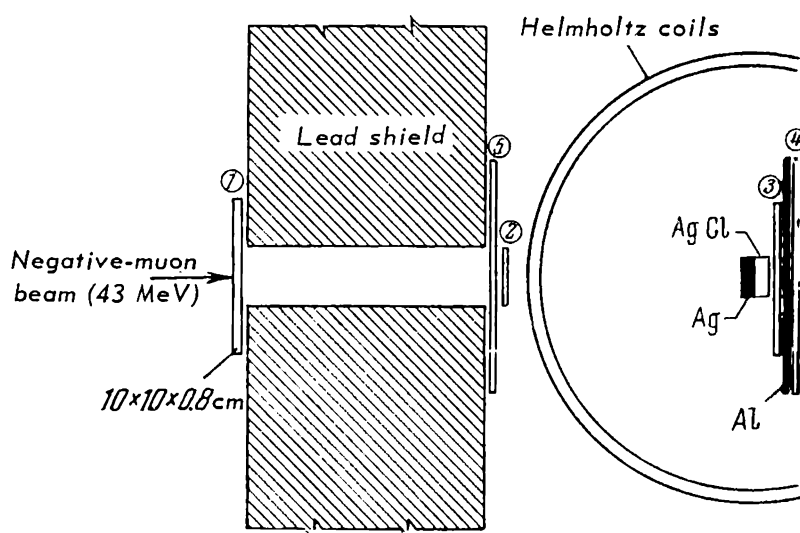


Fig. 3.20 Measurement of the isotope effect in the negative-muon capture probability in chlorine

The beam of 43-MeV negative muons was brought to rest in the AgCl target. Stopping negative muons were indicated by $12\bar{3}$ coincidences, and the emission of decay electrons from the target by $34\bar{5}$ coincidences. The Helmholtz coils were used to compensate the external magnetic field of the cyclotron in the vicinity of the apparatus, thus eliminating the sinusoidal modulation of the decay curve due to precession of the muon spin. The time distributions were analysed by performing a least-squares analysis of the experimental data to the formula

$$y_r = A e^{-\Lambda_t (Ag)} + B (\alpha_{35} e^{-\Lambda_t (35)} + \alpha_{37} e^{-\Lambda_t (37)}) + C e^{-\Lambda_t (C)} + D$$

where y_r is the number of counts in the r -th channel of the system used to measure the lifetime, A,B,C,D are constants, Λ_t is the probability of disappearance of a negative muon and the last terms represent the background due to decays in scintillator 3 (carbon) and random coincidences. $\Lambda_t (C)$ was taken to be $(4.899 \pm 0.007) \times 10^5 \text{ sec}^{-1}$, the result obtained by Reiter. The values obtained for Λ_t by this method were (cf. Table 3.10)

$$\Lambda_t (35) = (22.54 \pm 0.52) \cdot 10^5 \text{ sec}^{-1}$$

$$\Lambda_t (37) = (17.03 \pm 0.49) \cdot 10^5 \text{ sec}^{-1}$$

If the decay probability for the free muon is assumed to be $\Lambda = 4.52 \times 10^5 \text{ sec}^{-1}$, we obtain the following μ^- -capture probabilities for the chlorine isotopes:

$$\Lambda_c (35) = (18.02 \pm 0.49) \cdot 10^5 \text{ sec}^{-1}$$

$$\Lambda_c (37) = (12.51 \pm 0.52) \cdot 10^5 \text{ sec}^{-1}$$

Similar measurements for Ca^{44} and Ca^{40} have been reported by Cramer et al. [77], and for U^{238} and U^{235} by Diaz et al. [95]. The results of all three determinations are summarized in Table 3.11, which gives the ratio of the muon-capture probabilities in the heavy and light isotopes.

It is evident that the experimental data confirm the existence of a considerable isotopic effect whose magnitude is in qualitative agreement with the predictions of Primakoff's theoretical formula (3.28).

3.13 EFFECT OF THE HYPERFINE STRUCTURE OF THE MESONIC ATOM ON NUCLEAR μ^- CAPTURE

It has been pointed out that when a negative muon is captured by the proton in the hydrogen mesonic atom (μ^-p), the capture probability depends on the mutual orientation of the spins of the two particles: in the triplet state of the mesonic atom, where the spins are parallel, we have $\Lambda_+ = 0$, whilst in the singlet state, where the spins are antiparallel and the total spin of the system is zero, $\Lambda_- = 600 \text{ sec}^{-1}$. Let us now consider the calculated μ^- -capture probability for a proton in the most general case, where the Hamiltonian includes terms characterized by the Gamow-Teller and Fermi interaction constants. For a 'pure' $V - A$ interaction we have

$$G_{G-T} = G_A = -G_V \text{ and } x = -1$$

where $\frac{G_{G-T}}{G_F} = x$.

The μ^- -capture probability for a proton in the singlet and triplet states of the mesonic atom (μ^-p) respectively is given by

$$\Lambda_- \sim (1 - 3x)^2, \quad \Lambda_+ \sim (1 + x)^2 \quad (3.38)$$

and the capture probability averaged over the two spin states is

$$\bar{\Lambda} = n_+ \Lambda_+ + n_- \Lambda_- = \frac{1}{2I + 1} [(I + 1) \Lambda_+ + I \Lambda_-]$$

where n_+ and n_- are the populations of the two states and are respectively equal to $(I + 1)/(2I + 1)$ and $I/(2I + 1)$, where I is

Table 3.11 The isotope effect

Isotopes	Muon capture probability		
	Measured	Calculated	
$\text{Cl}^{37}/\text{Cl}^{35}$	0.69 ± 0.03	0.78	Calculations based on the assumption that the correlation coefficient in Primakoff's formula was equal to 3.15
$\text{Ca}^{44}/\text{Ca}^{40}$	0.71 ± 0.02	0.66	
$\text{U}^{238}/\text{U}^{235}$	0.88 ± 0.07	0.81	

the spin of the proton. It is assumed that the population is distributed statistically, i.e. relaxation effects are absent. The relative difference in the capture probabilities for the two states is therefore given by

$$\delta_p = \frac{\Lambda_- - \Lambda_+}{\Lambda} = \frac{\Delta\Lambda}{\Lambda} = \frac{8x(x-1)}{1+3x^2} \quad (3.39)$$

This parameter is very sensitive to the magnitude and sign of the ratio x of the Gamow-Teller and Fermi constants. For example, $\delta_p = 0$ for $x = 1$ ($V + A$ interaction) and $\delta_p = 4$ for $x = -1$ ($V - A$ interaction). The strong spin-dependence of the elementary process $\mu^- + p \rightarrow n + \nu$ leads to the fact that nuclear μ^- capture is very dependent on the spin states of the negative muon and nucleus.

If the nuclear spin I in the mesonic atom produced as a result of negative-muon capture is not zero, the muon can be captured from either of two K -shell states characterized by the following components of the following components of the total angular momentum

$$F_+ = I + \frac{1}{2} \quad \text{and} \quad F_- = I - \frac{1}{2}$$

Bernstein et al. [96] have pointed out that the capture probability should be different for these two states. They calculated this effect for a model consisting of a spinless core and an external proton, and showed that

$$\delta = \frac{\Delta\Lambda}{\Lambda} \approx \frac{1}{Z} \delta_p \frac{\langle IS_p \rangle}{I(I+1)} \frac{2I+1}{2} \quad (3.40)$$

where $\Delta\Lambda = \Lambda_{F_+} - \Lambda_{F_-}$ is the difference in the capture probability for two hyperfine-structure states, $\bar{\Lambda}$ the capture probability averaged over the two states, Z the nuclear charge, S_p the spin of the external proton and $\langle IS_p \rangle$ the expectation value of the scalar product of the two spins.

Überall [97] carried out more accurate calculations for Al^{27} and P^{31} using a simple shell model and the sum rule. He found that for Al^{27}

$$\frac{\Delta\Lambda}{\Lambda} = \frac{\Lambda(F=3) - \Lambda(F=2)}{7/12\Lambda(F=3) + 5/12\Lambda(F=2)} \approx -0.50 \quad (3.41)$$

whilst for P^3

$$\frac{\Delta\Lambda}{\Lambda} = \frac{\Lambda(F=1) - \Lambda(F=0)}{3/4\Lambda(F=1) + 1/4\Lambda(F=0)} \approx -0.45 \quad (3.42)$$

It is evident that the difference in the μ^- -capture probabilities for the two hyperfine-structure states constitutes a large effect even for nuclei. The first experimental attempt to detect this phenomenon was based on the fact that the $\mu^- - e$ curve $f(t)$, measured for stopping negative muons in elements such as Mg, Al and P, should consist of two exponentials corresponding to the two angular momenta F_+ and F_- . It can easily be shown that two such exponentials give rise to a decay curve with positive curvature

$$K = 2^{-3/2}n_+ \frac{\Delta\Lambda}{\Lambda} \cdot n_- \frac{\Delta\Lambda}{\Lambda} \quad (3.43)$$

Telegdi [98] showed that the presence of conversion transitions between the states F_+ and F_- will modify this expression to

$$K = K(\Delta\Lambda, R) = -2^{-3/2}n_+ \left(\frac{\Delta\Lambda}{\Lambda} \right) \frac{(R - n_- \Delta\Lambda)}{\Lambda} \quad (3.44)$$

where R is the probability of conversion of the mesonic atom from state F_+ to state F_- (assuming that the magnetic moment of the nucleus is positive). Telegdi suggested as a possible process for this conversion the magnetic interaction between the 'nucleus' of the mesonic atom (nucleus plus negative muon) and external S electrons in the atomic shell of the mesonic atom. If the probability of this conversion is such that $R > n_- \Delta\Lambda$, then the sign of the curvature of the decay curve changes from positive for $R < n_- \Delta\Lambda$ to negative elsewhere. Winston and Telegdi [99] estimated that in light nuclei the conversion probability is greater by one or two orders of magnitude than the capture probability $\Delta\Lambda$. Table 3.12 gives some calculated values of R and $\Delta\Lambda$.

Table 3.12

Nucleus	R, sec^{-1}	$\Delta\Lambda, \text{sec}^{-1}$	Nucleus	R, sec^{-1}	$\Delta\Lambda, \text{sec}^{-1}$
B ¹¹	1.7×10^5	5×10^3	Cl ³⁵	7.5×10^6	2.3×10^5
F ¹⁹	2.9×10^6	1.1×10^5	Y ⁸⁹	4.1×10^7	2.8×10^5

The first experiments were carried out by the Chicago group [98] and consisted of the determination of the decay curve for negative muons stopping in aluminium and phosphorous. At first the results did indeed indicate that the curvature was negative, but subsequent more careful measurements by different methods did not confirm the existence of such curvature. The final result was [72]

$$K = +(1.1 \pm 1) \cdot 10^{-3} \text{ for Mg}$$

and

$$K = +(2.4 \pm 1.7) \cdot 10^{-3} \text{ for Al}$$

The Mg nucleus has zero spin and there are no hyperfine-structure effects. Measurements of the decay curve for Mg can therefore be regarded as control measurements of the decay curve with zero curvature. A finite curvature was, however, detected when neutrons and γ rays emitted by the nucleus after decay were recorded instead of decay electrons.

By writing down the kinetic equations for the negative muons stopping in the target, including conversion from the F_+ to F_- states, it is quite easy to derive the expressions which follow for the number of negative-muon decays and captures:

$$\begin{aligned} N_d(t) dt &\sim e^{-\Lambda t} (1 - Ae^{-Rt}) dt \\ N_c(t) dt &\sim e^{-\Lambda t} (1 - A'e^{-Rt}) dt \end{aligned} \quad (3.45)$$

where A and A' determine the curvature of the decay curve. When the decay electrons are recorded

$$A = \frac{n_+(0) \Delta\Lambda}{R} \quad (3.46)$$

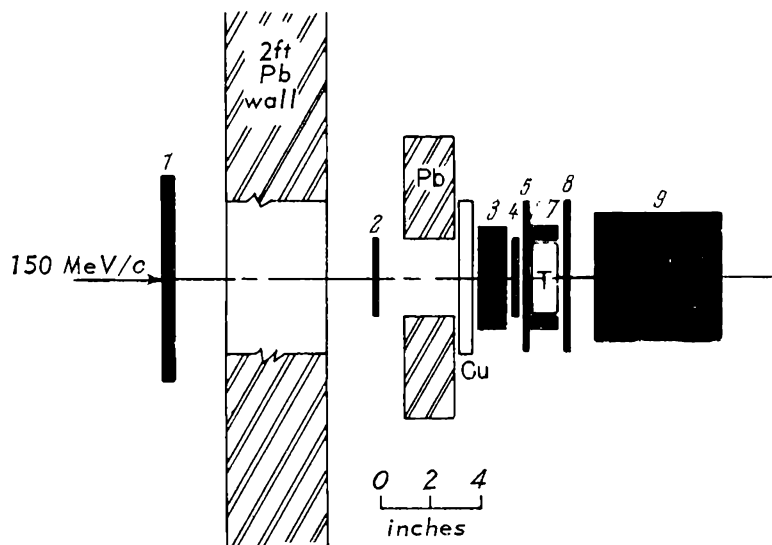
and when neutrons and γ rays emitted by the nucleus are recorded

$$A' = n_+(0) \frac{\Delta\Lambda}{\Lambda} \frac{1}{1 + n_+(0) \Delta\Lambda/\Lambda} \quad (3.47)$$

In these expressions the quantity $n_+(0)$ represents the population of the F_+ level at $t = 0$. Comparison of these formulæ shows that if $R \gg \Delta\Lambda$ which, as we have seen (Table 3.11), is in fact the case, it is more convenient to determine the curvature of the decay curve by recording neutrons and γ rays instead of the decay electrons.

This method was used by Culligan et al. [100], who measured the time distribution of the neutrons and γ rays emitted by F_9^{19} after negative-muon capture. An LiF target was employed and a control run was carried out with LiOH (spinless nucleus). Since the μ^- -capture probability is approximately proportional to Z^4 , capture by fluorine and oxygen is important in both cases.

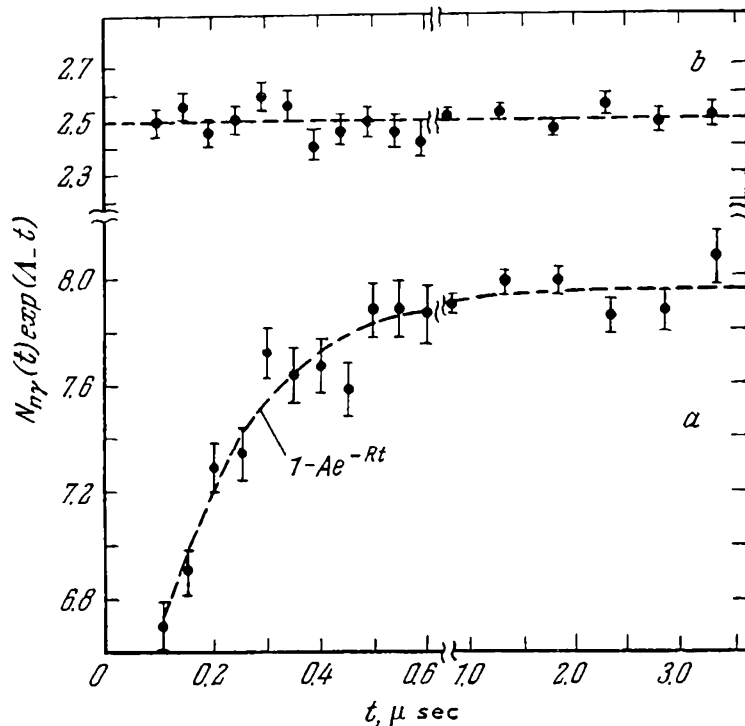
The experiment is illustrated in Fig. 3.21. The target T was surrounded by four scintillation counters 5, 6, 7 and 8, and four other scintillation counters 1, 2, 4 and 9 were placed in the direct beam. The lucite Cerenkov counter 3 was connected in anti-coincidence, and used to eliminate the electron impurity in the negative-muon beam. The liquid scintillation counter 9 used pulse-shape discrimination to distinguish between light and heavy charged particles. It was



1, 2, 3, 5, 8 - scintillators; 6, 7 - scintillators shielding the target 8; 9 - cylindrical liquid scintillator counter for neutrons and γ rays (12.5×12.5 cm)

Fig. 3.21 Measurements of the spin dependence of the negative-muon capture probability in F_9^{19}

used to detect neutrons (by their knock-on protons) and γ rays (detected by observing Compton and pair electrons). Counters 5, 6, 7, 8 were connected in anti-coincidence and were used to reduce the background of random coincidences and bremsstrahlung due to decay electrons. A negative muon stopping in the target was indicated by $\overline{2345678}$ coincidences, whilst a neutral decay product (neutron or γ ray) from negative-muon capture was indicated by $\overline{156789}$ coincidences.



a - LIF target; b - LiOH target

Fig. 3.22 The number of secondary neutral particles (neutrons and γ rays) plotted as a function of time. Data corrected for exponential decay

Fig. 3.22 shows the decay curves obtained with this apparatus for LiF and LiOH targets. The number of recorded neutrons and γ rays corrected for exponential decay, i.e. $N_{n\gamma}(t) \exp(+\Lambda t)$, is plotted as a function of time in μ sec. It is evident from this figure that capture by the spinless nucleus O^{16} yields a pure exponential (the experimental points lie on a straight line parallel to the time axis), whilst for negative-muon capture by F^{19} , the decay curve (a) has a negative curvature. If the experimental data (a) are fitted by (3.45), the parameters A' and R are found to be

$$A' = 0.31 \pm 0.02$$

$$R = (5.9 \pm 0.8) 10^6 \text{ sec}^{-1}$$

These results indicate a very appreciable hyperfine-structure effect in negative-muon capture by F^{19} . The presence of this effect confirms that the value of the parameter x in (3.39), which is equal to the ratio of the Gamow-Teller and Fermi interaction constants, is not very different from -1. In fact, for $x = -1.25$, the expected value of A' lies in the

range 0.25-0.37, whilst for $x = +125$ the range is 0.04-0.07.

It may therefore be concluded that this experiment has shown that the sign of the ratio $x = G_{G-T}/G_F$ is negative and that its magnitude is in agreement with the $V - A$ hypothesis.

3.14 NON-CONSERVATION OF PARITY IN NUCLEAR μ^- CAPTURE

3.14.1 Basic theoretical predictions

The non-conservation of parity in negative-muon capture is manifested in the asymmetry of the angular distribution of recoil nuclei and neutrons emitted as a result of the capture, and also in the longitudinal polarization of the emitted neutrons. The first of these effects has been observed by a number of workers, but experiments on the longitudinal polarization of neutrons are very difficult and have not been performed to date.

Let us suppose that a completely polarized muon is captured by a proton in accordance with the scheme $\mu^- + p \rightarrow n + \nu$. Huang, Yang and Lee [101] showed that if spatial or charge parity is not conserved, the angular distribution of the neutrons relative to the spin of the muon is given by

$$dN \sim (1 + \alpha \cos \vartheta) d\Omega \quad (3.48)$$

where ϑ is the angle between the neutron momentum and the spin of the muon, and α a parameter which depends on the constants of the four-fermion interaction. The two-component neutrino theory gives an expression for the asymmetry coefficient α as a function of the effective Fermi and Gamow-Teller constants. If the negative muon is fully polarized, but the protons are not, then

$$\alpha = \frac{G_F^2 - G_{G-T}}{G_F^2 + 3G_{G-T}^2} \quad (3.49)$$

If a neutrino is produced in negative-muon capture by a proton ($\mu^- + p \rightarrow n + \nu$), and

$$\alpha = \frac{G_{G-T}^2 - G_F^2}{G_F^2 + 3G_{G-T}^2} \quad (3.50)$$

If an antineutrino is produced ($\mu^- + p \rightarrow n + \bar{\nu}$). In these expressions $G_F = G_S + G_V$, $G_{G-T} = G_T + G_A$.

It follows from the above formulae that for a pure $V - A$ interaction with constants

$$\begin{aligned} G_V &= -G_A \\ G_S &= G_T = G_P = 0 \end{aligned}$$

the angular distribution of neutrons from the capture reactions $\mu^- + p \rightarrow n + \nu$ is isotropic ($\alpha = 0$). This will become understandable if we recall that the μ^- -capture probability for a proton in the triplet state is zero for pure $V - A$ interaction. Since it is only in the triplet state that the mesonic atom (μ^-p) has a definite total spin orientation and the singlet state is spherically symmetric, the absence of capture from the triplet state will explain the isotropic neutron angular distribution.

The asymmetry in this distribution is due to the fact that, owing to the strong interaction between protons and neutrons, the vector and the axial-vector constants are not exactly equal. However, this asymmetry is small and it follows from the above formulae that if $G_A = -1.21G_V$, the asymmetry coefficient is $\alpha = 0.09$.

The presence of a pseudoscalar term in the interaction Hamiltonian leads to the following modification of the expression (3.49) for the asymmetry coefficient:

$$\alpha = \frac{|G_F|^2 - 2|G_{G-T}|^2 + \left|G_{G-T} - \frac{\nu}{2M}G_P\right|^2}{|G_P|^2 + 2|G_{G-T}|^2 + \left|G_{G-T} - \frac{\rho}{2M}G_P\right|^2} \quad (3.51)$$

where ν is the neutrino energy and G_P the pseudoscalar constant due to virtual-pion exchange ($G_P = \kappa G_A$). It is evident from the above formula that for the $V - A$ interaction, the sign of the asymmetry coefficient depends on the sign of the ratio G_P/G_A .

Table 3.13 gives the values of the asymmetry coefficient calculated under different assumptions about the additional interaction constants [102]. It is evident from this table that the asymmetry coefficient reaches the value $\alpha = -0.45$ when all the additional terms are included in the Hamiltonian.

It is worth noting that the longitudinal polarization of the neutron from the reaction $\mu^- + p \rightarrow n + \nu$ is practically complete and is independent of the particular form of the interaction. This is a simple kinematic consequence of the total longitudinal polarization of the neutrino in the two-compon-

Table 3.13

'Weak magnetism' constant	G_P G_A	α	'Weak magnetism' constant	G_P G_A	α
Absent	0	-0.09	Absent	8	-0.33
Present	8	-0.45	Present	0	-0.23

ent theory. In fact, since capture occurs mainly from the state with zero total spin, and a longitudinally polarized neutrino carries off spin 1/2, the neutron should be longitudinally polarized in order to ensure that the total spin of the system is 0.

When a negative muon is captured by a nucleus, the asymmetry in the neutron distribution is reduced because of the internal motion and scattering of nucleons in the nucleus. This kinematic depolarization of neutrons in spinless nuclei has been estimated by Shapiro et al. [102], Überall [103], Akimova et al. [104], Dolinskii and Blokhintsev [105], Blokhintzev [106], Lubkin [15] and others.

The depolarizing effect of the nucleus can therefore be expected to modify the asymmetry for fully polarized negative muons so that it must be described by two parameters, i.e.

$$dN \sim (1 + \alpha \kappa \cos \vartheta) d\Omega \tag{3.52}$$

where α is the asymmetry coefficient for the original $\mu^- + p \rightarrow n + \nu$ reaction, and κ represents the reduction in the asymmetry due to the interaction between neutrons and internal nucleons. Akimova, Blokhintsev and Dolinskii [104] have calculated the reduction in the neutron asymmetry for the shell model with $j - j$ coupling and a square-well potential with radius $R = r_0 A^{1/3}$ where $r_0 = 10^{-13}$ cm. The interaction of the neutron with the nucleus was represented by a complex potential. Table 3.14 gives the values of κ for various light nuclei obtained from this calculation in the form of and average over the energy spectrum of direct neutrons. These data were obtained for three different values of the ratio of the real and imaginary parts of the potential, i.e. $\xi = 0, 0.10$ and 0.15 .

Similar shell-model calculations were performed by Lubkin [15], who calculated κ for directly interacting neutrons with energies greater than a given energy ϵ in the case of

Table 3.14

Nucleus \ ξ	ξ			Nucleus \ ξ	ξ		
	0	0.10	0.15		0	0.10	0.15
C ¹²	0.174	0.416	0.500	Si ²⁸	0.045	0.366	0.441
Ne ²⁰	0.388	0.578	0.641	S ³²	0.273	0.515	0.590

the spinless nuclei O¹⁶, Si²⁸ and Co⁴⁰. The results are given in Table 3.15 where ε is in MeV.

Calculations in which the internal protons and neutrons in the nucleus were described by the Fermi gas model have been reported by Überall [103] and Lubkin [15]. In the former paper it was found that $\kappa = 0.773$ for nuclei with an equal number of neutrons and protons. The results obtained in the second paper for directly interacting neutrons from Pb²⁰⁸ and Ca⁴⁰ with energies greater than ε are given in Table 3.16.

The calculations discussed above showed that the reduction in asymmetry due to the effect of the nucleus lies in the range 0.1-0.8, depending on the nuclear model adopted and the neutron energy, but the sign of the asymmetry remains the same ($\kappa > 0$). It must also be noted that values obtained for κ from the Fermi gas model are much greater than those for the shell model. This is due to the different ratio of the number of directly interacting neutrons and evaporation neutrons in the two models.

Calculations of the neutron asymmetry must also take into account the fact that, as a result of depolarization of negative muons in cascade transitions in the mesonic atom, the polarization of the negative muon at the interaction is not more than about 15% (see Chapter 6). It follows that the final asymmetry must be described by

$$1 + \alpha\kappa P \cos \vartheta \quad (3.53)$$

where P is the degree of longitudinal polarization of negative muons in the K shell. The observed asymmetry coefficient $\alpha\kappa P$ is then found to lie in the range 0.01-0.04.

Such low asymmetries are very difficult to detect. The situation is complicated by the fact that neutrons of sufficiently high energy must be recorded in order to reduce the background due to evaporation neutrons which are distributed isotropically in space, and the γ -ray background due to excited nuclei. Some idea about the possible ratio of

Table 3.15

O ¹⁶	1.15	2.30	9.21	20.72
	0.22	0.27	0.73	0.33
Si ²⁸	0.79	1.58	6.34	14.27
	0.10	0.18	0.28	0.07
Ca ⁴⁰	0.63	1.25	5.00	11.30
	0.01	0.10	0.27	0.31

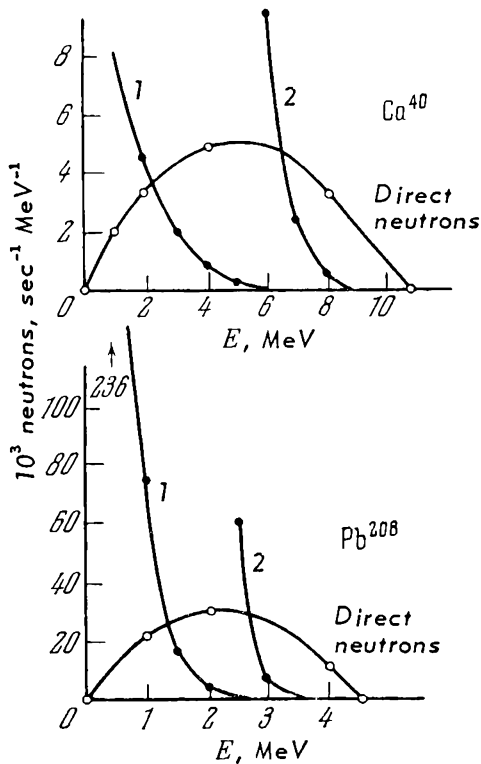
Table 3.16

Pb ²⁰⁸		Ca ⁴⁰		Pb ²⁰⁸		Ca ⁴⁰	
ϵ , MeV		ϵ , MeV		ϵ , MeV		ϵ , MeV	
1	0.68	1	0.62	4	0.79	4	0.65
2	0.73	2	0.65			8	0.80

directly interacting to evaporation neutrons is given by Fig. 3.23, which shows neutron spectra calculated by Lubkin [15] for Ca⁴⁰ and Pb²⁰⁸ using the Fermi gas model. Clearly the number of directly interacting neutrons constitutes a small fraction of evaporation neutrons. It is only at the end of the energy spectrum that this number becomes relatively high, and since the energy resolution of neutron detectors is not better than 15-25%, reliable separation of direct neutrons from evaporation neutrons demands the detection of high-energy neutrons only, which in turn leads to losses in intensity.

3.14.2 Experimental data on neutron asymmetry

Baker and Rubbia [107], who studied the neutron angular distribution from negative-muon capture in Mg and S, did not succeed in detecting the asymmetry. They obtained a positive value for the asymmetry coefficient but this differed from zero by only one standard deviation. It is possible, however, that this result is connected with the particular method used to detect the neutrons. In order to reduce the γ -ray background, the neutron counter which they employed consisted of 15 thin scintillators. The resolution of this counter was no better than 30% with a neutron energy threshold of 5 MeV. Under these conditions it is very probable that there was an



1 - Evaporation neutrons $\times 10^{-2}$
 2 - Evaporation neutrons

Fig. 3.23 Spectrum of direct and evaporation neutrons in negative-muon capture by Ca^{40} and Pb^{208} (Lubkin)

isotropic impurity of evaporation neutrons which masked asymmetry, due to directly interacting neutrons.

Astbury et al. [108] appear to have been the first to detect the neutron asymmetry and thus confirm the non-conservation of parity in this phenomenon. The experiment was performed on the Liverpool synchrocyclotron and is illustrated in Fig. 3.24. The negative-muon beam with initial momentum of $190 \text{ MeV}/c$ was brought to rest in an S^{32} target. A stopping negative muon was indicated by 236 coincidences (gating pulse), whilst the entry of a neutron into the neutron counter was indicated by $\overline{1345}$ coincidences (stopping pulse). The neutron detector was a liquid scintillator and pulse-shape discrimination was used to separate neutrons from γ -ray and electron background. The time interval between the gating and stopping pulses was measured in the usual way by time-to-amplitude conversion. A magnetic field perpendicular to the centres of counters 2, 3 and 5 produced a precession of the negative-muon spin in the plane defined by these centres. If spatial parity is conserved, the neutron intensity should depend exponentially on time. If on the other hand, parity is not conserved, the curve should be sinusoidally modulated as in the experiment of Garwin et al. with

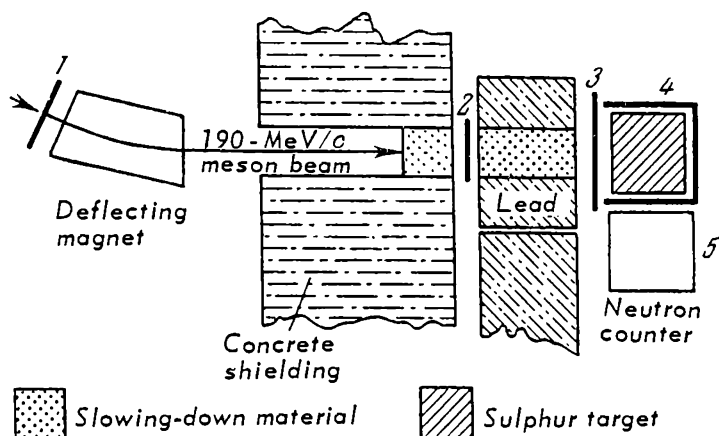


Fig. 3.24 Determination of the asymmetry in the angular distribution of neutrons from negative-muon capture S^{32} (Astbury et al.)

decay electrons. It follows that the neutron time distribution should be of the form

$$F(t) = N_0 e^{-\frac{t}{\tau}} [1 + \alpha \varphi P \cos(\omega t + \delta)] + B \quad (3.54)$$

where τ is the lifetime of negative muons in sulphur ($\tau = (540 \pm 20) \times 10^{-9}$ sec; Table 3.10) and P the polarization of the negative muon at the instant of capture by the nucleus. The polarization P was determined from the angular asymmetry of decay electrons emitted from the sulphur target and was found to be $15 \pm 4\%$. The quantity φ in the above expression represents the angular resolution of the experiment, the kinematic depolarization of neutrons in the S^{32} nucleus and the reduction in the asymmetry due to the presence of evaporation neutrons among the recorded neutrons and ω is the precession frequency of negative muons in the magnetic field. Since the nucleus S^{32} has zero spin, ω must be equal to the precession frequency of a free negative muon, i.e. $\omega = \frac{geH}{2m_\mu c}$. Finally, B is the background.

Fig. 3.25 shows a plot of the quantity $g = \frac{F(t) - B}{e^{-t/\tau}}$ as a function of channel number in the pulse-height analyser. As can be seen, the curve describing the neutron time distribution is sinusoidally modulated at the angular frequency ω . A least-squares analysis yields the following value for the asymmetry coefficient in (3.54)

$$a^{(n)} = \alpha \varphi P = -0.045 \pm 0.015$$

This experiment was recently repeated [109] using an improved method and the new result was

$$\alpha_{\mu P} = -0.027 \pm 0.007$$

Similar, although more accurate, experiments have been carried out by the Chicago group for sulphur and magnesium [110]. Their results for sulphur are shown in Fig. 3.26, in which the upper curve gives the neutron asymmetry and the lower curve the decay electron asymmetry for the same targets and experimental geometry. The asymmetry coefficients in Equation (3.54) were found to be

$$a^{(n)} = -0.020 \pm 0.005 \quad (\text{for Mg})$$

$$a^{(n)} = -0.019 \pm 0.007 \quad (\text{for S})$$

The asymmetry coefficient in the electron angular distribution from magnesium and sulphur targets was also measured in these experiments. The results were

$$a^{(e)} = -0.022 \pm 0.004 \quad (\text{for Mg})$$

$$a^{(e)} = -0.026 \pm 0.009 \quad (\text{for S})$$

Knowledge of these coefficients enables us to exclude the effect of the experimental geometry and the initial polarization of the negative muons at the instant of capture by the nucleus from the analysis, and to obtain the asymmetry coefficient for fully polarized negative muons due to capture in Mg and S:

$$\begin{aligned} a_{\text{Mg}}^{(n)} &= -\frac{0.020 \pm 0.005}{0.022 \pm 0.004} \cdot \frac{1}{3} = -0.30 \pm 0.10 \\ a_{\text{S}}^{(n)} &= -\frac{0.019 \pm 0.007}{0.026 \pm 0.009} \cdot \frac{1}{3} = -0.24 \pm 0.15 \end{aligned} \quad (3.55)$$

These coefficients contain only uncertainties connected with the nucleus itself. If we divide them by κ , which represents kinematic depolarization in the nucleus, we obtain the asymmetry coefficient in the elementary process $\mu^- + p \rightarrow n + \nu$. We have already seen that κ is very sensitive to the particular nuclear model employed in the calculations. If we use the result reported by Überall for light nuclei ($\kappa = 0.773$) and average the values of the asymmetry coefficients of magnesium and sulphur, we find that the asymmetry coefficient for the elementary process is

$$\alpha \approx -0.35 \pm 0.10$$

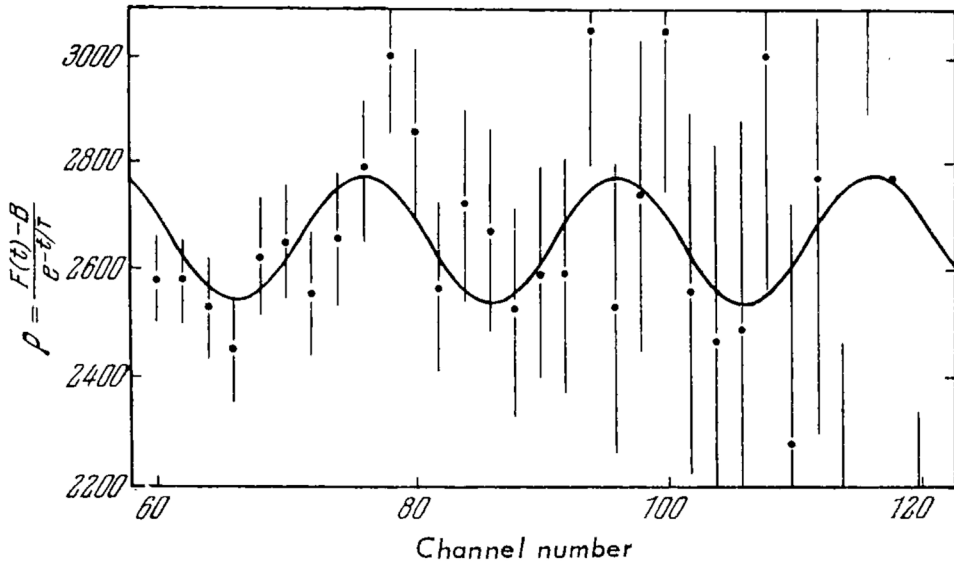


Fig. 3.25 Non-conservation of parity in negative-muon in S^{32} (asymmetry in the angular distribution of neutrons, corrected for exponential decay). The sinusoid is the result of a least-squares fit. B is the number of counts corrected for exponential decay

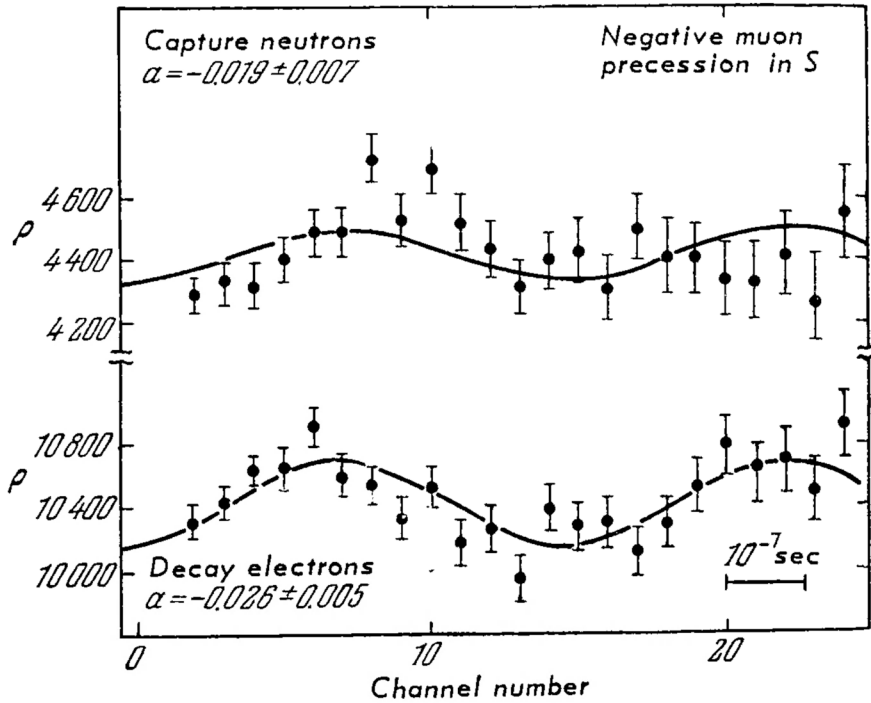


Fig. 3.26 Asymmetry in the angular distribution of neutrons from negative-muon capture in S , corrected for exponential decay. The upper curve is for capture neutrons and the lower curve for decay electrons

The expected asymmetry coefficients are given in Table 3.13. We see that the values of α obtained in different experiments are appreciably different from zero or from the very small values predicted by the pure $V - A$ interaction. It may therefore be concluded that these experiments indicate the presence of additional interactions in nuclear μ^- capture.

Komarov et al. [111] have measured the asymmetry of neutrons emitted from a calcium target using a similar method in which the neutrons were recorded by a multilayer scintillation counter with a 7-MeV neutron threshold. They found that $\alpha = -(0.067 \pm 0.022)$, which does not agree with the result obtained by the workers mentioned above.

The following conclusions may be drawn from the above experimental data:

1. Negative-muon capture by spinless nuclei leads to asymmetry in the angular distribution of directly interacting neutrons and confirms non-conservation of parity in the elementary reaction $\mu^- + p \rightarrow n + \nu$.

2. The magnitude of the observed asymmetry suggests that, in addition to the V and A variants of the interaction with approximately equal and opposite coupling constants, there are additional constants representing virtual-pion exchange and the 'weak magnetism' of Gell-Mann and Feynman.

3. The sign of the observed asymmetry confirms the presence of a positive coefficient in the pseudoscalar coupling constant due to virtual-pion exchange.

4. The contributions of the various additional weak-interaction constants cannot be separated experimentally at the present time. This appears to be impossible even if experimental data, become much more accurate, because theoretical estimates of the effect of the nucleus on the reduction in asymmetry are subject to large uncertainties.

3.14.3 Angular distribution of recoil nuclei in μ^- capture

In addition to the neutron asymmetry considered above, there are also other phenomena in which the non-conservation of parity can be deduced from measurements on nuclear μ^- capture. We shall review briefly some of these, despite the fact that they have not as yet been observed experimentally. One of these effects is the angular distribution of recoil nuclei produced as a result of the capture of polarized negative muons:

$$N_i + \mu^- \rightarrow N_f + \nu \quad (3.56)$$

where N_i is the initial state of the target nucleus and N_f is the final state of the recoil nucleus. An experiment of this kind would not only reveal non-conservation of parity in the reaction (3.56), but would also enable us to determine the helicity of the negative muon relative to the helicity of the neutrino. Let us confine our attention to, say, the 0-0 transition and recall that the neutrino has a left-handed polarization, i.e. its spin is antiparallel to its momentum q . Suppose that the neutrino is emitted in the direction of the negative-muon spin, so that if the muon has a right-handed helicity, the neutrino should be emitted in the direction opposite to p and the recoil nucleus should travel in the direction of p , i.e. in the direction of the negative-muon spin. If the negative muon has left-handed helicity, the recoil nuclei will be emitted in the opposite direction and the observed correlation between the initial direction of the μ^- momentum and the direction of emission of the recoil nucleus will be described by

$$1 + \cos \vartheta \quad (3.57)$$

where ϑ is the angle between the momentum of the neutrino and the spin of the muon. In the more general case of the $0 \rightarrow I$ transition with a parity change of $(-1)^{I+1}$ (the unique transitions in β decay), the observed correlation is

$$1 + \alpha P \cos \vartheta \quad (3.58)$$

where P is the final negative-muon polarization in the K shell of the mesonic atom, and α is determined by the form of the interaction and the transition matrix element. $C^{12} \rightarrow B^{12}$ ($0^+ \rightarrow 1^+$) and $O^{16} \rightarrow N^{16}$ ($0 \rightarrow 2^-$) are examples of such transitions. The magnitude of α for these transitions was calculated by Morita and Greenberg [112], Rose and Good [113] and Wolfenstein [114] for the usual model with $J - J$ coupling and a harmonic oscillator potential.

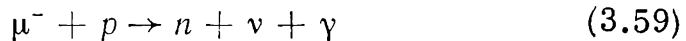
It follows from these calculations that the asymmetry in the angular distribution of the recoil nuclei is very sensitive to the presence of the pseudoscalar interaction, but that terms due to the conservation of the vector current ('weak magnetism') have a much smaller effect.

Shapiro and Blokhintsev [115] have drawn attention to a phenomenon which is very sensitive to the pseudoscalar term in the Hamiltonian. They calculated the probability of

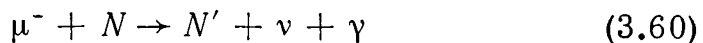
the transition $O^{16} + \mu^- \rightarrow N^{16} + \nu$, in which N^{16} is produced in the excited states 0^- and 1^- . They showed that the total μ^- -capture probability with excitation of these levels was about 5000 sec^{-1} and that the ratio of the capture probabilities for the levels 0^- and 1^- changed by a factor of 6 when the constant C_p^μ was changed from $-8C_A$ to $+8C_A$. Such a large change can be explained by the importance of the pseudo-scalar interaction in the transition $0^+(O^{16}) \rightarrow 0^-(N^{16})$. The ratio of capture probabilities to the levels 0^- and 1^- can be determined experimentally by measuring the relative intensities of γ rays produced in the radiative transitions $1^- \rightarrow 0^-$ (272 keV) or $1^- \rightarrow 2^-$ (392 keV) and $0^- \rightarrow 2^-$ (120 keV) of the excited N^{16} nucleus.

3.15 RADIATIVE μ^- CAPTURE BY NUCLEI

In this section we shall consider briefly theoretical predictions regarding the electromagnetic radiation resulting from nuclear μ^- capture, and the very sparse experimental data on this radiation. For a proton, the process may be written in the form



where γ represents the emitted photon, and if the negative muon is captured by the nucleus we have



The problem has been treated theoretically by Cantwell [116] and Bernstein [117]. We shall briefly review their results, bearing in mind the experimental possibilities which follow from them. Cantwell considered light nuclei ($Z/137 \ll 1$), using the Hamiltonian given by (3.8) without terms proportional to the neutrino momentum ν/M . This means that in his analysis the pseudoscalar constant was zero. He showed that the total probability of radiative μ^- capture was about 10^{-4} of the total probability of μ^- capture, i.e.

$$R = \frac{\Lambda_{\text{rad}}}{\Lambda} \approx 10^{-4}$$

The photon spectrum produced as a result of nuclear μ^- capture exhibits a maximum at 30 MeV and extends to 100

MeV. The appearance of high-energy photons should make it much easier to observe the radiative capture experimentally. In fact, for photon energies in excess of 50 MeV, there is no bremsstrahlung background associated with electrons from $\mu^- - e^-$ decays and the relaxation of nuclei excited as a result of negative-muon capture. We note that the probability of radiative decay is very sensitive to the form of the weak interaction. For example, if the constants g_P and g_M are taken into account, the radiative decay probability rises by a factor of 2 by comparison with the pure $V - A$ interaction. Detection of radiative capture may therefore be used to distinguish between possibilities A and B in Table 3.5.

If parity is not conserved in negative-muon capture, the emitted photons should be circularly polarized. The polarization should be right-handed and equal to 100% [101]. Bernstein showed that pseudoscalar coupling yielded photons with left-handed polarization, and therefore inclusion in the Hamiltonian of the pseudoscalar constant should reduce the right-handed polarization of photons by approximately 30%. These effects are smoothed out somewhat if the negative muon is captured not by a proton but by a complex nucleus. Another effect of non-conservation of parity in radiative μ^- capture is the asymmetry in the angular distribution of photons relative to the μ^- spin direction at the time of capture. Radiative μ^- capture in iron was investigated by Conforto et al. [118], using the very intense and pure negative-muon beam of the CERN accelerator. The apparatus included two spark chambers and a large NaI scintillator. One of the chambers was used to record negative muons stopping in thin iron plates and the other (placed above the first) was used to record e^+ , e^- pairs produced by photons in a tungsten converter. The pair energy was measured by a total absorption counter. About 10 photons due to radiative capture with energies in excess of 60 MeV were recorded in this experiment. This is in qualitative agreement with the value of about 10^{-4} for the fraction of radiative decays predicted by the theory.

ELECTROMAGNETIC INTERACTIONS OF MUONS

4.1 PRELIMINARY REMARKS

In this chapter we shall consider phenomena associated with the interaction of muons with the electromagnetic field. Analysis of these phenomena leads to the conclusion that in such interactions the muon is indistinguishable from the electron. There are no experiments at present which indicate with any degree of reliability that the opposite situation prevails. The principle of such experiments is to consider an electromagnetic process involving the participation of an electron, in one case, and a muon in another, and to compare the corresponding cross-sections, transition energies, probabilities, and so on. The muonic atom is a possible system for this purpose since the electron is replaced by a muon. We shall show that the muon in the mesonic atom does in fact exhibit an analogous behaviour to an electron, except that it is much heavier. The various electromagnetic interactions involving muons have been extensively investigated and have been reviewed by Fowler and Wolfendale.

In this chapter we will also consider topics such as muon pair production by high-energy photons, the nuclear scattering of muons and the measurement of the magnetic

moment of the muon. These topics were selected because they indicate that electrons and muons have identical electromagnetic properties in short-range interactions involving large momentum transfers.

4.2 MUONIC ATOMS

When a negative muon is slowed down in matter, it is captured by the Coulomb field of an atom and forms a bound system known as the muonic atom. As a result of cascade transitions between orbits, the negative muon passes through the electron shells of the atom and eventually experiences the entire nuclear Coulomb field. Experimental studies of the radiation emitted as a result of such cascade transitions have been in progress since 1949 and have led to results which are exceedingly important for the understanding of the properties of muons and their interaction with the electromagnetic field of the nucleus. For example, the nuclear radius was determined by observing the difference between the energies of photons emitted as a result of mesonic-atom transitions and the energies expected for a point nucleus. The agreement between the nuclear radii obtained by this method and the radii deduced from electron-scattering data suggests that the interaction between the negative muon and the nucleus at distances of the order of 10^{-10} - 10^{-13} cm (corresponding to the linear dimensions of the K shell of light and heavy mesonic atoms) is of an electromagnetic nature.

Another important result deduced from studies of muonic atoms is a very accurate value for the mass of the muon. The mass has been determined to one part in 10^4 by measuring the energy of the $3D - 2P$ transition in mesonic phosphorus atoms. This transition occurs at distances which are large enough for the nucleus to be replaced by a point charge and vacuum polarization is practically the only interaction which alters the energy of the emitted photon from the value predicted by the Dirac equation. The energy shift in the $3D - 2P$ transition due to this effect is approximately $\frac{\delta E}{E} = 3 \times 10^{-3}$, and the agreement between the muon mass obtained in this way with the mass measured by more usual methods confirms the validity of quantum-electrodynamic calculations of vacuum polarization for the muon.

The third result which will be discussed in this chapter has been deduced from studies of X rays emitted by light mesonic atoms. The experiments of Stearns and Stearns [25, 26], who found that the X-ray yield was low, have attracted the attention of theoreticians who suspected various anomalies in mesonic-atom transitions, e.g. the presence of metastable states from which no radiation is emitted. New experiments on X-ray and Auger-electron yields have shown, however, that all existing data are fully in agreement with the theory in which muon transitions in mesonic atoms are regarded as transitions of a heavy electron.

4.2.1 Energy levels of muonic atoms

In this section we shall consider calculations of the energy levels of muonic atoms performed on the assumption that the interaction between the muon and the nucleus is purely electromagnetic. If the finite dimensions of the nucleus are neglected, the energy levels of the mesonic atoms are given by the usual Bohr theory, except that the reduced mass of the electron is replaced by the reduced mass of the muon. The energy E_n , the orbital radius r_n and the 'classical' velocity v_n of a negative muon captured into an orbit with principal quantum number n are therefore given by

$$\begin{aligned} E_n &= -\bar{m}_\mu c^2 \frac{(Z\alpha)^2}{2n^2} \\ r_n &= \frac{n^2 \hbar}{\alpha Z \bar{m}_\mu c} \\ v_n &= \alpha c \frac{Z}{n} \end{aligned} \quad (4.1)$$

where $\bar{m}_\mu = \frac{m_\mu}{1+m_\mu/A}$ is the reduced mass of the muon and α the fine-structure constant given by $\alpha = e^2/\hbar c \approx 1/137$.

For the muonic atom, the energy terms are therefore increased by a factor of about 207 and the dimensions of the atom are reduced by the same factor, compared with the normal atom. It is interesting to note that the velocity is unaffected. The fine structure of the muonic levels is obtained by solving the Dirac equation for spin 1/2 particles in the Coulomb field of the nucleus. The energy terms are

given by [1]

$$E_{n,j} = -\bar{m}_\mu c^2 \frac{(Z\alpha)^2}{2n^2} \times \left\{ 1 + \frac{(Z\alpha)^2}{n^2} \left(\frac{n}{j + \frac{1}{2}} - \frac{3}{4} \right) \right\} \quad (4.2)$$

where $j = l \pm 1/2$, and l is the orbital angular momentum. The relative magnitude of the splitting due to the different spin orientations is the same as for the normal atom. Fig. 4.1 gives the energies of a number of transitions in muonic atoms, calculated from Equations (4.1) and (4.2) for Z in the range 1-100.

4.2.2 Finite nuclear dimensions and the energy levels of muonic atoms

Equations (4.1) and (4.2) and the plots of Fig. 4.1 are valid for a muon in the field of a point charge, specified by the Coulomb potential $U = -Ze^2/r$. The main correction to this simple estimate based on the Bohr theory is due to the finite dimensions of the nucleus and becomes progressively

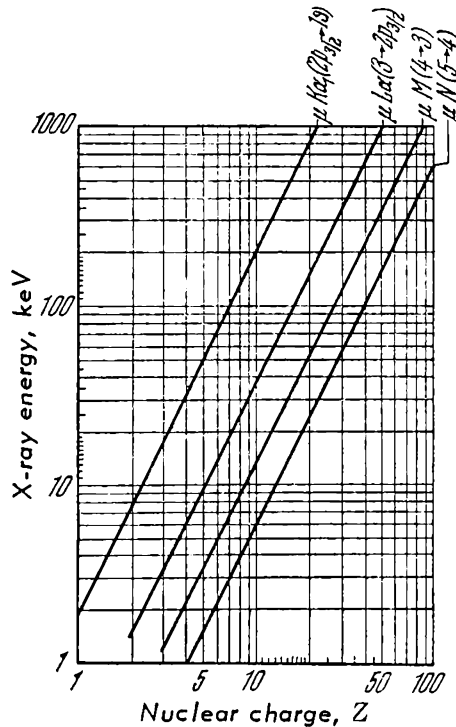


Fig. 4.1 Energy of four transitions in muonic atoms calculated from (4.1) for a point nucleus

more important as Z increases. The nuclear radius R is of the order of $1.2 \times 10^{-13} A^{1/3}$ cm, and the K orbit of the muon lies inside the nucleus if

$$\frac{1}{\alpha Z m_{\mu} c} < 1.2 \cdot 10^{-13} (2Z)^{1/3}$$

i.e. if $Z \gtrsim 30$. It follows that even for elements of moderate atomic weight, the departure of the nuclear electrostatic field from the field of a point charge is quite significant. The shift δE of the energy levels given by Equations (4.1) and (4.2) may be calculated in the usual way, at least for low Z , from first-order perturbation theory:

$$\delta E = -e \int \psi \psi^* \delta V dv$$

where ψ represents the muon wave functions for a point charge and δV is the perturbing potential, equal to the difference between the true electrostatic potential and the point-charge potential.

Cooper and Henley [2] estimated δE for the $1S$ state using a uniform charge distribution for the nucleus. The expression they obtained may be generalized for any S states and is given by

$$\frac{\delta E}{E_Z} = \frac{4}{5} \frac{1}{n^3} \left(\frac{ZR}{r_B} \right)^2 \quad (4.3)$$

where R is the nuclear radius, r_B the mesonic Bohr radius and E_Z the binding energy of the $1S$ level. This formula is valid for the K shell when $Z \lesssim 10$, in which case the shift is about 1%, but it can also be used for large Z when $n > 1$. The shift due to the finite dimensions of the nucleus is very small for the $2P$ level of the mesonic atom because the wave function for the P state vanishes at the nucleus ($r = 0$). The corresponding formula was obtained by Flügge et al. [3] and may be written

$$\frac{\delta E}{E} = \left\{ 0.0018 \left(\frac{ZR}{r_B} \right)^4 - 0.0010 \left(\frac{ZR}{r_B} \right)^5 + \dots \right\} \quad (4.4)$$

The shift in the $1S$ levels is appreciable for $Z > 10$, and first-order perturbation theory is not sufficient in this case.

The problem can only be resolved through rigorous solutions of the wave equations for potentials inside and outside the nucleus.

Fig. 4.2 illustrates the effect of the finite dimensions of the nucleus on the $2P-1S$ transition energy (without taking fine structure into account). The $2P-1S$ transition energy is plotted as a function of the nuclear charge [4]. The broken curve represents the situation for a point

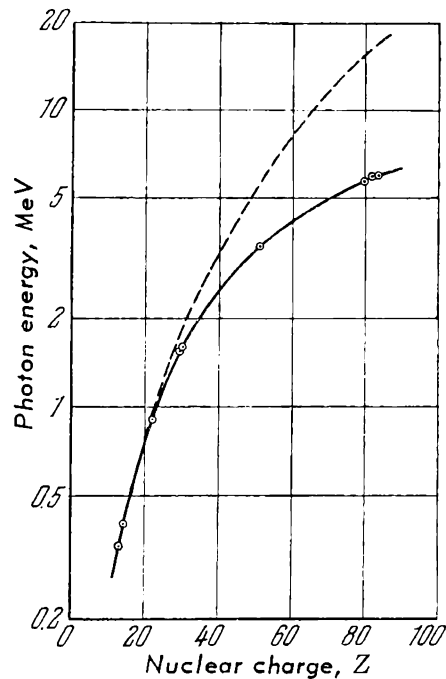
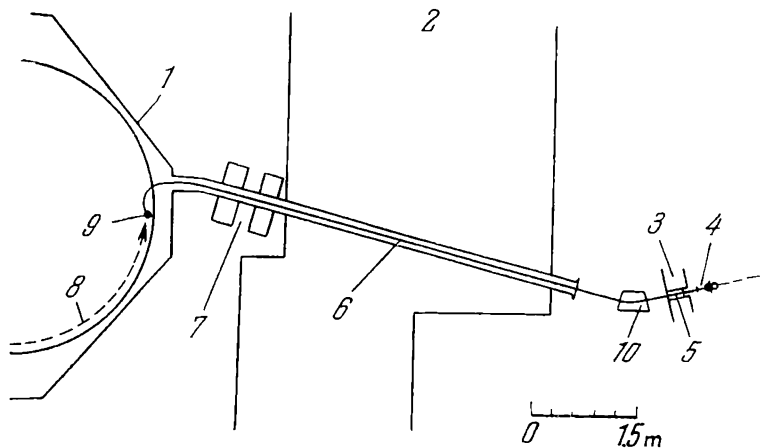


Fig. 4.2 Effect of the finite dimensions of the nucleus on the $2P-1S$ transition energy (Fitch and Rainwater). Broken-curve represents a point nucleus and solid curve a uniformly charged sphere of radius $R = 1.15 \times 10^{-13} A^{1/3}$ cm

charge and, apart from the fine structure, it is the same as the curve for the $\mu K_{\alpha 1} (2P_{3/2}-1S)$ transition in Fig. 4.1. The solid curve gives the energies of these transitions for a nucleus with a uniform charge distribution in a sphere of radius $R = 1.15 \times 10^{-13} A^{1/3}$. It is evident from these curves that the $2P-1S$ line shift due to the finite dimensions of the nucleus increases rapidly with nuclear charge. For example, the shift in the mesonic atoms of aluminium and silicon is only 2%, for titanium 5% and for copper 18%, but for antimony it is 70% and for lead as much as 170%. In the last case, a mesonic atom with a point charge would emit 16-MeV photons as a result of $2P-1S$ transitions, whilst the energy expected for an extended nucleus is only about 5.5 MeV.

4.2.3 Methods of measuring mesonic-atom transition energies

The first experiment in which radiation from mesonic atoms was successfully recorded was performed by Chang [5], who observed negative muons stopping in lead plates in a Wilson cloud chamber which were accompanied by low-energy electrons. These electrons had energies of a few MeV and could be due to the conversion of X rays emitted by mesonic atoms or to γ rays from excited nuclei. Butement [6], in an experiment using cosmic-ray negative muons, detected the K line due to the mesonic atom of carbon. However, quantitative experiments involving muonic atoms could only be successfully performed when intense and well-collimated muon beams from accelerators became available. Fig. 4.3 shows a typical experimental arrangement used with the Liverpool synchrocyclotron. The muons originated from pions decaying in flight, which in turn were generated by protons at an internal beryllium target. After deflection by the fringing field of the synchrocyclotron magnet, the pions entered the collimating pipe and were momentum-analysed by a magnet at the end of the pipe. The monochromatic pion beam selected by a second collimator contained 5-10% of muons and approximately 5% of electrons from $\pi \rightarrow \mu \rightarrow e$ decays. For 100-MeV pions, the energy of



1 - cyclotron chamber; 2 - concrete shield; 3 - additional shield; 4 - counter telescopes and X-ray spectrometer; 5 - polyethylene absorber; 6 - muon beam; 7 - strongly focusing magnets; 8 - circulating proton beam; 9 - Be target; 10 - deflecting magnet

Fig. 4.3 Measurement of mesonic atom transitions (Liverpool synchrocyclotron)

the muons and electrons in the beam at the exit was about 116 and 195 MeV, respectively. The separation of pions and muons was carried out by the absorption method: for a given momentum the muons have a longer range than the pions. The deflecting magnet was followed by an apparatus in which the muons were retarded in various absorbers, and the energies of photons emitted as a result of transitions in the mesonic atoms were determined.

As an example, Fig. 4.4 shows an arrangement for the detection and measurement of X rays emitted by muonic atoms [4]. The basic principles of this spectrometer have also been used by other workers. It consisted of four scintillation counters of which counters 1, 2 and 3 contained fast plastic scintillators and 4 was an NaI(Tl) spectrometer crystal. The first three counters were used to identify stopping muons by recording $12\bar{3}$ coincidences. A coincidence between a $12\bar{3}$ pulse and a pulse from the NaI(Tl) crystal was used as a gating pulse to enable the pulse produced in the NaI(Tl) crystal by the absorption of mesonic X rays to enter a pulse-height analyser.

Fig. 4.5 shows an improved spectrometer for the determination of photon energies emitted by mesonic atoms as described by Johnson et al. [7]. In this arrangement, the NaI(Tl) crystal was removed from the beam line, the dimensions of the crystals were increased and the shielding improved. The purity of the negative-muon beam was improved by introducing the threshold Cerenkov counter C and using $1234\bar{C}$ coincidences to select stopping muons.

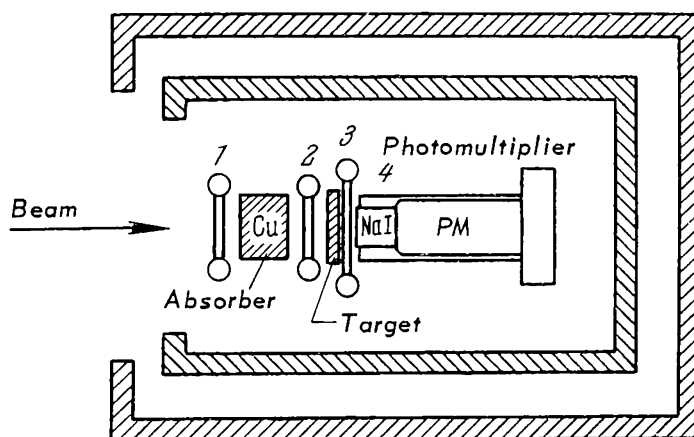


Fig. 4.4 Determination of the energies of transitions in muonic atoms (Fitch and Rainwater)

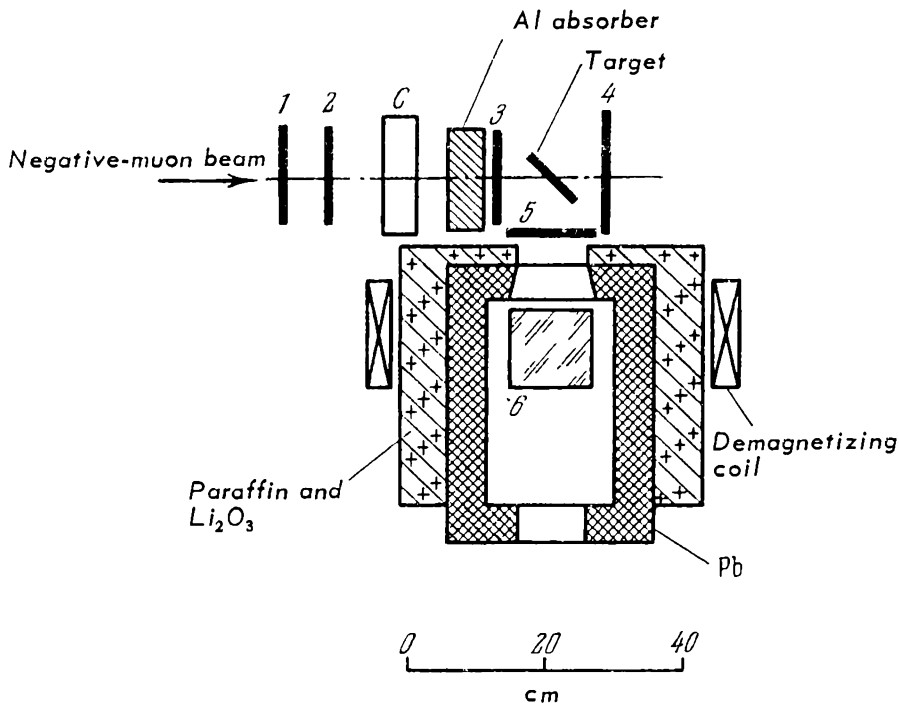


Fig. 4.5 Measurement of transition energies in muonic atoms (Johnson et al.). The NaI(Tl) crystal 6 is removed from the beam, the shielding of the crystal is improved and its dimensions are increased. 1–5 are scintillation counters

For photon energies below 100 keV there is a sharp reduction in the resolution of scintillation counters. For example, with the best NaI(Tl) crystals, the total width at half-height of the pulse-height spectrum produced by 60-keV X rays is about 25%. In this energy region, the mesonic-atom emission has been successfully recorded with proportional counters [8] filled with xenon which have a much better resolution (5% at 60 keV), but their detection efficiency decreases rapidly with energy.

As an example of the use of the proportional counter in mesonic-atom spectroscopy, let us consider the emission by phosphorus shown in Fig. 4.11 ($4F \rightarrow 3D, 3D \rightarrow 2P$ transitions).

Considerable success has been achieved during 1964–1966 in mesonic-atom spectroscopy. This was connected with the use of semiconductor (germanium) detectors doped with lithium. These detectors can be used to measure γ lines with widths of a few keV, and this opens up radically new possibilities. For example, it is possible to resolve the fine structure of K, L, M , and higher lines not only for

heavy mesonic atoms but even for those occupying intermediate positions in the periodic table. Moreover, relative intensities of the fine-structure lines, effects connected with the non-spherical shape of atomic nuclei, and isotopic effects have become measurable.

Let us now consider typical results of measurements on X rays emitted by mesonic atoms which have been performed with an NaI(Tl) spectrometer.

Fig. 4.6 shows the $2P \rightarrow 1S$ line recorded by Fitch and Rainwater [4]. Fig. 4.7 illustrates the analogous transition in the mesonic atom of Fe^{26} . The line width in these experiments was quite large and amounted to a few tens of keV.

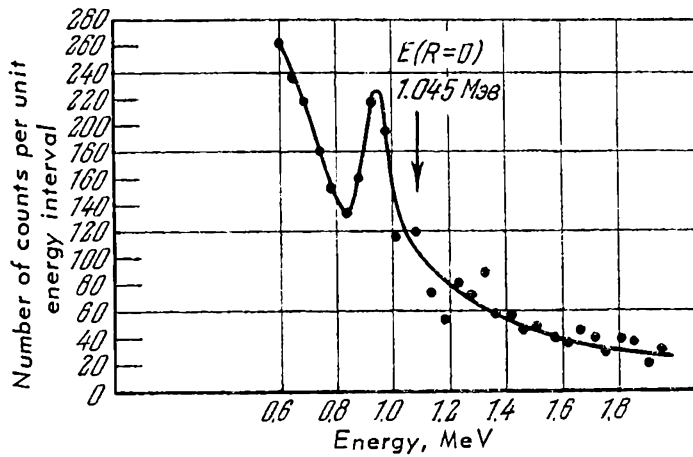


Fig. 4.6 K_α line of the muonic atom of Ti^{22} (Fitch and Rainwater). Arrow indicates the expected energy for a point charge ($R = 0$)

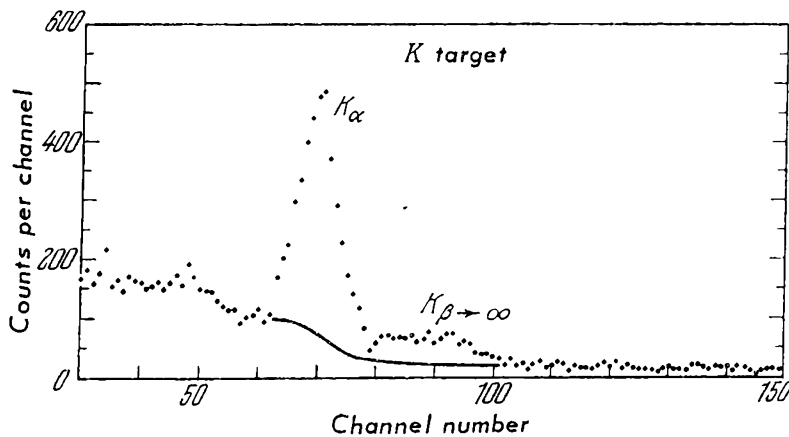


Fig. 4.7 K_α line for muonic atoms of Fe (Johnson et al.)

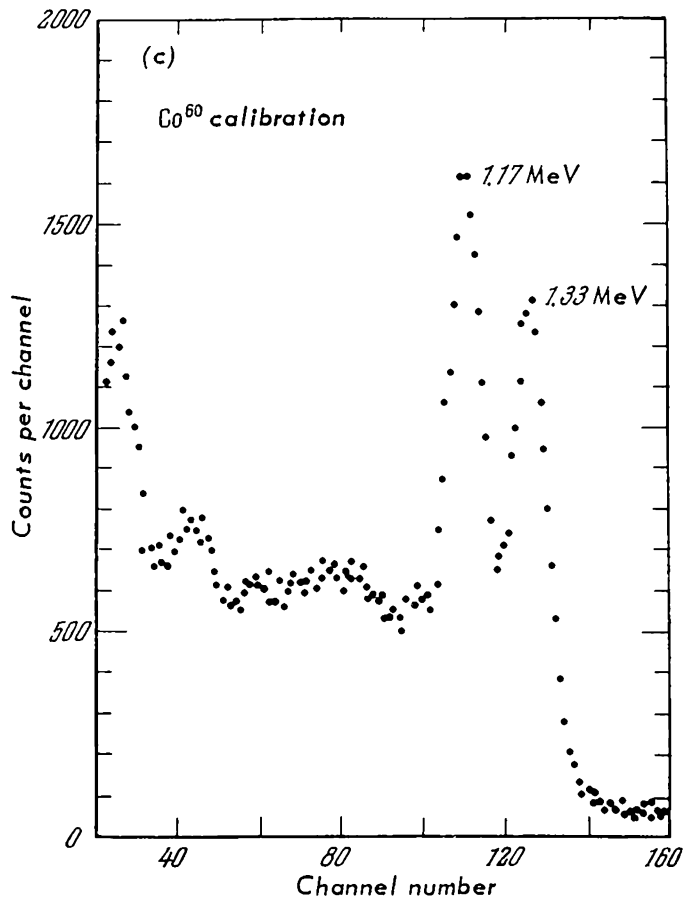
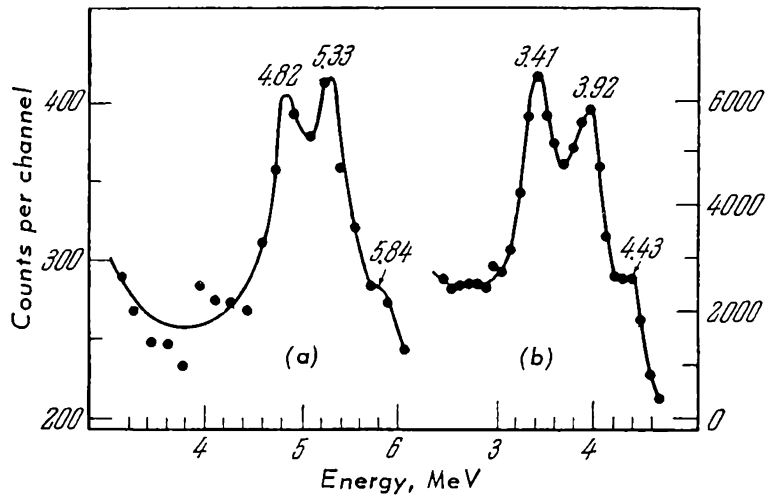


Fig. 4.8 Calibration of X-ray spectrometers: (a) the γ line of C^{12*} (Butement et al.); (b) the K line of the mesonic atom of lead; (c) the 1.17- and 1.33-MeV Co^{60} lines (Johnson et al.)

Calibration and analysis were performed by comparing these spectra with the spectra due to known γ transitions measured with the same spectrometer. The known γ -ray lines were, for example, the 1.38- and 2.76-MeV lines of Na^{24} , the 4.43-MeV line of C^{12} and C^{12*} from the reaction $\text{He}^4 + \text{Be}^9 \rightarrow \text{C}^{12*} + n$, and many others. Calibration of the spectrometers using known γ -ray lines showed that a monochromatic γ -ray line, for example, the 4.43-MeV line (Fig. 4.8), was reproduced by the NaI(Tl) spectrometer in the form of three lines at intervals of 0.51 MeV. The 4.43-MeV line corresponds to the absorption of the entire γ -ray energy in the spectrometer. The two other lines correspond to the escape from the crystal of one and two annihilation photons, respectively. Fig. 4.8 shows the spectrogram for the $2P - 1S$ transition in the mesonic atom of lead [4] which again shows the presence of three lines separated by 0.51 MeV. Fig. 4.8 also shows the calibration curve obtained with the Co^{60} γ -ray lines reported by Johnson et al. In this case, the pair production cross-section was small and the lines are represented by single photo-peaks. Comparison of the mesonic-atom spectra with standard γ -ray spectra of known and similar energy was used to determine the energies of the mesonic-atom transitions for the K lines of heavy elements to an accuracy approaching 1%, despite the fact that the line width was considerably greater.

As an example illustrating the possibilities of the γ -ray spectrometers incorporating solid-state detectors, we may quote the result obtained by Chasman et al. [61], who investigated the spectra of $2P \rightarrow 1S$ transitions in the mesonic atoms of molybdenum (Fig. 4.9). As can be seen, the fine structure is clearly resolved. The energy difference between the two transitions ($2P_{3/2} \rightarrow 1S_{1/2}$ and $2P_{1/2} \rightarrow 1S_{1/2}$) is 23.5 ± 0.9 keV. Comparison of these spectra clearly shows the presence of the isotopic effect which amounts to $\Delta (\text{Mo}^{98} - \text{Mo}^{96}) = +6.2 \pm 0.7$ keV.

Measurements by Cote et al. [62], who used an analogous detector to investigate the X-ray emission of muonic atoms of gold can be taken as another example (Fig. 4.10). Here again, the fine structure is clearly resolved. Moreover, it is evident that the $2P_{3/2} \rightarrow 1S_{1/2}$ line consists of two, or perhaps even three, components. This hyperfine structure appears to be associated with the presence of a static quadrupole effect, considered by Wheeler [63].

4.2.4 Mesonic X rays and the electric-charge distribution in the nucleus

Determinations of the energy of mesonic-atom transitions are a sensitive means of investigating nuclear sizes and the electric-charge distribution in nuclei. It is evident that the finite dimensions of the nucleus must have a particularly strong effect on the $2P - 1S$ transition energies. Theory shows that these energies are determined mainly by the second moment of the nuclear electric-charge distribution

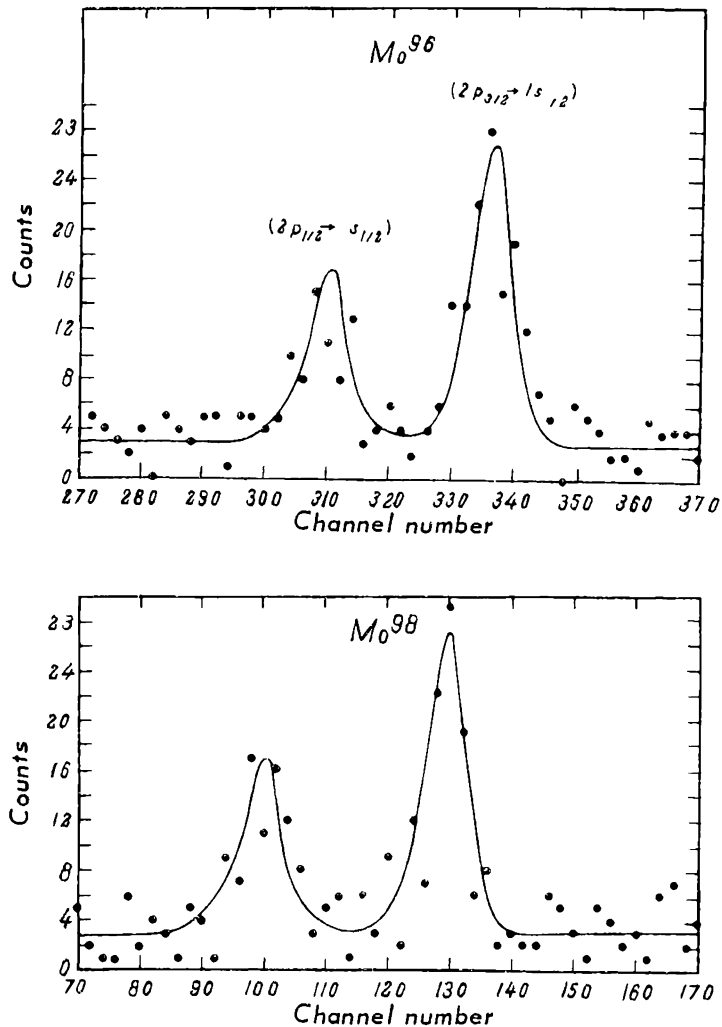


Fig. 4.9 Fine structure of the K_{α} line in the muonic X-ray spectrum of molybdenum and isotopic shift in Mo^{96} and Mo^{98} . The $2P_{3/2} \rightarrow 1S_{1/2}$ transition energy of Mo^{96} and Mo^{98} is 2713.3 ± 1.1 keV and 2707.1 ± 1.1 keV respectively

$$\alpha = \int_0^{\infty} z^2 4\pi z^2 \rho dz$$

where $\int 4\pi z^2 \rho dz$ is normalised to unity. If we adopt the simple assumption that the nucleus is a uniformly charged sphere of radius R , the relation between R and the parameter a determined from mesonic-atom experiments becomes

$$R = (5a/3)^{1/2}$$

In heavy nuclei the shift of the mesonic-atom levels relative to the levels of the point nucleus (see Equation (4.3)) is large in absolute magnitude and is proportional to $(ZR)^2$. For example, it is evident from Fig. 4.2 that, owing to the effect of the finite dimensions of the nucleus, the $2P - 1S$ transition energy in lead changes from 16 MeV for a point nucleus to about 5 MeV for a nucleus of radius $R = 1.3 \times 10^{-13} A^{1/3}$ cm. Measurements of the $2P - 1S$ transition energy is thus a sensitive method of investigating the electric structure of the nucleus.

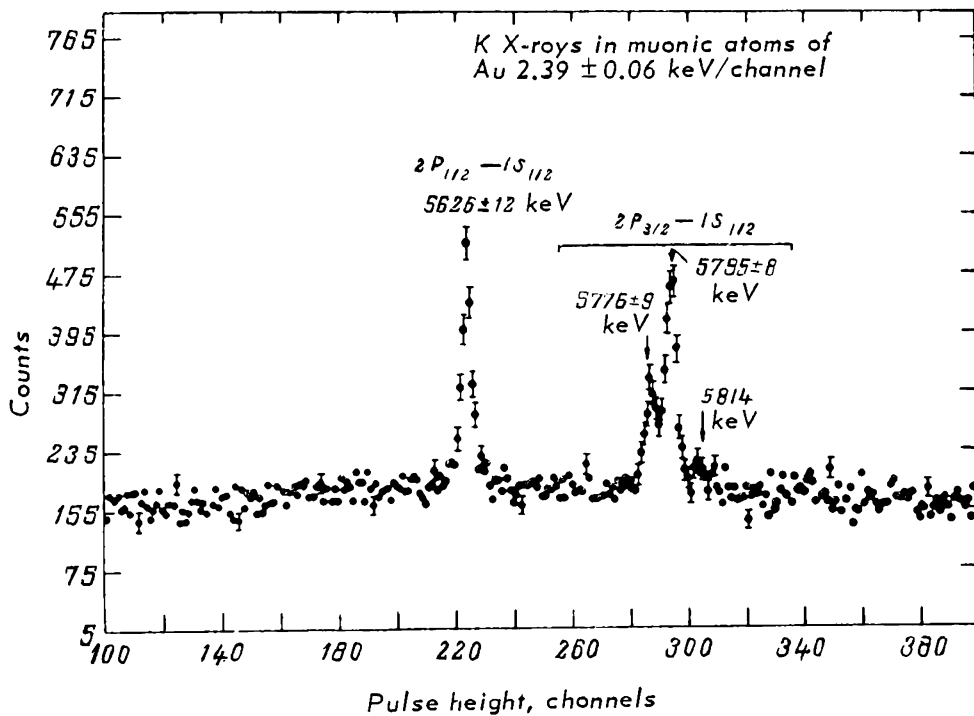


Fig. 4.10 Fine structure of the K_{α} line in muonic atoms of gold

Such experiments were first performed with the aid of the NaI(Tl) scintillation spectrometer for the K lines of the mesonic atoms of Ti^{22} , Cu^{29} , Sb^{51} and Pb^{82} by Fitch and Rainwater [4] and Butement [9]. Subsequent measurements by other workers were performed with a similar spectrometer. However, various improvements in the experimental techniques connected with the higher intensity of muon beams, larger NaI(Tl) crystals, improvements in the calibration techniques and so on, have led to extensive data on the $2P \rightarrow 1S$ transition energies in different mesonic atoms. For example, Anderson et al. [65] have measured the $2P \rightarrow 1S$ transition energies for 14 elements between $Z = 12$ and $Z = 50$, while Frati and Rainwater [64] have performed similar measurements for Ti, Fe, Cu, Zn, Tl, Pb and Bi. The most detailed measurements of the various transition energies were performed by the CERN group. Backenstoss et al. [66] have investigated the $2P \rightarrow 1S$ transition for 30 elements with Z between 16 and 83. In a recent paper by Acker et al. [77], the NaI(Tl) phosphor was replaced by a lithium-doped germanium crystal. They used this method to investigate 19 elements with spherical nuclei between $Z = 17$ and $Z = 83$. Above $Z = 50$ they obtained excellent resolution of fine-structure lines due not only to the $2P \rightarrow 1S$ but also the $3D \rightarrow 2P$ transitions, and were able to investigate not only the transition energies but the fine-structure line intensities also.

It was evident even from the first experiments of Fitch and Rainwater [4] that if the nucleus were considered as a charged sphere, the radius of this sphere for Ti ($Z = 22$), Cu ($Z = 29$), Sb ($Z = 51$) and Pb ($Z = 82$) could be well represented by the formula

$$R = r_0 A^{1/3} \times 10^{-13} \text{ cm}$$

where r_0 lay between 1.17 and 1.22

Subsequent measurements which we have already mentioned confirm this conclusion, in the sense that the values of r_0 deduced from the $2P \rightarrow 1S$ transition energies were in good agreement with the values of r_0 deduced from other experiments which are sensitive to the electric-charge distribution. It is well known that all these experiments indicate that the electric radius of the nucleus is smaller than the nuclear radius. Among these experiments, the

largest values are obtained from experiments on electron scattering, and therefore the problem arises whether the nuclear-charge distribution deduced from measurements of the mesonic-atom transition energies are in agreement with, for example, the analogous data obtained by Hofstadter et al. who investigated electron scattering. This problem was considered in detail by Hill et al. [10], Ford and Wills [68] and Pustovalov and Krechko [69]. Comparisons of calculations with experimental data of mesonic-atom transition energies showed that the two sets of results on the electric-charge distribution parameters were in agreement to within a few per cent.

Thus it is clear that there is again no evidence for any difference between electromagnetic interactions involving muons and nuclei on the one hand, and electrons and nuclei on the other. It is hoped that new experimental methods for the spectroscopic study of mesonic-atom emissions, which will yield information about the fine structure and the quadrupole and isotopic effects, will provide a means for further studies of the electromagnetic structure of the nucleus with the aid of muons.

To conclude this section, let us consider data on some of the $2P - 1S$ transition energies reported in recent papers. These data are summarized in Table 4.1 and are partly taken from the paper by Anderson et al. [70] and the data of the CERN group. Columns 1 and 2 of the table show the element, while columns 3, 4, 5, 6 and 7 give the experimental data and the transition energies. Columns 8 and 9 give the theoretical values of the $2P - 1S$ transition energies [68, 69].

4.2.5 Measurement of X-ray energies from light mesonic atoms

Measurements on X rays emitted by light mesonic atoms have been used to deduce the muon mass to an accuracy of 1 in 10^4 . This was done by using distant transitions in light mesonic atoms, so that corrections to the transition energy due to the finite dimensions of the nucleus and other effects were small. The mesonic-atom X-ray energies can be determined with great accuracy from the well-known rapid reduction in the X-ray absorption coefficient which occurs when the energy of the X rays is less than the energy necessary for the removal of an electron from the K shell of the absorbing atoms (the K edge of the absorption curve). Such

measurements were first performed by Koslov et al. [11] for muonic atoms and by Stearns et al. [12] for pionic atoms. The mesonic-atom X rays emitted by the target in which the mesons came to rest were recorded by a scintillation spectrometer. By placing different absorbers with monotonically decreasing Z between the target and the spectrometer, it was found that there was a rapid reduction in the intensity of a given line for the absorber for which the K edge on the absorption curve was near the energy of the given transition. At about 50 keV, the K levels of neighbouring elements differ by approximately 1.7 keV, and therefore this method will not yield a precise value for the X-ray energy. It is only by selecting suitable transitions that the upper and lower limits of this energy can be established accurately and the pion and muon masses be determined with high precision.

The nature of the meson-nucleus interaction, the finite dimensions of the nucleus, electron screening, vacuum polarization and other corrections must be applied before the meson mass can be established from the measured X-ray energy. These corrections are very small for transitions between outer orbits in light elements and can mostly be neglected. The most important is the correction due to vacuum polarization. Table 4.2 gives the limits for the muon mass obtained by Koslov et al.

According to these data, the mass of the muon must be in the range

$$(206.77 \pm 0.04) m_e \leq m_\mu \leq (208.95 \pm 0.04) m_e$$

A similar method was used for the $4F-3D$ transition in mesonic atoms of P, Al and K [12] to obtain the limits for the pion mass. The result was

$$(272.2 \pm 0.30) m_e \leq m_\pi \leq (273.51 \pm 0.04) m_e$$

A knowledge of the muon mass is very important for the determination of its magnetic moment: the error in the measured magnetic moment of the muon by the spin-precession method in a magnetic field is almost entirely determined by the error in its mass. The experimental situation connected with the determination of the muon mass from the absorption of X rays from mesonic phosphorus atoms by the K edge of lead has therefore been carefully re-investigated. Bearden [13] has determined the energy dependence of the X-ray

Table 4.2 Muon mass in units of m_e

Element	Transition	Transition energy, keV	Muon mass	
			Without correction for vacuum polarization	With correction
C	$2P - 1S$	76.123	<209.99	<208.95
P	$3D - 2P$	88.015	>207.55	>206.77
Si	$4F - 3D$	26.713	>206.82	>206.47

absorption coefficient of lead between 87.85 and 88.15 keV very accurately. This experiment was carried out with a double crystal spectrometer using the 2023 plane of quartz as a diffraction grating. The X rays were produced by a commercial high-voltage tube and the detector was an NaI(Tl) scintillator. The distances between the source, the first crystal, the second crystal and the detector were all equal to 1 m, and the signal-to-background ratio was never less than 100. The measured dependence of the absorption coefficient on photon energy for a 98% pure lead foil is shown in Fig. 4.11.

Petermann and Yamaguchi [14] then calculated the $3D - 2P$ transition energies for the mesonic atoms of phosphorus. For these transitions, the corrections for the finite dimensions of the nucleus are about 3.2 eV, and the most important correction is that for vacuum polarization which amounts to 329.23 eV. The algebraic sum of all the remaining corrections, including the fourth-order correction for vacuum-polarization screening by atomic electrons, the Lamb shift

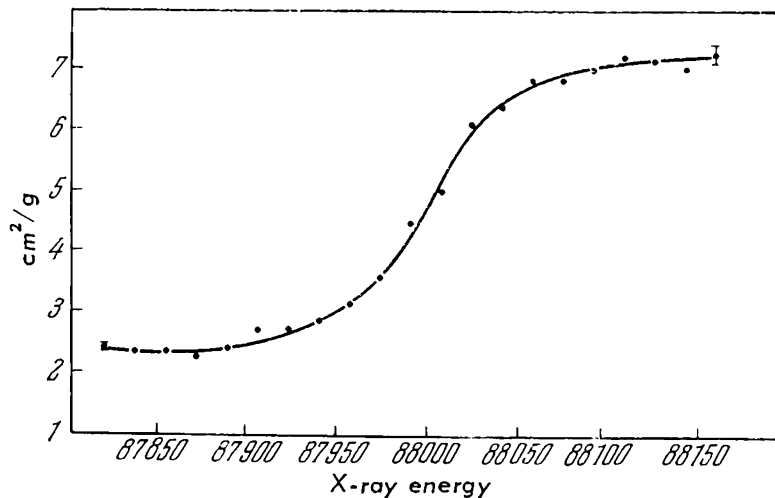


Fig. 4.11 X-ray absorption coefficient for lead as a function of energy near the K edge (Bearden)

and so on, amounts to 0.34 ± 2.0 eV. These calculations led to the following transition energies for the mesonic atom of phosphorus:

$$3D_{3/2} - 2P_{3/2} : 425.42 \cdot \frac{m_\mu}{m_e} (\text{eV}), \text{ relative intensity} = 1$$

$$3D_{5/2} - 2P_{3/2} : 425.65 \cdot \frac{m_\mu}{m_e} (\text{eV}), \text{ relative intensity} = 9$$

$$3D_{3/2} - 2P_{1/2} : 427.75 \cdot \frac{m_\mu}{m_e} (\text{eV}), \text{ relative intensity} = 5$$

where m_μ/m_e is the ratio of the mass of the muon to the mass of the electron. The level scheme is shown on the right-hand side of Fig. 4.12 (not to scale). To illustrate these results, Fig. 4.12 shows the position of the two main

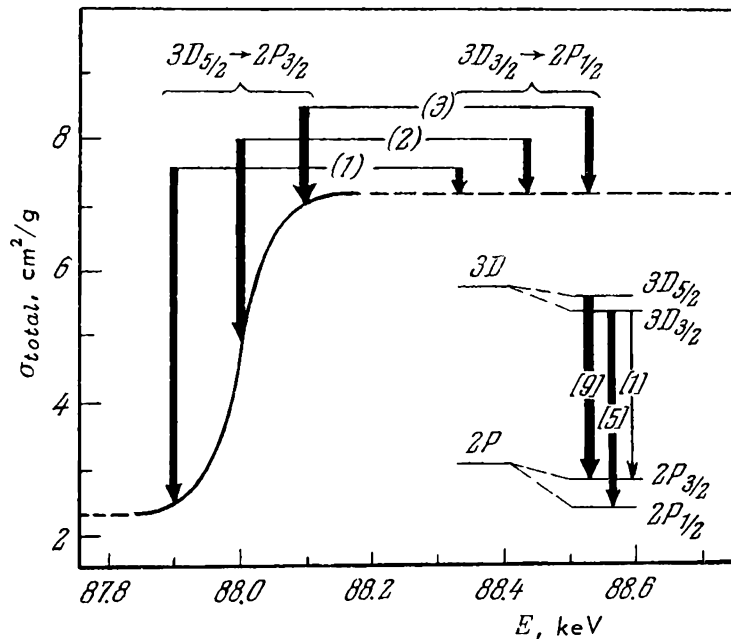


Fig. 4.12 Position of the two main intensity components for the $3D - 2P$ transition in the muonic atom of phosphorus relative to the K edge of the absorption curve for lead for three different muon masses: (1) $m_\mu = 206.56m_e$; (2) $m_\mu = 206.74m_e$; (3) $m_\mu = 206.92m_e$. Numbers in brackets represent the relative intensity of the transition

components of the $3D - 2P$ transitions on the curve representing the absorption coefficient of lead as a function of energy for the following assumed values of the muon mass.

$$(1) m_\mu = 206.56 m_e, (2) m_\mu = 206.74 m_e, (3) m_\mu = 206.92 m_e$$

The corresponding measurements of the absorption of X rays from $3D - 2P$ transitions in the mesonic atom of phosphorus by lead were performed by the Chicago [15] and Columbia [16] groups. These measurements were carried out by two methods: in the first case [15], the absorption was measured with an NaI(Tl) scintillator counter, and in the second [16], with a xenon-filled proportional counter (2.5 atm Xe + 2.5 cm HgCH₄). Fig. 4.13 shows a typical spectrum obtained with the proportional counter. The absorber, which was in the form of a thin lead foil, was placed between

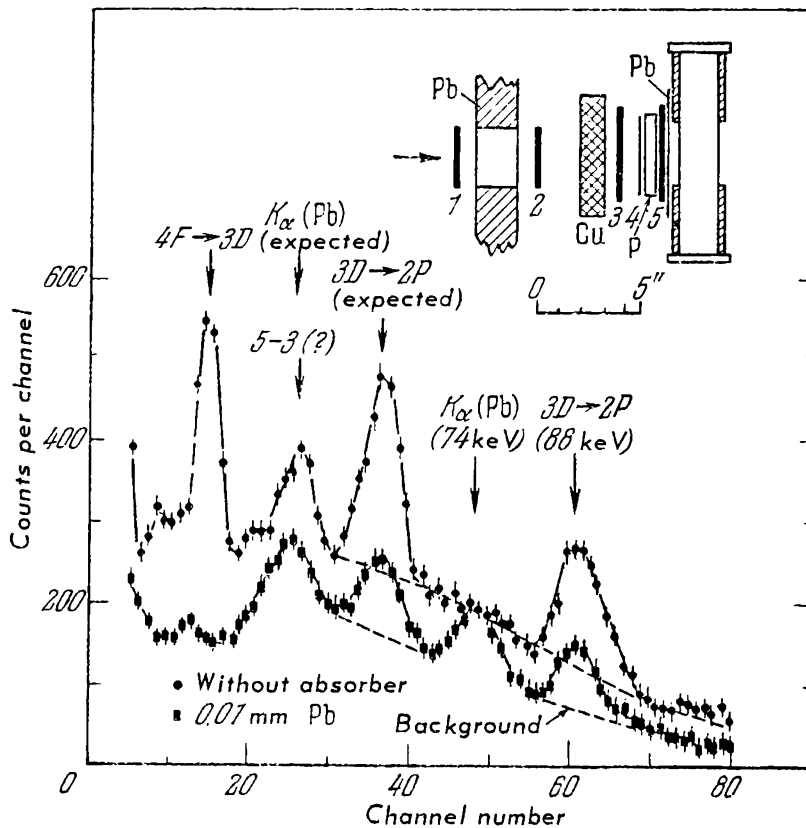


Fig. 4.13 Typical spectrum of the muonic-atom emission by phosphorus measured with a proportional counter filled with xenon (2.5 atm). The upper curve was obtained without the lead filter in front of the proportion counter; the lower curve with the filter. The disposition of counters 1-5 is shown in the upper part of the drawing

the target made of red phosphorus (2 g/cm^2) and the window of the proportional counter. The counter was calibrated with an Am^{241} source (60-keV line). The upper experimental curve corresponds to the spectrum measured without the lead foil between the phosphorus target and the proportional counter. The lower curve was obtained with an 0.01-cm lead foil. Transitions corresponding to the measured lines are indicated in Fig. 4.13.

The families of curves shown in Fig. 4.14 were obtained for five values of the muon mass between $206.62 m_e$ and

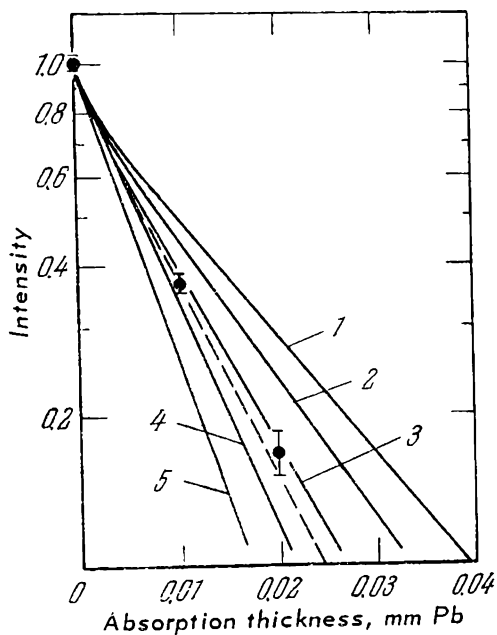


Fig. 4.14 Absorption curve for radiation due to the 3D - 2P transition in the mesonic atom of phosphorus. Curves 1-5 were calculated from the Bearden absorption curve using the following assumed values of the muon mass: 1 - $206.62 m_e$; 2 - $206.68 m_e$; 3 - $206.74 m_e$; 4 - $206.80 m_e$; 5 - $206.86 m_e$. The broken curve through the experimental points corresponds to $m_\mu = 206.76 m_e$

$206.86 m_e$ in steps of $0.06 m_e$ (with corrections for the geometry of the experiment). The three experimental points are shown and the best fit (dashed line) which corresponds to a muon mass of $206.76 m_e$. Analysis of the experimental errors leads to the following value for the muon mass

$$m_\mu = (206.76^{+0.02}_{-0.03}) m_e$$

Similar measurements carried out with the scintillation spectrometer yielded

$$m_\mu = (206.74^{+0.03}_{-0.04}) m_e$$

in the case of the Chicago group, and

$$m_\mu = (206.78^{+0.03}_{-0.02}) m_e$$

in the case of the Columbia group. These measurements are the most accurate determinations of the muon mass at the present time.

4.2.6 X-ray yield of muonic atoms and emission of Auger electrons

First let us briefly review the theory of radiative and non-radiative transitions in muonic atoms, as given by Burbidge and de Borde [17, 18] and by other workers [19-24]. It is well known that the probability of radiative transitions between an initial state (n_1, l_1) and final state (n_2, l_2) of an atom is proportional to the cube of the energy difference between these two states and the square of the dipole matrix element for the transition. Fig. 4.15 shows the radiative transition probabilities calculated by Burbidge and de Borde for the following changes in the principal and orbital quantum numbers:

$$(n = n_1, l = n_1 - 1) \rightarrow (n = n_1 - 1, l = n_1 - 2)$$

These radiative transitions are found to be dominant. The five parallel straight lines in Fig. 4.15 correspond to $n_1 = 2, 3, 4, 5$ and 8 . As can be seen, the radiative transition probability falls off rapidly with increasing n . The figure also shows the probability of Auger transitions with the same change in n and l . It is evident that the probability of Auger transitions is a very slowly-varying function of the nuclear charge Z , but increases rapidly

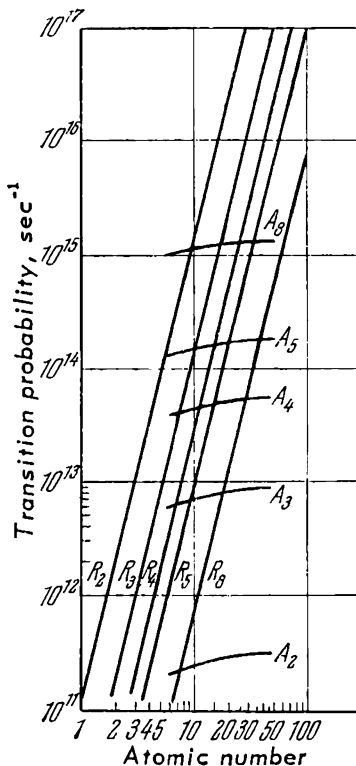


Fig. 4.15 Probability of main radiative transitions in muonic atoms (R) and Auger transitions (A) (Burbidge and de Borde)

with increasing n . It is also evident from the graphs of the transition probabilities that Auger transitions in light elements predominate for n greater than 3, whilst in heavy elements radiative transitions are comparable with Auger transitions for large n . The low probability of emission of Auger electrons by a muon in the lowest-lying orbits has a simple explanation. In the state with $n = 2$, the mesonic orbit has a radius which is smaller by a factor of about 50 than the K -shell radius for an electron, whilst the radius of the mesonic orbit in the state with $n = 1$ is smaller by a factor of 200. Consider the transition of a muon from the $2P$ state to the $1S$ state. For an electron in the K shell, and even more so for electrons in the more distant shells, the field produced by a muon in this transition is identical with the field of a dipole placed at the nucleus of the mesonic atom. In a field of this kind, the Auger transition can only compete with the radiative transition if the distance between the electron and the dipole is much less than the wavelength corresponding to the transition energy. This is analogous to the condition that the electron should not lie in the wave zone of the dipole but be directly in the Coulomb field. The condition may be written as $kR_e \ll 1$, where R_e is the radius of the electron K shell and $\lambda = 2\pi/k$ the wavelength. If the nuclear charge is Z and the muon is in the $n = 2$ shell, then

$$kR_e \approx \frac{3}{8} \left(\frac{\alpha\mu}{m} \right) \frac{Z^2}{Z-1} \approx 0.6 \frac{Z^2}{Z-1} \quad (4.6)$$

where μ/m is the ratio of the muon mass to the mass of the electron. For Z as low as 3, the product kR_e is approximately equal to 3, and Auger transitions cannot lead to a reduction in the yield for the K line. This very approximate calculation shows that Auger transitions should not compete with radiative transitions for small n in light elements.

We note that the entire cascade of transitions, beginning with the first level to which the negative muon is captured, must be considered in determining the radiative and non-radiative transition probabilities. The screening of the nuclear charge by the electron shells need not be taken into account, however, because the principal quantum number is sufficiently large for the negative muon whose orbit coincides with the electron K orbit (it is evident from the formulae that in this case $n \sim \sqrt{m_\mu/m_e} = 14$). For such

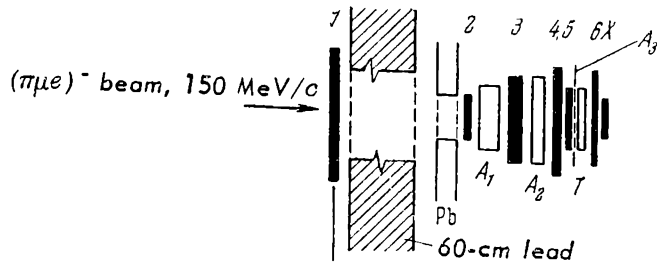
large n , the energy of the first few transitions is too small to produce Auger electrons. This energy is even lower for larger n , and therefore the analysis of the cascade usually begins with $n = 14$.

4.2.7 Experimental X-ray yield in the K and L shells of mesonic atoms

A mesonic atom which is excited as a result of negative-muon capture in one of its shells with a large principal quantum number n can release its excitation energy either through a radiative transition by emitting a photon, or through a non-radiative transition, in which the excitation energy is transferred to one of the electrons (emission of Auger electrons). The theory of radiative and non-radiative transitions in mesonic atoms, which was discussed above, shows that the yield of X rays in the K shell should approach 100% for all mesonic atoms, and that it is only in the L shells of atoms with $Z < 10$ that appreciable departures from 100% yields become possible as a result of a competing Auger process.

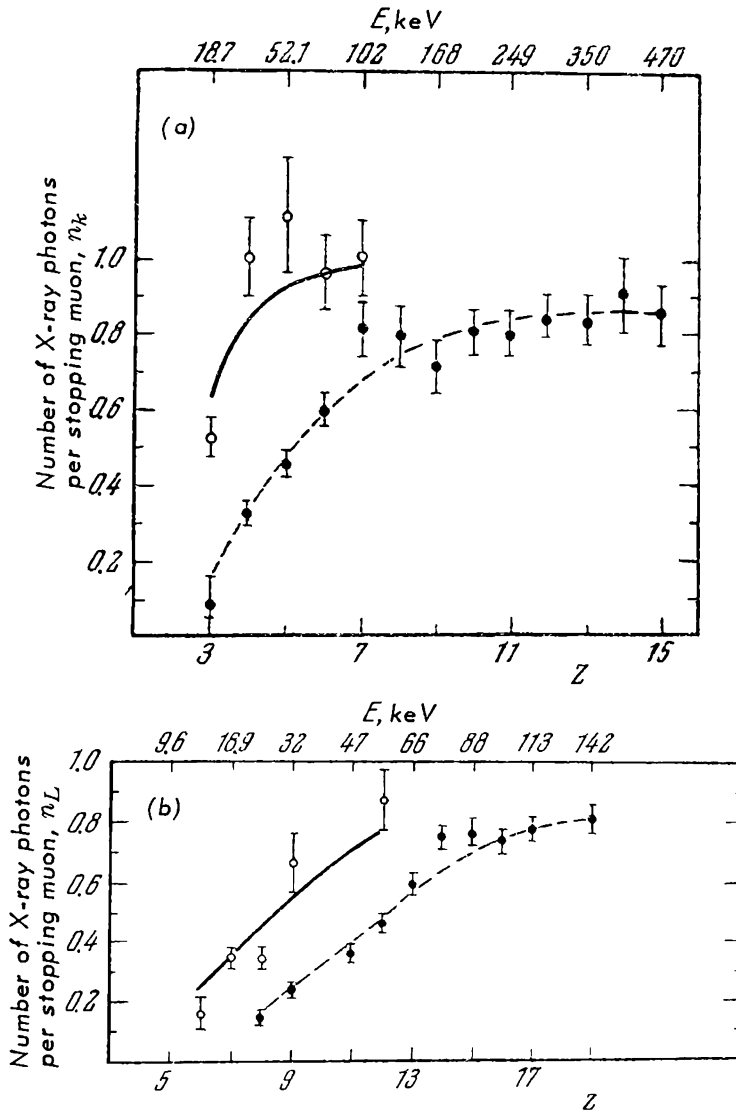
Measurements of the X-ray yield of a mesonic atom may be reduced to the determination of the number of X-ray photons emitted by the target per stopping muon. Such measurements have been performed for the K and L shells by Stearns et al. [25, 26] for elements between Li ($Z = 3$) and K ($Z = 19$), and a sharp discrepancy between theory and experiment was observed. The X-ray yield from the K and L shells of light muonic atoms was found to be much lower than predicted by the theory. Lathrop et al. [27] repeated the measurements of Stearns et al. under improved experimental conditions using the muon beam of the Chicago accelerator (Fig. 4.16). In this figure 1,2,4,5 and 6 are plastic scintillators, 3 is a Cerenkov counter used to eliminate the electron contamination of the muon beam and X is an NaI(Tl) scintillator used to detect the X-ray emission of mesonic atoms produced in the target T in which the muons come to rest.

The results obtained by Stearns and Stearns [25] and Lathrop et al. [27] are shown in Fig. 4.17, where the number of photons per stopping muon is plotted as a function of the nuclear charge Z (and the corresponding energy of the principal transition of the K or L shells). Fig. 4.17a gives the relative yield for the K shell and Fig. 4.17b the



1, 2, 4, 5, 6 - plastic scintillators; 3 - Cerenkov counter; X - NaI crystal; A_1, A_2, A_3 - absorbers; T - target in which the negative muons are brought to rest

Fig. 4.16 Measurement of the X-ray yield in the K and L series of light muonic atoms (Lathrop et al.,)



a - yield in the K series; b - yield in the L series
 Fig. 4.17 X-ray yield of muonic atoms (Stearnes et al. and Lathrop et al.)

yield for the L shell. The data of Stearns and Stearns are indicated by the black circles. Their results appear to indicate that the X-ray yield of light mesonic atoms tends to a limit of 80-85%. Since the probability of radiative transitions is proportional to the fourth power of the nuclear charge, whilst the probability of Auger transitions is approximately independent of Z (cf. Fig. 4.15), the observed X-ray yield should obey the following relationship:

$$y \approx \frac{Z^4}{C + Z^4} \quad (4.7)$$

The data of Stearns and Stearns can be represented by this function, but the experimental value of C is higher by a factor of about 300 than the expected value for the K shell, and by a factor of about 30 for the L shell. The data of Lathrop et al. (open circles in Fig. 4.17) did not show such low yields and indicate a deficiency which is lower by a factor of about 10 compared with the results of Stearns and Stearns. For example, according to Stearns and Stearns the value of C for the K shell is about 400, but according to Lathrop et al. it is approximately 45. A similar discrepancy occurs for the L shell. The discrepancy between experiment and theory has thus become much less startling, and its magnitude could be explained by the initial statistical distribution of the muons over the different possible values of the orbital angular momentum for a given principal quantum number n . It may be supposed that the effect observed by Stearns and Stearns was due to experimental errors, e.g. a reduction in the photon-detection efficiency at low photon energies. This appears even more probable in view of the fact that a similar effect was obtained for pionic atoms.

4.2.8 Emission of Auger electrons from muonic atoms

It is reasonable to suppose that a true reduction in the intensity of radiative transitions should be accompanied by an increase in non-radiative transitions, i.e. transitions accompanied by the emission of Auger electrons. Studies of the yield of Auger electrons in light and heavy mesonic atoms are therefore of particular importance.

Until recently, practically the only method of observing Auger electrons from mesonic-atom transitions has been

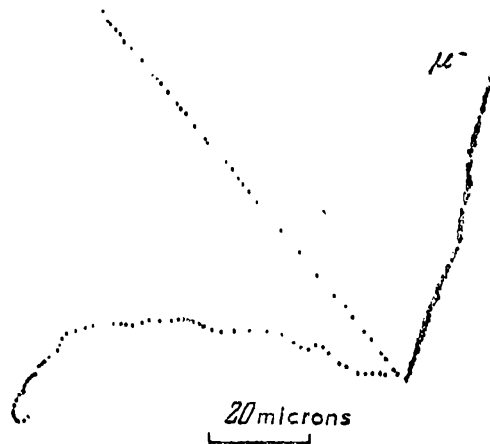


Fig. 4.18 Decay of a negative muon in an emulsion. An Auger electron of about 50 keV (wavy track) was emitted as a result of cascade transitions of the negative muon in the muonic atom

to use nuclear emulsions. Fig. 4.18 shows a typical example of a slow muon coming to rest in an emulsion, followed by the emission of an Auger electron. The photograph shows the track of the slow muon coming to rest and decaying. The straight track with low grain density is the relativistic decay electron. The wavy track originating at the point of decay is an Auger electron with energy of about 50 keV. Since both the slow electron and the decay electron are observed there is no doubt that the former must be an Auger electron, since the muon decayed and was not captured by a nucleus. Nuclear γ radiation which could be converted into electrons is therefore not present in this case.

The energy of Auger electrons in nuclear emulsions can be determined by measuring their range, but since these electrons have highly scattered tracks, such measurements are very inaccurate. At low electron energies there is a further uncertainty due to straggling and fluctuations in the number of developed grains. Moreover, the detection efficiency for Auger electrons is limited at low energies by the minimum electron range which can be recorded in a nuclear emulsion. If we assume that the presence of three or four grains is sufficient to reliably identify the track of a slow Auger electron in an emulsion with a low background grain density, then we can only identify Auger electrons with energies greater than 20-25 keV, and below 20 keV

there is a very rapid reduction in the detection efficiency. Hence although nuclear emulsions can be used to detect Auger electrons with energies above 20 keV, measurements of their energy spectra are only qualitative.

We shall now review the main experimental data on Auger electrons observed in nuclear emulsions. The first such observations were carried out by Cosyns et al. [28], Bonetti and Tomasini [29] and Fry [30]. The first two papers used slow cosmic-ray muons stopping in emulsions. Fry used negative muons from the decay in flight of negative pions from an accelerator. The energy spectrum he obtained is shown in Fig. 4.19. Of 1000 stopping muons observed in the emulsion 358 produced visible tracks of decay electrons, and only 32 gave rise to visible stars. There were 17 slow electrons among the 358 $\mu^- \rightarrow e^-$ decays, most of which occurred after the capture of the negative muons by light nuclei in the emulsion. Of the remaining 610 events, 355 were ρ events which were not accompanied by the appearance of a visible secondary track. In 180 cases there was a single track of a slow electron, in 57 cases two such tracks, and in 18 cases three tracks.

Weissenberg [31] and Pevsner et al. [32] carried out a more detailed study of mesonic-atom Auger transitions in nuclear emulsions, in connection with the problem of the low X-ray yield from the K and L shells of mesonic atoms of light nuclei. The first of these papers reported an analysis of 600 stars produced as a result of negative-muon capture by light nuclei in the nuclear emulsion. The presence of a

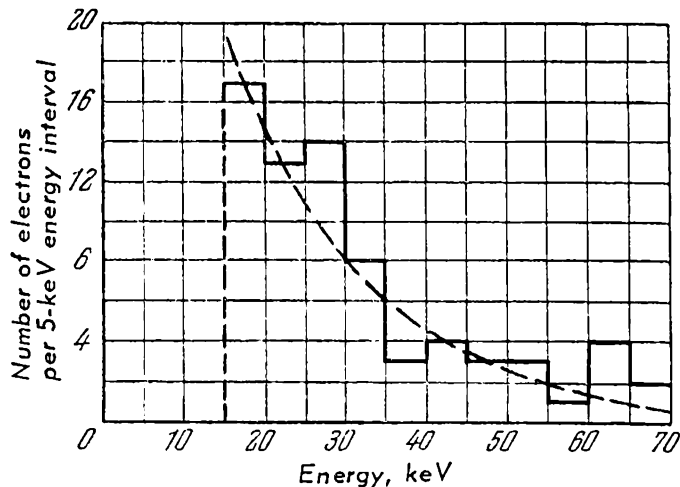


Fig. 4.19 Spectrum of Auger electrons due to stopping negative muons in an emulsion (Fry)

visible track due to the recoil nucleus in such stars was used to identify them with negative-muon capture by light nuclei. Among the 600 stars there were only two cases with Auger electrons having energies of approximately 20-25 keV. It is interesting to compare this result with the theoretically predicted number of Auger electrons. This can be done by using the calculated Auger-electron yield for mesonic atoms of C, N and O reported by Eisenberg and Kessler [21], and by assuming the validity of the Z law of Fermi and Teller for the distribution of stopping negative muons among light emulsion nuclei. If it is assumed that Auger electrons with energies greater than 20 keV can be effectively detected, the expected number of Auger electrons is about 5-10, which agrees with the experimental result to within the statistical error. If the deficiency in the X-ray yield was of the order indicated by the experiments of Stearns and Stearns, and was compensated by a corresponding increase in the Auger-electron yield, then one would expect about 200 low-energy Auger electrons. It may therefore be concluded that the yield of Auger electrons from light mesonic atoms in the emulsion is in qualitative agreement with the value predicted by the theory of non-radiative transitions. A similar conclusion was reached by Pevsner et al. [32].

The above data on Auger electrons are largely qualitative, but they do nevertheless indicate the absence of appreciable anomalies in the emission of Auger electrons by light and heavy muonic atoms in emulsions. This throws doubt on the validity of the deficiency of radiative transitions detected by Stearns and Stearns in the K and L shells of light mesonic atoms, especially since the subsequent work of Lathrop et al. reduced this effect by approximately one order of magnitude.

4.3 PRODUCTION OF μ^+, μ^- PAIRS BY PHOTONS

If the interaction of muons and electrons with the electromagnetic field is basically the same, then the well-known formulae of Bethe and Heitler for the electron-positron pair production cross-section should also be valid for μ^+, μ^- pair production. All that is necessary is to reduce the cross-section in the ratio $(m_e/m_\mu)^2 \approx (1/207)^2$, and take into account the nuclear form factor. The latter modification is due to the fact that there is a large momentum transfer to the nucleus during the meson pair production process. In fact,

even if the μ^+ , μ^- pair production occurs near the threshold, the momentum transfer to the nucleus is about $200 \text{ MeV}/c$. The de Broglie wavelength corresponding to this minimum momentum is

$$\lambda_q = \frac{h}{q} = \frac{1.865 \cdot 10^{-13}}{q/m_\mu c} \text{ cm} \quad (4.8)$$

which is less than the dimensions of the nucleus. The corresponding cross-sections have been calculated by Rawitscher [33] on the assumption that the nuclear charge is uniformly distributed in a sphere of radius $R_0 = 1.20 \times 10^{-13} A^{1/3} \text{ cm}$. The final result may be written in the form

$$\frac{d^2\sigma}{d\Omega dE} = \left(\frac{m_e}{m_\mu}\right)^2 \left(\frac{1}{2\pi}\right) \bar{\Phi} \left(\frac{1}{m_\mu c^2}\right) T \quad (4.9)$$

where $d^2\sigma/d\Omega dE$ is the cross-section for μ^+ , μ^- pair production for which one of the components has a fixed energy E and is emitted at an angle of 10° to the γ -ray beam, $\bar{\Phi} = \left(\frac{Z^2}{137}\right)$, $r_0^2 = Z^2 \cdot 5.793 \cdot 10^{-28} \text{ cm}^2$, (r_0 is the classical radius of the electron), $m_\mu c^2 = 106 \text{ MeV}$ is the rest energy of the muon and T is a function representing the effect of the nuclear form factor which depends on the photon energy. T is plotted as a function of photon energy in Fig. 4.20. The two families of curves shown in this figure correspond to the production of muons with energies of 101.0 and 251.9 MeV, which in turn correspond to γ -ray energy thresholds of 312.6 and 463.4 MeV respectively. The graph shows the variation of T for a point charge and for nuclei with mass numbers $A = 27, 63, 207$ and 238 . It is evident that the nuclear form factors have an important effect on the cross-section. The ordinates of the curves multiplied by

$$\bar{\Phi} \left(\frac{1}{207}\right)^2 \left(\frac{1}{2\pi}\right) \left(\frac{1}{106}\right) = Z^2 \cdot 2.0346 \cdot 10^{-35} \text{ cm}^2/\text{MeV}$$

yield the cross-sections for the production of meson pairs and are found to be lower by 6-7 orders of magnitude than the cross-sections for the electron-positron pair production, i.e. are very small.

The first experiments in which muon pair production by photons was observed were carried out by Masek and

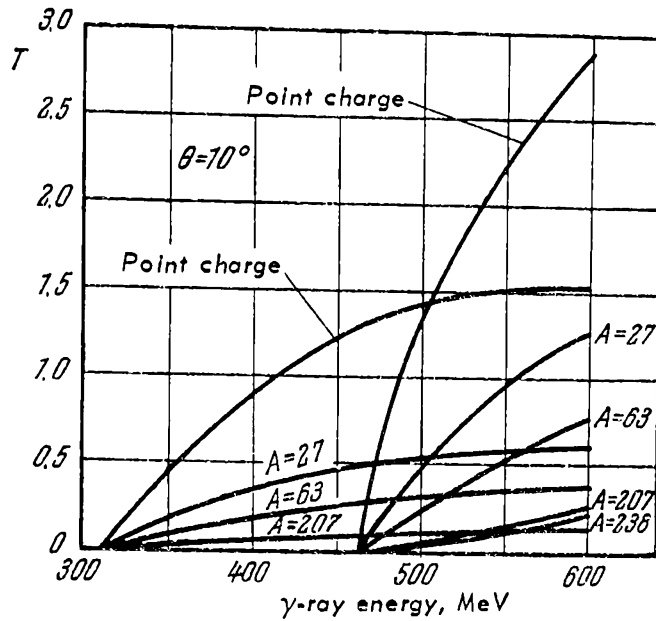


Fig. 4.20 Cross-section for μ^+ , μ^- pair production by photons. The left-hand family of curves corresponds to a muon energy of 101.0 MeV; the right-hand family corresponds to a muon energy of 251.9 MeV. In all cases the angle between the momenta of the photon and of the observed muon is 10°

Panofsky [34] and Masek et al. [35], using the Stamford linear electron accelerator. An electron beam with energy of 450, 575 or 600 MeV traversed an aluminium target. Bremsstrahlung photons produced muon pairs in the target, and the experiment consisted of recording negative muons leaving the target. The experiment is illustrated in Fig. 4.21, which shows the direction of the electron beam, the aluminium target and the channel in the magnetic field for the transmission of the negative muons. Charged particles emitted from the target at 10° to the γ -ray beam (approximately 30° in another experiment) entered a deflecting magnet and, after passing through a channel in this magnet and through an absorber A_2 , struck absorber A_3 which was sufficiently thick to stop muons which had been deflected through the channel. The mesons came to rest and decayed in A_3 and their decay electrons were recorded by a scintillation counter telescope.

The distribution of decays over the channels of the delayed coincidence system was used to determine the muon lifetime, and hence to verify that the system was recording muons. Although this method is very simple in itself, it leads to

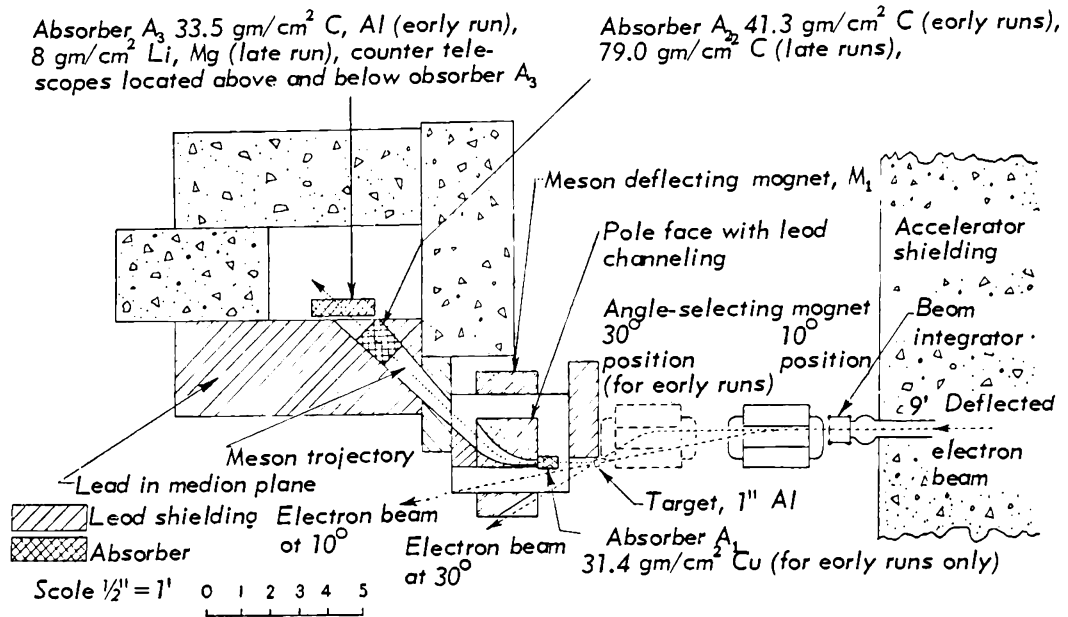


Fig. 4.21 μ^+ , μ^- pair production by photons (Masek and Panofsky). The electron beam from a linear accelerator is deflected by the magnet on to the aluminium target. The trajectory of the observed muon is indicated by the broken line (the muon is produced by bremsstrahlung photons)

considerable practical difficulties, the most important being that the measured effect was small by comparison with the muon background due to $\pi \rightarrow \mu$ decays in the target, in the absorber A_1 and in its immediate neighbourhood. $\pi \rightarrow \mu - e$ decays in the target itself were excluded by the fact that only negative muons were recorded: negative pions stopping in the target were captured by the nuclei and therefore could not produce negative muons. To reduce the background due to $\pi \rightarrow \mu$ decays in flight, the absorber A_2 was introduced to stop pions emerging from the magnet channel. Another source of background was the appreciable number of neutrons which accompanied each electron pulse. These neutrons were moderated for a few microseconds and could enter the scintillation counters of the electron telescope and be counted as a result of the conversion of γ rays from (n, γ) reactions. In order to reduce this background, A_3 was made of either carbon or aluminium or, in another variant of the experiment, of lithium or magnesium. Since the μ^- -capture probability for a light nucleus is proportional to the fourth power of the nuclear charge, a change of a carbon target ($Z = 6$) for an aluminium target ($Z = 13$) of the same stopping power should considerably reduce the effect (by a factor of more than 8) without affecting the background. In

this way it was possible to separate negative-muon decays from the neutron background.

The measurements were carried out by a relative method: a determination was made of the ratio of the μ^- production cross-section to the cross-section for the photo-production of positive pions. This was due to difficulties in the absolute calibration of the instrument. The cross-section for the photo-production of positive pions is almost isotropic in the angular range $10-30^\circ$, whilst the cross-section for muon pair production was expected to be strongly anisotropic. For example, it should fall by a factor of 2 between $10-30^\circ$. Hence practically the entire effect measured at large angles was due to the muon background from the decay in flight of pions produced by the photons. The muon production cross-section was therefore determined as follows.

For a given (small) angle and given currents in the coils of the deflecting magnets, two measurements were carried out with the absorber A_3 having first a small and then a large nuclear charge (Al followed by C or Mg followed by Li). The difference in the counts obtained with the two absorbers is a measure of all effects leading to the production of negative muons. To reduce the background due to $\pi - \mu$ decays in flight, it is necessary to subtract the corresponding difference obtained at large angles. The production cross-section for muons at, say, 10° was thus determined by measuring the following cross-section differences: difference for 10° (C - Al) less the difference for 30° (Ca - Al) or the same for the Mg - Li differences.

The results obtained for an aluminium target and photons with a maximum energy of 600 MeV are given below. The cross-section difference $\Delta\sigma_\mu$ for negative-muon production at 10° and 30° and at 12° and 23° obtained in two series of measurements for 190-MeV negative muons was found to be

$$\begin{aligned}\Delta\sigma_{\mu \text{ exp}}(10-30^\circ) &= (11.39 \pm 4.99) \cdot 10^{-34} \text{ cm}^2/\text{sterad MeV} \\ \Delta\sigma_{\mu \text{ exp}}(12-23^\circ) &= (7.64 \pm 4.58) \cdot 10^{-34} \text{ cm}^2/\text{sterad MeV}\end{aligned}$$

For 210-MeV negative muons the result was

$$\Delta\sigma_{\mu \text{ exp}}(12-23^\circ) = (5.84 \pm 1.86) \cdot 10^{-34} \text{ cm}^2/\text{sterad MeV}$$

whilst the corresponding theoretical values predicted by

Rawitcher [40a] are

$$\begin{aligned}\Delta\sigma_{\text{theor}} &= 5.6 \cdot 10^{-31} \text{ cm}^2/\text{sterad MeV} \\ \Delta\sigma_{\text{theor}} &= 4.3 \cdot 10^{-34} \text{ cm}^2/\text{sterad MeV} \\ \Delta\sigma_{\text{theor}} &= 4.7 \cdot 10^{-34} \text{ cm}^2/\text{sterad MeV}\end{aligned}$$

The average ratio of the measured to calculate cross-sections can be shown from these data to be

$$\frac{\Delta\sigma_{\text{exp}}}{\Delta\sigma_{\text{theor}}} = 1.42 \pm 0.34$$

This result was substantially improved by Alberigi-Quaranta et al. [36] using the Frascati electron synchrotron which produces 1-GeV electrons. Alberigi-Quaranta observed μ^+ , μ^- pairs produced by bremsstrahlung photons in graphite at about 10° to the direction of the photon beam. The momentum of the negative muons exceeded 446 MeV/c, while the momentum of the positive muons selected by the magnetic spectrometer lay in the range 330-393 MeV/c. The ratio of the experimental to the theoretical muon pair production cross-section was found to be

$$\frac{\Delta\sigma_{\text{exp}}}{\Delta\sigma_{\text{theor}}} = 1.00 \pm 0.05$$

An important advance in the region of high momentum transfers to the muon pair was recently achieved by DePachter et al. [71] who used the bremsstrahlung beam (maximum energy of 5 GeV) from the Cambridge electron accelerator. The muon pair was recorded by two identical telescopes located symmetrically on either side of the γ -ray beam (Fig. 4.22). The counters shown in the figure were in fact composite hodoscopic systems of 154 counters. The hodoscopic system was capable of separating the polar angle range defined by the telescope (4.5 - 11.5°) into nine equal intervals, and the ranges of the muons into five intervals corresponding to energies between 1.8 and 2.4 GeV. The transferred momentum region corresponding to q^2 between 1.3 and 8.0 F^2 was investigated. In this region of q^2 , the ratio of the measured to expected muon pair production cross-section is

$$\frac{\Delta\sigma_{\text{exp}}}{\Delta\sigma_{\text{theor}}} \approx 1.18 \pm 0.15$$

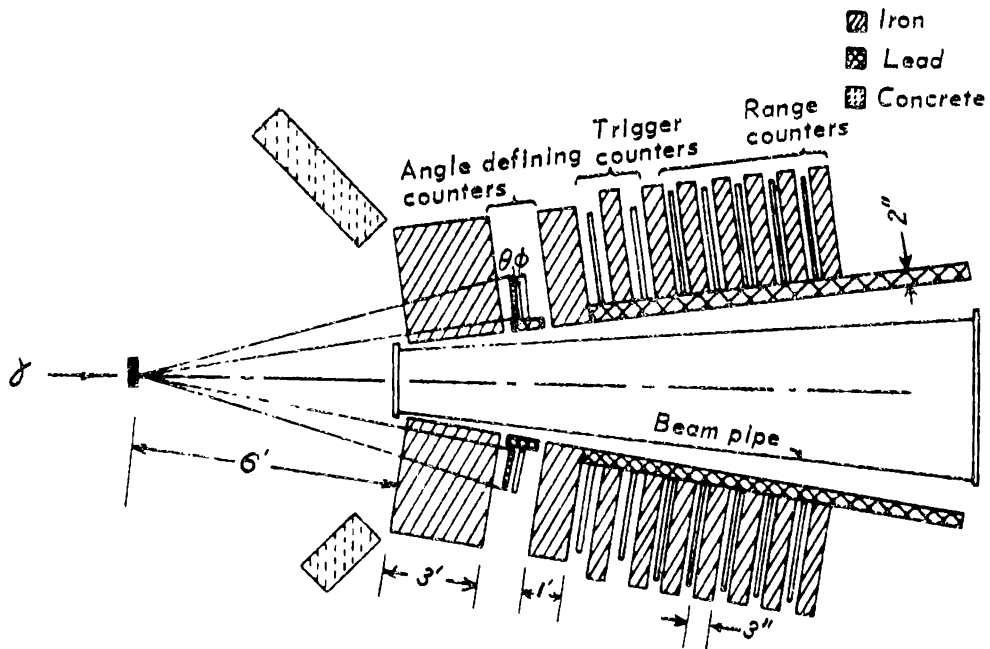


Fig. 4.22 Measured muon pair production cross-section [71] (Cambridge electron accelerator)

It is thus evident that the measured production cross-section is in agreement with the electromagnetic theory throughout the range of transferred momenta which was investigated (200 MeV/c to 1 GeV/c approximately).

4.4 SCATTERING OF MUONS BY NUCLEI

The scattering of high-energy muons by nuclei is very easy to observe and shows that the electromagnetic interactions of fast muons are identical with the electromagnetic interactions of fast electrons. Hoffstadter et al. [37] have measured the scattering of electrons by nuclei for large momentum transfers up to electron energies of about 1 GeV. Experiments involving muons may therefore be reduced to the comparison of the scattering of muons by nuclei with the scattering of electrons. In practice this means that in comparing the experimental data on muon scattering with theoretical predictions, one must use the electron-nucleon and electron-nucleus form factors obtained from electron-scattering data. If muon-scattering data turn out to be in agreement with a scattering theory in which the structure

of the nucleon and of the nucleus is deduced from electron experiments, one can conclude that the electron and meson form factors are the same, i.e. that both the electron and the muon interact in the same way with the electromagnetic field of the nucleus.

A large number of scattering experiments involving high-energy muons have been carried out during the last decade. Most of them were performed with cosmic rays, and only a few with high-energy muons produced by accelerators.

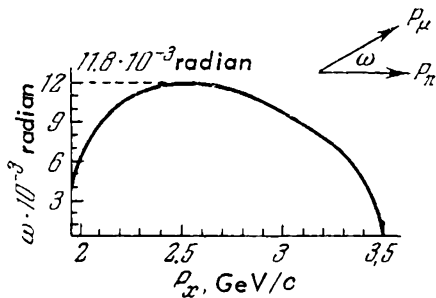
Many of the cosmic-ray experiments indicated the existence of the 'scattering anomaly', i.e. scattering which cannot be described within the framework of the usual electromagnetic interaction between the muon and the nucleus. However, other very careful experiments with cosmic-ray muons did not show the presence of this anomaly. A detailed review of all these experiments has been given by Fowler and Wolfendale [38]. An analysis of cosmic-ray data on the anomalous scattering of muons shows that, whenever this scattering was observed, it was not possible to reduce completely the background of particles which interacted strongly with nuclei (protons, pions and other nuclear-active particles). Moreover, high-energy muon scattering using cosmic-ray muons is subject to considerable errors due to uncertainties in the momentum of the incident muon, and finally the statistics of all these measurements have in general been exceedingly poor. It may therefore be concluded that there is no definite evidence for the existence of anomalies due to non-electromagnetic interactions between muons and nuclei.

The production of high-energy muon beams by accelerators enabled these experiments to be repeated under much improved conditions, i.e. with accurately known muon energy, good geometry and the absence of particle impurities in beams whose intensity was higher than the cosmic-ray intensity by several orders of magnitude.

The muon beams are usually produced in basically the same way. First, a high-intensity pion beam is produced, and the muons originating in pion decays in flight are collected and focused by magnetic fields. The production of high-intensity pure muon beams is facilitated by the fact that a muon is a relatively long-lived particle ($\tau \sim 2.2 \times 10^{-6}$ sec), whilst the mean life of the pion is lower than this by two orders of magnitude. Therefore, if one forms a muon beam from pion decays over a large path length,

most of the pions will be removed by decays at the end of the path. If muons of given momentum can then be collimated by magnetic fields, it is possible in principle to produce a pure muon beam.

Let us consider the 2-GeV muon beam of the Berkeley Bevatron which is a 6.3-GeV proton synchrotron [39]. The muon beam is derived from a high-intensity pion beam of 3.5 ± 0.3 GeV/ c , and magnetic analysis is used to separate muons with momenta of 2 GeV/ c from the main pion beam. The kinematics of $\pi \rightarrow \mu$ decay for a 3.5-GeV/ c pion is shown in Figs. 4.23 and 4.24. Fig. 4.23 shows the dependence of the angle of emission of the muon in the laboratory



ω – angle between the pion and muon momenta in the laboratory system

Fig. 4.23 Kinematics of a π - μ decay for 3.5-GeV/ c pions

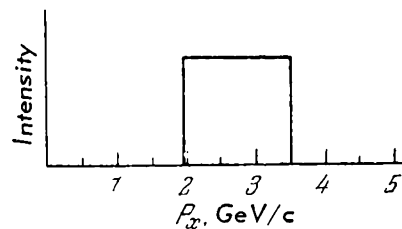


Fig. 4.24 Kinematics of π - μ decay for 3.5-GeV/ c pions. Muon momentum spectrum in the laboratory system

system on the muon momentum, whilst Fig. 4.24 shows the muon momentum spectrum in the laboratory system. It is evident that the muon beam is collimated in the direction of the primary pion beam (the maximum angle of emission of a muon in the laboratory system is $\pm 0.68^\circ$) and is uniformly distributed in momentum between the minimum of about $0.6 P_\pi$ corresponding to a backward decay in the pion system, and the maximum of 3.5 GeV/ c , which is taken up by a muon emitted in the direction of the primary pion.

The experimental arrangement at the Bevatron is shown in Fig. 4.25. The target T_1 intercepts the proton beam and serves as the source of pions. Magnets M_1 and M_2 and quadrupoles Q_1 and Q_2 select and focus pions with momenta of 3.5 GeV/ c leaving target T_1 . About 6% of the 3.5-GeV/ c pions decay in the space between M_2 and the deflecting magnet M_3 which separates 2-GeV/ c muons from the main 3.5-GeV/ c pion beam. Magnet M_4 produces further clearing of

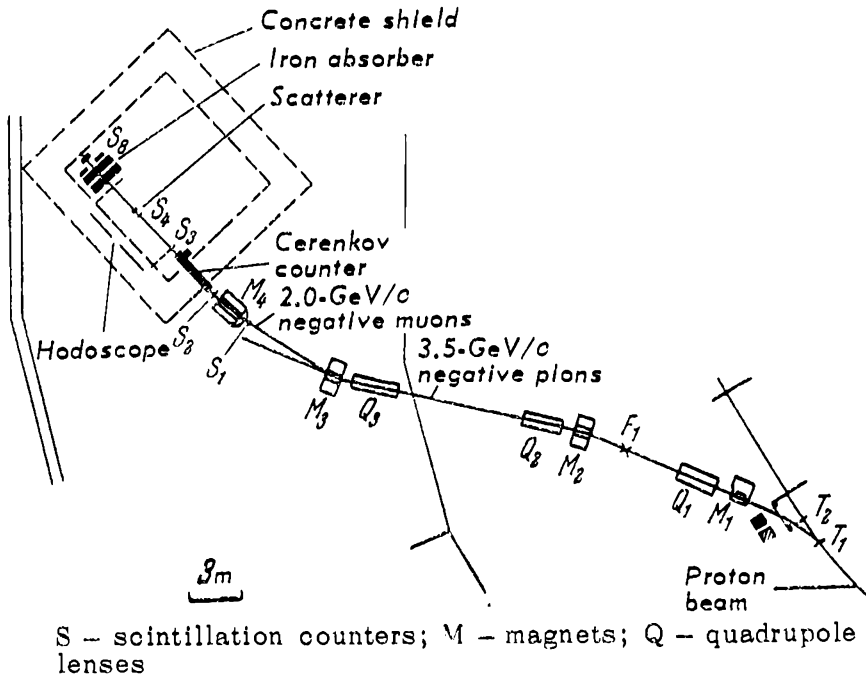


Fig. 4.25 Arrangement for producing the 2-GeV/c muon beam with the Berkeley bevatron. This beam has been used to measure muon scattering for momentum transfers up to about 0.4 GeV

the muon beam and deflects pions which have entered the beam through scattering, and electrons originating in $\mu - e$ decays in flight. Electrons lose energy by producing cascade showers in an 0.6-cm lead plate placed in front of magnet M_4 and are deflected out of the beam.

The pion impurity in the beam thus produced is not more than 3%, but this has an appreciable effect on muon-scattering studies. The differential Coulomb cross-section for muons on nuclei in the energy range between 2 and 3 GeV is of the order of 10^{-28} cm²/sterad, whilst the differential cross-section for pions is of the order of 10^{-25} cm²/sterad. Hence to ensure that the background from the scattering of pions should be less than 10% of the expected effect due to muons, the pion impurity must be less than 1 in 10^4 .

An iron filter, 105-cm thick, was used to remove the remaining pions from the muon beam. The thickness of this filter is about 7 radiation lengths for pions, whilst the energy spread of 2-GeV/c muons due to ionization losses in the filter is not more than 0.15 GeV. In addition, a gas-filled Cerenkov counter was placed in the beam, and used to exclude particles with velocities smaller than the velocity of 2-GeV/c muons. These measures succeeded in reducing

the relative proportion of pions in the beam to about 5×10^6 . A chamber designed for studying the scattering of muons by nuclei was placed in the path of the final focused muon beam. The chamber used by Masek et al. [39] is shown on an enlarged scale in Fig. 4.26. It forms a hodoscope consisting of scintillation counters in four identical blocks A_A , A_B , A_C and A_D . Each block consisted of 20 scintillators arranged as shown in the upper part of the drawing. Scintillator blocks A_A and A_B defined the direction of the muon before it entered the scattering target (lead or carbon) placed immediately behind A_B , whilst blocks A_B and A_C or A_B and A_D defined the direction of the scattered muon. Each of the scintillators was viewed by its own photomultiplier. Pulses from the photomultipliers were fed into a delay line, and finally to the deflecting plates of a quadrupole-beam oscilloscope whose screen was photographed.

The identification of scintillators traversed by the muons in blocks A_A , A_B , A_C and A_D was achieved by measuring the delay of the pulses relative to a gating pulse. This was produced by coincidences between S_1 , S_2 , S_3 , S_4 and S_5 or S_6 . Pulses from the Cerenkov counter C and the shielding counters S_7 and S_9 , which excluded events in which the muon was accompanied by high-energy δ rays, were also photographed from the screen of the oscilloscope. Counters C and

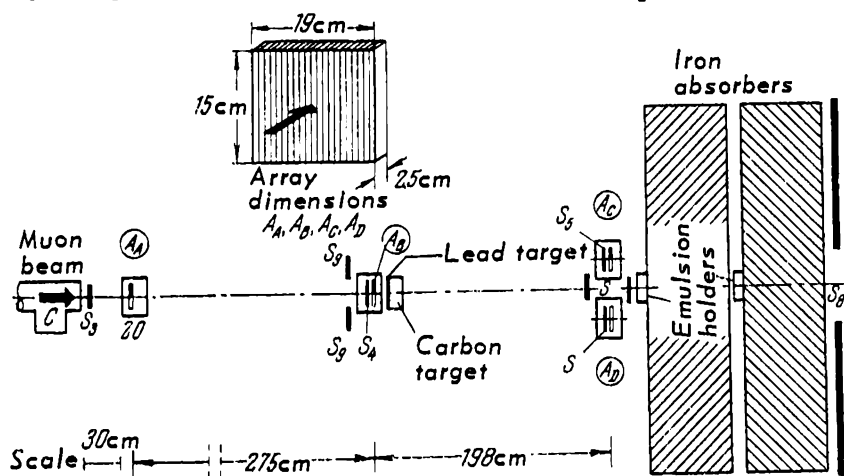


Fig. 4.26 Scattering chamber for 2-GeV/c negative muons: A_A , A_B , A_C and A_D are hodoscope scintillation counter arrays. Each system consists of 20 scintillators (cf. upper part of the figure in which the arrow indicates the direction of the muon beam). A lead or graphite target was placed behind A_B . The shielding counter S^9 surrounds S^4 ; C is the Cerenkov counter.

S_8 were used to exclude the pion impurity in the muon beam. The system permitted the detection of scattered muons in the angular range between 2° and 14° . In addition, nuclear emulsions were placed in the muon beam as indicated in Fig. 4.26. They were used to determine the angular distributions between 0.5° and 3° .

734 m of track were followed in nuclear emulsions exposed to the 2-GeV/c negative-muon beam. Departures of the projection of the muon track on the plane of the emulsion

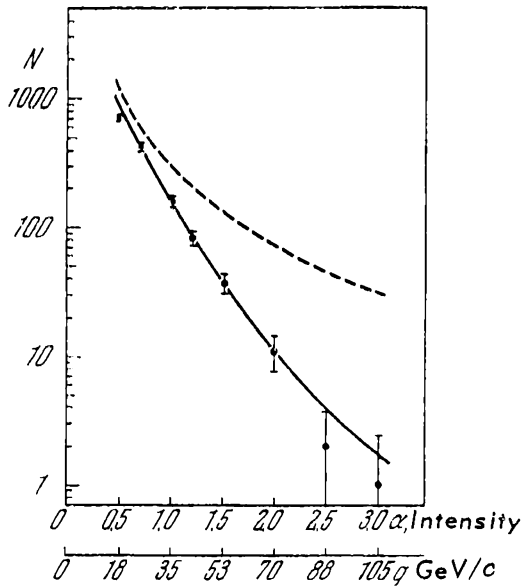


Fig. 4.27 Scattering of 2-GeV muons in a nuclear emulsion. The number of scatters through an angle greater than a given angle is plotted as a function of the projected angle of scattering α in degrees, and the momentum transferred to the nucleus in MeV/c. Broken curve shows single scatters by a point nucleus; solid curve shows single scatters by an extended nucleus

from a straight line were measured and the results are shown in Fig. 4.27, where the number of scatters through an angle greater than ϑ is plotted as a function of the projected angle ϑ . These data cover the angular range between 0.5 - 3.0° , which corresponds to a transferred-momentum range ($\Delta q = 2p \sin \vartheta / 2$) between 18 and 105 MeV/c. The experimental results are compared with the theory of single scattering by point and by extended nuclei. If the magnetic interaction is neglected, the cross-section for a point nucleus is given by the usual Mott formula [37] obtained on the Born approximation:

$$\sigma(\vartheta) = \frac{1}{4} Z^2 \left(\frac{e^2}{p\nu} \right)^2 \frac{\cos^2 \frac{\vartheta}{2}}{\sin^4 \frac{\vartheta}{2}} \left[1 + \frac{2p\nu}{Mc^2 \sin^2 \frac{\vartheta}{2}} \right]^{-1} \quad (4.10)$$

where ϑ is the angle of scattering in the laboratory system, p and v are the momentum and velocity of the muon respectively, and Z and M are the charge and mass of the target nucleus respectively. This formula is represented by the broken curve in Fig. 4.27. It is evident that at angles between 0.5 - 3.0° scattering by a point nucleus is not a realistic approximation. The formula is considered here, however, because experiments on the multiple scattering of cosmic-ray muons have been found to agree with the Molière distribution for a point nucleus based on (4.10).

To evaluate scattering by an extended nucleus, the Mott formula was multiplied by the proton form factor $F_p^2(q^2)$ and by the nuclear form factor $F_N^2(\vartheta)$. The function $F_p(q^2)$ was equated with the proton form factor obtained from Hoffstadter's experiments on electron-proton scattering:

$$F_p = \left[1 + \frac{q^2 a^2}{12} \right]^{-2} \quad (4.11)$$

where q is the transferred momentum and $a = 0.7 \times 10^{-13}$ cm. The Cooper-Rainwater approximate expression [41] was used for the nuclear form factor $F_N(\vartheta)$. The resulting angular distribution is indicated by the solid curve in Fig. 4.27, which is clearly in good agreement with the experimental distribution.

The fact that experimental data are in good agreement with theories based on the proton and nuclear form factors deduced from electron-scattering experiments has also been confirmed by Conolly et al. [40], who studied the scattering of positive and negative muons in nuclear emulsions. They used a 27-MeV muon beam and looked for the ends of muon tracks ($\mu^+ \rightarrow e^+$ decays) in that region of the emulsion which could only be entered by scattered particles. By following such tracks back until a scatter was found, they succeeded in examining events with momentum transfers up to about 160 MeV/c.

The single-scattering emulsion measurements were extended to large angles and larger values of transferred momentum by means of scintillation counter hodoscopes. In these experiments, the target was either graphite (27 g/cm²) or lead (14.4 g/cm²). Measurements with graphite target are the more important because the experimental conditions were such that single scatters predominated.

For example, at a scattering angle of 2.3° , the expected contribution due to multiple scattering was 25%. At an angle of scattering of 8° , the multiple-scattering contribution was only 2%.

Experimental data obtained with the carbon target are shown in Fig. 4.28. A full theoretical analysis of the data is difficult because in this particular case the apparatus recorded both elastic and inelastic scattering. The effective scattering cross-section has been given by Masek et al. [39]:

$$\frac{d^2\sigma}{d\Omega dp'} = \frac{z^2 e^4}{4E^2} \frac{\cos^2 \frac{\vartheta}{2}}{\sin^4 \frac{\vartheta}{2}} \left\{ Q(q^2, \Delta E) + \tan \frac{\vartheta}{2} \left[\frac{q^2}{2M} R(q^2, \Delta E) \right] \right\} \quad (4.12)$$

where $d^2\sigma/d\Omega dp'$ is the cross-section for scattering through an angle ϑ into a solid angle element $d\Omega$ in which the momentum of the scattered muon is p' . The quantities E and p are respectively the energy and momentum of the muon before the scatter and

$$\begin{aligned} \Delta E &= E - E' \\ q^2 &= |\mathbf{p} - \mathbf{p}'|^2 - (\Delta E)^2 \end{aligned} \quad (4.13)$$

We thus see that ΔE is the energy lost on collision and q^2 is the square of the transferred four-momentum. The functions Q and R , which depend only on ΔE and q^2 , contain all nuclear factors which influence scattering. Among them is the electromagnetic structure of the nucleus, magnetic scattering and the nuclear form factor. These functions were estimated by Drell and Schwartz [42] and correctly describe the scattering of electrons by nuclei. This has been verified, for example, by Friedman [43], who studied the scattering of 600-MeV electrons by deuterons and found excellent agreement between experimental data and the calculations of Drell and Schwartz [42].

The experimental data are compared with the theory in Fig. 4.28, from which it is evident that the scattering of muons by carbon is in agreement, within the experimental error, with the theoretical formula based on the electron-proton form factors and nuclear-structure data obtained from high-energy electron scattering.

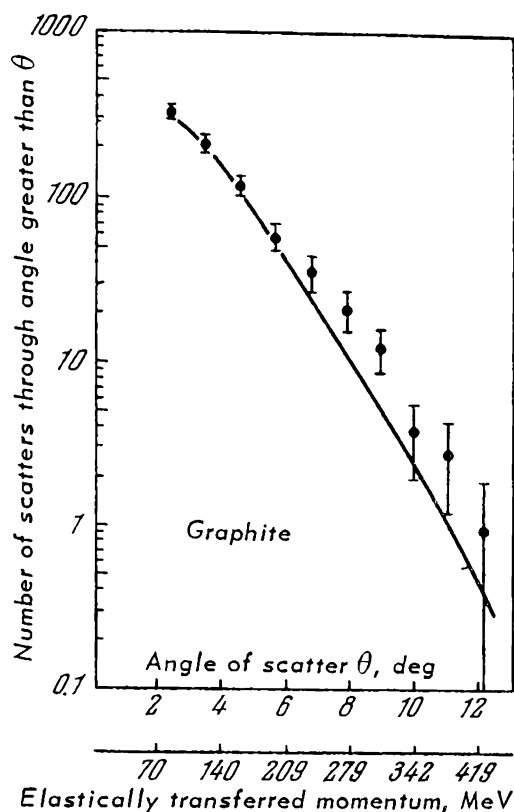


Fig. 4.28 Scattering of 2 GeV/c muons in 27 g/cm² of graphite. The solid curve was calculated from (4.12)

The absence of anomalous scattering of muons has also been indicated by studies of the scattering of muons in lead. Here, however, multiple scattering predominates, and these data are less reliable.

Masek et al. [42] performed a direct comparison of the scattering of electrons in graphite with the above data on the scattering of 2-GeV/c negative muons in graphite. Experiments on the scattering of electrons in graphite were designed to determine directly the form factors Q and R for two values of the angle of scattering of the negative muons (5.73° and 8.03°), corresponding to momentum transfers in elastic collisions of 200 and 280 MeV/c. These experiments also confirmed the absence of anomalies in the scattering of muons by nuclei.

Citron et al. [73] investigated the scattering of negative-muons by graphite up to transferred momenta of about 250 MeV/c ($q^2 \approx 1.5F^2$). This work was performed on the CERN muon beam and was distinguished by high statistical accuracy (7-13%) of the measured scattering cross-sections.

The results obtained are also in good agreement with the scattering cross-section calculated from the Mott formula.

Let us now consider recent work on muon-proton scattering (liquid-hydrogen target). Davis et al. [74] and Cool et al. [75], who performed these experiments, did not find any difference between muon and electron scattering. The idea of these experiments will be clear from an examination of Fig. 4.29. The figure shows a hydrogen target and two large spark chambers for the recoil proton and the scattered muon. Four threshold Cerenkov counters in the muon beam (the last of these can be seen in Fig. 4.29) were used to separate the pions from the muons by an electronic technique. Identification of elastic events required a knowledge of the muon momentum ($\pm 1\%$), the muon and proton scattering angles (better than 1%) and the kinematics of events (coplanarity, kinematic criteria). Fifty-nine scattering events were observed in which the transferred momenta lay in the range 450-850 MeV/c. Cool et al. performed their experiments on the Brookhaven accelerator, using a similar technique. They achieved better statistics: 500 scattering events were observed in the transferred-momentum region between 700 and 1100 MeV/c.

The results obtained by both groups are shown in Fig. 4.30, where the measured cross-section is plotted as a function of q^2 . The solid curve shows the expected scattering and was obtained from the formula

$$\frac{d\sigma}{dq} = \frac{4\pi\alpha^2}{q^4} \frac{G(q^2)}{1 + q^2/4M^2} (1 - q^2/2MP_0 + \dots)$$

where a is the fine-structure constant, q the transferred momentum, M the proton mass, and P_0 the primary muon momentum. We note that the expected cross-section is determined by the transferred momentum and is not very dependent on P_0 . The function

$$G(q^2) = G_E^2 + (q^2/4M^2) G_M^2$$

is determined by the proton form factors G_E and G_M . The solid curve was obtained for values of G_E and G_M deduced from data on electron-proton scattering. They were calculated by averaging over the primary particle momentum P_0 . We thus see that muon scattering in this range of transferred momenta is again very similar to electron scattering.

In conclusion, let us consider the above estimation of the

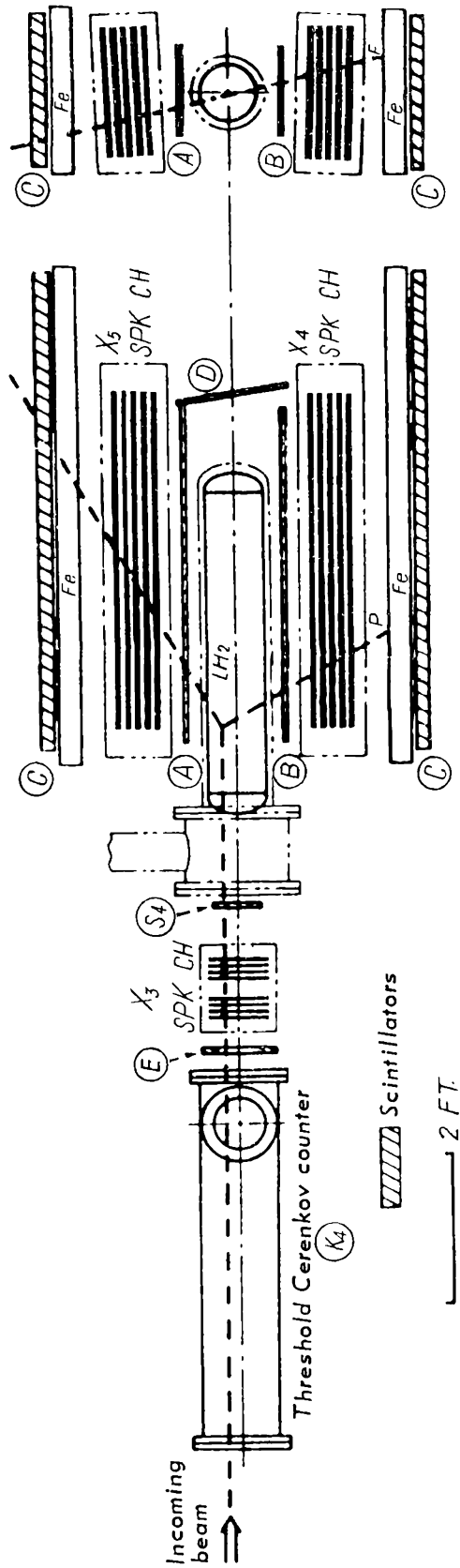


Fig. 4.29 Experiment of Davis et al. [74] on muon-proton scattering. The scattered muon left the instrument and the recoil proton from the liquid-hydrogen target came to rest in the iron absorber. The spark chambers X₃, X₄, and X₅ were used to verify the kinematics of the events and to select cases of elastic scattering.

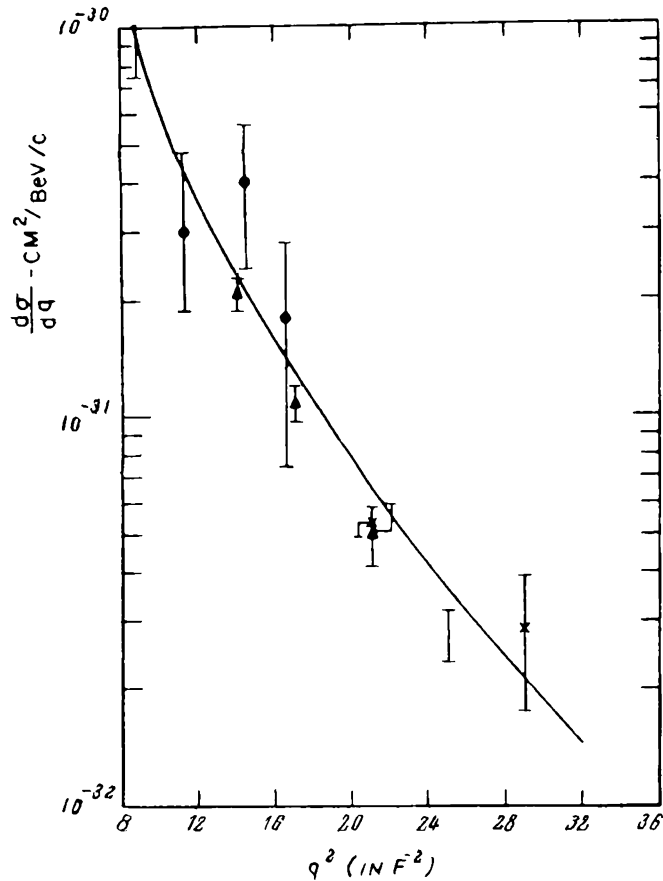


Fig. 4.30 Dependence of the muon scattering cross-section on the square of the transferred momentum. Solid curve shows calculated results assuming that the form factor ratio $G_M/G_E = \mu$ is equal to the value obtained from electron-scattering experiments

possible difference between the electromagnetic muon and electron form factors. If it is admitted that the lepton form factor can be written in the form

$$f(q^2) = 1 / (1 - q^2/\Lambda^2)$$

the muon-to-electron form factor ratio is

$$f_\mu / f_e = 1 / (1 - q^2/D^2)$$

where $1/D^2 \cong 1/\Lambda_\mu^2 - 1/\Lambda_e^2$ represents the dimensions of the region where the form factor difference becomes significant. From the experiments by Cool et al. we have $|D^2| 7220 F^{-2}$. This corresponds to distances of the order of 6×10^{-15} cm

and transferred momenta approaching $3 \text{ GeV}/c$. These are the limiting values of distances and transferred momenta for which, according to the most recent scattering experiments, we can speak of the identity of the electromagnetic properties of the electron and muon.

4.5 THE MAGNETIC MOMENT OF THE MUON

4.5.1 Preliminary remarks

Recent measurements of the magnetic moment of the muon are extremely accurate, and confirm that the electromagnetic interactions of the muon and the electron are the same. If the muon is in fact a 'heavy electron', its magnetic moment should be given by the Dirac equation. The magnetic moment of a Dirac particle is

$$\mu_0 = \frac{eh}{2mc}$$

This must be corrected for interactions with zero-point electromagnetic fields. Radial corrections have been estimated by Karplus and Kroll [45] and by Sommerfield [46] and Petermann [47] up to the fourth order. Currently accepted theoretical magnetic moments of the electron and muon, calculated with these corrections included, are

$$\mu = \mu_0 \left(1 + \frac{\alpha}{2\pi} - 0.328 \frac{\alpha^2}{\pi^2} \right) = 1.0011596\mu_0 \quad (4.16a)$$

$$(g_e = 2 \cdot 1.0011596)$$

for the electron, and

$$\mu = \mu_0 \left(1 + \frac{\alpha}{2\pi} + 0.75 \frac{\alpha^2}{\pi^2} \right) = 1.0011654\mu_0 \quad (4.16b)$$

$$(g_\mu = 2 \cdot 1.0011654)$$

for the muon. In these expressions the fine-structure constant α has been taken to be $\alpha^{-1} = 137.039$ [48], and the gyromagnetic ratio g is expressed in units of $e/2mc$.

The most accurate direct determination of the magnetic

moment of the electron is due to Schupp et al. [49], who measured the difference between the spin precession frequency and the cyclotron frequency for free electrons. The electrons were polarized by Mott scattering and the left-right asymmetry in a second scattering was used to determine the degree of polarization after traversal of the magnetic field by the electrons. The result,

$$g_e = 2 \cdot (1.0011612 \pm 0.0000024)$$

is in good agreement with the theoretical prediction and the accuracy exceeds by a factor of about 5 the accuracy of determinations of the electron magnetic moment in which the moment was compared with the magnetic moment of the proton.

4.5.2 Measurement of the magnetic moment of the positive muon

Let us now consider experiments in which the magnetic moment of the muon has been determined. The first measurement of the muon magnetic moment was performed by Garwin et al. in their work on the non-conservation of parity in $\pi \rightarrow \mu \rightarrow e$ decay. They determined the precession frequency ω for the muon spin in a magnetic field H :

$$\omega = g \frac{eH}{2m_\mu c} \text{ rad/sec}$$

and hence, knowing the mass m_μ of the muon and the field H , they determined the gyromagnetic ratio. Their result was

$$g_{\mu^+} = 2 \cdot (1.00 \pm 0.01)$$

The spin precession method has also been used by Kessel et al. on the Liverpool synchrocyclotron. They obtained the more accurate result

$$g_{\mu^+} = 2 \cdot (1.002 \pm 0.007)$$

where the uncertainty includes both statistical fluctuations (0.4%), the error in the magnetic field, the uncertainty due to drift in the electronic equipment and the error due to

the uncertainty in the muon mass. It follows that determinations of the muon magnetic moment from precession in a constant magnetic field yield a result which agrees to within 0.7% with the magnetic moment of a particle described by the Dirac equation. However, this is still not sufficient to establish the validity of the formula for the radiative correction to the magnetic moment whose relative magnitude is of the order of $1/1000$.

A further improvement in the value of the muon magnetic moment was achieved by Coffin et al. [51], who used the magnetic resonance method. The asymmetry in the angular distribution of positrons from positive-muon decay was used as an indication of positive-muon spin flip. The experiment is illustrated in Fig. 4.31. The target in which

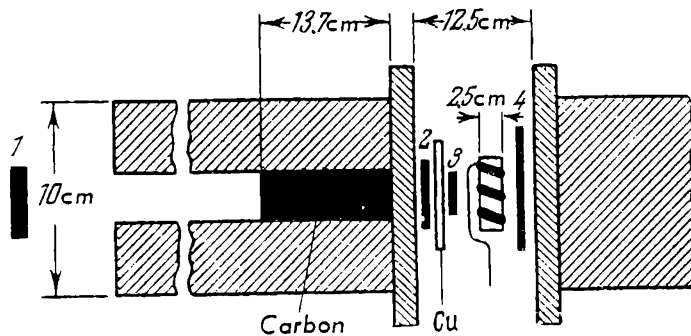


Fig. 4.31 Determination of the magnetic moment of the muon by the magnetic resonance method (Coffin et al.)

the positive muons came to rest was placed in a solenoid in which a high-frequency field was produced. Both the target and the scintillators were placed in a constant magnetic field parallel to the spin of the positive muons. The muons were first slowed down in a graphite absorber placed in a channel in one of the electromagnet poles, and came to rest in the target. Stopping positive muons were indicated by $123\bar{4}$ coincidences. The $123\bar{4}$ pulse was also used to switch on the high-frequency pulse coil and to gate the decay resonance detector. This detector was open for 3μ sec after a 2μ sec interval following the $123\bar{4}$ coincidence. Positrons emitted in the backward direction within the 3μ sec interval were signalled by $231\bar{4}$ coincidences, and recorded by the system. The pulsed radio-frequency field H_1 , which was excited in the solenoid surrounding the target, produced the muon spin flip. At resonance, when the field frequency

in the solenoid was $\omega = g(eH_1/2mc)$ rad/sec, the angle through which the spin rotated in a time t was

$$\vartheta = 1/2 \int_0^t \left(\frac{eH_1}{2mc} \right) dt$$

Rotation through 180° , which from the quantum-mechanical point of view corresponds to 100% probability of transition from state $S_m = \pm 1/2$ to the state $\pm 1/2$, requires a high-

frequency field pulse of $\int_0^t H dt = 70$ gauss μ sec. The system

recorded decay electrons emitted in the backward direction, and therefore the maximum intensity was recorded in the absence of transitions. A reduction in the intensity indicated the onset of magnetic transitions.

The resonance curve obtained in this experiment is shown in Fig. 4.32, in which the number of $123\bar{4}$ counts in the electron telescope per 64 000 stopping positive muons is plotted as a function of the ratio of the proton-resonance frequency to the frequency of the solenoid field. The solid curve shows the calculated shape of the resonance curve. The centre of the experimental distribution from which the resonance frequency was obtained, was found by a least-squares analysis assuming that it was symmetrical about the minimum. The resonance value of f_μ/f_p was found to be 3.1865 ± 0.0022 , and hence, for $m_\mu = 206.86 \pm 0.11$ electron masses we obtain $g_\mu = 2 \times (1.0026 \pm 0.0009)$

A further increase in the accuracy of f_μ/f_p at resonance was achieved by Lundy et al. [52], who used the very effective and ingenious method of 'stroboscopic coincidences'. The principle of this method is as follows. Suppose that a beam of muons polarized in the direction of their momenta is brought to rest at time $t = 0$ in a target placed in a magnetic field which is perpendicular to the muon spin. Suppose further that a counter recording decay electrons is placed at a given distance from the target. As a result of the precession of the spin in the magnetic field, the number of electrons emitted from the target in the direction of the counter is proportional to

$$\exp\left(-\frac{t}{\tau}\right) (1 - a \cos \omega_H t) \quad (4.17)$$

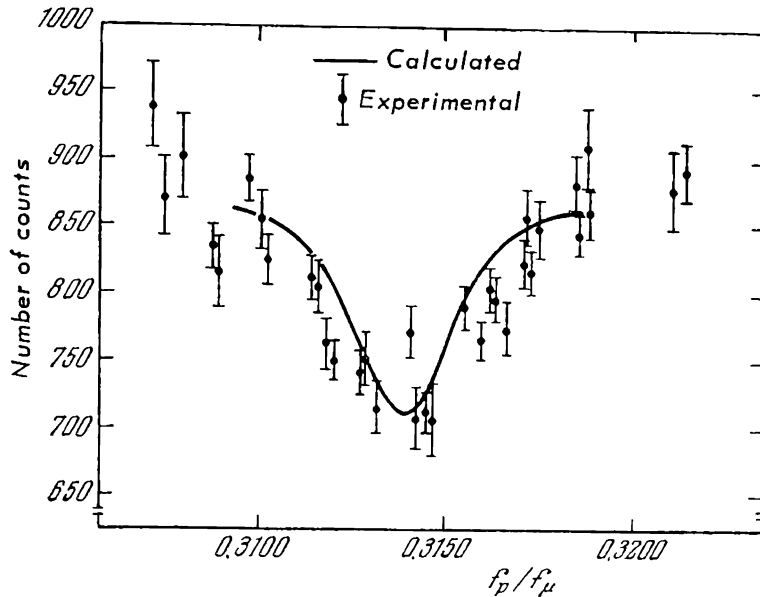


Fig. 4.32 Resonance curve obtained by the magnetic resonance method

where τ is the muon lifetime, a the asymmetry coefficient and $\omega_H = g \frac{eH}{2m_\mu c}$ rad/sec. It follows that the intensity of decay electrons recorded by the counter should be modulated in accordance with (4.17). If the counter is switched on at time $t = 0$ and then periodically with a frequency of $\omega/2\pi$, the counting rate for high-energy electrons will be a maximum when this frequency is equal to the muon spin precession frequency. The experiment is illustrated in Fig. 4.33. The muon beam indicated by the arrow was stopped in the target T (graphite or CHBr_3 ; 8 g/cm^2). The magnetic field, which was produced by a large permanent magnet was perpendicular to the muon beam, and therefore to the muon spin. Muons stopping in the target were indicated by $\overline{123}$ coincidences, whilst decay electrons were indicated by $\overline{234}$ coincidences. The $\overline{123}$ coincidence pulse turned on a 48.63-Mc/s oscillator for $6\ \mu\text{sec}$ and the train of high-frequency oscillations was fed into the parallel inputs of two coincidence systems R and AR, which were sensitive to negative pulses. Other inputs of the coincidence circuits received pulses from counter 3 which were delayed so that a pulse from counter 3 which was simultaneous with a pulse in counter 2 reached R at the centre of one of the early positive half-cycles of the oscillator and AR half a cycle later. When the precession frequency is equal to the oscillator frequency, the pulse due to the decay electron in 3

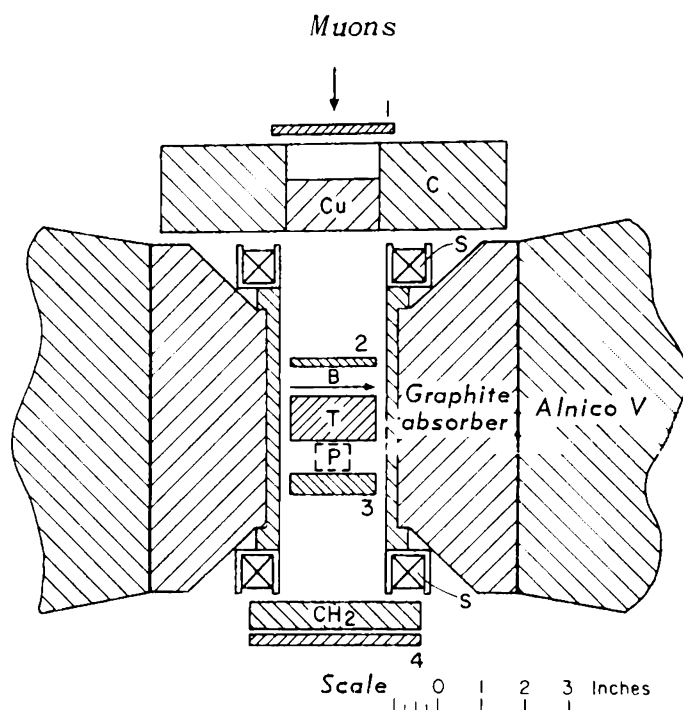


Fig. 4.33 Measurement of the magnetic moment of the muon by the method of stroboscopic coincidences (Lundy et al.). The sample lies just below target T. 1-4 are scintillation counters; the direction of the magnetic field is indicated by the arrow

will produce a coincidence in R but not in AR. Therefore, by measuring the ratio of coincidences in R and in AR as a function of the oscillator frequency, it is possible to determine the resonance frequency which corresponds to a maximum value of this ratio. In fact, the measurements were performed by varying the mean magnetic field of 3700 Oe by $\pm 1\%$ and detecting a resonance in the ratio R/AR. Since the magnetic field was measured by proton resonance, and the muon precession frequency at the peak of the R/AR curve was 48.63 Mc/s, the ratio of the proton resonance frequency at the peak to 48.63 Mc/s gave the ratio of the proton and muon magnetic moments directly. The response curve, in which the coincidence ratio is plotted as a function of the ratio f_{μ^+}/f_p is shown in Fig. 4.34.

At the maximum of the curve it was found that

$$\frac{f_{\mu^+}}{f_p} = 3.1830 \pm 0.0011$$

The accuracy of the method of 'stroboscopic coincidences' was appreciably exceeded by Garwin et al. [53, 54]. These workers increased the precession frequency and consider-

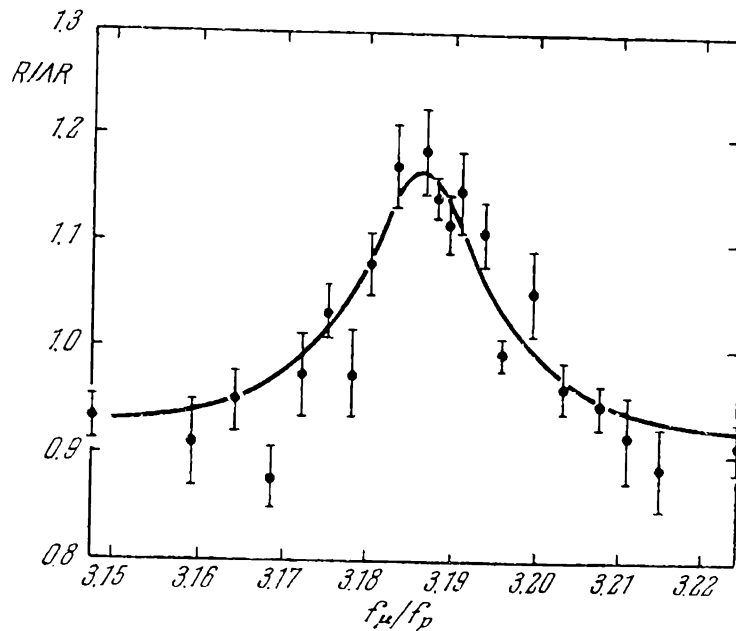


Fig. 4.34 Resonance curve obtained by the method of stroboscopic coincidences

ably improved the accuracy with which they measured the time interval between the entry of the muon into the target and the emission of the decay electron. Their method, which is in fact a modification of the stroboscopic-coincidence method, is illustrated in Fig. 4.35. Particles stopping in the target were indicated by $123\bar{4}$ coincidences, and the emission of decay electrons in the forward and backward directions by $45\bar{1}\bar{3}$ and $23\bar{1}\bar{4}$ coincidences respectively. These coincidences were recorded if they lay within a $5.7\text{-}\mu\text{sec}$ long gating pulse whose leading edge was delayed by $0.15\text{-}\mu\text{sec}$ relative to the $123\bar{4}$ pulse. The target and counters 2-5 were placed between the poles of an electromagnet. A uniform field was obtained by carefully shimming the pole pieces, and was measured and stabilized by means of proton resonance signals from a probe located immediately above the target.

The circuits recorded the time interval between the stopping of a positive muon and the appearance of a decay electron. Time measurements were carried out by counting the number of oscillations of a stabilized standard oscillator operating at 86.2 Mc/s in the first experiments, and 170 Mc/s in subsequent, more accurate, measurements. The actual quantity measured was not the entire time interval between the entry of the muon into the target and the emission of the decay electron, but only the difference between this

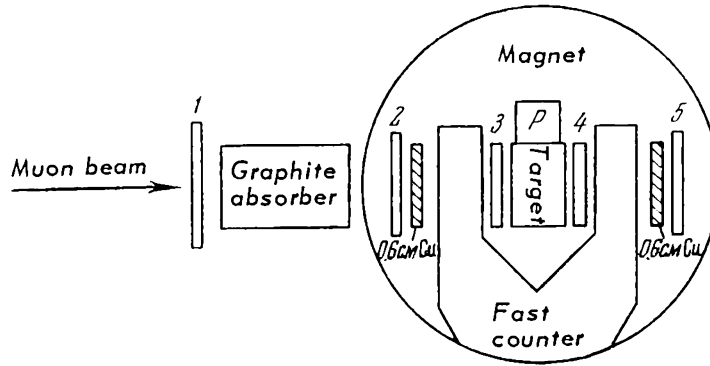


Fig. 4.35 Measurement of the magnetic moment of the muon (Garwin et al.)

interval and the nearest integral number of periods of the standard oscillator. This time difference was determined by time-to-amplitude conversion, using a multichannel pulse-height analyser. Owing to the subtraction of the nearest number of integral periods, time intervals differing by an integral number of cycles of the oscillator entered the same channel of the analyser. When the frequency of the oscillator was not equal to the positive-muon spin precession frequency, there was a random interference between these contributions and the resulting distribution of the number of periods over the analyser channels was uniform. When the two frequencies were equal, contributions from different decays to each channel were in phase, and the distribution over the time channels could be approximately described by

$$e^{-\lambda t} (1 + a \cos \omega_s t) \quad (4.18)$$

where a is the amplitude of the distribution, ω_s the muon spin precession frequency, and $\lambda = 1/\tau$ the probability of the decay of the positive muon. A more accurate formula for this distribution may be obtained as follows. The phase difference between the stopping positive muon and the time at which the decay electron is emitted is $\Phi = \omega_0 t$, where ω_0 is the frequency of the standard oscillator, and the phase distribution function is

$$N_{\Phi} d\Phi = e^{-\Phi/\omega_0 \tau} \left[1 + a \cos \left(\frac{\omega_H}{\omega_0} \Phi - \vartheta \right) \right] \frac{d\Phi}{\omega_0 \tau} \frac{d\Omega}{4\pi} \quad (4.19)$$

This distribution may be obtained from (4.18) by substituting $t = \Phi/\omega_0$. The quantity ϑ in (4.19) is a constant phase which is related to the operation of the circuits and the presence

of an angular interval between the initial μ^+ spin direction and the momentum of the decay electron recorded by the coincidence system.

It has already been pointed out that a given channel recorded time intervals differing by an integral number of periods. To obtain the phase distribution corresponding to this method of measurement, we must replace Φ in (4.19) by $\Phi + 2\pi n$ and sum over all periods n . This is analogous to the summation of intensities from the individual slits of a diffraction grating. The larger the number of such slits (n) the sharper the diffraction maximum.

Near resonance, i.e. when $|\omega_s - \omega_0| \ll \omega_0$, this procedure yields

$$N_{\vartheta} d\Phi = \left[1 + \frac{1}{1 + (\tau\Delta\omega)^2} a \cos\left(\frac{\omega_s}{\omega_0} \Phi - \vartheta - \alpha_0\right) \right] \times e^{-\Phi/\omega_0\tau} f(\omega_0) \frac{d\Phi}{2\pi} \frac{d\Omega}{4\pi} \quad (4.20)$$

where $\tan \alpha_0 = (\omega_0 - \omega_H) \tau$ is a function of the time interval during which the decay electrons are counted. When the precession frequency and the frequency of the standard oscillator are equal, we have $\Delta\omega = 0$ and the amplitude of the cosine term is a maximum. This is one method for determining the resonant frequency, but the sensitivity is not very high. A much more sensitive method is to find the frequency at which α_0 passes through zero. However, N_{ϑ} can be obtained from experiment and from this one can determine, not α_0 , but the total phase shift $\alpha = \alpha_0 + \vartheta$. To exclude the large uncertainty due to the initial phase ϑ (determined by the geometry of the experiment), the 5.7- μ sec gate length was divided into two parts, i.e. 0-1.75 μ sec and 1.75-5.7 μ sec, and instead of measuring α itself, a determination was made of the phase for the 'early' and 'late' parts of the gating pulse. The difference between these phases is zero when $\omega_s = \omega_0$, and is independent of the geometry of the experiment, the initial phase ϑ , and drift in the electronic circuits, since all these disturbances influence $(\alpha_0)_p$ and $(\alpha_0)_n$ in the same way. Hence

$$\Delta = (\alpha_0)_p - (\alpha_0)_n = f(t_1, t_2) \Delta\omega \quad (4.21)$$

where $f(t_1, t_2)$ is a function which depends on the way in

which the gate is divided into the two parts t_1 and t_2 ($t_1 + t_2 = 5.7 \mu\text{sec}$). The quantity Δ was determined for different values of the magnetic field H , and the passage of Δ through zero determined the resonance field, for which

$$\omega_s = \omega_0 = g \frac{eH}{2m_\mu c}$$

Fig. 4.36 shows the experimental values of the difference $\alpha_p - \alpha_n$ as a function of the magnetic field H expressed in terms of the proton NMR frequency f_p [54]. These data were obtained for a target consisting of an aqueous solution

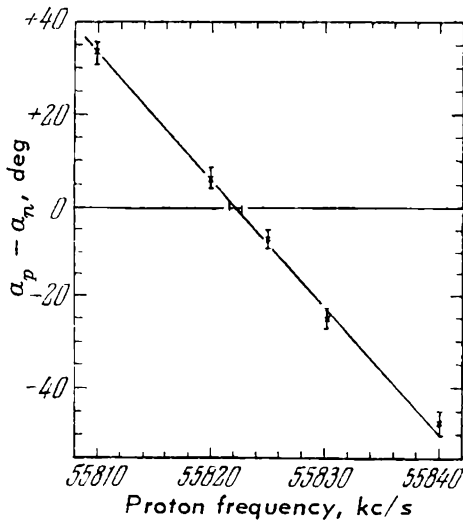


Fig. 4.36 Phase difference as a function of the magnetic field expressed in terms of the proton resonance frequency

of HCl. The passage of the phase difference through zero in this graph corresponds to $f_p = 55\,823.01 \pm 0.43 \text{ kc/s}$, and the ratio of the frequency of the standard oscillator f_μ to f_p is

$$\frac{f_\mu}{f_p} = 3.18334 \pm 0.00005$$

Since the g factor for the positive muon is given by

$$g_\mu = g_p \left(\frac{f_\mu}{f_p} \right) \left(\frac{m_\mu}{m_p} \right)$$

we find that

$$g_\mu = \frac{2.79275}{1836.12} \cdot \left(\frac{f_\mu}{f_p} \right) m_\mu$$

where we have assumed, following Cohen et al. [48], that $g_p = 2.79275 \pm 0.00003$ nuclear magnetons, and $m_p = 1836.12 \pm 0.02$ electron masses. The quantities g_p and m_p are known to within 1 in 10^5 , and the accuracy of the ratio f_μ/f_T is about 2×10^{-5} . Since the mass of the muon is known much less precisely (about 1 in 10^4), the uncertainty in g is determined largely by the error in the muon mass.

The mean mass of the muon obtained from mesonic-atom data is

$$m_\mu = 206.76 \pm 0.02 m_e$$

and hence

$$g_{\mu^+} = 2 (1.00110 \pm 0.00016)$$

which is in good agreement with the theoretical result

$$g_{\mu^+} = 2 (1.0011654)$$

It may therefore be concluded that the magnitude of the radiative correction to the muon magnetic moment is within 15% of its theoretical value. More accurate determinations of this correction will, of course, require a more accurate knowledge of the muon mass, or the application of experimental methods which do not involve a knowledge of this mass.

4.5.3 Magnetic moment of the negative muon

Hutchinson et al. [54], who measured the magnetic moment of the positive muon, have also determined the magnetic moment of the negative muon. They used graphite, oxygen (water), magnesium, silicon, and sulphur (spinless nuclei). The magnetic moment of the negative muon was measured when it was in the ground state of the mesonic atom, and was found to be somewhat smaller than that of the free positive muon. Corrections to the negative-muon magnetic moment in the $1S$ state of a mesonic atom with a spinless nucleus surrounded by a spinless electron cloud have been discussed by Ford et al. [55]. The most important correction is the correction for the coupling of the negative muon to the nucleus. This is given by

$$\frac{g_3}{g_0} = - \left(\frac{4}{3} \right) \int_0^\infty F^2 dr \quad (4.22)$$

where g_0 is the g factor for the free muon and F a small component of the radial wave function of the muon in the nuclear Coulomb field. It is interesting to note that this correction depends on the distribution of charge in the nucleus. Its magnitude calculated from the nuclear-charge distribution obtained from high-energy electron-scattering data, characterized by a nuclear radius r and a surface thickness n , increases rapidly with Z and becomes greater than the radiative correction for $Z > 8$. Other corrections include those for the polarization of the nucleus and the diamagnetism due to electron screening. Table 4.3 gives the resultant values of the gyromagnetic ratio g after the introduction of these corrections.

It follows from these data that the observed difference between the magnetic moments of negative and positive

Table 4.37

Target	$\frac{g^- - g^+}{g^+} \times 10^4$	Resultant correction $\times 10^4$
C	-7.5 ± 0.3	-8.32
O	-9.3 ± 1.0	-14.3
Mg	-26.3 ± 0.7	-29.84
Si	-36.1 ± 1.1	-39.17
S	-48.1 ± 1.6	-49.16

muons can be explained almost entirely by the above corrections. It follows that the two moments are equal to within 1 in 10^4 . We note that it is a consequence of CPT invariance that the magnetic moments of the negative and positive muons, when these are regarded as a particle-antiparticle pair, should be equal.

4.6 MEASUREMENTS OF $g-2$

We shall now discuss another method of measuring g which does not require a knowledge of the muon mass. This method has been used to determine the quantity $1/2(g-2)$ to an accuracy of about 2%, but further improvements in the accuracy appear to be possible. The principle of the method is to compare the muon cyclotron frequency in a magnetic field H , which is given by

$$\omega_c = \frac{eH}{mc}$$

with the spin precession frequency

$$\omega_s = g \frac{eH}{2mc}$$

These frequencies are equal when $g = 2$, and their difference is proportional to $g - 2$, i.e. to the anomalous magnetic moment

$$\omega_s - \omega_c = \frac{g-2}{2} \frac{eH}{mc} = a \frac{eH}{mc} \quad (4.23)$$

Let us suppose that a longitudinally polarized muon with momentum \mathbf{P} moves in the magnetic field which is at right angles to the plane of the diagram (Fig. 4.37). Suppose that at point A the momentum \mathbf{P} is parallel to the spin of the muon. At point B, owing to the fact that the spin precesses faster than the momentum ($g > 2$), the two vectors will be at an angle

$$\alpha = (\omega_s - \omega_0) t$$

where t is the time taken to reach B from A. The rotation of the spin relative to the momentum after N revolutions in a magnetic field is

$$\varphi = \omega_c \gamma a t = 2\pi N \gamma a \quad (4.24)$$

where $\gamma = (1 - \beta^2)^{-1/2}$ and $a = \frac{g-2}{2}$. It follows that longitudinally polarized non-relativistic muons ($\gamma \approx 1$) will become transversely polarized after

$$N = \frac{\frac{\pi}{2}}{2\pi a} \approx \frac{1}{4 \cdot 0.001165} \approx 214$$

revolutions, and after 428 revolutions the polarization of the muons will change sign, i.e. a 100-MeV longitudinally polarized muon will become transversely polarized after 214 revolutions. This experiment is similar to that of Schupp et al. [49] who have measured $g - 2$ for electrons. In the latter work, the electrons were polarized by Mott scattering. The left-right asymmetry in Mott scattering was then used to establish the rotation of the electron spin

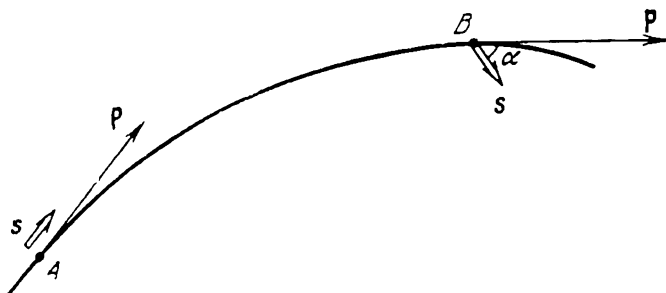


Fig. 4.37 Muon trajectory and muon spin precession in a constant magnetic field

after a given number of revolutions in a magnetic field.

In the muon experiments, the muon beam entering the magnetic field is at first completely longitudinally polarized, and the rotation of the spin in the magnetic field is determined from the spatial asymmetry of the decay electrons: for muons which have executed, say, a small number of rotations, the asymmetry is a maximum, whilst for muons which have remained in the field so long that the spin is perpendicular to the trajectory, the asymmetry is zero. The asymmetry then changes sign, and so on. The whole process can be described by a sine curve with a period proportional to $g - 2$. This experiment was carried out by Charpak et al. [56], and is illustrated in Fig. 4.38. Longitudinally polarized positive muons produced in $\pi \rightarrow \mu$ decays in flight were focused by a deflecting magnet and a pair of focusing lenses on the entrance to a vacuum chamber placed in the gap of a magnet with 6-m-long pole pieces. The muon beam intercepted the horizontal plane of symmetry of the chamber at about 90° . The muons lost part of their energy in a beryllium absorber, so that the radius of their trajectories in a field of 15.8 kgauss was $r = 19$ cm. Owing to the presence of a field gradient in the y direction, the trajectory was displaced along the x axis at the rate S of about 2 cm/revolution at the entrance and 4 mm/revolution at the centre of the chamber. This figure reaches 10 cm/revolution near the exit from the chamber. Careful shimming of the pole pieces was necessary to ensure this rate of displacement of the trajectory. A special detector system for recording the asymmetry of decay electrons from muons stopping in the target was located at the exit of the chamber. $11'$ coincidences indicated electrons emitted in the backward direction, whilst electrons emitted in the forward directions were indicated by $22'$ coincidences. The

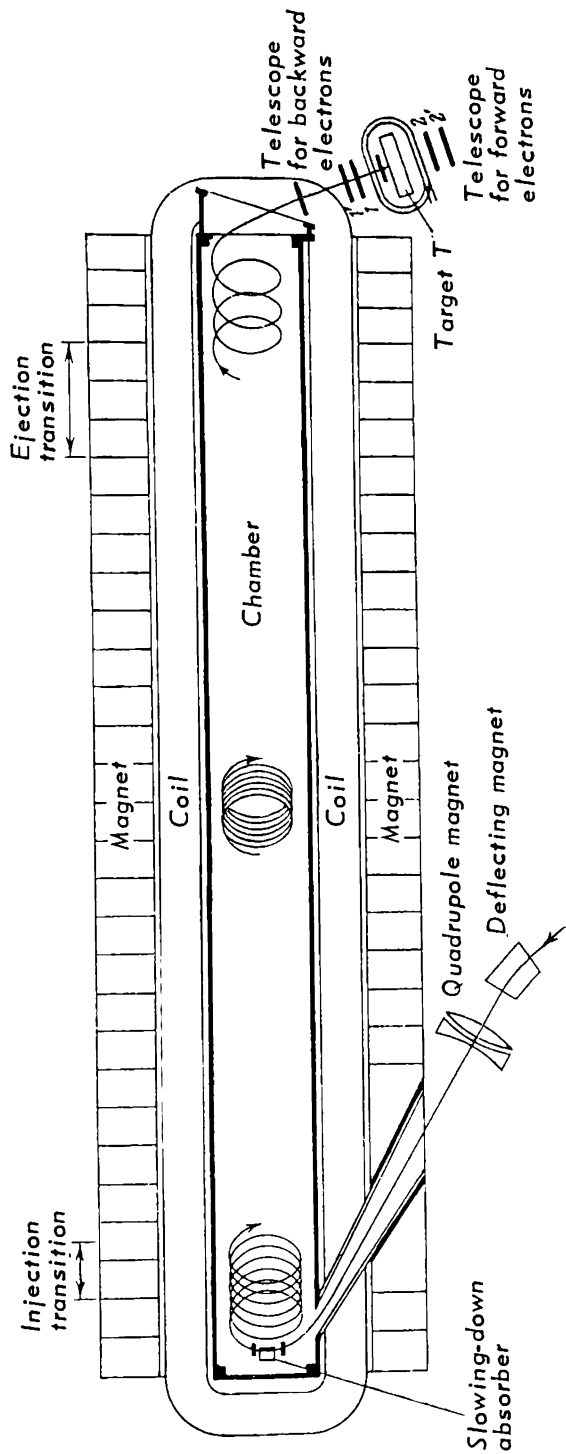


Fig. 4.38 Determination of $g-2$ for positive muons (Charpak et al.). The vacuum chamber is placed between the poles of an electromagnet. Positive muons which have lost some of their original energy in the absorber arrive in spirals inside the chamber. On leaving the chamber they come to rest in the target of the analysing system which measures the polarization of the muons from the asymmetry in $\mu-e$ decays. Decay electrons are noted by $1, 1'$ or $2, 2'$ coincidences. The coil wound on the target T is used to rotate the muon spin by $+90^\circ$ and -90° after stopping. This is used to exclude systematic errors in the measured asymmetries which are connected with differences between the telescopes $1, 1'$ and $2, 2'$

instrumental asymmetry due to residual differences between counters recording forward and backward decays was excluded by switching on a vertical pulsed magnetic field after each entry of a positive muon into the target T. This rotated the spin of the muon in the clockwise direction by $+90^\circ$, and after the next entrance of a positive muon in the clockwise direction by -90° , and so on. The electron telescopes 11' and 22' were thus used alternately as the forward- and backward-decay indicator, and instrumental asymmetries were therefore eliminated.

In addition to the direction of emission of decay electrons for all positive muons stopping in the target, the time of flight through the chamber was also measured. This is uniquely related to the number of revolutions in the magnetic field.

The data obtained are shown in Fig. 4.39, in which the asymmetry coefficients for the eleven time channels are

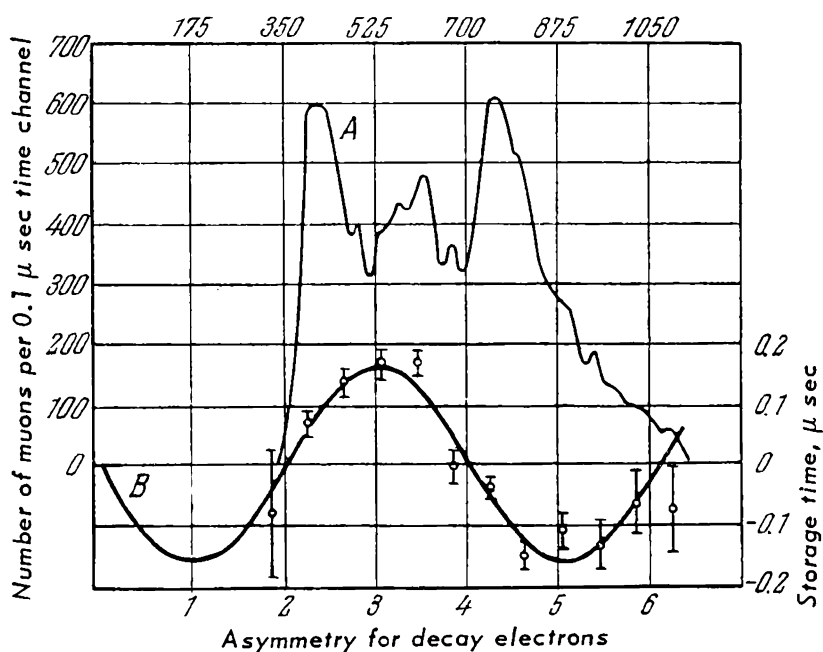


Fig. 4.39 Data obtained in the $g-2$ experiment

plotted against the time spent by the muon in the magnetic field (which is proportional to the number of revolutions). It is evident that if C_{n+} and C_n are the number of counts in the electron telescopes recorded for spin rotations of $+90^\circ$ and -90° respectively, then the asymmetry coefficient is

given by

$$A_n = \frac{C_{n+} - C_{n-}}{C_{n+} + C_{n-}} = A \sin(aB\omega_0 t_n) \quad (4.25)$$

where A is proportional to the initial polarization of the original beam, B is the magnetic field, ω_0 is the cyclotron frequency of positive muons, and t_n is the time spent by the muon beam in the chamber. It follows that the period of the sine curve yields directly the quantity

$$a = \frac{g-2}{2}$$

The solid curve B in Fig. 4.39 is the 'best fit' to the experimental data. The parameter a thus obtained was found to be

$$a_{\text{exp}} = a_{\text{theor}}(0.983 \pm 0.019) = 0.001145 \pm 0.000022$$

Of the 1.9% uncertainty in $\frac{g-2}{2}$ measured in this way, 1.7% was due to the statistical error. Charpak et al. [57] subsequently improved this result considerably, obtaining

$$a_{\text{exp}} = a_{\text{theor}}(0.9974 \pm 0.0042) = 0.001162 \pm 0.000005$$

It may be concluded from the above data that the measured $g - 2$ difference agrees to within about 0.4% with the magnitude of the radiative correction. Consequently, possible departures from quantum electrodynamics for muons interacting with the natural electromagnetic field can only lie within the limits of this error. To deduce from this result the magnitude and nature of the possible departures, it is necessary to assume some definite model for them, i.e. to indicate their origin. For example, it may be supposed that quantum electrodynamics begins to fail for large momenta P transferred to virtual photons [58, 59]. This will have the effect of reducing the radiative correction from $a = \frac{\alpha}{2\pi}$ to

$$a = \frac{\alpha}{2\pi} \left(1 - \frac{2}{3} \Lambda^{-2} \right) \quad (4.26)$$

where

$$\Lambda = \frac{pc}{m_\mu c^2}$$

is the ratio of this momentum to the muon rest energy.

Another possible mechanism suggested by de Tollis [60] involves the introduction of a fundamental length L below which quantum electrodynamics begins to fail. This model again leads to Equation (4.26) where

$$\Lambda \approx \hbar (4m_{\mu}cL)^{-1} \quad (4.27)$$

It is evident from the above formulae that corrections due to the failure of quantum-electrodynamics are proportional to the square of the particle mass. Hence they become negligibly small for the electron, but can be observed in the case of the muon.

We can now estimate, with the aid of these formulae, the upper limit for L which corresponds to 0.4% in the measured magnitude of $g - 2$. We have

$$\frac{2}{3}\Lambda^{-2} < \frac{4}{1000}$$

and hence $pc \gtrsim 3 \text{ GeV}$ and $L \lesssim 2 \times 10^{-15} \text{ cm}$. Measurements of $g - 2$ thus indicate that, within the framework of the above models, quantum electrodynamics does not fail up to transferred momenta of about $3 \text{ GeV}/c$, and down to distances of about $2 \times 10^{-15} \text{ cm}$.

4.7 DIPOLE MOMENT OF THE MUON

It is a consequence of CPT invariance that the dipole moment of elementary particles should be zero. Landau has shown that the conservation of combined parity, i.e. invariance under CP transformation, will also give rise to a zero dipole moment. Let us now establish to what accuracy this requirement is satisfied.

Measurements of the dipole moments of the electron, positron, proton and neutron have shown that the first three particles have dipole moments of less than about $10^{-13} e \text{ cm}$, and the last less than $10^{-17} e \text{ cm}$, where e is the electron charge. Charpak et al. tried to determine the dipole moment of the muon by a method based on the following considerations. Suppose that the muon has a dipole moment which is parallel to the spin of the particle and is given by

$$D = f \frac{e\hbar}{mc} \quad (4.28)$$

The existence of this dipole moment will give rise to additional precession in the $g - 2$ experiment discussed above.

In fact, in the rest system of the muon which revolves in the magnetic field (Fig. 4.38), this dipole moment will experience an electric field

$$E = \gamma \beta \times B \quad (4.29)$$

where $\beta = \frac{v}{c}$ and $\gamma = \frac{1}{\sqrt{1-\beta^2}}$ and B is the magnetic field in the magnet gap. The result of this will be that the dipole moment of the positive muon will precess round an instantaneous axis, perpendicular to the magnetic field B and to the velocity β , with a frequency $\omega_e = 2f\beta\omega_c$, where $\omega_c = \frac{eB}{m_0c}$ is the cyclotron frequency for a non-relativistic muon. The combined effect of the precession of the magnetic moment about B and of the dipole moment about the direction of $\beta \times B$ gives rise to a vertical polarization

$$P_v \approx P_0 \frac{2f\beta}{\sqrt{a^2 + 4f^2\beta^2}} \sin \omega_a t \quad (4.30)$$

where ω_a is the muon spin precession frequency relative to β due to the difference $g - 2$. Fig. 4.38 shows the electron-telescope system used in the $g - 2$ experiment. These telescopes record the muon spin precession frequency in the horizontal plane. To detect the spin precession in the vertical plane, it is sufficient to rotate these telescopes so that their axes become vertical, and to repeat the $g - 2$ experiment under these new conditions. Precession in the vertical plane will indicate the existence (or otherwise) of the muon dipole moment.

The results of this experiment are shown in Fig. 4.40, where the asymmetry in the angular distribution of decay electrons is plotted as a function of the time spent by the muon in the magnetic field, which is proportional to the number of revolutions. For comparison, curve D is the asymmetry curve due to the $g - 2$ difference taken from Fig. 4.39. This curve was determined with the aid of electron telescopes lying in the horizontal plane. The points show the asymmetry associated with the vertical component of polarization. As can be seen, these points lie very close to the zero axis, indicating the absence of a dipole moment.

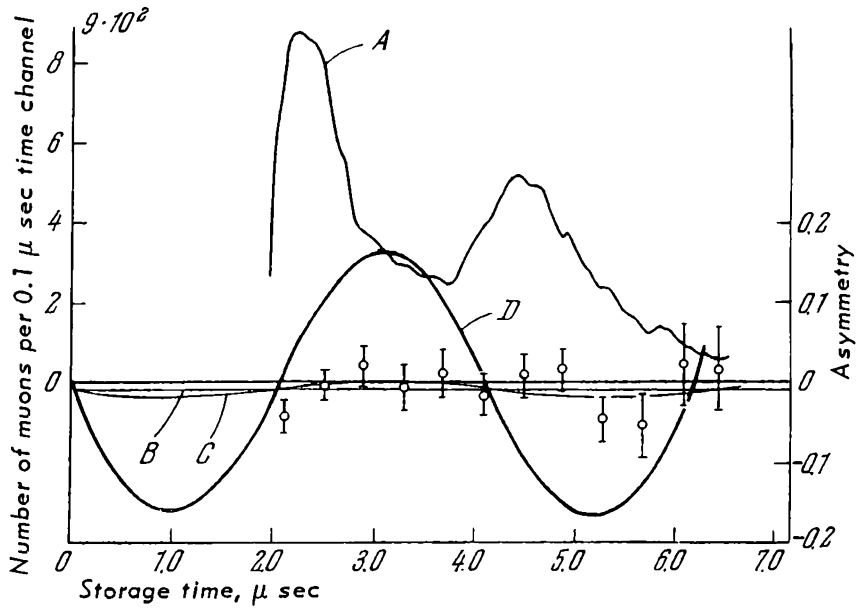


Fig. 4.40 Results of the determination of the dipole moment of the positive muon

The upper limit for the factor f (4.28) for the positive muon was found to be

$$f = (3 \pm 6) \cdot 10^{-5}$$

which corresponds to a dipole moment of

$$e (0.6 \pm 1.1) \cdot 10^{-17} \text{ cm}$$

Chapter 5

MESOMOLECULAR PHENOMENA

5.1 CATALYTIC EFFECT OF NEGATIVE MUONS IN FUSION REACTIONS INVOLVING HYDROGEN ISOTOPES

A negative meson stopping in matter and forming a mesonic atom will either decay or be absorbed by the nucleus. However, this is preceded by various atomic and molecular processes in which the meson participates and which are particularly important for the negative muon which has a relatively long lifetime and interacts weakly with nuclei.

In this chapter we shall consider some of the atomic and molecular phenomena which arise when negative muons are absorbed in liquid hydrogen. These phenomena are interesting in themselves, and must also be understood in order to interpret experimental data on the interaction between negative muons and protons.

The main phenomenon in this connection is the muon catalysis of the proton-deuteron fusion reaction. This reaction was first detected by Alvarez et al. [1] and was predicted by Frank [2], Sakharov [3] and Dzhelepov [5]. Fig. 5.1a is a photograph of a negative muon stopping in a hydrogen bubble chamber in a field of 11 kOe [1]. The photograph shows the track of the negative muon which

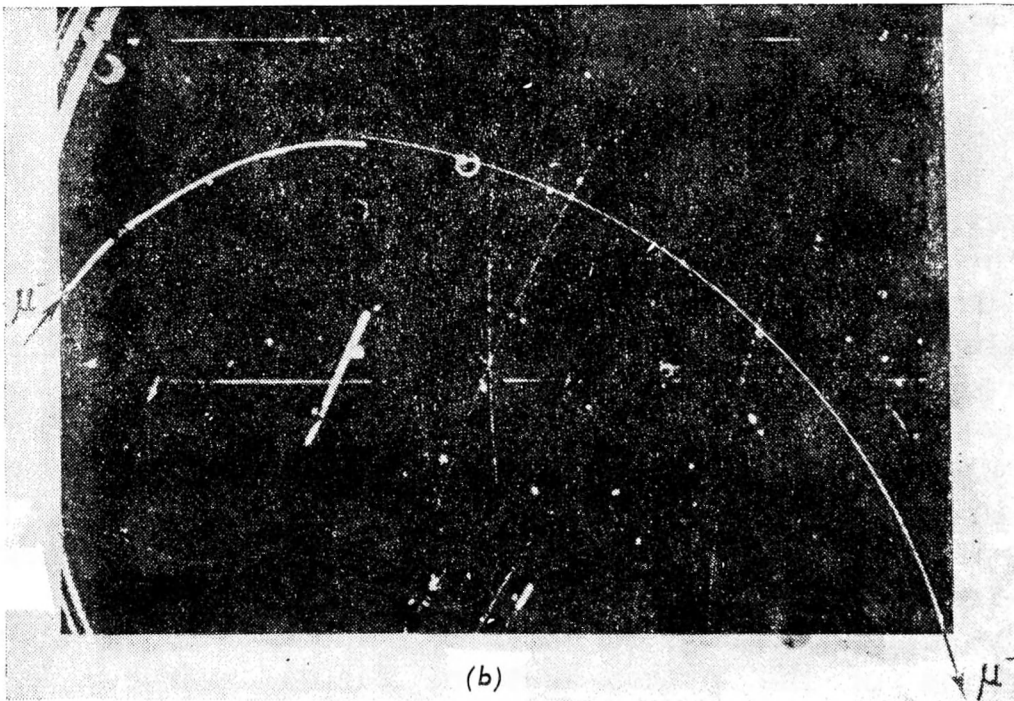
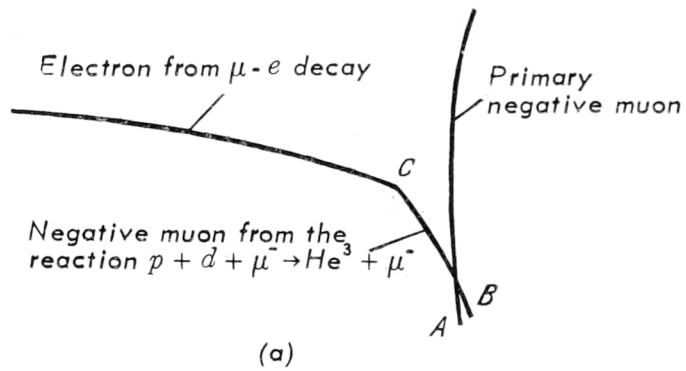
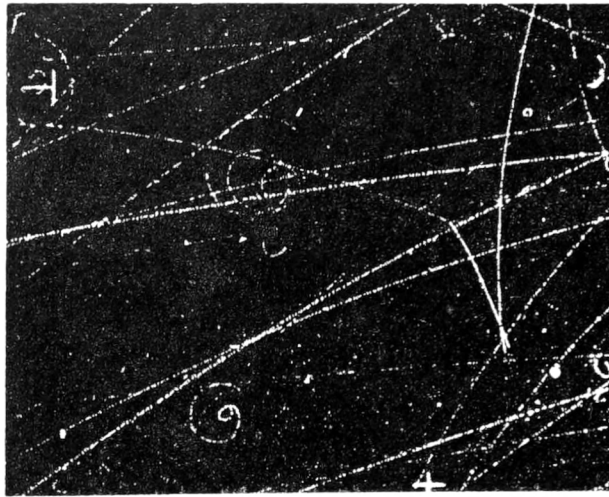
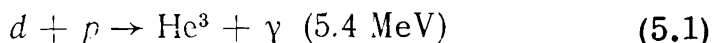


Fig. 5.1 (a) $p + d$ fusion reaction in a liquid-hydrogen bubble chamber (Alvarez et al.). Photograph shows the characteristic X break between the track of the primary muon and the beginning of the track of the new muon; (b) analogous phenomenon in a hydrogen diffusion chamber (Dzhelepov et al.)

stops at the point B, and a second negative-muon track which starts at a small distance from B. The second negative muon has a range of about 1.7 cm and decays on stopping, forming a visible decay-electron track. Alvarez et al. found 15 cases of this kind among 2541 negative muons stopping in a chamber filled with natural hydrogen. Fig. 5.1b shows a photograph of the same phenomenon in a hydrogen-filled diffusion cloud chamber situated in a magnetic field [5]. The track of the particle entering on the left is that of a negative muon stopping in the chamber. The track of the 'rejuvenated' negative muon which eventually leaves the chamber is shown on the right. The new meson is faster, and its track starts near the end of the original negative-muon track.

All the secondary muons have very nearly equal ranges. The range spectrum of 442 bubble-chamber events of this type obtained by Schiff [6] is shown in Fig. 5.2. The mean range obtained from this spectrum is 1.73 ± 0.05 cm of liquid hydrogen, corresponding to a muon energy of 5.3 ± 0.1 MeV.

These results were explained by Alvarez et al. as being due to the fusion of a proton and a deuteron into the He^3 nucleus, which occurs because of the catalytic action of the negative muon. This reaction occurs with the emission of a 5.4-MeV γ ray:



and is one of the possible fusion reactions involving hydrogen isotopes. Other reactions of this kind involving protons,

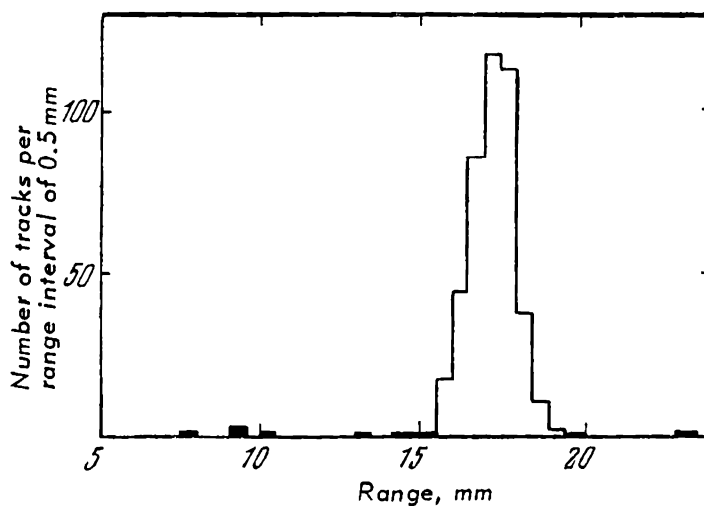
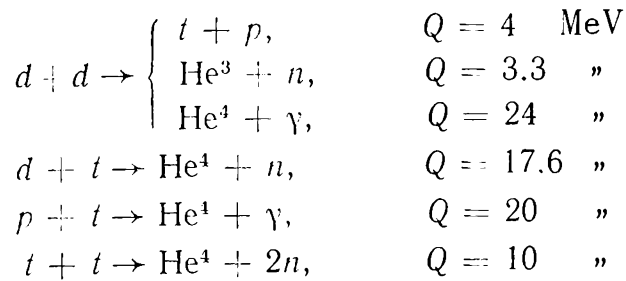


Fig. 5.2 Range spectrum for 'rejuvenated' negative muons in a hydrogen bubble chamber

deuterons and tritons are also well known. They lead to the formation of tritium or helium nuclei, and are accompanied by the liberation of energy Q :



These reactions do not occur at ordinary temperatures since the kinetic energies are too low to enable the particles to overcome the Coulomb barriers. The reactions will occur only if the colliding particles have large kinetic energies, e.g. when the particles are accelerated to energies of the order of 100 keV, or at high temperatures in a nuclear explosion or gas discharge.

The catalytic action of the negative muon, which makes possible the reaction (5.1) in liquid hydrogen, is explained in terms of the formation of the mesonic molecule ($p\mu^-d$) in which the separation of the proton and the deuteron is about 200 times smaller than the separation in the ordinary molecule, owing to the large mass of the negative muon.

Another example of a fusion reaction catalysed by a negative muon is shown in Fig. 5.3. Here, the negative muon became part of the ($d\mu^-d$) molecule. The reaction



results in the formation of a tritium nucleus and a proton, which are emitted in opposite directions. The ejected muon receives very little energy, does not travel very far from the point at which the reaction occurred, and decays by emitting a fast electron.

The phenomena occurring when a negative muon comes to rest in liquid hydrogen are illustrated in Fig. 5.4. The slowing down of the negative muon from a few MeV to energies at which, as a result of cascade transitions, it is found in the $1S$ state of the mesonic atom (μ^-p) occurs in a very short time by comparison with its lifetime. The mesonic atom (μ^-p) and the similar mesonic atom (μ^-d) have radii of about 2.5×10^{-11} cm. At large distances this electrically neutral system resembles a neutron: it can approach another nucleus to within distances of the order of 10^{-11} cm, which is

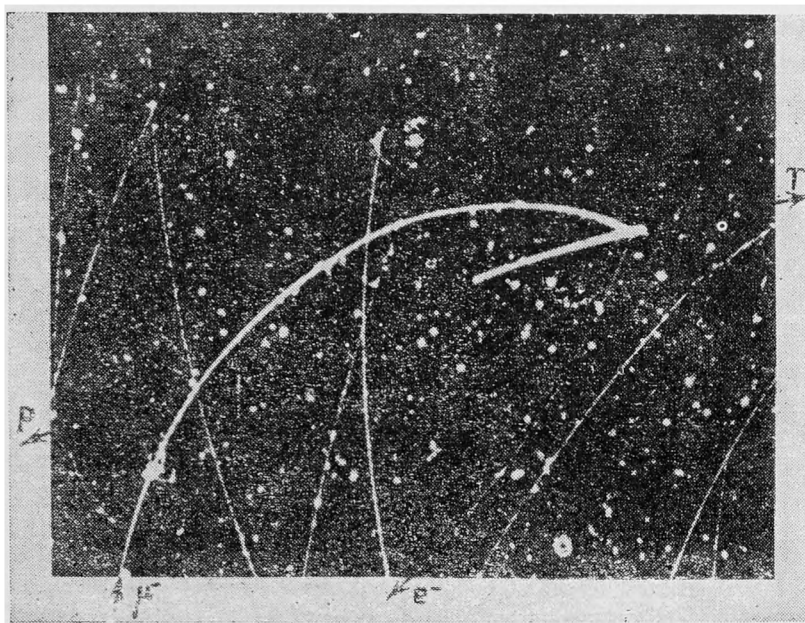
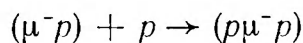
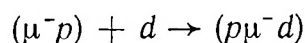


Fig. 5.3 Muon catalysis of the $d + d \rightarrow t + p$ reaction in a hydrogen diffusion chamber enriched with deuterium. t and p are emitted in nearly opposite directions, and the energy transferred to the muon is small so that it decays near the end of the heavy track (Dzhelepov et al.)

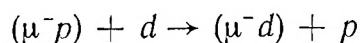
impossible for an isolated proton because of the nuclear Coulomb field. When the mesonic atom (μ^-p) collides with hydrogen and deuterium in natural hydrogen, the mesonic molecules $(p\mu^-p)$ and $(p\mu^-d)$ are produced. The formation of these molecules is indicated by the left-hand and central branches of Fig. 5.4, where λ_{HH} represents the probability of the reaction



and λ_{HD} the probability of the reaction



However, a more probable process in liquid hydrogen is the formation of (μ^-d) mesonic atoms as a result of the reaction



The probability of this reaction (the right-hand branch of Fig. 5.4) is represented by λ_{pd} .

The concentration of deuterium in naturally occurring hydrogen is about 150×10^{-6} , while according to mass-spectrometric data [6], the deuterium impurity in commercial

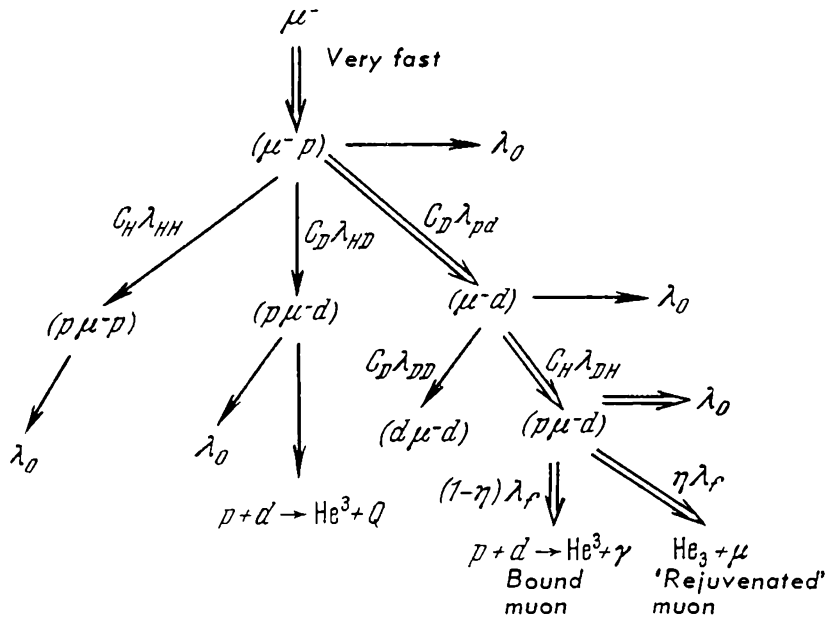


Fig. 5.4 Mesomolecular phenomena associated with stopping negative muons in liquid hydrogen. For deuteron saturation, only the double arrows are significant

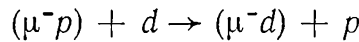
hydrogen used in hydrogen-filled chambers is $(40 \pm 14) \times 10^{-6}$. In spite of this low concentration of deuterium, the probability $C_D \lambda_{pd}$ is very high because the difference in the reduced masses of the mesonic atoms (μ^-p) and (μ^-d) ensures that the binding energy of the (μ^-d) atom is 135 eV larger than the binding energy of the (μ^-p) atom. Belyaev et al. [7] have shown that $\lambda_{pd} = 1.4 \times 10^{10} \text{ sec}^{-1}$, which even for $C_D = 40 \times 10^{-6}$ yields a total probability

$$C_D \cdot \lambda_{pd} = 40 \cdot 10^{-6} \cdot 1.4 \cdot 10^{10} = 5.6 \cdot 10^5 \text{ sec}^{-1}$$

which is not very different from the negative-muon decay probability.

Since in the transition of a negative muon from the proton to the deuteron, an energy of 135 eV is liberated, the mesonic atom (μ^-d) has a recoil kinetic energy of 48 eV giving it a range of approximately 1 mm in liquid hydrogen. This recoil explains the gap at the end of the negative-muon track in photographs similar to those of Fig. 5.1. The role of the deuterium impurity in the formation of such gaps is clearly illustrated by the experiments of Dzhelepov et al. [8] who used a hydrogen-filled diffusion chamber exposed to the negative-muon of the synchrocyclotron at the USSR Joint Institute for Nuclear Studies. They investigated gaps between the

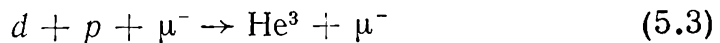
end of negative-muon tracks and the beginning of decay-electron tracks in a chamber filled with hydrogen gas at 22.7 atm. In a second experiment, about 0.44% deuterium impurity was added. Whilst in the first experiment the gap in the track explained by the recoil of the (μ^-p) atom was of the order of 1 mm, in the second experiment, after the addition of deuterium, the length of the gap was much greater. Fig. 5.5 shows the distribution of gap lengths in the two experiments. It is evident that the addition of deuterium increases the mean length of the gap by approximately one order of magnitude. These experiments establish the probability of the reaction



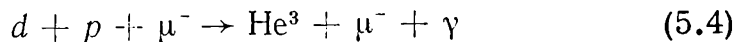
When referred to the number of hydrogen nuclei per cc (3.5×10^{22}), this probability was found to be

$$\lambda_{pd} = (0.95_{-0.21}^{+0.34}) \cdot 10^{10} \text{ sec}^{-1}$$

Collisions between mesonic atoms (μ^-d) and hydrogen nuclei (Fig. 5.3) lead to the formation of mesonic molecules $(p\mu^-d)$. In these molecules, the proton and deuteron are separated by a distance of 10^{-10} cm and therefore have a large probability λ_f of penetrating the Coulomb barrier. The result of this penetration is either the reaction



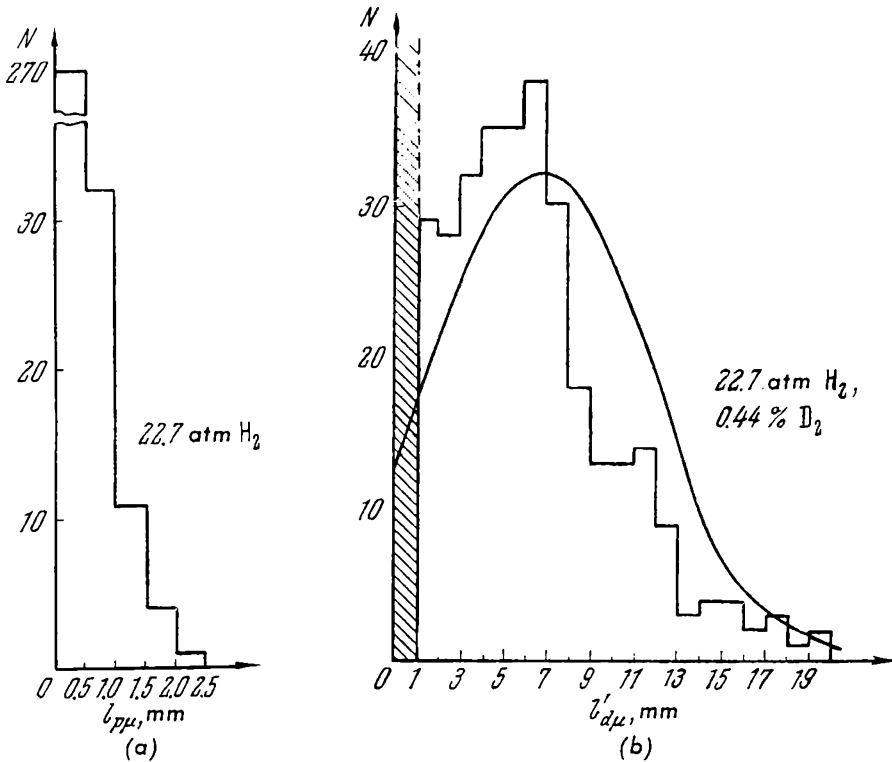
in which the entire liberated energy is given to the 'rejuvenated' negative muon, or the reaction



in which the energy is carried off by γ rays and the muon remains in a bound state of the mesonic atom ($\text{He}^3\mu^-$).

A characteristic feature of processes in which the negative muon acts as a catalyst of the fusion reaction between the proton and the deuteron is that their probability reaches saturation at very low deuterium concentrations ($\approx 10^{-3}$). Experimental data on the yield of the reaction (5.3) as a function of the deuterium concentration are given in Table 5.1.

The double arrows in Fig. 5.4. indicate reactions which are most important under saturation conditions, i.e. for deuterium concentrations $\gtrsim 10^{-3}$. It is interesting to note that the catalysis of the $p + d$ reaction by a meson was first



a – no deuterium; b – 0.44% of deuterium

Fig. 5.5 Distribution of μ^-e breaks in the experiment of Dzheleпов et al. Pressure of hydrogen in the diffusion chamber was 22.7 atm

considered by Frank in 1947 in connection with the discovery of $\pi - \mu$ decay by Lattes, Occhialini and Powell. Frank attempted to explain the observed phenomenon by the appearance of a 'new' meson near the 'old' meson without introducing new elementary particles, and considered the

Table 5.1

Deuterium concentration, C_D	Natural hydrogen	300×10^{-6}	650×10^{-6}	4300×10^{-6}
Reaction yield in % of the number of stopping mesons	0.7 ± 0.2 (a) 0.69 ± 0.8 (b)	2.3 ± 0.2 (a)	2.27 ± 0.20 (b)	2.5 ± 0.4 (a)

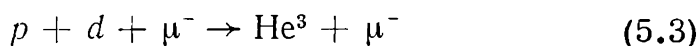
(a) Cresti and Gottstein et al. [9]

(b) Schiff [6]

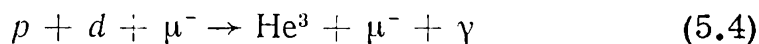
various possible processes in which the energy would be transferred to the 'new' meson, not from the 'old' meson, but from the nuclear emulsion itself. Among the various possibilities rejected by Frank, there was in fact the catalysis of the $p + d$ reaction by a meson in which an energy of 5.4 MeV is transferred to the negative muon. He rejected this process because of the low concentration of deuterium in nuclear emulsions. We note that the range of negative muons released in the reaction (5.2) is 1.73 cm, whilst the range in hydrogen of muons from $\pi - \mu$ decays is about 1 cm.

5.2 KINETICS OF NEGATIVE-MUON CATALYSIS OF THE $p + d \rightarrow \text{He}^3 + \gamma$ REACTION

Alvarez et al. and, later, Fetkovich et al. [10], Cresti et al. [9] and Schiff [6] studied the reaction



using bubble chambers filled with liquid hydrogen and deuterium. In this reaction, all the released energy is transferred to the negative muon. However, another branch of the reaction, i.e.



has a much greater yield. Here, practically the entire energy is carried off by the γ ray, and the negative muon remains in the bound state. Owing to the large yield of the reaction (5.4) and the appearance of the γ ray, this reaction is convenient for studies of the kinetics of the catalysis process. This was first carried out by Ashmore [11] on the Liverpool synchrocyclotron. The experiment is illustrated in Fig. 5.6, where B is a liquid-hydrogen target. Stopping negative muons are indicated by 1234 coincidences in the scintillation counter telescope. The NaI(Tl) scintillation spectrometer recorded γ rays from reaction (5.3) with energies between 3.0 and 7.5 MeV. Practically all the negative muons stopping in the hydrogen target ended their life in $\mu - e$ decays, so that the target was a source of bremsstrahlung from decay electrons, which considerably increased in the γ -ray background. Another source of γ -ray background was muon capture by nuclei with large Z in the surrounding materials, or by impurity nuclei in the target

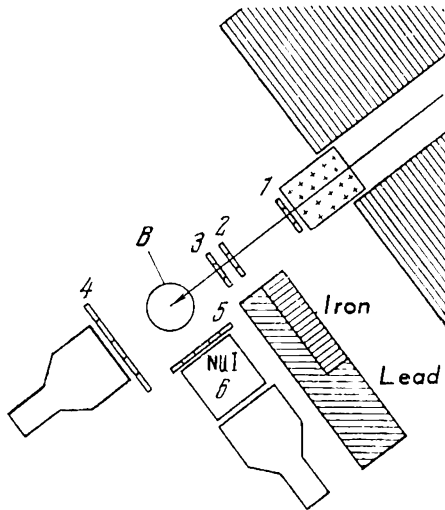


Fig. 5.6 Determination of γ -ray yield from the reaction $(\mu^-, d) + p \rightarrow He^3 \mu^- + \gamma$ (Ashmore et al.)

itself. The experiment of Ashmore et al. was performed with a target containing natural hydrogen and a second target in which 1.8% deuterium impurity was introduced. The experimental time distribution of γ -ray intensity from reaction (5.4) showed that a very large increase in the γ -ray yield was achieved by increasing the deuterium concentration to 1.8%. It was thus demonstrated that reaction (5.3) does occur, and its yield was found to be 0.34 ± 0.06 5.3-MeV photons per negative muon stopping in the hydrogen target. According to the data of Alvarez et al., the yield of 'new' muons from the reaction (5.3) under conditions of saturation was 0.022 ± 0.003 . Hence, the coefficient representing the conversion of reaction energy into the kinetic energy of the 'new' muon is

$$\eta = \frac{0.022 \pm 0.003}{0.34 \pm 0.022} = 0.061 \pm 0.014$$

When the amount of deuterium introduced into the hydrogen target is sufficient to saturate reaction (5.4), the reaction kinetics are determined by the probability λ_{DH} which characterizes the rate of formation of the mesonic molecules $(p\mu^-d)$ from collisions of the type $(\mu^-p) + p \rightarrow (p\mu^-d)$, and the probability λ_f characterizing the rate of fusion of protons and deuterons in the resulting molecules. The time dependance of the reaction yield is of the form

$$n(t) = (1 - \eta) \lambda_f \lambda_{DH} e^{-\lambda_0 t} \frac{1}{\lambda_f - \lambda_{DH}} \{ e^{-\lambda_{DH} t} - e^{-\lambda_f t} \} \quad (5.5)$$

where λ_0 is the decay probability of the free muon and the remaining symbols are defined in Fig. 5.4.

The measurements of Ashmore et al. show that Equation (5.5) is valid, but since the $n(t)$ curve is symmetric in λ_p and λ_{DH} , it cannot be used unambiguously to separate the two exponents. According to Ashmore et al., one of the coefficients lies in the range

$$0.19 \cdot 10^6 \text{ sec}^{-1} < \lambda_{\text{slow}} < 0.88 \cdot 10^6 \text{ sec}^{-1}$$

and the other within the range

$$0.55 \cdot 10^6 \text{ sec}^{-1} < \lambda_{\text{fast}} < 2 \cdot 10^7 \text{ sec}^{-1}$$

These results were substantially improved by Bleser et al. [12] using the accelerator at Columbia University. This experiment is illustrated in Fig. 5.7, where H_2 is the liquid-hydrogen target. The target was either filled with deuterium-enriched liquid hydrogen having a deuterium concentration,

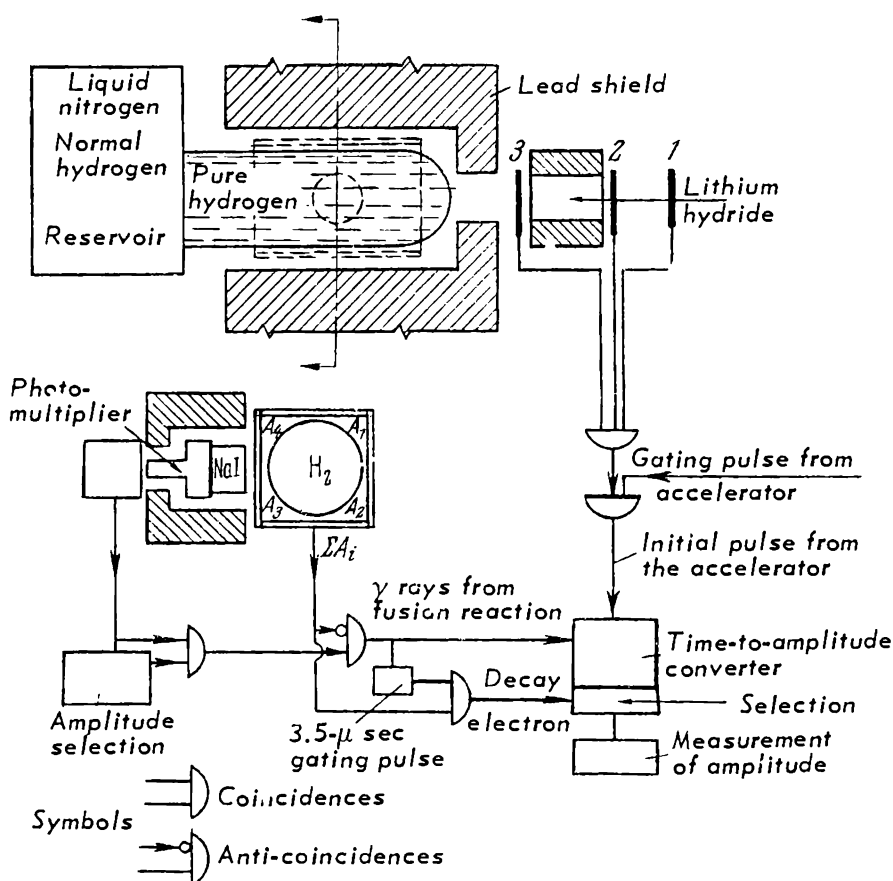


Fig. 5.7 Measurement of the γ -ray yield from the reaction $(\mu^-, d) + p \rightarrow He^3 + \mu^- + \gamma$ (Bleser et al.). The hydrogen target H_2 is surrounded by anti-coincidence counters A_1, A_2, A_3, A_4

C_D , of 8×10^{-3} , or with almost pure liquid hydrogen having a deuterium concentration of 5×10^{-6} . The scintillation counter telescope 1, 2, 3 detected the 125-MeV/c negative-muon beam stopping in the hydrogen target, and the NaI(Tl) crystal spectrometer was used as in the experiments of Ashmore et al. for the detection of γ rays with energies between 4 and 6 MeV. The bremsstrahlung background, due to electrons from $\mu^- - e$ decays and from photons produced in negative-muon capture in high Z nuclei in the material surrounding the hydrogen target, was eliminated by the following technique. The hydrogen target was surrounded by four scintillation counters A_1, A_2, A_3, A_4 which detected decay electrons, and γ -ray pulses in the NaI(Tl) counter were only recorded if they were followed within $3.5 \mu\text{sec}$ by a decay-electron pulse in one of these counters. This method eliminated γ rays which were in coincidence with decay electrons.

The time dependence of the reaction yield obtained in this experiment is shown in Fig. 5.8 for deuterium concentrations

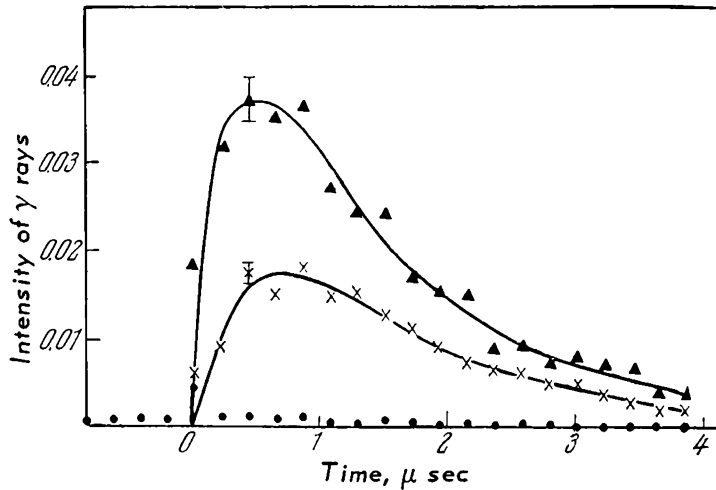


Fig. 5.8 Time dependence of the yield of the reaction $(\mu^-, d) + p \rightarrow \text{He}^3 + \mu^- + \gamma$ (Bleser et al.)

of 5×10^{-6} (points), 110×10^{-6} (crosses) and 8000×10^{-6} (triangles). The last concentration corresponds to saturation. From these results it follows that

$$\lambda_f = (0.26 \pm 0.03) \cdot 10^6 \text{ sec}^{-1}$$

$$\lambda_{DH} = (5.5 \pm 1.1) \cdot 10^6 \text{ sec}^{-1}$$

Identification of the 'slow' exponential with λ_f and of the 'fast' exponential with λ_{DH} was successful because Fetkovich

et al. [10] established a lower limit for λ_{DH} of

$$\lambda_{\text{DH}} > 1 \cdot 10^6 \text{ sec}^{-1}$$

The total reaction yield for any deuterium concentration can easily be obtained by solving the kinetic equations and integrating the resulting solutions. This gives

$$\begin{aligned} N_1 &= \int_0^{\infty} n(t) dt \\ &= (1-\eta) \frac{\lambda_f}{\lambda_f + \lambda_0} \cdot \frac{\lambda_{\text{DH}}}{\lambda_{\text{DH}} + \lambda_0} \cdot \frac{C_{\text{D}} \lambda_{pd}}{\lambda_{\text{HH}} + \lambda_0 + C_{\text{D}} \lambda_{pd}} \quad (5.6) \\ N_2 &= \int_0^{\infty} n(t) e^{\lambda_0 t} dt = (1-\eta) \frac{C_{\text{D}} \lambda_{pd}}{\lambda_{\text{HH}} + C_{\text{D}} \lambda_e} \end{aligned}$$

The yield N_2 , unlike N_1 , is corrected for the exponential decay of the negative muons. The reciprocal yields can also be expressed in terms of the reciprocal concentration:

$$\begin{aligned} \frac{1}{N_1} &= A \left\{ \frac{\lambda_{\text{HH}} + \lambda_0}{\lambda_{pd}} \frac{1}{C_{\text{D}}} + 1 \right\} \\ \frac{1}{N_2} &= B \left\{ \frac{\lambda_{\text{HH}}}{\lambda_{pd}} \frac{1}{C_{\text{D}}} + 1 \right\} \end{aligned} \quad (5.7)$$

It follows from these formulae that the ratio of the slope to the intercept of the straight lines obtained by plotting $1/N$ against $1/C_{\text{D}}$ yields $\frac{\lambda_{\text{HH}} + \lambda_0}{\lambda_{pd}}$ or $\frac{\lambda_{\text{HH}}}{\lambda_{pd}}$. The two probabilities

λ_{HH} and λ_{pd} were obtained in this way. Experimental data obtained by Bleser et al. for $1/N$ as a function of $1/C_{\text{D}}$ are shown in Fig. 5.9. The probabilities λ_{pd} and λ_{HH} obtained from this figure are

$$\lambda_{pd} \approx 1.9 \cdot 10^{10} \text{ sec}^{-1}$$

$$\lambda_{\text{HH}} = (1.4 \pm 0.5) \cdot 10^6 \text{ sec}^{-1}$$

Table 5.2 summarizes published results on muon catalysis. The penultimate column gives the theoretical values of some of the probabilities. The theoretical calculations have been reviewed by Zel'dovich and Gershtein [13].

Table 5.2 Probabilities and yields of various mesomolecular processes in hydrogen

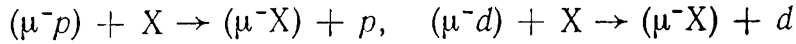
Reaction	Measured value	Reference	Theoretical estimate	Reference
$(p + d + \mu^-) \rightarrow \text{He}^3 + \mu^-$	$\lambda_\gamma = (0.26 \pm 0.03) \times 10^6 \text{ sec}^{-1}$	[12]	$0.33 \times 10^6 \text{ sec}^{-1}$	[14]
$\rightarrow (\text{He}^3 + \mu) + \gamma$	$(0.19 - 0.88) \times 10^6 \text{ sec}^{-1}$	[11]	$(0.18 - 0.48) \times 10^6 \text{ sec}^{-1}$	[13]
Yield, %, per stopping negative muon	γ rays: 33 \pm 8 31 \pm 3 34 \pm 6	[12] [12] [11]		
	'Rejuvenates' 2.4 \pm 0.2			
	Negative muons 2.64 \pm 0.35			
$(\mu^- \bar{p}) + p \rightarrow (p \mu^- \bar{p})$	$\lambda_{\text{HH}} = (1.4 \pm 0.5) \times 10^6 \text{ sec}^{-1}$	[12]	$1.3 \times 10^6 \text{ sec}^{-1}$	[15]
$(\mu^- \bar{p}) + d \rightarrow (\mu^- \bar{d}) + p$	$\lambda_{pd} \approx 1.9 \times 10^{10} \text{ sec}^{-1}$	[12]	$1.36 \times 10^{10} \text{ sec}^{-1}$	[7]
	$\lambda_{pd} = (0.95^{+0.34}_{-0.21}) \times 10^{10} \text{ sec}^{-1}$	[8]	Less accurate estimates yield values in the range $10^9 - 1.8 \times 10^{10} \text{ sec}^{-1}$	
	$\sigma_{pd} = \lambda_{pd} / (\lambda_0 + \lambda_{\text{HH}})$	[12]		
	$= (9.4 \pm 1.0) \times 10^3$ $= (8.9^{+6.2}_{-3.6}) \times 10^3$	[6]		

$(\mu^-d) + p \rightarrow (p\mu^-d)$	$\lambda_{DH} = (5.5 \pm 1.0) \times 10^6 \text{ sec}^{-1}$ $\lambda_{DH} > (6.5 \pm 2) \times 10^6 \text{ sec}^{-1}$ $0.55 \times 10^6 < \lambda_{DH} < 20 \times 10^6 \text{ sec}^{-1}$	[12] [10] [11]	$1.2 \times 10^6 \text{ sec}^{-1}$ $2.9 \times 10^6 \text{ sec}^{-1}$	[7] [16]
$(\mu^-p) + \text{Ne} \rightarrow (\mu^- \text{Ne}) + p$	$x_p \text{Ne} = \lambda_p \text{Ne} + \lambda_{HH}$ $= (9.5 \pm 3.0) \times 10^3$	[5]		
$(\mu^-d) + \text{Ne} \rightarrow (\mu^- \text{Ne}) + d$	$x_d \text{Ne} = \lambda_0 + \lambda_{DH}$ $= (2.7 \times 0.9) \times 10^4$	[6]		
$(\mu^-p) + \text{C or O} \rightarrow (\mu^- \text{C or O}) + p$	$\lambda_p (\text{C or O})$ $= (1.2_{-0.5}^{+0.8}) \times 10^{10} \text{ sec}^{-1}$	[8]		

Note. The methods employed were as follows: Cresti et al., Schiff – hydrogen bubble chamber; Fetkovich et al. – deuterium bubble chamber; Dzhelepov et al. – diffusion hydrogen chamber in a field of 7 kOe; Ashmore et al., Bleser et al. – hydrogen target, γ -ray spectrum for photons from $p + d + \mu^- \rightarrow (\text{He}^3 + \mu^-) + \gamma$

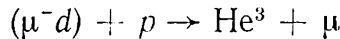
5.3 NEGATIVE-MUON CAPTURE BY IMPURITY NUCLEI IN HYDROGEN

Schiff investigated the probability of transfer of a negative muon, stopping in liquid hydrogen with different deuterium concentrations, to impurity nuclei such as neon and helium, i.e. the probability of reactions of the form



where X is a helium or neon nucleus. To do this, he introduced these nuclei into a hydrogen bubble chamber with different deuterium concentrations. The resulting data are very important for the interpretation of experiments on μ^- capture by protons. It is known that the μ^- -capture probability for nuclei with $Z \leq 20$ is approximately proportional to Z^4 , so that very small impurities of heavy gases in hydrogen may lead to overestimates in the measured probability for protons. The results which were obtained by Schiff are shown in Fig. 5.10.

The solid curve in this figure gives the yield of the reaction



as a function of deuterium concentration in the absence of impurities other than deuterium. With increasing deuterium concentration the yield curve reaches saturation in accordance with the data given in Table 5.1. The remaining points

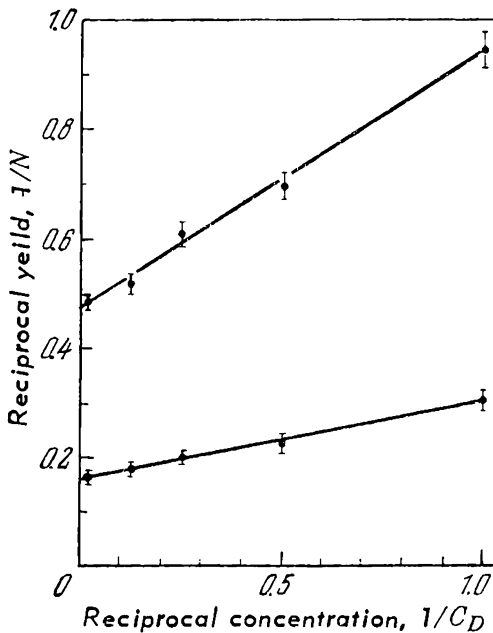


Fig. 5.9 Dependence of the yield of the reaction $(\mu^-, d) + p \rightarrow \text{He}^3 + \mu^- + \gamma$ on deuterium concentration

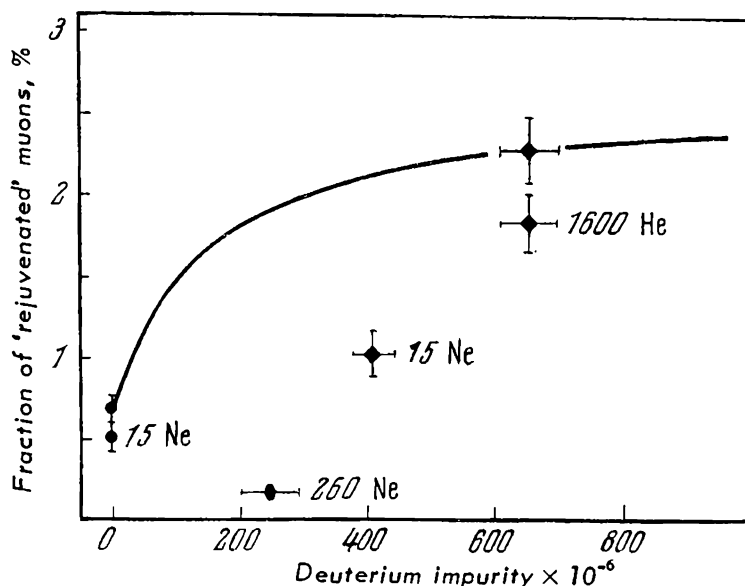
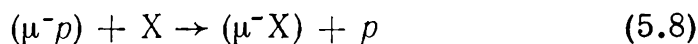


Fig. 5.10 Capture of negative muons by He and Ne impurity nuclei in hydrogen (Schiff)

on the graph represent the yield of 'rejuvenated' negative muons when neon or helium is added to the liquid hydrogen with a given deuterium concentration. The neon or helium impurity concentrations in parts per million are indicated by the numbers against the experimental points. It is clear that a neon concentration of 15×10^{-6} is sufficient to reduce the number of transfers to deuterons by a factor of about 2 with a deuterium concentration of 400×10^{-6} . The relative probability of negative-muon transfer to impurity nuclei X in the reaction



(where X represents deuterium, neon or helium) may be defined by

$$f(C_X) = \frac{C_X \lambda_{pX}}{\lambda_0 + \lambda_{HH} + C \lambda_{pX}} = C_X \frac{1}{\frac{\lambda_0 + \lambda_{HH}}{\lambda_{pX}} + C_X} \quad (5.9)$$

where the numerator includes the probability of (5.8) in sec^{-1} and the denominator the total probability of all possible transfers for the mesonic atom (μ^-p) . The quantity

$$x_{pX} = \frac{\lambda_{pX}}{\lambda_0 + \lambda_{HH}} = \frac{1}{C_{pX}} \quad (5.10)$$

is called the transfer ratio and is equal to the reciprocal of of the concentration, C_{pX} , at which 50% of the mesons are transferred to the impurity nuclei. The values of x_{pX} estimated by Schiff [6] are given in Table 5.2. For deuterium and helium they are given by

$$x_{pd} = \frac{\lambda_{pd}}{\lambda_0 + \lambda_{HH}} = (8.9 \pm_{3.6}^{6.2}) \cdot 10^3$$

$$x_{pNe} = \frac{x_{pNe}}{\lambda_0 + \lambda_{HH}} = (9.5 \pm 3.0) \cdot 10^3$$

For the transfer from deuterium to neon Schiff found

$$x_{dNe} = \frac{\lambda_{dNe}}{\lambda_0 + \lambda_{DH}} = (2.7 \pm 0.9) \cdot 10^4$$

It follows that in the case of hydrogen with minimum deuterium concentration (40×10^{-6}), a neon concentration of

$$C_{pNe} = (105 \pm_{25}^{50}) \cdot 10^{-6}$$

is necessary to ensure that 50% of stopping negative muons are transferred to neon nuclei. For hydrogen with an appreciable deuterium concentration for which the yield of 'rejuvenated' mesons reaches saturation, this quantity becomes

$$C_{dNe} = (37 \pm_{9}^{18}) \cdot 10^{-6}$$

The relative probability of the transfer of a negative muon from the mesonic atom (μ^-d) to Ne is therefore greater than the relative probability of the transfer of a negative muon from the mesonic atom (μ^-p) to Ne by a factor of approximately 2.5. Schiff used the phenomenon of transfer of negative muons to neon to investigate stars produced as a result of μ^- capture by neon nuclei (Section 6.2). The transfer probability of a negative muon from a proton to C and O nuclei was investigated by Dzhelepov et al. using a hydrogen diffusion chamber. Their results are given in Table 5.2 together with other data on mesomolecular processes in liquid hydrogen.

Chapter 6

DEPOLARIZATION OF MUONS. MUONIUM

6.1 KINEMATIC DEPOLARIZATION OF MUONS

According to the $V - A$ theory of weak interactions, the asymmetry coefficient in the angular distribution of electrons from $\pi \rightarrow \mu \rightarrow e$ decays should be $a = -1/3$. It was shown in Chapter 2 that under certain experimental conditions it was possible to approach this value very closely. Usually, however, measured values of $|a|$ are appreciably less than $1/3$. This reduction in the asymmetry coefficient differs for different materials, but even in a given target exposed to different positive-muon beams, the asymmetry coefficient may be found to vary. The observed reduction in the asymmetry coefficient compared with its limiting value is due to depolarization of the positive muons. Part of this depolarization is explained by the kinematic conditions which are involved in the formation of the muon beam from $\pi \rightarrow \mu$ decays in flight. Another part depends on the particular material used for the target, and occurs after the muon has been stopped in the target. In contrast to kinematic depolarization, which is independent of the charge of the muon, target depolarization is quite different for positive and negative muons.

In most counter experiments, muon beams are produced

from pion decays in flight. In all such beams there is an appreciable kinematic muon depolarization because the muons selected by momentum analysis and a collimator are produced over a relatively large angular range in the rest system of the pion. Since muons emitted forwards and backwards in the pion rest system have opposite polarization it is obvious that the polarization of the muon beam emerging from the collimator will be less than unity even if the muon is fully polarized in the rest system of the pion. This problem has been investigated quantitatively by Gol'dman [1], Werle [2], Hayakawa [3] and others. These workers have come to the following conclusions.

Let u and η be the velocity and energy, respectively, of the pion in the laboratory system (in units of c and $m_\mu c^2$), and let v , v' and ε , ε' be the muon velocities and energies (in the same units) in the pion rest system and in the laboratory system respectively. It is then immediately evident that the muon velocity v in the pion system is approximately equal to 0.27, and the total muon energy ε in the pion system must be approximately 1.04. Let ϑ and ϑ' be the angles between the pion and muon momenta in the two systems respectively, and let us suppose that at the instant of decay the muon is fully polarized along its momentum in the pion rest system ($\xi = 1$). The polarization in the laboratory system is then given by

$$\xi' = \frac{\eta v \varepsilon}{v' \varepsilon'} \left(1 + \frac{u \cos \vartheta}{v} \right) \quad (6.1)$$

or, after a simple kinematic transformation,

$$\xi' = \frac{1}{v' v} \left(1 - \frac{\eta}{\varepsilon \varepsilon'} \right) \quad (6.2)$$

Consider the following special cases.

1. Let $u \cos \vartheta = u$, i.e. the muon is emitted in the direction of motion of the pion. To produce a muon with energy ε' , the pion must have the minimum energy

$$\eta_{\min} = \varepsilon' \varepsilon (1 - v' v) \quad (6.3)$$

and the muon remains completely polarized ($\xi' = 1$), which is easily verified by substituting (6.3) into (6.2).

2. Suppose that the muon is now emitted in the opposite direction. We then have $\cos \vartheta = -1$, and to produce a muon with energy ε' , the pion must have the maximum energy

$$\eta_{\max} = \varepsilon' \varepsilon (1 + v' v) \quad (6.4)$$

and the muon emitted backwards in the pion system must have a polarization of opposite sign in the laboratory system ($\xi' = -1$).

3. It is of interest to determine the angle ϑ in the pion rest system for which $\xi' = 0$, i.e. the angle of emission corresponding to the transverse polarization of the muon in the laboratory system.

It follows from the expression for ξ' that $\xi' = 0$ when $\cos \vartheta = -\frac{v}{u}$. In the laboratory system, the angle ϑ' corresponding to this value of ϑ is given by

$$\tan \vartheta' = \eta^{-1} \frac{\sin \vartheta}{\cos \vartheta + \frac{u}{v}} = \eta^{-1} \frac{\sqrt{1 - \frac{v^2}{u^2}}}{\frac{u}{v} - \frac{v}{u}} \quad (6.5)$$

We note that this is the maximum possible angle of emission of muons in the laboratory system (threshold angle).

Let us suppose that we record muons with given energies and velocities ε' and v' . Such muons may originate from pions with energies between η_{\min} and η_{\max} , and the mean polarization $\langle \xi' \rangle$ of the recorded muons may be obtained by integrating the expression for ξ' over the pion spectrum $N(\eta)$ between η_{\min} and η_{\max} . Two cases are then of practical interest. One of these is important for accelerator experiments and the other for cosmic-ray experiments.

a. Kinematic depolarization of muons in accelerator experiments

The conditions governing the formation of muon beams in accelerators are such that the muons leaving the collimator originate from pions with energies in a small range between η_{\min} and $\eta_{\min} + \Delta\eta$. This means that not all angles ϑ between 0 and π are used in the pion system, but only a small part of the angular range near $\vartheta = 0$. Integration of the expression for ξ' over the range $\Delta\eta$ can now be performed by neglecting the change in the intensity of the muon beam, and the result is

$$\langle \xi' \rangle = 1 - \frac{\Delta\eta}{2\varepsilon' \varepsilon v'} \quad (6.6)$$

since

$$\varepsilon v = 1.04 \cdot 0.27 = 0.28$$

and $\varepsilon' \approx 2$ and $v' \approx 0.9$ in the asymmetry experiments described earlier,

$$\xi' = 1 - \frac{\Delta\eta}{0.28 \cdot 2 \cdot 0.9} \approx 1 - 2\Delta\eta \quad (6.7)$$

and hence for, say, $\Delta\eta = 0.1$, we have approximately 80% polarization, i.e. a 20% loss due to kinematic effects.

b. Kinematic depolarization of cosmic-ray muons

The other limiting case of kinematic depolarization is found in cosmic rays. Here, the geometry of the experiments is such that muons emitted in the angular range between 0 and π in the pion rest system are detected, corresponding to the energy range η_{\min} to η_{\max} . Assuming that the atmospheric energy spectrum of cosmic-ray pions can be described by the power law

$$N(\eta) d\eta = \eta^{-n} d\eta$$

and averaging the expression for ξ' over this spectrum between η_{\min} and η_{\max} , we obtain the following result for the mean muon polarization [1]

$$\langle \xi' \rangle = \frac{1}{v'} - \frac{1+n}{n} \cdot \frac{1-v'}{v'} \frac{\left[1 - \left(\frac{1-v'}{1+v'} \right)^n \right]}{\left[1 - \left(\frac{1-v'}{1+v'} \right)^{1+n} \right]} \quad (6.7a)$$

Substituting $n \approx 2$, we find that $\langle \xi' \rangle \approx 0.34$, from which it follows that cosmic-ray muons retain only about 1/3 of their polarization. The polarization of cosmic-ray muons has been investigated by Clark et al. [4], Fowler et al. [5], Barmin et al. [6], Dolgoshein [7], Alikhanyan et al. [8] and others [9-12]. The muons were brought to rest in targets with low depolarization power, e.g. graphite or copper, and the numbers of decay positrons emitted 'upwards' and 'downwards' were measured. After correcting for the experimental geometry and for the absorption of decay positrons in the target (the depolarizing power is known from accelerator experiments),

the measured asymmetry (down - up)/(down + up) may be used to deduce the polarization of muons stopping in the targets, assuming the $V - A$ theory.

The most accurate values of the polarization measured in this way have errors of 10-15%. They were found to lie in the range $\xi' = 0.20 - 0.35$ and showed a slight tendency to increase with increasing positive-muon energy. This tendency apparently reflects an increase of the exponent n in the pion production spectrum with increasing pion energy.

6.2 DEPOLARIZATION OF POSITIVE MUONS IN MATTER

6.2.1 Asymmetry of $\mu^+ - e$ decays in various materials

The asymmetries measured in nuclear emulsions are a characteristic example of depolarization in matter. In this case, the asymmetry in $\mu^+ \rightarrow e$ decays is determined for muons from positive pions stopping in the emulsion and there is no kinematic depolarization. Moreover, the asymmetry coefficient for the angular distribution of decay electrons in nuclear emulsions is very different from the limiting value $a = -0.33$ corresponding to fully polarized muons [13-25].

Consider now the results quoted in [26] where most of the published data were summarised. The weighted asymmetry coefficients obtained with NIKFI-R emulsion was found to be

$$a = -0.095 \pm 0.009$$

whilst the result for Ilford G-5 emulsion was

$$a = -0.139 \pm 0.014$$

It follows that the asymmetry coefficient for the angular distribution of electrons from $\pi \rightarrow \mu \rightarrow e$ decays in nuclear emulsions is lower than the limiting value by a factor of 3 and even differs for different emulsions. This suggests the existence of strong positive-muon depolarization processes between production and decay. It has also been found that an increase in the concentration of gelatine in the emulsion produces an increase in the asymmetry coefficient. The experiments were carried out by Chadwick et al. [24], Gurevich et al. [22], Weissenberg [26] and Ivanov and Fesenko [25]. The asymmetry coefficient obtained after diluting the nuclear

Table 6.1 Asymmetry coefficients for positive muons

Medium	Asymmetry coefficient	Error	Medium	Asymmetry coefficient	Error
Graphite	0.229	0.008	HCl pH = 1.2	0.158	0.011
"	0.29*	0.05			
"	0.24**	0.04	Polyethylene	0.146	0.012
Soot	0.253	0.021	"	0.20*	0.03
Bromine	0.34*	0.06	Polystyrene	0.070	0.010
Al	0.209	0.010	Polystyrene +		
Diamond	0.045	0.008	2% <i>p</i> -ter-		
"	0.25*	0.02	phenyl	0.06**	0.04
" Be	0.222	0.012	Propane	0.170	0.020
" Li	0.201	0.014	Benzene	0.046	0.012
" Mg	0.254	0.013	Phenylcyclo-		
"	0.20*	0.05	hexane	0.084	0.011
" Si	0.253	0.012	Chloroform	0.184	0.015
"	0.21*	0.06	P	0.025	0.017
" Cu	0.24**	0.02	S	0.014	0.011
SiC	0.213	0.011		0.03*	0.06
B ₄ C	0.23	0.02	CsI	0.031	0.013
Al ₂ O ₃	0.022	0.009	NaCl	0.041	0.009
	0.03*	0.03	MgF ₂	0.136	0.009
Fused quartz			MgO	0.079	0.012
(SiO ₂)	0.038	0.009	Emulsion	0.087	0.009
Crystalline			Emulsion	0.13*	0.02
quartz	0.01	0.02	AgBr	0.02*	0.02
Water pH=6.5	0.141	0.011	Gelatine	0.12*	0.03
Distilled			CCl ₄ (liquid)	0.26**	0.05
water	0.14*	0.03	Methyl		
NaOH = 12	0.131	0.012	alcohol	0.16**	0.05

Note. * refers to data from [29]; ** refers to data from [28]. All the remaining numbers are taken from [27]. All the data given in the table are subject to an uncertainty connected with the kinematic depolarization of positive muons which may be different for beams with different energies and different methods of collimation

emulsion by a factor of 2 with gelatine was found to be

$$a = -0.134 \pm 0.019$$

for NIKFI-R emulsion, and

$$a = -0.190 \pm 0.033$$

for Ilford G-5 emulsion. Swanson [27] and Cassels et al. [28]

have measured the asymmetry coefficient a for different target materials. They used a constant magnetic field for the muon spin precession and measured the time between the passage of the muon into the target and the emission of the decay electron from it for each $\mu \rightarrow e$ decay. Since the muon spin precesses with a constant frequency in a constant magnetic field, a definite and known spin orientation corresponds to each such time. This method uses all decays to obtain the asymmetry coefficient and thus ensures a higher statistical accuracy than the experiments of the Columbia group.

A similar method has been developed by the Liverpool group [28]. The effectiveness of the method in increasing the statistical accuracy of the results is evident from the following figures. In the Chicago experiment the monitoring counters recorded 15×10^6 coincidences in one hour, which corresponded to 10^6 stopping muons and 4×10^4 decay positrons. This enabled the asymmetry coefficient a to be determined to within ± 0.01 .

Table 6.1 gives the values of a for the materials investigated in these experiments. The asymmetry coefficients in this table are corrected for the exponential decay of the positive muons, the geometry of the experiments, and energy losses and scattering of decay positrons in the target in which the positive muons came to rest.

It is evident from the table that for some materials - mainly metals and graphite - the asymmetry coefficient is relatively large and amounts to between 0.22 and 0.28; for the remaining media, the coefficient varies within wide limits. The very low values of a found for aluminium oxide, silver bromide, and quartz indicated a practically complete depolarization of the positive muons in these materials.

6.2.2 Relaxation time for the positive-muon spin

The spin relaxation time for positive muons was also estimated in the above measurements. It was found that there was a very rapid depolarization of the positive muons in all the media investigated. This is evident, for example, from curves such as that given in Fig. 6.1, which was obtained for graphite ($a \sim 0.22 - 0.29$). The curve is corrected for decays and it is clear that the precession amplitude was constant for the few microseconds during which the decay positrons were recorded.

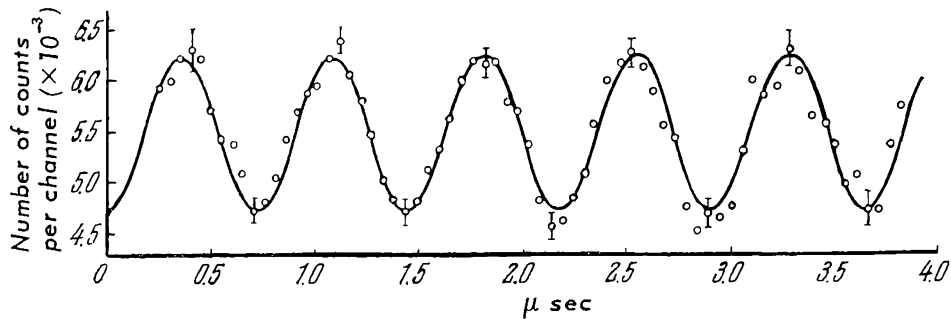


Fig. 6.1 Asymmetry in μ -e decays in graphite (corrected for exponential decay). The asymmetry coefficient is proportional to the amplitude of the sinusoid and is independent of time

Similar curves with a constant modulation amplitude were obtained for other materials, independent of the measured value of the asymmetry coefficient. The fact that the amplitude remains constant for several microseconds shows that the depolarization occurs before the decay electrons are recorded, i.e. the spin relaxation time for the positive muon is less than $0.1-1 \mu$ sec. A similar result was obtained by Swanson [27], who estimated the relaxation time by doubling the magnetic field rotating the spin of the positive muon, and at the same time reducing by a factor of 2 the delay time and width of the gating pulse. He did not find a change in the modulation amplitude, which indicates rapid depolarization. These results suggest that depolarization is produced by a universal mechanism.

The only known exception to this rule is boron carbide (Fig. 6.2), for which the asymmetry has a maximum at the beginning of a cycle ($a = 0.23$) and falls off with a relaxation time of 6.5μ sec, which suggests a different depolarization mechanism in this particular material.

6.2.3 Depolarization of muons during the slowing-down process

The depolarization of a muon in a medium in which it is slowed down may be divided into two stages: depolarization in flight, which occurs during the slowing-down process and depolarization after the muon has been practically brought to rest. The former is due to scattering by the Coulomb

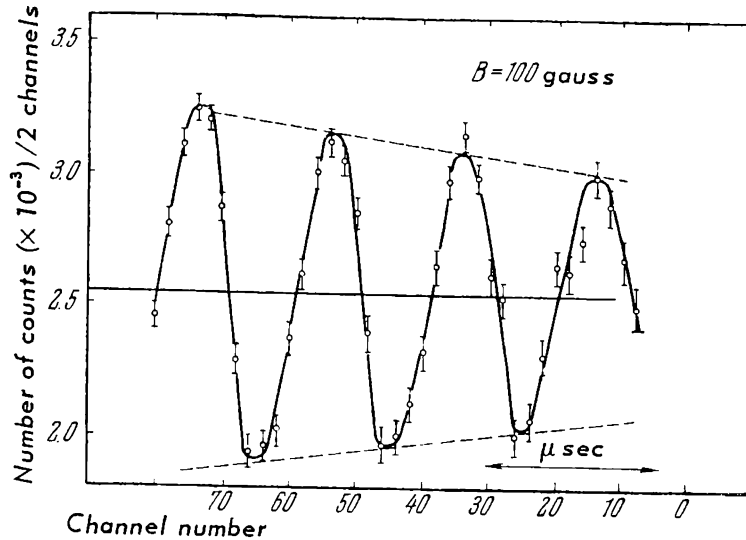


Fig. 6.2 Asymmetry in μ -e decays in boron carbide (corrected for exponential decay). The asymmetry decreases with a relaxation time of $6.5 \mu\text{sec}$

fields of nuclei and electrons, and has been calculated by Ford and Mullin [30], Bincer [31] and Wentzel [32], who showed that this depolarization is negligible. For example, Wentzel [32] obtained the following expression for the mean square angle of rotation of the spin during the slowing down of a particle by Coulomb scattering from nuclei:

$$\langle \vartheta^2 \rangle = \frac{7}{32} \frac{m_e}{m_\mu} \left(\frac{v}{c} \right)^4$$

This quantity is negligible for muons from $\pi \rightarrow \mu$ decays in emulsions ($v/c = 0.27$), and even for $v/c \sim 0.8 - 0.9$, which corresponds approximately to the case of accelerator experiments, $\langle \vartheta^2 \rangle$ is very small.

Depolarization of very slow muons is due to two mechanisms: the effect of magnetic fields in the medium on the magnetic moment of the free positive muon and the formation of atomic systems, i.e. muonium in the case of positive muons and mesonic-atom systems, for negative muons. Consider the first process. The magnetic field perpendicular to the spin of the positive muon produces a precession with Larmor frequency

$$\omega = g \frac{eH}{2m_\mu c} \approx 10^5 \cdot H \text{ rad/sec}$$

It follows that a magnetic field of 5 gauss will produce complete depolarization ($\omega\tau \approx 1$) during the lifetime of the positive muon ($\sim 2 \mu\text{sec}$). It is evident that the effect of strong but short-term internal magnetic fields will be much weaker. Consider, for example, the depolarization of a positive muon in a gas at a pressure of 100 atm, and let us estimate the depolarization occurring as a result of slowing down to thermal velocities ($v \sim 10^6 \text{ cm/sec}$) by collisions with atoms and molecules in the gas. The precession angle due to magnetic fields of electrons acting on the positive muon is $\vartheta_0 = 10^5 H\tau$. If we assume that the collision time τ corresponds to the time taken by the positive muon to traverse one Bohr radius, we have $\tau \approx \frac{10^{-8}}{10^6} = 10^{-14} \text{ sec}$, and if H is taken to be the magnetic field of an electron at a distance of one Bohr radius ($H \sim 10^5 \text{ gauss}$), we find that the precession angle per collision is $\vartheta_0 = 6 \times 10^{-5} \text{ rad}$. The mean precession angle during the lifetime of the positive muon will therefore be equal to about $\vartheta_0 \sqrt{n}$, where n is the number of such collisions. The number of collisions in a gas at 100 atm is 10^{11} - 10^{12} sec^{-1} which yields 10^6 collisions per muon lifetime, and hence $\vartheta = 0.1 \text{ rad}$. It is evident that local fields due to electrons in the gas cannot give rise to appreciable depolarization, and therefore depolarization due to the formation of atomic systems is the only important depolarization mechanism. The large asymmetry coefficient observed for positive muons stopping in graphite and in metals (Table 6.1), i.e. media with high concentrations of conduction electrons, is indirect evidence for the validity of this conclusion. In media such as these, the coupling between the spin of the captured electron and of the positive muon is broken by strong Coulomb interactions with conduction electrons, atomic systems cannot form and there is no depolarization. The magnitude of this effect was obtained by Yakovleva [33].

The effect of the density of conduction electrons on the depolarization of muons was investigated by Feher et al. [34], who studied the asymmetry in $\mu^+ \rightarrow e^+$ decays for positive muons stopping in n - and p -type germanium and silicon. By varying the concentration of the n -impurity (phosphorus) in the n -silicon, the density of conduction electrons could be varied between 10^{12} and 10^{19} per cm^3 . When this was done, an increase was observed in the asymmetry coefficient from very low values (-0.02 to -0.04) to $a \approx -0.3$, which is not very different from the limiting value of $-1/3$.

6.2.4 Effect of magnetic field on positive-muon polarization

It was shown in Chapter 2 that when a nuclear emulsion was placed in a magnetic field of the order of 20,000 Oe, the asymmetry coefficient a increased by a factor of about 3. This phenomenon has been qualitatively explained as a reduction in depolarization due to the formation of muonium. In this section we shall review in greater detail experimental data confirming the validity of the above discussion of the depolarization of positive muons through the formation of muonium.

If the above theory is correct, the role of the magnetic field in eliminating depolarization reduces to the decoupling of the interaction between the magnetic moments of the positive muon and the electron in the muonium atom. The necessary condition for this to occur is that the magnetic energy of the muonium in the magnetic field H , which is equal to $\mu_\mu H - \mu_e H$, should be much greater than the hyperfine-structure splitting energy

$$\Delta W \approx -\frac{32\mu_e\mu_\mu}{3a_{e\mu}^3} \quad (6.8)$$

where μ_e and μ_μ are the magnetic moments of the electron and the muon respectively, and $a_{e\mu}$ is the radius of the first Bohr orbit of muonium. The hyperfine splitting ΔW is equal to 1.84×10^{-5} eV, which corresponds to a frequency $\Delta\nu \approx \frac{\Delta W}{h}$.

The precise value of this quantity, including radiative corrections for the magnetic moments of the muon and electron, the reduced mass of the electron in muonium, and the Breit relativistic effect, is

$$(\Delta\nu)_{\text{theor}} = 4463.13 \pm 0.10 \text{ Mc/s}$$

Depolarization is absent if

$$(\mu_\mu - \mu_e) H \gg \Delta W \quad (6.9)$$

Let $H_0 = \frac{\Delta W}{2(\mu_e - \mu_\mu)}$. The field $H_0 \approx 1588$ gauss can be interpreted as the magnetic field due to the positive muon at the electron orbit in the $1S$ state of the muonium atom, and the condition given by (6.9) is equivalent to $H \gg 1588$ gauss. The principle of experiments in which the magnetic field is used

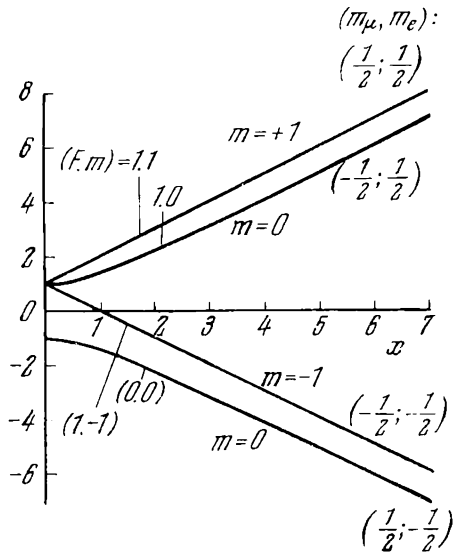


Fig. 6.3 Breit-Rabi diagram for the energy levels of the ground states of muonium in a magnetic field. The level energy ϵ for different F , m_F (weak fields) and m , m_e (strong fields) is plotted as a function of $x = H/H_0$. To obtain the energy, the magnitude of ϵ must be multiplied by $\frac{1}{2}\Delta F$ where $\Delta F = 1.84 \times 10^{-5}$ eV is the hyperfine splitting corresponding to $\nu = \Delta E/h \approx 4460$ Mc/s

to eliminate the depolarization of positive muons may be understood from the Breit-Rabi diagram for the energy levels of the ground state of muonium (Fig. 6.3). Let the direction of the applied field H be opposite to that of the positive-muon beam which we shall assume to be completely polarized. When such positive muons capture unpolarized electrons from the medium, the total angular momentum F of the resulting muonium atom may be either 1 or 0, and the hyperfine-structure states characterized by the total angular momentum F and the z component m_F of this angular momentum along the direction of H are of the form (cf. Breit-Rabi diagram for low x)

$$(F, m_F) = \begin{cases} 1, & -1, \\ 1, & 0, \\ 0, & 0, \\ 1, & +1. \end{cases}$$

The first state (1, -1) cannot be achieved because the magnetic moment of a completely polarized muon is parallel to the magnetic field and therefore the level population is 0, 1/4, 1/4 and 1/2 respectively. In the (1, +1) state, the positive muon retains its polarization completely, whilst in the states (1, 0) and (0, 0) the muon is completely depolarized. This may be interpreted physically as follows. The electron spin precesses in the magnetic field of the positive muon. In the $m_F = 1$ state the electron cannot change the direction of its spin because $m_F = 1$ is a good quantum number. However, the electron spin can change its direction in the

$m_F = 0$ states. This produces a change in the direction of the spin of the positive muon, so that the resultant component of the angular momentum remains equal to zero ($m_F = 0$). This preferential rotation of the positive-muon spin will occur with a frequency $\Delta\nu \approx 4463$ Mc/s, which means that there will be complete depolarization of positive muons in the (1, 0) and (0, 0) hyperfine-structure states.

In very strong magnetic fields $H \gg H_0$, the magnetic coupling between the meson and the electron is disrupted and the magnetic quantum numbers of the electron and the muon, m_e and m_μ , are good quantum numbers. Hence, instead of the states (F, m_F) we have the states

$$(m_\mu; m_e) = \begin{cases} -1/2, & -1/2, \\ -1/2, & +1/2, \\ +1/2, & -1/2, \\ +1/2, & +1/2 \end{cases}$$

with relative populations of 1/2, 1/2, 0 and 0 (cf. the Breit-Rabi diagram for large x). Both the populated states conserve the polarization of the muon. Simple quantum-mechanical calculations (cf. for example [35], [36], [37], [38]) show that in the general case the positive-muon polarization is given by

$$P = P_0 \left\{ \frac{1}{2} + \frac{1}{2} \frac{x^2}{1+x^2} \right\} \quad (6.10)$$

where $x = H/H_0$. The first term in this formula corresponds to polarization connected with the formation of the triplet state of muonium, and the second represents the restoration of polarization by the magnetic field, which is connected with the state $m_F = 0$. The observed asymmetry in the angular distribution of electrons is then of the form

$$N_{e^+}(\vartheta) d\Omega = (1 + Pa \cos \vartheta) d\Omega$$

where a is the maximum possible asymmetry coefficient and ϑ the angle between the muon spin direction and the momentum of the electron at the instant of decay.

Measurements of the asymmetry coefficient $a = \frac{P}{3}$ for decays in emulsions placed in a high magnetic field were performed by Barkas et al. [39], Orear et al. [40], Ali-Zade [41], Weissenberg et al. [43, 44] and Gurevich et al. [62]. The

last authors have carried out measurements in a pulsed 140-kgauss field, using the Dubna synchrocyclotron. The measured asymmetry coefficients are listed in Table 6.2.

It is evident from the table that data on the magnitude of the asymmetry coefficient in the range between 17 and 35 kgauss show that there is practically no increase in the asymmetry with increasing magnetic field. On the other hand, it follows from the $V - A$ theory that at the maximum value of 140 kgauss the asymmetry coefficient approaches the limiting value of $1/3$. This may be regarded as evidence for a slow approach of the asymmetry coefficient to the limiting value with increasing magnetic field. Fig. 6.4 [63] combines nearly all the known published data on the magnetic-field dependence of the asymmetry coefficient. This figure plots $P = 3a$ as a function of $x = H/H_0$. The last point $a = -0.325 \pm 0.010$ for $H = 140$ kgauss is not shown on the graph. Analysis of all the emulsion data shows that they cannot be fitted with the function $P(x)$ obtained on the assumption of single muonium production and that an additional depolarization mechanism must be postulated. This may be charge transfer in which the emitted muon loses and captures an electron several times. This mechanism was considered by Ferrell et al. [38]. If the mean lifetime of muonium after each such capture (expressed in units of $\hbar/\Delta E = 3.6 \times 10^{-11}$ sec) is denoted by $\tau/2$, the dependence of the polarization on the magnetic field is

$$P = P_0 \left[1 - \frac{1}{2} \left(\frac{1}{1 + \tau^{-2} + x^2} \right) \right]^n$$

If there is only one capture ($n = 1, \tau = \infty$), this formula becomes identical with (6.10). For a high magnetic field this yields $P \rightarrow P_0$, whereas for low fields it is capable of explaining the fact that the initial polarization is not equal to $P_0/2$ because of the term τ^{-2} .

The effect of electrons in the medium on the muonium depolarization mechanism was discussed in the most general form by Nosov and Yakovleva [63]. These workers derived the following formula for the polarization as a function of field in emulsions:

$$P = P_0 \left\{ f \frac{1 + 2x^2}{2(1 + x^2)} + (1 - f) \frac{1 + 2x^2}{2(1 + x^2 + v\tau)} \right\} \quad (6.11)$$

where f is the fraction of muons slowed down in gelatine, ν the electron spin flip frequency which is a parameter representing the interaction of an electron in the muonium atom with the medium, and τ the chemical relaxation time for muonium in the medium. Muonium turns out to be chemically bound for an average time of τ and its depolarization ceases (for the ordinary chemical bonding with compensated

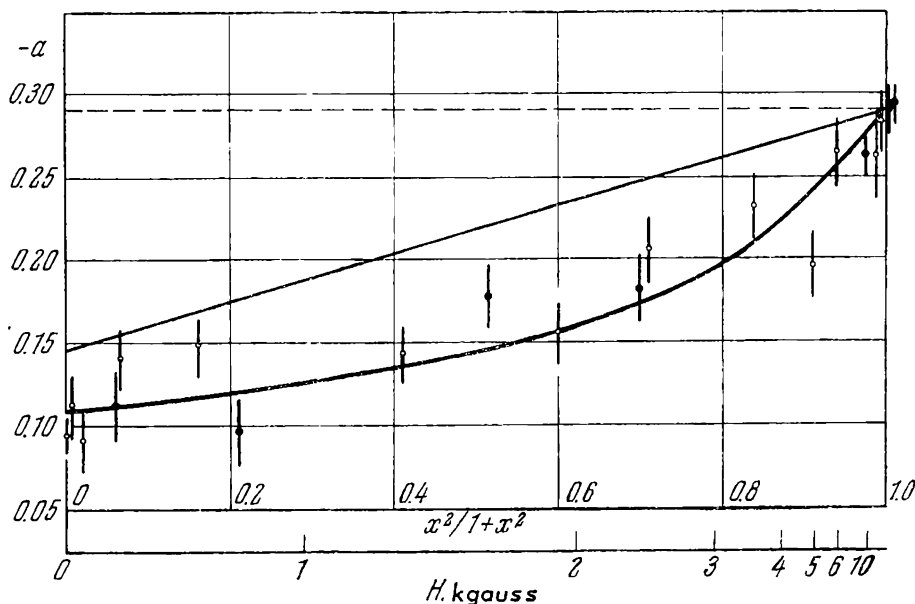


Fig. 6.4 Dependence of the asymmetry coefficient for $\mu-e$ decays in emulsions on the magnitude of the magnetic field [63]

spin pairs). The quantity f in (6.11) represents the fraction of muons, which have slowed down in gelatine, for which $\nu\tau \ll 1$.

The solid curve in Fig. 6.4 shows the dependence described by Equation (6.11) with $f \approx 0.6$ and $\nu\tau = 80$ (these parameters represent the best fit). It is clear that this curve is in good agreement with all the experimental data. For very high fields, when $x^2 \gg \nu\tau \gg 1$, Equation (6.11) assumes the simpler asymptotic form

$$P \approx 1 - 30/x^2$$

This explains the slow approach of the polarization to unity which was demonstrated by Gurevich [62] (Table 6.2).

6.3 SEARCH FOR THE TRIPLET STATE OF MUONIUM

In this section we shall consider data on muonium obtained by other methods. Sens et al. [45] placed a target consisting of fused quartz or a nuclear emulsion in the longitudinal magnetic field of a solenoid, and measured the asymmetry in the emitted positrons with scintillation counters. Their results are in agreement with the emulsion data and show that the asymmetry rises rapidly as the magnetic field is increased from 0 to 7 kgauss, and that additional depolarization connected with multiple losses and captures of electrons by the positive muon must be taken into account. Quantitative analysis of these data is, however, difficult because it is not easy to correct for instrumental effects and systematic errors.

The most direct indication of the existence of muonium is the detection of its triplet state from the precession of the muonic atom. These experiments are analogous to the experiments of Lederman et al., except that the precession of the

Table 6.2

Reference	Magnetic field, kgauss	$-a$
[43]	17	0.280 ± 0.014
[42]	20	0.272 ± 0.023
[42]	25	0.313 ± 0.016
[40]	25	0.290 ± 0.013
[42]	27	0.284 ± 0.016
[42]	35	0.290 ± 0.014
[62]	140	0.325 ± 0.010

triplet state of muonium, whose magnetic moment is higher by a factor of about 207 than the magnetic moment of the positive muon and whose spin is higher by a factor of 2, should occur with a frequency which is higher by a factor of 103.

Swanson [27], and Cassels et al. [28] have tried to detect the triplet state of muonium. The principle of the experiment is that, in a field which is about 100 times smaller than the field used for the precession of the free muon, the triplet state of muonium will precess with a frequency approximately equal to the precession frequency of a free positive muon. Swanson reduced the field to 0.4 gauss and looked for

the precession of the magnetic moment of triplet muonium in fused quartz, liquid glass and teflon.

The Liverpool group [28] investigated polystyrene containing 2% *p*-terphenyl, carbon tetrachloride, methyl alcohol and water in a field of 0.7 gauss. Liquids were chosen for some of these experiments because it was hoped that the effect of local magnetic fields capable of changing the spin direction of muonium in the triplet state would be lower than in solids. Swanson's experiments show that the amplitude of the modulation in the intensity of decay electrons corresponding to the triplet muonium was $0 \pm 8\%$ of the amplitude of the corresponding precession of the free positive muon in graphite. The result of the Liverpool group was $0 \pm 2\%$.

Although the first search for the triplet state in solids and liquids was unsuccessful, the triplet state of the muonium atom has been detected for positive muons stopping in gaseous targets. The first successful experiment of this kind was due to McColm et al. [48], who observed Zeeman transitions induced by high-frequency fields between the $F = 1$ magnetic sub-levels of muonium (Fig. 6.3) for positive muons stopping in N_2O at a pressure of 50 atm. The triplet state was also detected by Hughes et al. [47], who used an argon target at a pressure of 50 atm and observed the precession of triplet muonium. This experiment is illustrated in Fig. 6.5. The Helmholtz coils surrounding the gas target produced a field of 3-5 gauss at right angles to both the initial

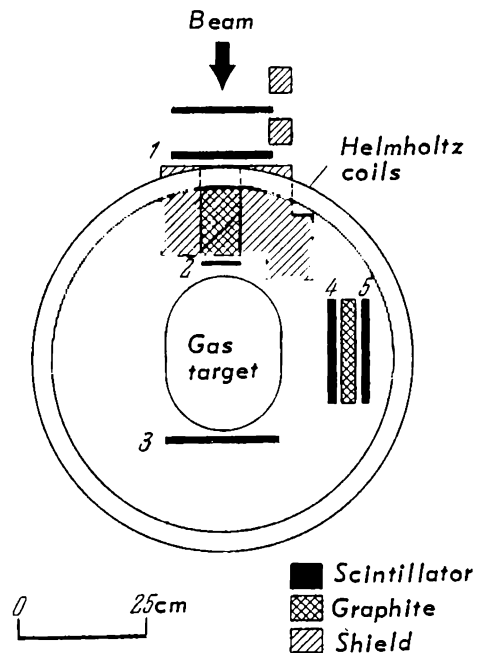


Fig. 6.5 Experiment on the transition of the triplet state of muonium produced by stopping positive muons in argon (gas target)

direction of the positive-muon spin (which was parallel to the direction of the beam, indicated by the arrow) and the direction of a line drawn from the gas target to the counter telescope detecting decay positrons. The time interval between the entry of a positive muon into the argon target ($12\bar{3}$ coincidences) and the 45 pulse in the positron telescope was recorded providing it appeared within the time interval 0.2-20 μ sec following the first pulse. The measured decay-time distribution was subjected to harmonic analysis in order to determine the amplitude corresponding to the precession frequency of the triplet muonium. This analysis clearly showed the presence of a resonance at 6.2 Mc/s in a field of 4.5 gauss, and at 5.3 Mc/s in a field of 3.9 gauss. These frequencies agree to within 5% with the expected precession frequencies for triplet muonium in these fields. Analysis of the data has also shown that practically all the positive muons stopping in argon form muonium and that the mean lifetime of the muonium atom in argon at 50 atm is roughly the same as the lifetime of the free positive muon.

Prepost et al. [46] used an argon-gas target in an experiment similar to that discussed above using emulsions in a magnetic field. On increasing the field from 0 to 6000 gauss, he observed an increase in the asymmetry, which was in qualitative agreement with a characteristic field $H_0 = 1560$ gauss.

Finally, Bailey et al. [49] succeeded in observing transitions induced by high-frequency fields from the states $(m_\mu, m_e) = (1/2, 1/2)$ to the states $(-1/2, 1/2)$. This experiment is illustrated in Fig. 6.6, in which the argon-gas target includes a resonant cavity fed from a microwave source at 1850 Mc/s. The target was in a constant magnetic field which was varied in steps of 20-60 Oe in the range $5700 \pm \sim 250$ Oe. Positive muons stopping in the gas target were indicated by $12\bar{3}$ coincidences and the emission of decay positrons by $34\bar{2}$ coincidences delayed by 0.1-3.3 μ sec relative to the $12\bar{3}$ pulse. The experiment involved determining the coincidence ratio $R = (34\bar{2})/(12\bar{3})$ with and without the high-frequency field for different values of the steady magnetic field. The magnetic field at resonance corresponding to the transition

$$(m_\mu, m_e) = \left(\frac{1}{2}, \frac{1}{2} \right) \rightarrow \left(\frac{1}{2}, -\frac{1}{2} \right)$$

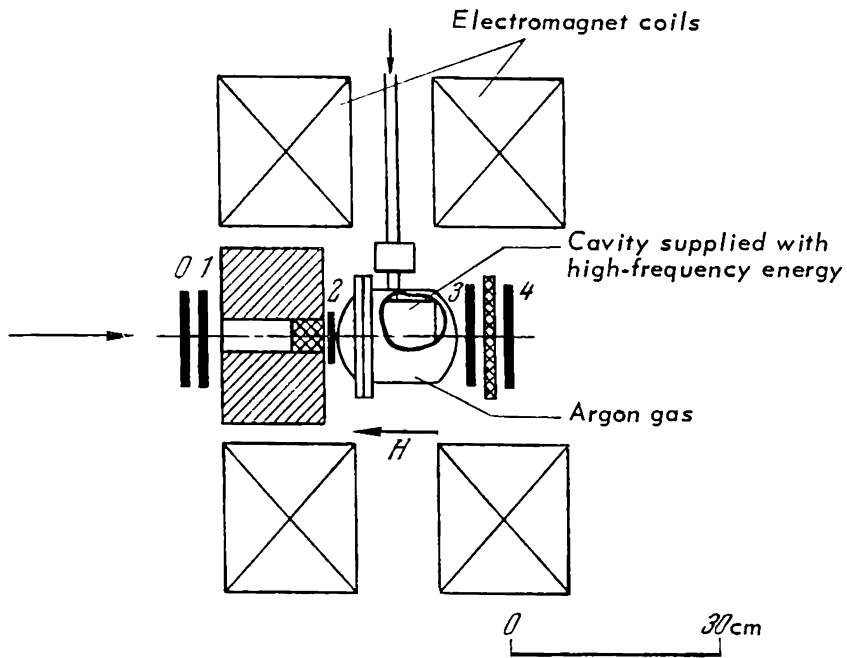


Fig. 6.6 Measurement of the hyperfine splitting in the $1^2S_{1/2}$ state of muonium. The direction of the magnetic field (≈ 5700 gauss) is parallel to the direction of the spin of the positive muons. Positive muons stopping in the gas are indicated by 123 coincidences, decay electrons leaving the target by 342 coincidences

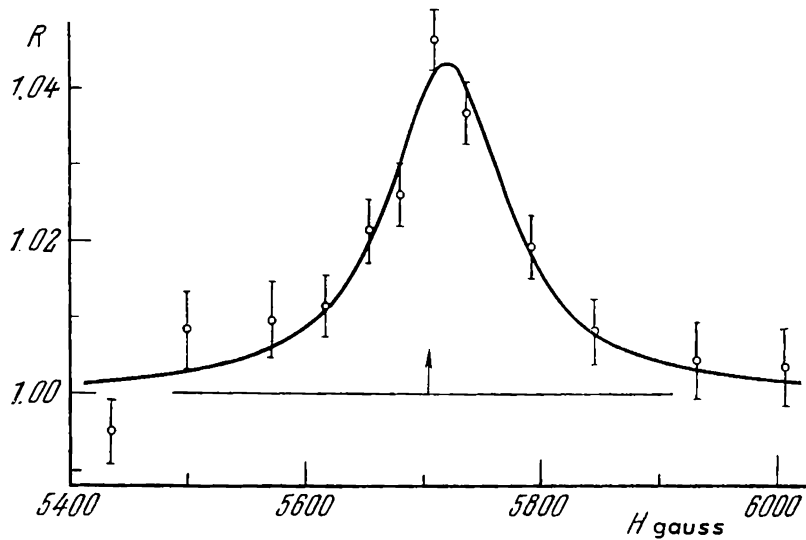


Fig. 6.7 Resonance curve showing R as a function of the constant magnetic field

can readily be deduced from the Breit-Rabi diagram (Fig. 6.3). One of the resonance curves obtained in this experiment is shown in Fig. 6.7. The experimental resonance frequency

$$\Delta\nu = 4461.3 \pm 2.2 \text{ Mc/s}$$

is in good agreement with the theoretical result

$$\Delta\nu_{\text{theor}} = 4463.13 \pm 0.10 \text{ Mc/s}$$

predicted by quantum electrodynamics.

It has recently become possible to observe the precession of triplet muonium in materials other than argon. Zichichi [60] observed the precession at the frequency of triplet muonium in an organic scintillator cooled to -196°C , while Babaev et al. [61] observed this precession during the slowing down of positive muons in crystalline quartz.

6.4 DEPOLARIZATION OF NEGATIVE MUONS

In the first paper of Garwin et al., which demonstrated non-conservation of parity in $\pi \rightarrow \mu \rightarrow e$ decays, it was shown that the asymmetry coefficient of the angular distribution of decay electrons for negative muons stopping in graphite had the same sign as for positive muons, but was smaller by a factor of approximately 7. This result showed that at decay the negative muons had lost a considerable proportion of their initial polarization.

Table 6.3 shows the asymmetry coefficient for negative muons stopping in different elements. All the main isotopes of these elements have zero spin except for fluorine.

The asymmetry coefficient observed for negative muons may be written in the form

$$a_{\mu}^{-} = P_1^{-} \cdot P_2^{-} \cdot a^{-}$$

where a^{-} is the asymmetry coefficient expected for negative muons in the absence of depolarization. The $V - A$ theory predicts $a^{-} = -1/3$. The coefficient P_1^{-} is equal to the polarization of negative muons entering the target and $(1 - P_2^{-})$ is the depolarization produced by the target itself. P_2^{-} is therefore the polarization retained at the instant of decay by muons which are fully polarized on entering the target. For positive muons we have

$$a_{\mu}^{+} = P_1^{+} \cdot P_2^{+} \cdot a^{+}$$

Table 6.3

Element	Nuclear spin	$-a$	P_2^- , %	Reference
H ₂	½	0.01 ± 0.01	3 ± 3	[56]
C	0	0.040 ± 0.005	14 ± 4	[56]
		0.054 ± 0.006	19 ± 3	[57]
		0.069 ± 0.011	24 ± 4	[58]
O	0	0.043 ± 0.005	15 ± 4	[56]
F	½	0.011 ± 0.010	4 ± 4	[58]
Mg	0	0.058 ± 0.008	20 ± 5	[56]
		0.053 ± 0.009	18 ± 4	[58]
Si	0	0.046 ± 0.009	16 ± 4	[58]
S	0	0.042 ± 0.006	15 ± 3	[56]
		0.040 ± 0.006	14 ± 3	[58]
Zn	0	0.056 ± 0.011	19 ± 5	[56]
Cd	0	0.055 ± 0.012	19 ± 5	[56]
Pb	0	0.054 ± 0.013	19 ± 6	[56]

P_1 represents the kinematic depolarization of the positive muons. Assuming that this parameter is the same for muons of either sign, and recalling that $a^- = a^+$, we obtain

$$P_2^- = \frac{a_\mu^-}{a_\mu^+} P_2^+$$

To find the polarization of negative muons at the instant of decay, we must therefore know the asymmetry coefficient a_μ^+ and the residual polarization P_2^+ in a given target. Table 6.1 shows that for graphite $a_\mu^+ = -0.229 \pm 0.008$ and $P_2^+ = 0.79 \pm 0.07$ (Lynch et al. [40]). The corresponding values of P_2^- are given in Table 6.3. It is evident from these data that hydrogen and fluorine will depolarize stopping negative muons almost entirely, whilst the remaining materials depolarize negative muons more effectively than positive muons by a factor of about 5.

A negative muon decays in matter from the K shell of the mesonic atom and therefore the mechanism responsible for depolarization is very different from the mechanism in the case of positive muons, which decay either from the free state or after forming muonium. The history of a negative muon in matter may be considered in the following stages:

1. Slowing down to velocities at which capture into an orbit of a mesonic atom becomes possible.
2. Transition from the continuous spectrum to a bound

state in one of the distant orbits of the mesonic atom with large n and l .

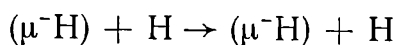
3. Cascade transitions to the ground state of the K shell in which the negative muon decays.

The first of these stages does not contribute appreciably to depolarization. Depolarization in the last two stages is determined mainly by the spin-orbit interaction and, if the nucleus has a spin, there is also a contribution due to the hyperfine interaction between the spins of the muon and the nucleus. The magnitude of depolarization on capture to higher levels and in the process of cascade transitions was calculated for spinless nuclei by Shmushkevich [50], Dzhrbashyan [51] and Mann and Rose [52], who arrived at the following conclusions. After the initial capture, the negative muon retains about 1/3 of its initial polarization. In light elements, this is followed by the emission of a few Auger electrons until the negative muon reaches a state with principal quantum number 3 or 4. Further radiative transitions take the negative muon to the ground state and as a result it loses a further 50% of the remaining polarization. The final polarization of the muon is therefore about $1/3 \times 1/2$, approximately 17% of its initial value. This figure is in good agreement with the magnitude of P_2^- obtained for spinless nuclei (Table 6.3). If the spin of the nucleus is not zero, the spin-spin interaction between the muon and the nucleus gives rise to additional depolarization in the K shell. Überall [53], Lubkin [54] and Bukhvostov and Shmushkevich [55] have shown that this additional depolarization is equal to

$$\frac{1}{3} \left[1 + \frac{2}{(2I+1)^2} \right]$$

when only the hyperfine splitting of the $1S$ level is taken into account, where I is the spin of the nucleus. For a nucleus with $I = 1/2$ this amounts to 50%. It follows that the expected value of P_2^- for fluorine nuclei is 8%. This is consistent with the experimental result $4 \pm 4\%$ (Table 6.3).

Liquid hydrogen is another medium with very low residual polarization. The mechanism responsible for the depolarization of negative muons stopping in liquid hydrogen was elucidated by Bukhvostov et al. [55], who showed that the main process was the scattering of neutral mesonic atoms of hydrogen by protons:



There is a high probability for proton exchange and the simultaneous transition of the mesonic hydrogen atom to a lower hyperfine state characterized by zero total angular momentum. Since the exchange probability in liquid hydrogen (approximately 10^9 sec^{-1}) is larger by three orders of magnitude than the decay probability of the negative muon ($0.45 \times 10^6 \text{ sec}^{-1}$), the mesonic atoms will all undergo transitions to the hyperfine ground state during the lifetime of the negative muon. This process will result in the depolarization of negative muons.

Chapter 7

COSMIC-RAY MUONS

7.1 ORIGIN OF THE MUON COMPONENT

There are two sources of muons: cosmic rays and pion beams produced by accelerators. Despite the fact that the muon intensity in cosmic rays is lower by several orders of magnitude than the intensity which can be produced with modern accelerators, all the main properties of the muon, such as charge, mass, decay scheme, spin, mean lifetime, and even the nature of its interaction with nuclear matter, were established before the advent of large accelerators. Throughout this book we have not referred to cosmic-ray experiments to any great extent because accelerator data which were obtained subsequently are, of course, more accurate.

In this final chapter, we shall review the main properties of the muon component of cosmic rays. This component is of secondary origin since it is produced by the decay of high-energy pions. Muons penetrating the atmosphere carry traces of the characteristic features of the interactions in which the primary pions were produced. Studies of the properties of the muon component, such as its variation with altitude, its energy spectrum, geomagnetic effects and its

genetic connection with other cosmic-ray components, may throw light on the elementary processes leading to the formation of pions and other primary particles. This latter problem, however, lies outside the scope of this book.

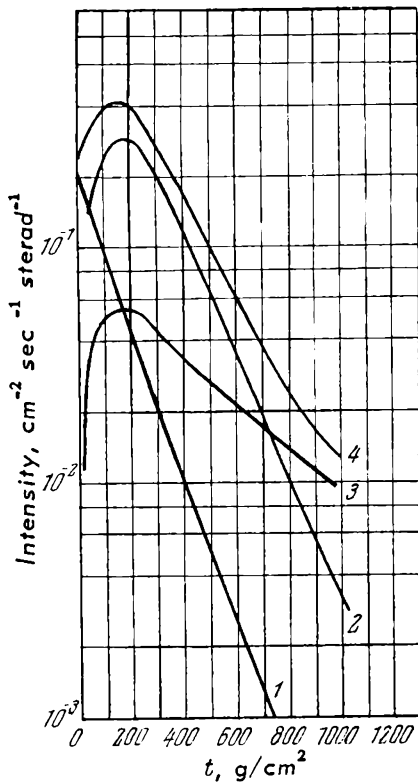
This chapter is concerned mainly with the properties of the muon component as a source of muons. In some respects, this is a most convenient source. The spectrum of cosmic-ray muons extends from low momenta of the order of 10 MeV/ c to an enormous value of the order of 10^6 - 10^8 MeV/ c . This means that experiments can be carried out either with slow muons, which can be brought to rest in a few grammes of matter, or with high-energy muons which are capable of penetrating hundreds of metres of dense material. The range of phenomena corresponding to this energy spectrum is also enormous: at one end, for example, there are the properties of muonic atoms and, at the other, searches for anomalous phenomena in the interaction of high-energy muons with matter.

7.2 MAIN COSMIC-RAY COMPONENTS

The basic experimental fact about cosmic rays in the earth's atmosphere is that they consist of a hard and a soft component. This can be easily demonstrated by measuring the absorption of cosmic rays with a Geiger-counter telescope together with additional devices consisting of small counter hodoscopes for recording cascade showers produced by high-energy electrons in lead plates as they pass through the telescope. This method may be used to show that the soft component is completely absorbed by 10-15 cm of lead and consists mainly of electrons. The hard component, which amounts to about 80% of all particles incident on the instrument at sea level, consists of high-energy muons, a proportion of which are capable of penetrating enormous amounts of matter.

Let us consider some of the data on the absolute intensity of the hard component. For example, at sea level near the geomagnetic latitude 50°N the intensity of the hard component in the vertical direction is $I_v = 0.89 \times 10^{-2} \text{ sec}^{-1} \text{ cm}^{-2} \text{ sterad}^{-1}$. At 4300 m above sea level $I_v = 2.50 \times 10^{-2} \text{ sec}^{-1} \text{ cm}^{-2} \text{ sterad}^{-1}$.

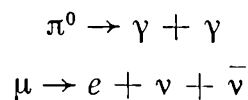
Fig. 7.1, which is taken from Puppi's review [1], illustrates the composition and the altitude variation of cosmic rays.



1 - protons and α particles
 2 - electrons; 3 - mesons;
 4 - total intensity

Fig. 7.1 Altitude variation of the main components of cosmic radiation for 50°N. The intensity is plotted as a function of the depth in the atmosphere

The intensity of the various components is shown as a function of depth t in the atmosphere (sea level corresponds to $t = 1030 \text{ g/cm}^2$). Curve 1 gives the intensity of protons and α particles which form the main part of the primary cosmic radiation incident on the earth's atmosphere from outer space. Curve 2 gives the intensity of the electron-photon component of cosmic radiation which is almost entirely absorbed by 10 cm of lead. This component is of secondary origin, having been produced mainly from the decay of neutral pions into high-energy photons and muons into electrons and neutrinos in accordance with the decay schemes



and subsequent electromagnetic cascade processes. Curve 3 shows the altitude variation of the intensity of the meson component of cosmic rays which consists mainly of muons. In fact, the mean lifetime of muons is about $2.2 \mu \text{ sec}$, which is longer by roughly two orders of magnitude than the lifetimes of pions and kaons. Moreover, muons have a very

weak interaction with nuclei, while the interaction range for pions is of the order of 100 g/cm^2 . Therefore, only muons survive and penetrate large thicknesses of matter, while pions and kaons decay, or are absorbed, near the point at which they are produced.

7.3 MUON ENERGY SPECTRUM AT SEA LEVEL

The energy spectrum of muons at sea level is the most thoroughly investigated characteristic of cosmic rays. Most of the early measurements, i.e. those carried out prior to 1948, were reviewed and unified by Rossi [2]. Most of them were performed with Wilson cloud chambers in magnetic fields. The final spectrum obtained in this review extends to momenta of $pc \approx 2 \times 10^{10} \text{ eV}/c$ and is shown in Fig. 7.2 (solid curve) on a logarithmic scale. The spectrum obtained by Rossi passes through a maximum in the region $(4-6) \times 10^8 \text{ eV}/c$ and falls off rapidly with increasing momentum. For momenta greater than $4 \times 10^9 \text{ eV}/c$ it may be represented by a power law $M(p) dp \approx p^{-n} dp$, with $n \sim 1.8$. Glaser et al. [3] extended the measured muon spectrum to $7 \times 10^{10} \text{ eV}/c$ using two cloud chambers separated by a magnetic field produced by an electromagnet. By measuring the magnetic deflection for 1547 particles of the hard component they showed that the spectrum may be described by the power law $p^{-n} dp$, with $n = 1.8 \pm 0.2$ for $(2.5-10) \times 10^9 \text{ eV}/c$ and $n = 2.1 \pm 0.6$ for $(10-70) \times 10^9 \text{ eV}/c$.

An important disadvantage of the cloud-chamber method is the small relative aperture which makes it difficult to accumulate adequate statistics at large momenta, and also appreciable distortions of the trajectory in the filling gas, which restricts measurements of high momenta. Large hodoscope systems consisting of Geiger counters in a magnetic field are free from these disadvantages. This method, which was first used by Alikhanyan et al. [4], led to a very rapid increase in the available statistics and to an increase in the maximum measurable momentum by several orders of magnitude. The experiment is illustrated in Fig. 7.3, where N,S are the poles of the permanent magnet (pole area $50 \times 12.5 \text{ cm}^2$, air gap 8 cm, field 3840 gauss). The first three rows of counters were used to determine the coordinates of the trajectories of the particles which passed through the instrument and were deflected by the magnet.

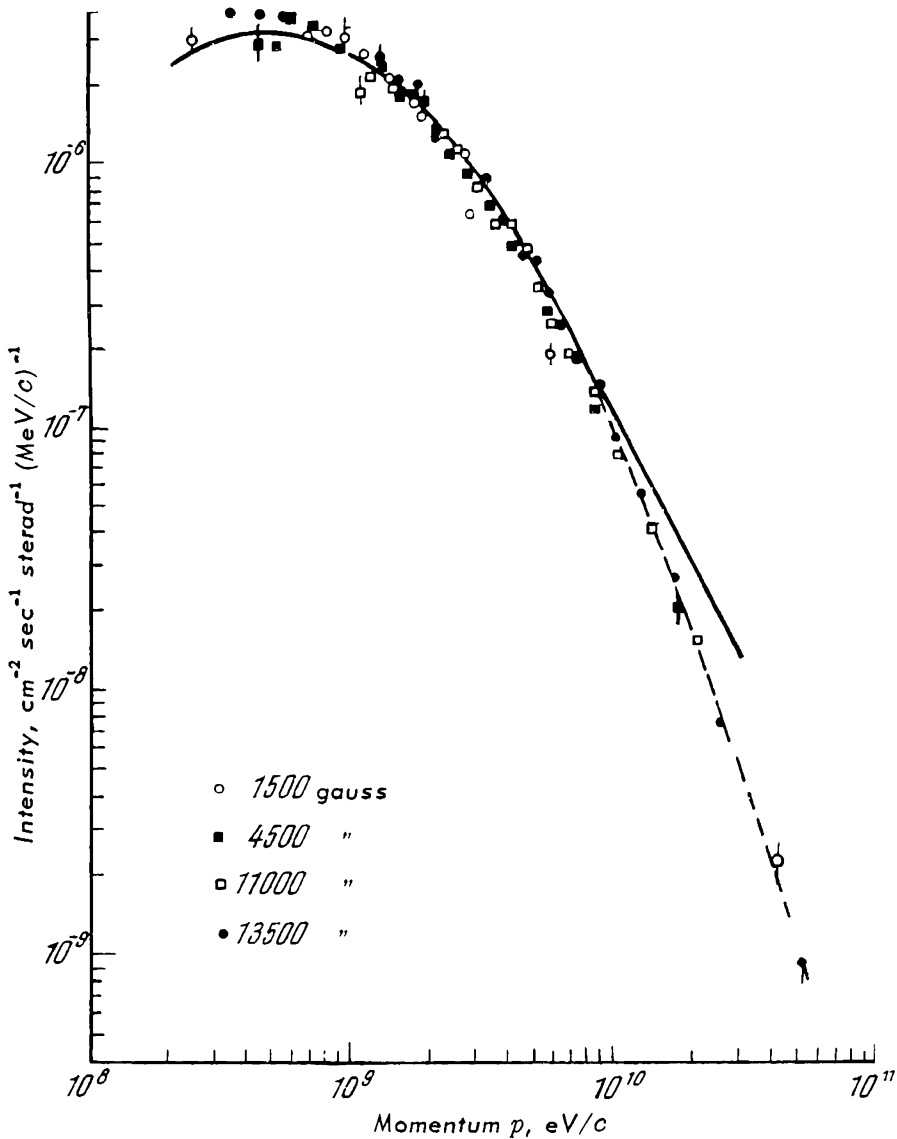
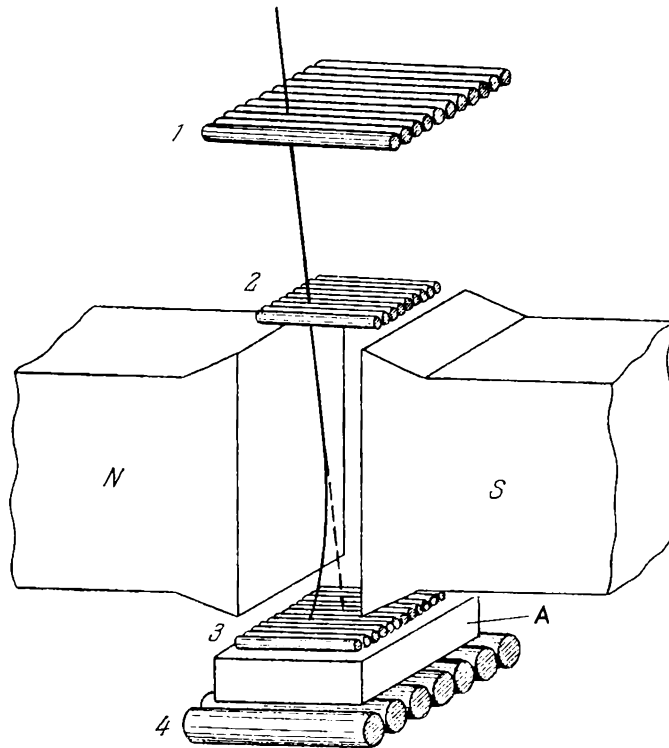


Fig. 7.2 The Rossi spectrum based on measurements performed up to 1948 and the spectrum of Caro et al. obtained with the Melbourne magnetic spectrometer

Counters in the last (fourth) row could be used to distinguish the soft component from the hard, which consists mainly of muons. The soft component, which consists mainly of electrons, can be identified more efficiently by adding one or more hodoscope counters separated by lead absorbers. In such a system, hodoscope counters detect cascade multiplication of electrons in lead, while muons pass through the telescope as single particles.

Fig. 7.2 also shows the muon spectrum obtained with the large magnetic spectrometer built by Caro et al. [5]. This



N, S – magnet poles; 1, 2 – hodoscopic counters defining particle track direction; 3 – counters defining the deflection of the particle in the magnetic field; 4 – counters for the separation of the soft and hard components; A – absorber

Fig. 7.3 Principle of the cosmic-ray spectrometer (Alikhanyan and Alixhanov)

spectrum extends to 5×10^{10} eV/c. The Rossi and Caro spectra are in good agreement for momenta below 10^{10} GeV/c. At higher momenta the spectrum measured with the magnetic spectrometer falls off more rapidly than Rossi's spectrum. This is probably due to an underestimate of the uncertainty in the early momentum measurements which are included in Rossi's spectrum. These uncertainties may be due, among other things, to turbulence in the cloud chamber.

Similar measurements were carried out by the Manchester group in the momentum range $(0.5 < p < 20) \times 10^9$ eV/c [6, 7]. Their magnetic spectrometer consisted of two electromagnets, one above the other, and counter hodoscopes. They examined the spectra of 60 000 particles and because of the improved statistical precision these measurements may be taken as standards in this range. The resulting spectrum is shown together with the Rossi spectrum in Fig. 7.4.

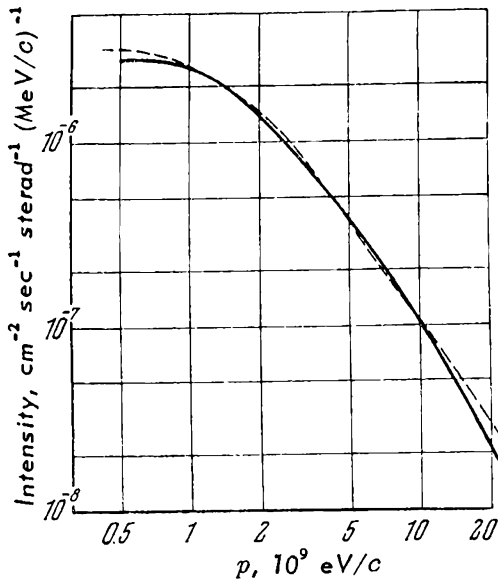


Fig. 7.4 Muon momentum spectrum obtained by Owen and Wilson with the Manchester spectrometer in the range 0.5×10^8 – 2×10^{10} eV/c. Broken curve shows Rossi's spectrum. The two spectra are normalized to $p = 10^9$ eV/c

Measurements of the muon spectrum for mesons arriving in the vertical direction have been extended by Pine et al. [8] to higher momenta (Cornel University), Holmes et al. [9] (Manchester) and Ashton et al. [10] (Durham spectrometer). All these experiments used large magnetic spectrometers and the muon spectra were established up to momenta equal to 1.75×10^{11} , 1.16×10^{12} and 1.7×10^{12} eV/c respectively. In the Manchester spectrometer [11] cloud chambers were placed above each of the Geiger-counter trays. The upper window of each chamber carried a coordinate grid and the measurements involved the determination of the coordinates of the point at which the trajectory cut the grid. The principle of these measurements is clear from Fig. 7.5, where the shaded regions show the magnetic fields produced by the upper and lower electromagnets and A,B,C are the points of intersection of the trajectory with the cloud chambers. A similar method has been used by the Cornell group. The spectrum reported by Ashton et al. was obtained with a large magnetic spectrometer 5-m long and the maximum momentum measured was about 10^{12} eV/c. The deflection of muons by the magnetic field was measured with the aid of Geiger counters and neon-filled tubes [12].

The intensities of the muon component per unit solid angle in the vertical direction obtained with these three spectrometers are shown together in Fig. 7.6. Below 10^{11} eV/c the statistical uncertainties are very small and the corresponding experimental points are therefore not shown

aa', bb', cc' – plane Wilson chambers; ABC – straight line joining the points of entry and exit of the muon; $A'BC'$ – muon trajectory

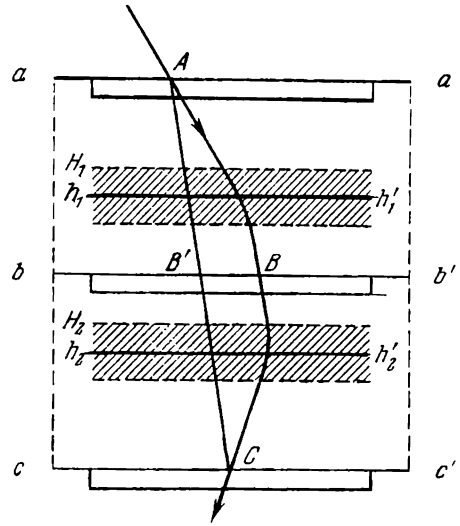


Fig. 7.5 Principle of the Manchester experiment. Shaded area corresponds to the region occupied by the magnetic field of the upper and lower electromagnets

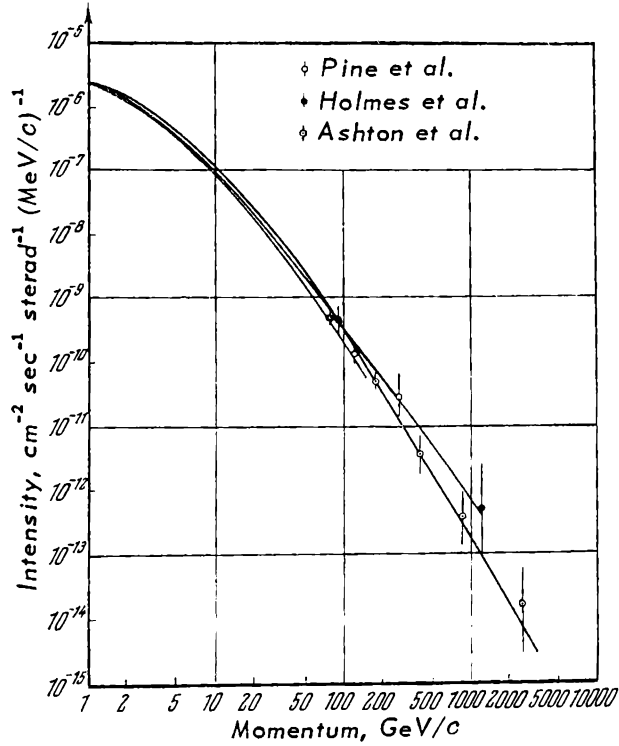


Fig. 7.6 Muon momentum spectrum obtained by Pine et al., Holmes et al. and Ashton et al. Experimental points are indicated only for momenta greater than 80 GeV/c. The spectra are normalized to $p = 10^9$ eV/c

in this figure. The intensity decreases very rapidly with increasing momentum and can be described by a power law of the form $p^{-n}dp$ with n between 2 and 3 for momenta between approximately 10^9 and 10^{11} eV/c.

7.4 THE ENERGY SPECTRUM OF MUONS AT LARGE ZENITH ANGLES

The intensity of the muon component is a maximum in the vertical direction. Its total intensity falls off very rapidly with increasing angle to the zenith. As an example, consider the data of Allen and Apostolakis [13] obtained with a magnetic spectrometer at sea level. These results are shown in Fig. 7.7 in which the intensity of muons with momenta greater than 10^9 eV/c is plotted as a function of the zenith angle. It is evident that with increasing zenith angle there is an exceedingly rapid reduction in the total intensity of the muon component.

Very interesting data were obtained on the intensity and energy spectrum of high-energy muons arriving at large angles to the vertical. Such muons arrive from an almost horizontal direction and originate from pions travelling in this direction. The pions are produced in the rarefied gas of the upper atmosphere and those travelling horizontally have a much longer path before interaction than those travelling vertically. Pions travelling in the horizontal direction therefore have a much greater probability of producing decay muons than those arriving in the vertical direction. The muon energy spectrum will therefore

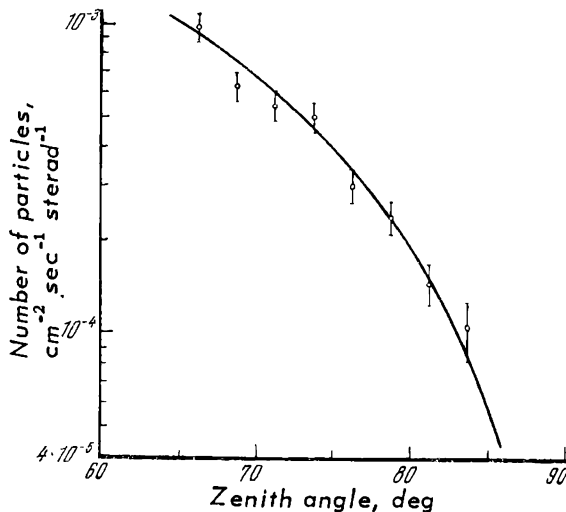
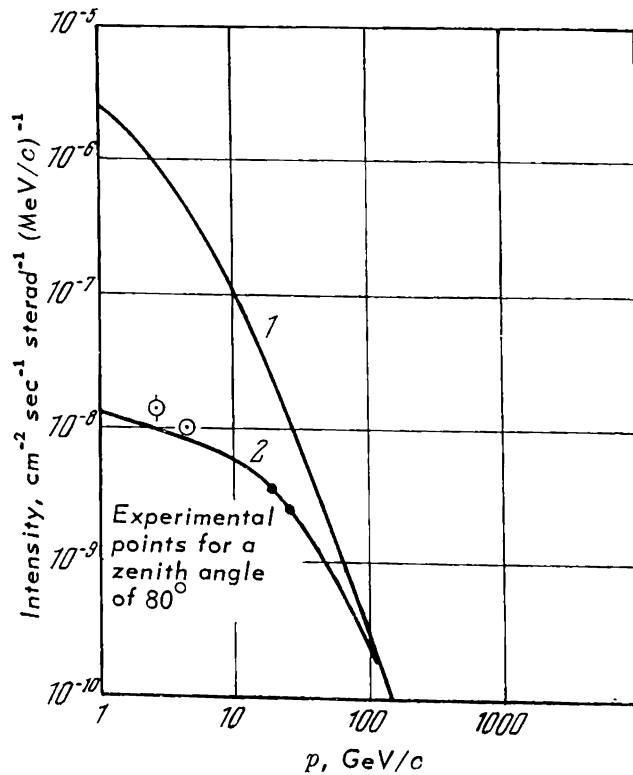


Fig. 7.7 The intensity of muons with momenta greater than 10^9 eV/c as a function of the zenith angle (Allen and Apostolakis)

become enriched with high-energy muons as the zenith angle increases, and the muon intensity at very high momenta may even exceed the muon intensity in the vertical direction. This effect was first pointed out by Jakeman [14] who measured the intensity of muons with momenta greater than 400 GeV/c arriving in the horizontal direction at sea level. He showed that the intensity was much greater than the intensity of high-energy muons in the vertical direction. A similar result was obtained by Wilson [15]. Fig. 7.8 shows the results of Ashton and Wolfendale [16] who deflected muons arriving at 80° to the zenith in magnetized iron. The muon spectrum for the vertical direction is shown together with the theoretical spectrum obtained by Apostolakis and Allen [13] on the assumption that the only source of muons is $\pi-\mu$ decay. It is evident that the intensities are equal for momenta of the order of 10^{11} eV/c, and that muons arriving at 80° have a harder spectrum. Sheldon and Duller [17] used



1 - spectrum for vertical direction (Ashton et al.); 2 - theoretical spectrum obtained from curve 1 by Apostolakis and Allen

Fig. 7.8 The spectrum of muons arriving at a zenith angle of 80° (experimental points)

a counter telescope to determine the intensity of the muon component at different depths underground for a zenith angle of $69 \pm 3^\circ$. They showed that, at depths greater than about 140 m of water equivalent, the muon intensity begins to exceed the intensity of the muon component arriving in the vertical direction through the same layer of matter.

It follows from the above data that interactions involving muons with energies greater than about 10^{11} eV are best investigated with muons arriving at angles near the horizontal.

7.5 ENERGY SPECTRUM OF LOW-ENERGY COSMIC-RAY MUONS

The muon energy spectrum shown above exhibits a rapid reduction in intensity with increasing momentum, and can be described by the power law $p^{-n} dp$, with n between 2 and 3, for momenta between 10^9 and 10^{11} eV/c.

We will now consider the low-energy end of the spectrum, to the left of, or near, the maximum. It is this part of the spectrum which is the source of slow muons in experiments in which muons are brought to rest in a target in order to study decay or capture reactions.

The maximum in the muon momentum spectrum is due to the fact that as the muon energy decreases, there is an increase in the specific ionization loss and a reduction in the relative importance of the relativistic time dilatation effect so that the lifetime approaches the lifetime of the muon at rest ($\tau_0 \approx 2.2 \mu\text{sec}$). These two factors lead to a reduction in the number of slow mesons, and the spectrum falls off rapidly with decreasing momentum below $(4-6) \times 10^8$ eV/c (see Fig. 7.2). Fig. 7.9 shows measurements of the hard component in the range $(2-20) \times 10^8$ eV/c [18] at a height of 3250 m above sea level, using the spectrometer illustrated in Fig. 7.3. Again, there is a clearly defined maximum at about 6×10^8 eV/c, with a rapid decrease in intensity with decreasing momentum.

At low momenta, the usual absorption method, or the absorption method operated in conjunction with delayed coincidences, become just as effective as the magnetic deflection method in measurements of the intensity and energy spectrum of the muon component. In the simple absorption method, the differential range spectrum is determined by counting the number of mesons which have passed through

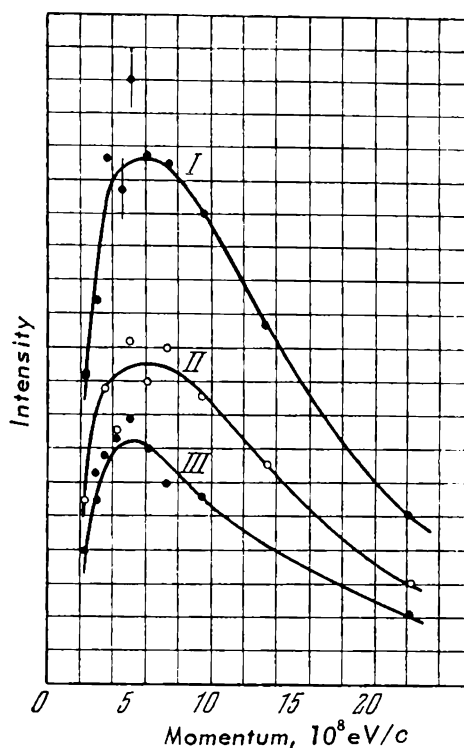


Fig. 7.9 Muon momentum spectrum obtained at 3250 m above sea level (I - $\mu^+ + \mu^-$, II - μ^+ , III - μ^-). Particles included in this spectrum passed through 6.6 cm of lead and 8 cm of graphite. Electrons were separated with the aid of absorption and multiplication in a 1.5-cm lead filter placed under the third row of counters (cf. Fig. 7.3)

an absorber of thickness R and those which have stopped in the next layer ΔR . The method of delayed coincidences is similar to the last method, except that muons stopping in the layer ΔR are observed by detecting delayed counts produced by decay electrons leaving the layer ΔR . This method is particularly useful for eliminating particle impurities, e.g. protons.

To obtain quantitative information on the intensities of slow pions and muons, we will consider the results of Fotino [19] who used a cylindrical plastic scintillator of height 7 cm and volume 600 cm³ to determine the slow-muon intensity at 91, 3260, and 4310 m above sea level. His results are shown in Fig. 7.10, where the intensity given is averaged over all directions. It is evident from these data that at sea level the number of slow muons stopping in the scintillator exceeds the number of pions by a factor of 15. Even at a height of 3410 m this factor is still 2.5.

Detailed measurements of the intensity of the meson and proton components of cosmic rays for ranges equivalent to 10-300 cm of air were performed by Conversi [20], at heights between sea level and 10 km and at geomagnetic latitudes between 9 and 50°N. Some of the data are given in Fig. 7.11, which shows the intensity of slow mesons

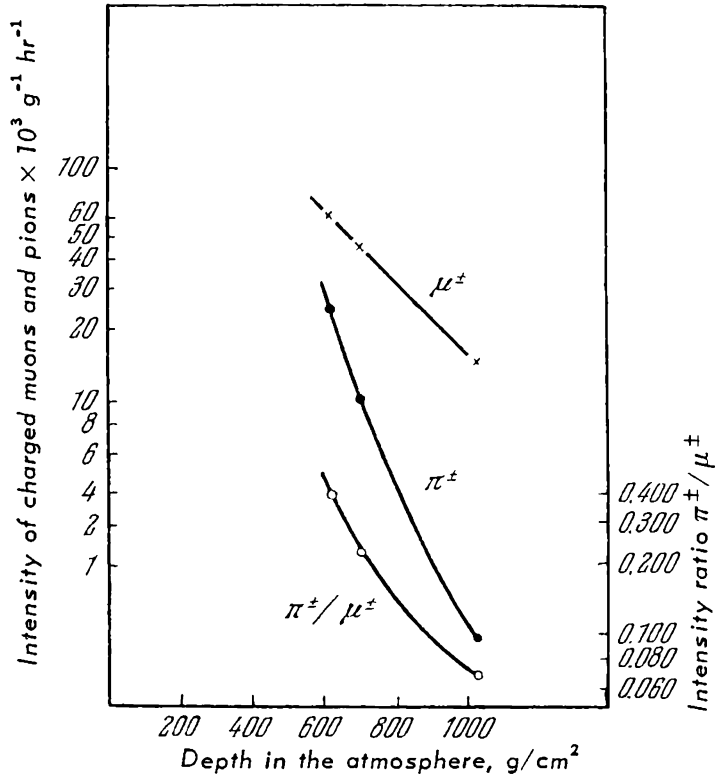


Fig. 7.10 Intensity of slow pions and muons at sea level and at high altitudes

and protons as a function of altitude for the geomagnetic latitude 50°N . Muons or protons which penetrated 15 cm of lead and came to rest in a following 10-cm layer of lead were recorded in these measurements. It is evident that near sea level the meson component has a much higher intensity than the proton component in the same interval of range: at sea level they differ by a factor of 6. The altitude variation of intensity is well approximated by the formula

$$N(t) dt \sim e^{-t/L} dt$$

where L is approximately equal to 150 g/cm^2 for mesons and 280 g/cm^2 for protons. Because of this difference, the two components are equal in intensity at about 500 g/cm^2 , and at higher altitudes the proton component predominates. Conversi also investigated the latitude effect for slow mesons. At a height of 10 km, the muon intensity in the momentum band 315-348 MeV/c changes by a factor of 1.87 ± 0.12 between 9° and 50° latitude. These results are shown in Fig. 7.12.

The latitude effect for slow muons near sea level was

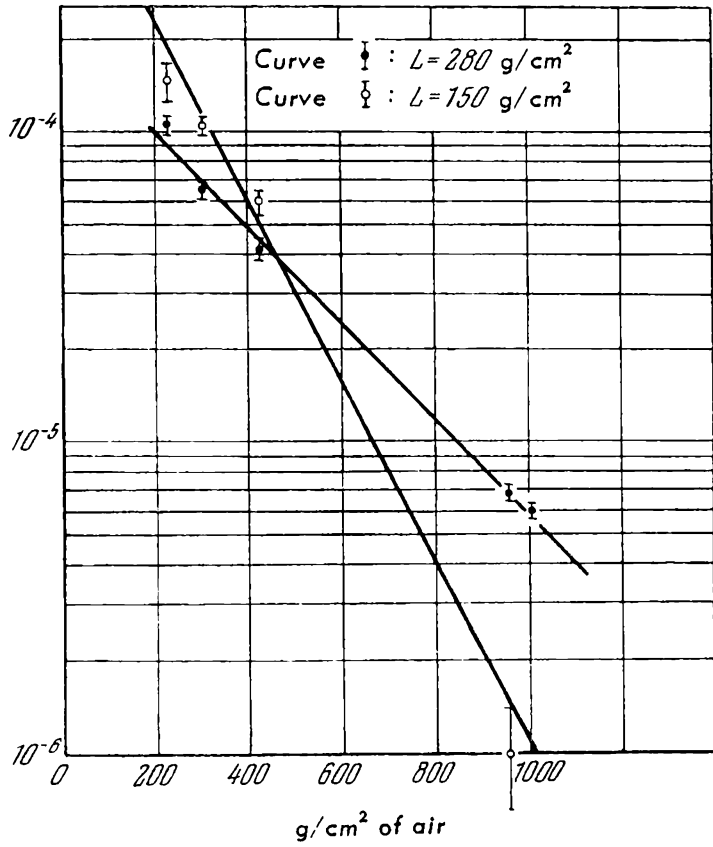


Fig. 7.11 Altitude variation in the intensity of slow muons and protons at geomagnetic latitude of 50°N , (Conversi). The intensity is plotted as a function of depth in the atmosphere in g/cm^2

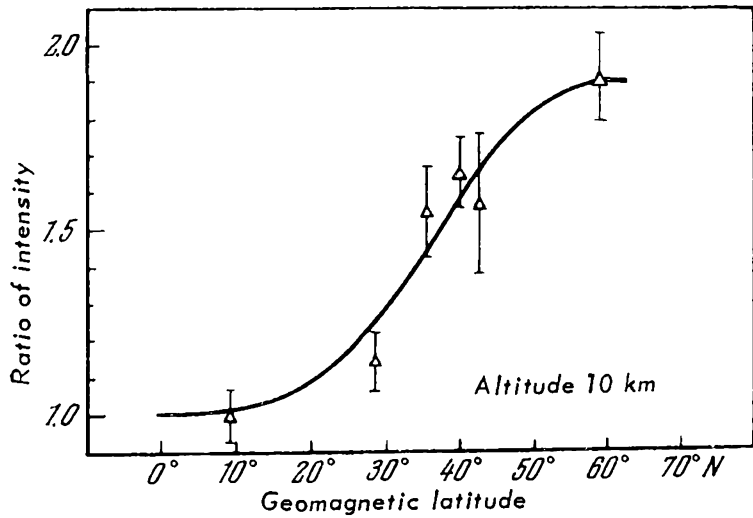


Fig. 7.12 Latitude effect for slow mesons with ranges $15 \text{ cm Pb} < R < 15 \text{ cm Pb} + 10 \text{ cm graphite}$ at a height of 10 km. The ratio of the intensity at latitude λ to the intensity near the chamber is plotted as a function of the geomagnetic latitude λ

determined by Sabramanian et al. [21] who carried out measurements under a depth of 800 g/cm² of the atmosphere. They showed that the intensity of slow muons (ranges 47-64 g/cm²) at a latitude of 50°N is greater by a factor of 3 than the intensity at the Equator. The latitude effect for slow muons is much greater than the latitude effect averaged over the entire energy spectrum of cosmic-ray muons, which amounts to about 10-15%. This result is explained by the fact that low-energy muons are generated mainly by relatively low-energy primary cosmic rays which are more sensitive to the earth's magnetic field.

Finally we will discuss data on the absolute intensity of slow muons at sea level. Del-Rosario and Dávila-Aponte [22] have found that the intensity of muons with residual range of 100 g/cm² at a latitude of 29°N is $(4.25 \pm 0.13) \times 10^{-6} \text{ g}^{-1} \text{ cm}^2 \text{ sec}^{-1} \text{ sterad}^{-1}$. Mishra and Sinha [23] have used a multi-plate Wilson cloud chamber to determine the mean intensity of muons with ranges between 15 and 60 g/cm². Their result was $(5.90 \pm 0.15) \times 10^{-6} \text{ g}^{-1} \text{ cm}^2 \text{ sec}^{-1} \text{ sterad}^{-1}$.

It is clear from this data that cosmic radiation at sea level, and to a greater extent at high altitudes, is a source of slow muons with intensity which is adequate for many experimental purposes. Absorbers used in cosmic-ray studies to bring slow mesons to rest (metal plates, liquid and plastic scintillators and so on) can easily have volumes of the order of 10 litres, so that many experiments on the decay and absorption of slow mesons can be performed with cosmic-ray muons.

7.6 POSITIVE EXCESS IN THE MUON COMPONENT

An interesting feature of the muon component is an appreciable excess of positively charged particles. This positive excess may be characterized by the ratio $r = N_{\mu^+} / N_{\mu^-}$, which is considerably greater than 1 over practically the entire momentum range examined to date. Most of the measurements of the positive excess were carried out using magnetic deflection to determine the muon charge with simultaneous determination of the energy spectrum. Fig. 7.13 shows the positive-excess spectrum obtained by Weissenberg [18] at an altitude of 3250 m. The upper curve gives the positive excess for unfiltered cosmic rays from air; the lower curve gives the same plot for the hard com-

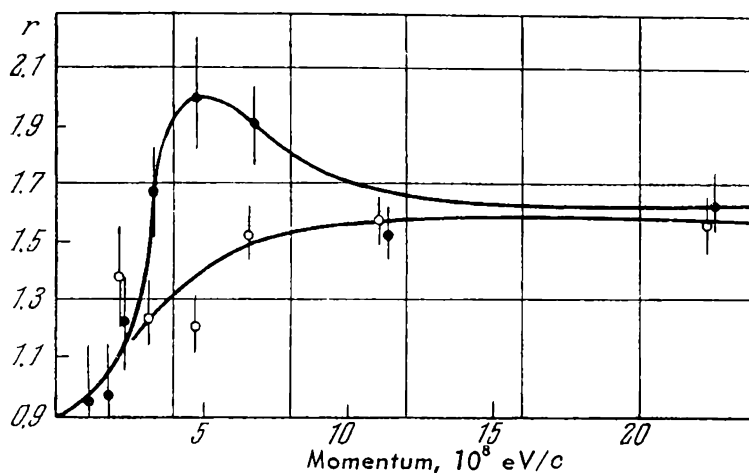


Fig. 7.13 Spectrum of positive excess at 3250 m above sea level

ponent filtered by 9 cm of lead. We see that there is no positive excess for momenta below 2×10^8 eV/c. In this part of the spectrum the soft electron-positron component has an appreciable intensity. This component is genetically related to γ rays from neutral pion decays and one would expect an equal number of electrons and positrons in the spectrum at these momenta.

In the spectrum of unfiltered radiation the positive excess commences near 2×10^8 eV/c and increases rapidly, reaching a maximum of $r = 2$ in the region of 5×10^8 eV/c. The appearance of the positive excess begins near the minimum proton momentum recorded by the apparatus (the total wall thickness of the counters in the magnetic spectrometer was 0.2 mm of copper which corresponds to a proton momentum of 2.4×10^8 eV/c). This means that at low momenta the positive excess appears as soon as the recorded particles include protons. Further increase in the momentum ($p > 5 \times 10^8$ eV/c) leads to a slow reduction in the excess, which tends to approach a steady value of 1.5-1.6. It might be expected that the entire excess was due to protons, but an analysis of the spectrum of the hard component contradicts this conclusion. In fact, the spectrum of the positive excess in the hard component (see Fig. 7.13) does not include protons with ranges of less than 9 cm of lead, i.e. protons with momenta less than 7.7×10^8 eV/c. Comparison of the spectra of positive excess for unfiltered radiation and for the hard component clearly shows that a considerable part of the positive excess in the spectrum of unfiltered radiation

is connected with protons. However, it is clear from this curve that after the protons have been absorbed (and the electron-positron component has been removed) there remains a finite positive excess which must be ascribed to the meson component. This positive excess is $r = 1.25 \pm 0.06$ in the momentum band $(2.4-7.7) \times 10^8$ eV/c. Alikhanyan and Weissenberg [24] have extended these measurements to 2×10^{10} eV/c. Fig. 7.14 shows a summary of most of the published measurements of the positive excess in the muon component [5, 6, 8, 11, 25, 26, 27].

Analysis of the above data shows that in the momentum range $(1-50) \times 10^9$ eV/c the excess lies between 1.2 and 1.3, and passes through a broad maximum, falling to zero at higher momenta. The existence of a positive excess in the muon component and the nature of its distribution over the spectrum has a simple qualitative explanation: it is due to the fact that the primary radiation is positively charged. Owing to charge conservation, this excess is transmitted from pions generated during interactions between primaries and atmospheric nuclei to muons produced in their decay.

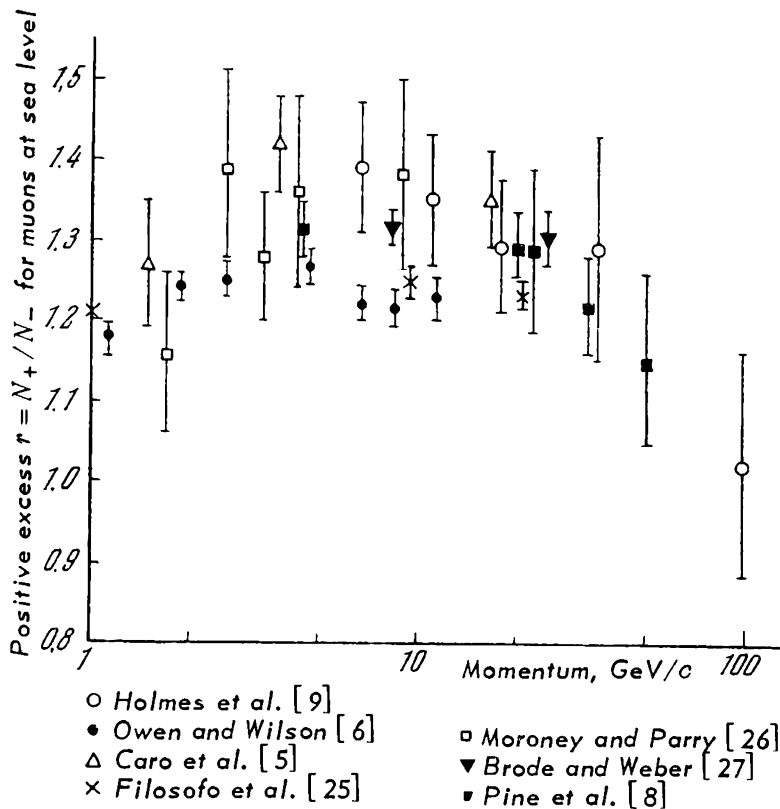


Fig. 7.14 Spectrum of positive excess in the muon component at sea level

It is clear that the magnitude and energy spectrum of this excess should be connected with the pion generation multiplicity. For large multiplicities the excess is distributed among the large number of secondary mesons, and should therefore decrease with increasing primary energy, i.e. with increasing multiplicity. Since with increasing multiplicity there is an increase in the energy of the secondary particles, the positive excess should decrease with increasing muon energy. Fig. 7.14 shows that this is in fact the case. The positive excess is also found to decrease with decreasing muon energy. For muon energies of about 10^8 eV it is about 1 or even slightly less than 1. This rapid reduction in the excess at low energies again has a simple explanation. Slow muons originate in the decays of slow pions produced in the lower atmosphere where the primary component has almost completely disappeared through absorption. Slow pions are therefore produced by secondary nuclear-active particles, half of which are neutrons. Pions produced by neutrons do not exhibit a positive excess, thus explaining the reduction in the excess with decreasing muon energy.

7.7 MUON INTENSITY AT GREAT DEPTHS

The final point which we must discuss is the cosmic-ray flux at great depths underground where it consists mainly of muons. Underground measurements of the vertical muon flux have been performed by many workers beginning with Ehmert [28] who used Geiger-counter telescopes. They have been made to depths approaching 2×10^5 g/cm² water equivalent and are summarized in Fig. 7.15, which is based on all measurements between 1937 and 1955 [28-33]. The extension of these measurements to larger depths introduces several problems. The principal difficulty is to find a sufficiently deep shaft in which the natural radioactivity of the surrounding rocks is low. Even in the most suitable shafts the flux due to radioactive contamination with an energy greater than a few centimetres of water equivalent is 9-10 orders of magnitude larger than the muon flux.

Barton [34] has carried out underground measurements of the vertical muon flux at depths of 1660, 3280 and 5050 m water equivalent, using a wide-angle telescope consisting of two rows of Geiger counters with an intermediate plastic scintillator. According to Barton, the cosmic-ray intensity

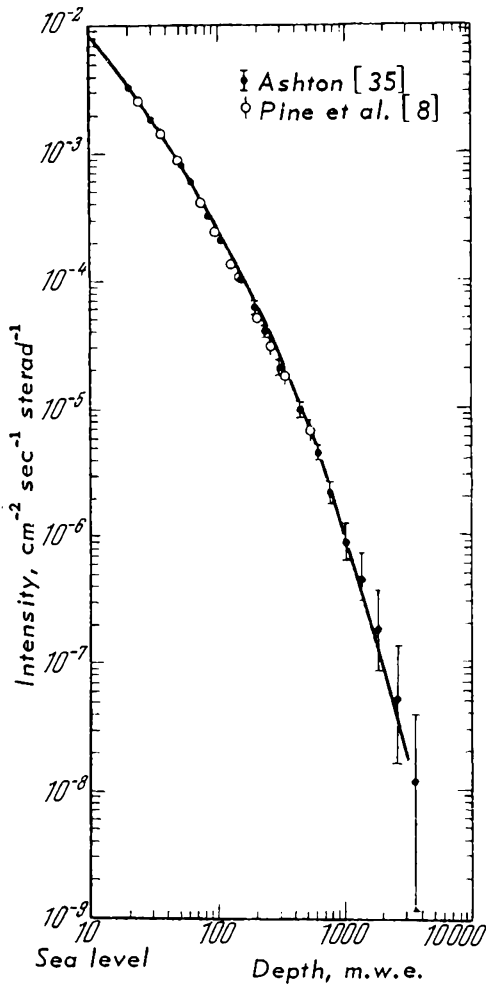


Fig. 7.15 *Hard component of cosmic rays at large depths underground. Solid curve shows the results of under-ground measurements. Experimental points represent intensities deduced from momentum spectra at sea level and the muon range-energy relation*

at the first two depths, at which it probably consists entirely of muons, is 3×10^{-5} and 10^{-6} of the intensity at the earth's surface respectively. No cosmic rays were observed at 5050 m water equivalent, and as an upper limit of the intensity Barton gives the figure of 10^{-7} of the intensity at sea level. Underground measurements of cosmic-ray intensity at such great depths are in fact measurements of the integral range spectrum $N(>R)$ of the muon component of cosmic rays. This range spectrum may be obtained from the measured muon spectrum at sea level and the range-energy relation for high-energy muons. Comparison of the spectra will verify the validity of assumptions about the mechanism responsible for energy losses experienced by muons traversing large amounts of matter. Calculations of such losses have been performed by Ashton [35], George [36], Barrett et al. [37], and others.

Ashton derived an expression for the energy loss (in MeV

$\text{g}^{-1} \text{cm}^2$) of fast muons in the ground. He assumed that the average values of the atomic number Z , the atomic weight A and density ρ were 10, 20 and 1.9 g/cm^3 respectively. Ashton's formula is

$$-\frac{dE}{dx} = 1.51 + 0.0766 \left\{ \ln \frac{E'_m}{m_\mu c^2} + \frac{1}{4} \frac{E'_m}{E + m_\mu c^2} \right\} + 0.15 \cdot 10^{-6} E \left\{ \ln \frac{E}{m_\mu c^2} - 0.23 \right\} + 2.1 \cdot 10^{-6} E \text{ MeVg}^{-1} \text{cm}^2 \quad (7.1)$$

where the first two terms describe ionization energy losses with a correction for the Fermi density effect. The quantity

$E'_m = \frac{E^2}{E + m_\mu c^2 / 2m_e}$ is the maximum energy which a muon of mass m_μ can transfer to an electron of mass m_e . The third term in this formula gives the muon energy lost through bremsstrahlung:

$$-\left(\frac{dE}{dx}\right)_{\text{brems}} = 0.15 \cdot 10^{-6} E \left\{ \ln \frac{E}{m_\mu c^2} - 0.23 \right\} \text{ MeVg}^{-1} \text{cm}^2$$

The main contribution to the last term in this formula is due to energy losses through pair production:

$$-\left(\frac{dE}{dx}\right)_{\text{pair}} \approx 1.6 \cdot 10^{-6} E \text{ MeVg}^{-1} \text{cm}^2$$

All of these energy-loss mechanisms involve the usual electromagnetic interactions. They are calculated subject to various approximations, and depend on the assumed average values of the atomic weight, atomic number and density of the ground. Calculations reported by other workers may therefore differ from those given above by 10-20%. This discrepancy is not, however, too important since the statistical errors in the measured muon energy spectrum are large at high energies, and the accuracy with which the cosmic-ray intensity is measured at great depths underground is therefore not very high.

The last term in the above formula includes a contribution due to 'nuclear' interactions of muons which we discussed earlier. According to approximate estimates carried out by

Ashton this is of the order

$$\left(\frac{dE}{dx}\right)_{\text{nucl}} \approx 0.5 \cdot 10^{-6} E \text{ MeVg}^{-1} \text{cm}^2 \quad (7.2)$$

Experimental data confirming the existence of this mechanism for high-energy muons have been confirmed by many workers. They have been reviewed by George [36] and Fowler and Wolfendale [39]. It has been shown that high-energy muons give rise to nuclear disintegrations in matter, and that the cross-section for this process increases logarithmically with increasing muon energy. The observed phenomena can be explained as a non-classical electromagnetic effect with the framework of the Weiszäcker-Williams theory. In this effect the motion of a charged meson gives rise to the appearance of a field of virtual photons which interact through the nuclear photo-effect with the nuclei in the medium. Assuming that the virtual photons are equivalent to the electromagnetic field of the high-energy muon, and that the cross-section for the photo-nuclear process is constant and roughly equal to $2 \times 10^{-28} \text{ cm}^2$, we are led to the expression given by (7.2). This mechanism can be used to explain all the nuclear interactions of fast muons known at present. We note that as the energy of the muon increases, the relative importance of non-ionization losses increases rapidly. For example, at energies of about 200 GeV, ionization losses amount to about 80% of the total energy loss, whilst at 1000 GeV the fraction is only about 40%.

Fig. 7.16 shows the range-energy relation for fast muons obtained by Ashton on integrating Equation (7.1). He used this relation and the muon spectrum at sea level obtained with the large Durham spectrometer (curve 3, Fig. 7.6) to deduce the expected muon intensity at various depths underground (experimental points in Fig. 7.15). This is compared with the result of an analogous analysis performed by Pine et al. who used their own spectrum (curve 1, Fig. 7.6).

These data confirm the validity of the assumed energy-loss mechanisms for fast muons. The satisfactory agreement of the muon intensity predicted from the range-energy relation and the sea-level spectrum with experimental data on the intensity of the muon component underground shows that no substantial loss mechanisms have been ignored in

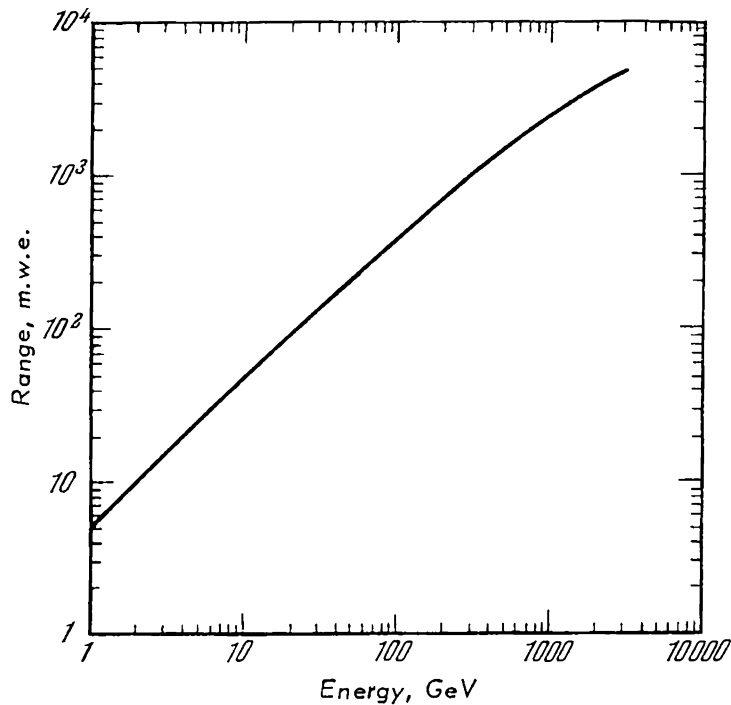


Fig. 7.16 Range-energy relation for high-energy muons

this calculation. It is evident from the curves of Fig. 7.6 that this result is valid up to muon momenta of the order of 10^{12} eV/ c , although in this region statistical uncertainties in the results are high, so that the existence of the photo-nuclear mechanism for muons at this energy cannot as yet be established.

In addition to the integral intensity of the hard component at great depths underground, there have recently been some measurements of the muon momentum spectrum in underground laboratories at depths of about 40 m. The most detailed measurements of this kind have been carried out with magnetic spectrometers by Dayon and Potapov [40], Ashton et al. [41] and Cousins and Nash [42]. Comparison of surface spectra with those obtained at these relatively small depths has again confirmed the absence of muon interactions other than those due to electromagnetic effects.

REFERENCES

CHAPTER 1

1. ANDERSON, C. D., and NEDDERMEYER, S. H., *Phys. Rev.*, V 50, p 263 (1936); V 51, p 884 (1937); V 54, p 88 (1938).
2. STREET, J. C., and STEVENSON, E. C., *ibid.*, V 52, p 1003 (1937).
3. ANDERSON, C. D., *Am. J. Phys.*, V 29, p 825 (1961).
4. LATTES, C. M. G., MUIRHEAD, H., OCCIALINI, G. P. S., and POWELL, C. F., *Nature, Lond.*, V 159, p 694 (1947).
5. LATTES, C. M. G., MUIRHEAD, H., OCCIALINI, G. P. S., and POWELL, C. F., *ibid.*, V 160, pp 453 and 486 (1947).
6. POWELL, C. F., FOWLER, P. H., and PERKINS, D. H., 'The study of elementary particles by the photographic method', Pergamon Press (1959).
7. BARKAS, W. H., BIRBAUM, W., and SMITH, F. M., *Phys. Rev.*, V 101, p 778 (1956).
8. PANOFSKY, W. K. H., AAMODT, L., and HADLEY, J., *ibid.*, V 81, p 565 (1951).
9. CROWE, K. M., and PHILLIPS, R. H., *ibid.*, V 96, p 470 (1954).
10. KOSLOV, S., FITCH, V., and RAINWATER, J., *ibid.*, V 95, p 291 (1954).
11. STEARNS, M., STEARNS, M. B., DeBENEDETTI, S., and LEIPUNER, L., *Phys. Rev.*, V 97, p 240 (1955).
12. LATHROP, J., LUNDY, R. A., TELEGGI, V. L., WINSTON, R., and YOVANOVITCH, D. D., *Nuovo Cim.*, V 17, pp 109 and 113 (1960).
13. DEVONS, S., GIDAL, G., LEDERMAN, L. M., and SHAPIRO, G., *Phys. Rev. Lett.*, V 5, p 830 (1960).
14. CROWE, K. M., *Nuovo Cim.*, V 5, p 541 (1957).
15. PANOFSKY, W. K. H., AAMODT, L., and HADLEY, J., *Phys. Rev.*, V 78, p 825 (1950); V 80, p 565 (1951).
16. CHINOWSKY, W., SACHS, A., and STEINBERGER, J., *ibid.*, V 93, p 917 (1954).

17. LEIGHTON, R. B., ANDERSON, C. D., and SERIFF, A. J., *Phys. Rev.*, V 75, p 1432 (1949).
18. ZHDANOV, G. B., and KHAIDAROV, A. A., *Dokl. Akad. Nauk. SSSR*, V 65, p 287 (1941).
19. STEINBERGER, J., *Phys. Rev.*, V 74, p 500 (1948).
20. HINCKS, E. P., and PONTECORVO, B., *ibid.*, V 73, p 257 (1948); V 75, p 698 (1950).
21. SARD, R. D., and ALTHAUS, E. J., *ibid.*, V 74, p 1364 (1948).
22. PICCIONI, O., *ibid.*, V 74, p 1754 (1948).
23. MINERVINA, Z. V., and PESOTSKAYA, E. A., *Zh. eksp. teor. Fiz.*, V 36, p 444 (1959).
24. CHRISTY, R. F., and KUSAKA, S., *Phys. Rev.*, V 59, pp 405 and 414 (1941).
25. SCHEIN, M., and GILL, P. S., *Rev. Mod. Phys.*, V 11, p 267 (1939).
26. BELEN'KII, S. Z., 'Shower processes in cosmic rays', *Gostekhizdat* (1948).
27. HIROKAWA, S., KOMORI, H., and OGAWA, S., *Nuovo Cim.*, V 4, p 736 (1956).
28. GARWIN, R. L., LEDERMANN, L. M., and WEINRICH, M., *Phys. Rev.*, V 105, p 1415 (1957).
29. KULENKAMPF, H., *Verh. dt. phys. Ges.*, V 19(3), p 92 (1938).
30. RASETTI, F., *Phys. Rev.*, V 59, p 706 (1941); V 60, p 198 (1941).
31. ROSSI, B., and NERESON, N., *ibid.*, V 62, p 417 (1942).
32. BELL, W. E., and HINCKS, E. P., *ibid.*, V 84, p 1243 (1951).
33. REITER, R. A., ROMANOWSKI, T. A., SUTTON, R. B., and CHIDLEY, B. G., *Phys. Rev. Lett.*, V 5, p 22 (1960).
34. FISCHER, J., LEONTIC, B., LUNDBY, A., MEUNIER, R., and STROOT, J. P., *ibid.*, V 3, p 349 (1959).
35. ASTBURY, A., HATTERSLEY, P. M., HUSSAIN, M., KEMP, A., and MUIR-HEAD, H., *Proc. 1960 Ann. Rochester Conf.*, p 542.
36. TELEGDI, V. L., *Proc. 1960 Ann. Rochester Conf.*, p 713.
37. LUNDY, R. A., *Phys. Rev.*, V 125, p 1686 (1962).
38. CONVERSI, M., PANCINI, E., and PICCIONI, O., *ibid.*, V 68, p 232 (1945); V 71, p 209 (1947).
39. PONTECORVO, B., *ibid.*, V 72, p 246 (1950).
40. HILDEBRAND, R. H., *Phys. Rev. Lett.*, V 8, p 34 (1962).
41. PYKA, M., *Nuovo Cim.*, Supplement 1, p 112 (1962).
42. ZAYMIDOROGA, O. A., KULYUKIN, M. M., PONTECORVO, B. M., SULYAEV, R. M., FILIPPOV, A. P., TSUPKO-SITNIKOV, V. I., and SHCHERBAKOV, Yu. A., *Zh. eksp. teor. Fiz.*, V 41, p 1804 (1961); see also *Proc. Int. Conf. on High-Energy Physics, CERN, Geneva* (1962).
43. KLEIN, O., *Nature, Lond.*, V 161, p 897 (1948).
44. CLEMENTEL, E., and PUPPI, G., *Nuovo Cim.*, V 5, p 505 (1948).
45. TIOMNO, J., and WHEELER, J. A., *Rev. Mod. Phys.*, V 21, p 144 (1949).
46. LEE, T. D., ROSENBLUTH, M., and YANG, C. N., *Phys. Rev.*, V 75, p 905 (1949).
47. FERMI, E., 'Elementary particles' (1953).
48. PONTECORVO, B., *Zh. eksp. teor. Fiz.*, V 39, p 1166 (1960).
49. REINES, F., and COWAN, C. L., *Phys. Rev.*, V 113, p 273 (1959); CARTER, R., REINES, F., WAGNER, J. J., and WYMAN, M. E., *ibid.*, V 113, p 280 (1959).
50. DAVIS, R., *Bull. Am. Phys. Soc.*, V 1, p 219 (1956).
51. WU, C. S., 'Theoretical physics in the 20th century' (1962) (in Russian).
52. LEE, T. D., and YANG, C. N., *Phys. Rev. Lett.*, V 4, p 307 (1960).
53. YAMAGUCHI, Y., *Proc. theor. Phys., Osaka*, V 23, p 1117 (1960).
54. GABIBBO, N., and GATTO, R., *Nuovo Cim.*, V 15, p 304 (1960).
55. SCHWARTZ, M., *Phys. Rev. Lett.*, V 4, p 306 (1960).
56. DANBY, G., GAILLARD, J. M., GOULIANOS, K., LEDERMAN, L. M., MISTRY, N. B., SCHWARTZ, M., and STEINBERGER, J., *ibid.*, V 9, p 36 (1962).
57. ECKHAUSE, M., *Carnegie Institute of Technology Report* 9286 (1962).
58. FARLEY, F. J. M., MASSAM, T., MULLER, T., and ZICHICHI, A., *Proc. Int. Conf. High-Energy Phys., CERN, Geneva*, p 415 (1962).

59. MEYER, S. L., ANDERSON, E. W., BLESER, E. J., LEDERMAN, L. M., BOTHBERG, J. E., and WANG, I. I., Columbia University, Nevis, Report 114 (1963).
60. BIENLEIN, J. K., BÖHM, A., VON-DARDEL, G., FAISSNER, H., FERRERO, F., GAILLARD, J. M., GERBER, H. J., HAHN, B., KAFTANOV, V., KRIENEN, F., REINHARZ, M., SALMERON, R. A., SEILER, P. G., STAUDE, A., STEIN, J., and STEINER, H. J., *Phys. Lett.*, V 13, p 80 (1964).
61. BLOCK, M. M., BURMEISTER, H., GUNDY, D. C., EIBEN, B., FRANZINETTI, C., KEREN, J., MOLLERUD, R., MUATT, G., NICOLI, M., ORKIN-LECOURTOIS, A., PATY, M., PERKINS, D. H., RAMM, C. A., SCHULTZE, K., SLETTEN, H., SOOP, K., STUMP, R., VENUS, M., and YOSHIKI, H., *Phys. Lett.*, V 12, p 281 (1964).

CHAPTER 2

1. LEE, T. D., and YANG, C. N., *Phys. Rev.*, V 104, p 248 (1956).
2. DALITZ, R., *Phil. Mag.*, V 44, p 1068 (1953); *Phys. Rev.*, V 94, p 1046 (1954).
3. LEE, T. D., and YANG, C. N., *Phys. Rev.*, V 105, p 1671 (1956).
4. LANDAU, L. D., *Zh. eksp. teor. Fiz.*, V 32, pp 2, 405 and 407 (1957).
5. SALAM, A., *Nuovo Cim.*, V 5, p 299 (1957).
6. GARWIN, R. L., LEDERMAN, L. M., and WEINRICH, M., *Phys. Rev.*, V 105, p 1415 (1956).
7. FRIEDMAN, J., and TELEGGI, V. L., *ibid.*, V 105, p 1681 (1957).
8. WEISSENBERG, A. O., Dissertation (1961).
9. WU, C. S., AMBLER, E., HAYWARD, R. W., HOPPES, D. D., and HUDSON, R. P., *Phys. Rev.*, V 105, p 1413 (1957).
10. PAULI, W., 'General principles of wave mechanics'.
11. COOMBES, C. A., and CORK, B., et al., *Phys. Rev.*, V 108, p 1348 (1957).
12. COFFIN, T., GARWIN, R. L., PENMAN, S., LEDERMAN, L. M., and SACHS, A. M., *ibid.*, V 109, p 973 (1958).
13. LARSEN, S., LUBKIN, E., and TAUSNER, M., *ibid.*, V 107, p 856 (1957).
14. OKUN', L., and RUDIK, A., *Zh. eksp. teor. Fiz.*, V 32, p 627 (1957).
15. KINOSHITA, T., and SIRLIN, A., *Phys. Rev.*, V 108, p 844 (1957).
16. OKUN', L., and SHEKHTER, V., *Zh. eksp. teor. Fiz.*, V 34, p 1250 (1958).
17. SHARP, R., and BACH, G., *Can J. Phys.*, V 35, p 199 (1957).
18. MICHEL, L., *Proc. Phys. Soc.*, V A63, pp 514 and 1371 (1950).
19. See reference 70.
20. SUDARSHAN, E. C. G., and MARSHAK, R. E., *Proc. Padua-Venice Conf. (1957)*; *Phys. Rev.*, V 109, p 1860 (1958).
21. FEYNMAN, R. P., and GELL-MANN, M., *Phys. Rev.*, V 109, p 193 (1958).
22. SAKURAI, J. J., *Nuovo Cim.*, V 7, p 649 (1958).
23. BARDIN, R. K., BARNES, C. A., FOWLER, W. A., and SEEGER, P. A., *Phys. Rev. Lett.*, V 5, p 323 (1960).
24. WU, C. S., 'Theoretical physics in the 20th century' (1962) (in Russian).
25. GERSHTEIN, S. S., and ZEL'DOVICH, Ya. B., *Zh. eksp. teor. Fiz.*, V 2, p 576 (1956).
26. ROSENSON, L., *Phys. Rev.*, V 109 (13), p 958 (1958).
27. PLANO, R. J., *ibid.*, V 119, p 1400 (1960).
28. ANDERSON, H. L., FUJII, T., MILLER, R. H., and TAU, L., *ibid.*, V 119, p 2050 (1960).
29. WEISSENBERG, A. O., SMIRNITSKII, V. A., and KOLCHANOVA, E. D., *Zh. eksp. teor. Fiz.*, V 40, p 1042 (1961).
30. DUDZIAK, W. F., SAGANE, R., and VEDDER, J., *Phys. Rev.*, V 114, p 336 (1959).
31. CROWE, K. M., *Nuovo Cim.*, V 5, p 541 (1957).

32. BONETTI, A., LEVI-SETTI, R., PANETTI, M., ROSSI, G., and TOMASINI, A., *ibid.*, V 3, p 33 (1956).
33. BESSON, C., and BRISSON-FOUCHÉ, V., *ibid.*, V 10 (6), p 1143 (1958).
34. GUREVICH, I. I., NIKOL'SKII, B. A., and ALI-ZADE, C. A., *Zh. eksp. teor. Fiz.*, V 40, p 452 (1961).
35. WEISSENBERG, A. O., and SMIRNITSKII, B. A., *ibid.*, V 39, p 242 (1960).
36. LYNCH, R., OREAR, J., and ROSENDORFF, S., *Phys. Rev.*, V 118, p 284 (1960).
37. BABAYAN, Kh. P., MARUTYAN, N. A., MATEVOSYAN, K. A., and MARINYAN, M. G., *Zh. eksp. teor. Fiz.*, V 35, p 561 (1958).
38. CASTAGNOLI, C., MANFREDINI, A., and MERRISON, A. W., *Nuovo Cim.*, V 9, p 186 (1958).
39. BARMIN, V. V., KANAVETS, V. P., MOROZOV, B. V., and PERSHIN, I. I., *Zh. eksp. teor. Fiz.*, V 34, p 830 (1958).
40. ALIKHANYAN, A. I., KIRILLOV-UGRYUMOV, V. G., KOTENKO, L. P., KUZNETSOV, E. P., and POPOV, Yu. S., *ibid.*, V 34, p 1101 (1958).
41. BALANDIN, M. P., MOISEYENKO, V. A., MUKHIN, A. I., and OTVINOVSKII, S. Z., *ibid.*, V 36, p 424 (1959).
42. PLESS, I. A., BRENNER, A. E., WILLIAMS, R. W., BIZZARRI, R., HILDEBRAND, R. H., MILBURN, R. H., et al., *Phys. Rev.*, V 108, p 159 (1957).
43. ALSTON, M. H., EVANS, W. H., MORGAN, T. D. N., NEWPORT, R. W., WILLIAMS, P. R., and KIRK, A., *Phil. Mag.*, V 2, p 1143 (1957).
44. WEINRICH, M., Preprint (1957).
45. MUKHIN, A. I., OZEROV, E. B., and PONTECORVO, B., *Zh. eksp. teor. Fiz.*, V 35, p 340 (1958).
46. CASSELS, J. M., O'KEEFE, T. W., RIGBY, M., and WORMALD, J. R., *Proc. Phys. Soc.*, V 72, p 781 (1958).
47. KRUGER, H., and CROWE, K. M., *Phys. Rev.*, V 113 (1) (1959).
48. GOLDHABER, M., GRODZINS, L., and SUNYAR, A. W., *ibid.*, V 106, p 826 (1957); *ibid.*, V 109, p 1015 (1958).
49. ÜBERALL, H., *Nuovo Cim.*, V 6, p 376 (1957).
50. CULLIGAN, G., FRANK, G. F., and HOLT, J. R., *Proc. Phys. Soc.*, V 73, pp 2 and 169 (1958).
51. MACQ, P. C., CROWE, K. M., and HADDOCK, R. P., *Phys. Rev.*, V 112, p 2061 (1958).
52. ALIKHANOV, A. I., GALAKTIONOV, Yu. V., GORODKOV, Yu. V., YELISEEV, G. P., and LYUBIMOV, D. A., *Zh. eksp. teor. Fiz.*, V 38, p 1918 (1960).
53. ALIKHANOV, A. I., LYUBIMOV, D. A., *ibid.*, V 36, p 1334 (1959).
54. BACKENSTOSS, G., HYAMS, B. D., KNOPP, G., MARIN, P. C., and STIERLIN, U., *Phys. Rev. Lett.*, V 6, p 415 (1961).
55. BINCER, A. M., *Phys. Rev.*, V 107, p 1467 (1957).
56. MOROZ, L. G., *Zh. eksp. teor. Fiz.*, V 39, p 589 (1960).
57. FROLOV, G. V., *ibid.*, V 40, p 296 (1961).
58. RAWITSCHER, G. H., *Phys. Rev.*, V 112, p 1278 (1958).
59. FRANKLIN, J., and MARGOLIS, B., *ibid.*, V 109, p 525 (1958).
60. BARDON, M., FRANZINI, P., and LEE, J., *Phys. Rev. Lett.*, V 7, p 23 (1961).
61. HERRMANNFELDT, W. B., BURMAN, R. L., STÄHELIN, P., ALLEN, J. S., and BRAID, T. H., *Phys. Rev. Lett.*, V 1, p 61 (1958); HERRMANNFELDT, W. B., STÄHELIN, P., and ALLEN, J. S., *Bull. Am. phys. Soc.*, V 3, Series 11, p 52 (1958).
- 62.
63. HERRMANNFELDT, W. B., MAXSON, D. R., STÄHELIN, P., and ALLEN, J. S., *Phys. Rev.*, V 107, p 641 (1957).
64. LAUTERJUNG, K. H., SCHIMMER, B., and MAIER-LEIBNITZ, H., *Z. Phys.*, V 150, p 657 (1958).
65. ALFORD, W. P., and HAMILTON, D. R., *Phys. Rev.*, V 105, p 673 (1957).
66. MAXSON, D. R., ALLEN, J. S., and JENTSCHKE, W. K., *ibid.*, V 97, p 109 (1955).

67. GOOD, M. L., and LAUER, E. J., *ibid.*, V 105, p 213 (1957).
68. RIDLEY, B. W., *Proc. R. Soc.*, V 246, p 471 (1958).
69. TEREKHOV, A. B., BURGOV, N. A., *Zh. eksp. teor. Fiz.*, V 6, p 502 (1958).
70. BURG, M. T., KROHN, V. E., NOVEY, T. B., RINGO, G. R., and TELEGDI, V. L., *Phys. Rev.*, V 110, p 1214 (1958a); *ibid.*, V 107, p 1731 (1957); BURG, M. T., KROHN, V. E., NOVEY, T. B., RINGO, G. R., and TELEGDI, V. L., *Phys. Rev. Lett.*, V 1, p 324 (1958).
71. HUGHES, D. J., 'Pile neutron research', Addison-Wesley (1953).
72. SOSNOVSKII, A. N., SPIVAK, P. E., PROKOF'EV, A. Yu., KUTIKOV, P. E., and DOBRYNIN, Yu. P., *Nucl. Phys.*, V 10, p 395 (1959); *Zh. eksp. teor. Fiz.*, V 36, p 1012 (1959).
73. RUDERMAN, M., and FINKELSTEIN, R., *Phys. Rev.*, V 76, p 1458 (1949).
74. STEINBERGER, J., *ibid.*, V 76, p 1180 (1949).
75. FRIEDMAN, H. L., and RAINWATER, J., *ibid.*, V 84, p 684 (1949).
76. LOKANATHAN, S., and STEINBERGER, J., *Nuovo Cim.*, Supplement 1, p 151 (1955).
77. ANDERSON, H. L., and LATTES, C. M. G., *ibid.*, V 6, p 1356 (1957).
78. FAZZINI, T., FIDECARO, G., MERRISON, A. W., PAUL, H., and TOLLESTRUP, A. V., *Phys. Rev. Lett.*, V 1, p 247 (1958).
79. ASHKIN, J., FAZZINI, T., MERRISON, A. W., PAUL, H., and TOLLESTRUP, A. V., *Nuovo Cim.*, V 13, p 1240 (1959).
80. IMPEDUGLIA, G., PLANO, R., PRODELL, A., SAMIOS, N., SCHWARZ, M., and STEINBERGER, J., *Phys. Rev. Lett.*, V 1, p 249 (1958).
81. ANDERSON, H. L., FUJII, T., MILLER, R. H., TAU, L., and KINOSHITA, T., *ibid.*, V 2, p 477 (1959).
82. ZEL'DOVICH, Ya. B., *Dokl. Akad. Nauk SSSR*, V 97, p 421 (1954).
83. DUNAITSEV, A., PETRUKHIN, V., PROKOSHKIN, Yu. D., and RYKALIN, V. I., *Zh. eksp. teor. Fiz.*, V 42, p 1680 (1962); *Phys. Rev. Lett.*, V 1, p 138 (1962).
84. DEPOMMIER, P., HEINTZE, J., MUKHIN, A., RUBBIA, C., SOERGEL, V., and WINTER, K., *Phys. Rev. Lett.*, V 2, p 23 (1962).
85. BACSTROW, R. B., ELLIOFF, T., LARSEN, R. R., WIEGAND, C., and YPSILANTIS, T., *ibid.*, V 9, p 400 (1962).
86. BEHREND, R. E., FINKELSTEIN, R. J., and SIRLIN, A., *Phys. Rev.*, V 101, p 866 (1956).
87. BERMAN, S. M., *ibid.*, V 112, p 267 (1958).
88. KINOSHITA, T., and SIRLIN, A., *Phys. Rev.*, V 107, p 593 (1957).
89. KUZNETSOV, V. P., *Zh. eksp. teor. Fiz.*, p 1721 (1960).
90. FERRETTI, B., *Nuovo Cim.*, V 6, p 999 (1957).
91. GATTO, R., and LÜDERS, G., *ibid.*, V 7, p 806 (1958).
92. TZOAR, N., and KLEIN, A., *ibid.*, V 8, p 482 (1958).
93. PRATT, R. H., *Phys. Rev.*, V 111, p 649 (1958).
94. FRONSDAL, C., and ÜBERALL, H., *ibid.*, V 113, p 654 (1959).
95. ECKSTEIN, S. G., and PRATT, R. H., *Ann. Phys.*, V 8, p 297 (1959).
96. KINOSHITA, T., *Phys. Rev. Lett.*, V 2, p 196 (1959); KINOSHITA, T., and SIRLIN, A., *Phys. Rev.*, V 113, p 1652 (1959).
97. KROLL, N. M., and WADA, W., *ibid.*, V 98, p 1355 (1955).
98. LENARD, A., *ibid.*, V 90, p 968 (1953).
99. GUREVICH, P. P., NIKOL'SKII, B. A., and SURKOVA, L. V., *Zh. eksp. teor. Fiz.*, V 37, p 318 (1959).
100. LEE, J., and SAMIOS, N. P., *Phys. Rev. Lett.*, V 3, p 55 (1959).
101. CRITTENDEN, R. R., and WALKER, W. D., and BALLAM, J., *Phys. Rev.*, V 121, p 1823 (1961).
102. ASHKIN, J., FAZZINI, T., FIDECARO, G., LIPMAN, N. H., MERRISON, A. W., and PAUL, H., *Nuovo Cim.*, V 14, p 1270 (1959).
103. KIM, C. O., KERNAN, W. J., and YORK, C. M., *Phys. Rev.*, V 120, p 983 (1960).
104. FRY, W. F., SCHNEPS, J., SNOW, G. A., and SWAMI, M., *ibid.*, V 99, p 1055 (1955).

105. FRY, W. F., *ibid.*, V 91, p 130 (1953); *ibid.*, V 86, p 418 (1953); *ibid.*, V 83, p 1268 (1951).
106. CASTAGNOLI, C., and MUCHNIK, M., *ibid.*, V 112, p 1779 (1958).
107. IOFFE, B., and RUDIK, A., *Dokl. Akad. Nauk. SSSR*, V 82, p 359 (1952).
108. FIALHO, G. E. A., and TIOMNO, J., *Anais Acad. brasil. Cienc.*, V 24, p 245 (1952).
109. BINNIE, D. M., de S. BARROS, S. L., and HYAMS, B. D., *Nuovo Cim.*, V 20, p 140 (1961).
110. HUANG, K., and LOW, F. E., *Phys. Rev.*, V 109, p 1400 (1958).
111. ONEDA, S., and KAMEFUCHI, S., *Nucl. Phys.*, V 6, p 114 (1958).
112. VAKS, V. G., and IOFFE, B. L., *Zh. eksp. teor. Fiz.*, V 35 (1), (7), p 221 (1958).
113. IWATA, K., OKAWA, S., OKONOJI, H., SACITA, B., and ONEDA, S., *Proc. theor. Phys.*, Japan, V 13, p 19 (1955).
114. TREIMAN, S. B., and WYLD, H. W., Jr., *Phys. Rev.*, V 101 (1955).
115. CASSELS, J. M., RIGBY, M., WETHERELL, A. M., and WORMALD, J. R., *Proc. Phys. Soc.*
116. LEE, T. D., *Proc. Int. Conf. on High-Energy Phys.*, p 567, Rochester (1960).
117. GELL-MANN, M., *Rev. Mod. Phys.*, V 31 (3), p 834 (1959); MEYER, Ph., and SALZMAN, G., *Nuovo Cim.*, V 14, p 1310 (1959).
118. KRESTNIKOV, Yu. S., MESHKOVSKII, A. G., SHALAMOV, Ya. Ya., SHEBANOV, V. A., and KOBZAREV, I. Yu., *Zh. eksp. teor. Fiz.*, V 37, p 873 (1959).
119. LOKANATHAN, S., and STEINBERGER, J., *Phys. Rev.*, V 98, p 240(A) (1955).
120. DAVIS, H. F., ROBERTS, A., and ZIPF, T. F., *Phys. Rev. Lett.*, V 2, p 211 (1959).
121. FRANKEL, S., HAGOPIAN, V., HALPERN, J., and WHETSTONE, A. L., *Phys. Rev.*, V 118, p 589 (1960).
122. O'KEEFE, T. W., RIGBY, M., and WORMALD, J. R., *Proc. phys. Soc., Lond.*, V 73, p 951 (1959).
- 123a. ALIKHANOV, A. I., BABAEV, A. P., BALATS, M. Ya., KAFTANOV, V. S., LANDSBERG, L. G., LYUBIMOV, V. A., and OBUKHOV, Yu. V., *Zh. eksp. teor. Fiz.*, V 42, p 630 (1962).
123. BERLEY, D., LEE, J., and BARDON, M., *Phys. Rev. Lett.*, V 2, p 357 (1959).
124. FRANKEL, S., HALPERN, J., HOLLOWAY, L., and WALES, W., et al., *Phys. Rev. Lett.*, V 8, p 123 (1962).
125. BARTLETT, D., DEVONS, S., and SACHS, A. M., *Phys. Rev. Lett.*, V 8, p 120 (1962).
126. WEISSENBERG, A. O., *Dissertation* (1961).
127. PARKER, S., and PENMAN, S., *Nuovo Cim.*, V 23, p 485 (1962).
128. BABAEV, A. P., BALATS, M. Ya., KAFTANOV, V. S., LANDSBERG, L. G., LYUBIMOV, V. A., and OBUKHOV, Yu. V., *Zh. eksp. teor. Fiz.*, V 42, p 1685 (1962).
129. STEINBERGER, J., and WOLFE, H. B., *Phys. Rev.*, V 100, p 1490 (1955).
130. SARD, R. D., CROWE, K. M., and KRUGER, H., *ibid.*, V 121, p 619 (1961).
131. CONVERSI, M., Di LELLA, L., EGIDI, A., RUBBIA, C., and TOLLER, M., *Nuovo Cim.*, V 19, p 987 (1961); V 18, p 1283 (1960); V 19, p 999 (1961); *Phys. Rev.*, V 122, p 687 (1961).
132. BLOCK, M. M., FIORINI, E., KIKUCHI, T., GIACOMELLI, G., and RATTI, S., *Nuovo Cim.*, V 23, p 1114 (1962).
133. BARDON, M., NORTON, P., PEOPLES, J., and SACHS, A. M., *Phys. Rev. Lett.*, V 14, p 449 (1965).
134. TERENT'EV, M. V., *Zh. eksp. teor. Fiz.*, V 44, p 1320 (1963).
135. DUNAITSEV, A. F., PUTRUKHIN, V. P., PROKOSHKIN, Yu. D., and RYKALIN, V. P., *Zh. eksp. teor. Fiz.*, V 47, p 84 (1964).
136. DEPOMMIER, P., HEINTZE, J., RUBBIA, C., and SORGEL, V., *Phys. Lett.*, V 5, p 61 (1963).
137. BARTLETT, D., DEVONS, S., MEIER, S. L., and ROSEN, J. L., *Phys. Rev.*, V 136, p 1425B (1964).

138. FRANKEL, S., FRATI, W., HALPERN, J., HOLLOWAY, L., WALLEES, W., and CHAMBERLAIN, O., *Nuovo Cim.*, V 27, p 894 (1963).
139. PARKER, S., ANDERSON, H. L., and REY, C., *Phys. Rev.*, V 133, p 768B (1964).
140. FRANKEL, S., FRATI, W., HALPERN, J., HOLLOWAY, L., WALLS, W., and CHAMBERLAIN, O., *ibid.*, V 130, p 351 (1963).

CHAPTER 3

1. SARD, R. D., ITTNER, W. B., CONFORTO, A. M., and CROUCH, M. F., *Phys. Rev.*, V 74, p 97 (1948).
2. GROETZINGER, G., and McCLURE, G. W., *ibid.*, V 74, p 341 (1948).
3. WIDGOFF, M., *ibid.*, V 90, p 891 (1953).
4. JONES, D. R., *ibid.*, V 105, p 1591 (1957).
5. KAPLAN, S. N., *ibid.*, V 112, p 968 (1959).
6. SARD, R., and CROUCH, M., 'Progress in cosmic ray physics', V 2, pp 7-52, North-Holland Publishing Company (1956).
7. ALTHAUS, E. J., *Phys. Rev.*, V 81, p 647 (1951).
8. GROETZINGER, G., BERGER, M. J., and McCLURE, G. W., *ibid.*, V 81 (1951).
9. CONFORTO, A. M., and SARD, R. D., *ibid.*, V 86, p 465 (1952).
10. WINSBERG, L., *ibid.*, V 95, p 205 (1954).
11. TIOMNO, J., and WHEELER, J. A., *Rev. Mod. Phys.*, V 21, p 153 (1949).
12. ROSENBLUTH, M. N., *Phys. Rev.*, V 75, p 532 (1949).
13. LANG, J. M. B., *Proc. Phys. Soc.*, (London), V 65A, p 995 (1952).
14. COLE, F. T., Thesis, Cornell University (1953).
15. LUBKIN, E., *Ann. Phys.*, V 11, p 414 (1960).
16. SINGER, P., *Nuovo Cim.*, V 23, p 669 (1962).
17. CAMERINI, U., MUIRHEAD, H., POWELL, C. F., and RISON, D. H., *Nature, Lond.*, V 162, p 433 (1948).
18. GEORGE, E. P., and EVANS, J., *Proc. Phys. Soc.*, V 63A, p 124 (1950); *ibid.*, V 64A, p 193 (1951).
19. MORINAGA, H., and FRY, W. F., *Nuovo Cim.*, V 10, p 308 (1953).
20. STANNARD, F. R., *Phys. Rev. Lett.*, V 4, p 523 (1960).
21. SCHIFF, M., *Nuovo Cim.*, V 22, p 66 (1961).
22. DZHELEPOV, V. P., YERMOLOV, P. F., et al., *Zh. eksp. teor. Fiz.*, V 42, p 439 (1962).
23. MENON, M. G. K., MUIRHEAD, H., and ROCHAT, O., *Phil. Mag.*, V 41, p 583, (1950).
24. ISHII, C., *Prog. theor. Phys. (Kyoto)*, V 21, p 670 (1959).
25. SINGER, P., *Phys. Rev.*, V 124, p 1602 (1961).
26. CHANG, W. Y., *Rev. Mod. Phys.*, V 21, p 166 (1948).
27. HARRIS, G. G., and SHANLEY, T. J. B., *Phys. Rev.*, V 89, p 983 (1953).
28. SENS, J. C., *ibid.*, V 113, p 685 (1959).
29. GOLDBERGER, M. L., and TREIMAN, S. B., *ibid.*, V 111, p 355 (1958).
30. WOLFENSTEIN, L., *Nuovo Cim.*, V 8, p 882 (1958).
31. GERSHTEIN, S. S., and ZEL'DOVICH, Ya. B., *Zh. eksp. teor. Fiz.*, V 29, p 698 (1955).
32. FEYNMAN, R. P., and GELL-MANN, M., *Phys. Rev.*, V 109, p 193 (1958).
33. PRIMAKOFF, H., *Rev. Mod. Phys.*, V 31, p 802 (1959).
34. BERTOLINI, E., CITRON, A., and GIALANELLA, G., et al., *Proc. Int. Conf. on High-energy Phys.*, p 421, CERN (1962).
35. BLESER, E., LEDERMAN, L., ROSEN, J., ROTHBERG, J., and ZAVATTINI, E., *Phys. Rev. Lett.*, V 8, p 288 (1962).
36. ZEL'DOVICH, Ya. B., and GERSHTEIN, S. S., *Zh. eksp. teor. Fiz.*, V 35,

- p 649 (1958); *Usp. fiz. Nauk*, V 71, p 581 (1960); ZEL'DOVICH, Ya. B., *ibid.*, V 33, p 310 (1957).
37. GERSHTEIN, S. S., *ibid.*, V 34, p 463 (1958); V 34, p 933 (1958).
 38. WEINBERG, S., *Phys. Rev. Lett.*, V 4, p 575 (1960).
 39. COHEN, S., JUDD, D. L., and RIDDELL, R. J., Atomic Energy Commission Report, UCRL., V 8, p 391 (1959); *Phys. Rev.*, V 110, p 1471 (1958).
 40. SKYRME, T. H. R., *Phil. Mag.*, V 2, p 910 (1957).
 41. JACKSON, J. D., *Phys. Rev.*, V 106, p 330 (1957).
 42. GODFREY, T. N. K., *ibid.*, V 92, p 512 (1953); Thesis, Princeton University, New Jersey (1954).
 43. FUJII, A., and PRIMAKOFF, H., *Nuovo Cim.*, V 12, p 327 (1959).
 44. WERNTZ, C., *Nucl. Phys.*, V 16, p 59 (1960).
 45. FUJII, A., *Phys. Rev.*, V 118, pp 3 and 870 (1960).
 46. BURGMAN, J. O., FISCHER, J., LEONTIC, B., LUNDBY, A., et al., *Phys. Rev. Lett.*, V 1, p 469 (1958).
 47. LOVE, W. A., MARDER, S., NADELHAFT, I., SIEGEL, R. T., and TAYLOR, A. E., *Bull. Am. phys. Soc.*, V 4, p 81 (1959) (see also Conference on Weak Interaction, Tennessee (1958)).
 48. BLOCH, G. B., Thesis, Cornell Institute of Technology (1960).
 49. MAIER, E. J., BLOCH, B. L., EDELSTEIN, R. M., and SIEGEL, R. T., *Phys. Rev. Lett.*, V 6, p 417 (1961).
 50. FETKOVICH, J., FIELDS, T., and McILWAIN, R. L., *Phys. Rev.*, V 118, p 319 (1960).
 51. ARGO, H. V., HARRISON, F. B., KRUSE, H. W., and McGUIRE, A. D., *ibid.*, V 114, p 626 (1959).
 52. WOLFENSTEIN, L., *Nuovo Cim.*, V 13, p 319 (1959).
 53. MORITA, M., and FUJII, A., *Phys. Rev.*, V 118, p 606 (1960).
 54. FUJII, A., and PRIMAKOFF, H., *Nuovo Cim.*, V 12, p 327 (1959).
 55. FERMI, E., and TELLER, E., *Phys. Rev.*, V 72, p 399 (1947).
 56. FRY, W. F., and WHITE, G. R., *ibid.*, V 93, p 1427 (1954).
 57. FIELDS, T. H., YODH, G. B., DERRICK, M., and FETKOVICH, J. G., *Phys. Rev. Lett.*, V 5, p 690 (1960).
 58. ALBERIGI-QUARANTA, A., and PANCINI, E., *Nuovo Cim.*, V 9, p 959 (1952).
 59. ALBERIGI-QUARANTA, A., and PANCINI, E., *ibid.*, V 11, p 607 (1954).
 60. ALBERIGI-QUARANTA, A., DORE, U., and PIERACCINI, F., *ibid.*, V 14, p 48 (1959).
 61. KEUFFEL, J. W., HARRISON, F. B., GODFREY, T. N. K., and REYNOLDS, G. T., *Phys. Rev.*, V 87, p 942 (1952).
 62. MEYER, A. J., and KEUFFEL, J. W., *Phys. Rev.*, V 90, p 349 (1953); MEYER, A. J., Thesis, Princeton University, New Jersey (1954).
 63. NEDDERMEYER, S. H., ALTHAUS, E. J., ALLISON, W., and SCHATZ, E. R., *Rev. Scient. Instrum.* V 18, p 488 (1947).
 64. HILLAS, A. M., GILBOY, W. B., and TENNENT, R. M., *Phil. Mag.*, V 3, p 109 (1958).
 65. GILBOY, W., and TENNENT, R., *ibid.*, V 3, p 109 (1958).
 66. BARRETT, W. A., HOLMSTROM, F. E., and KEUFFEL, J. W., *Phys. Rev.*, V 113, p 661 (1959).
 67. HOLMSTROM, F. E., and KEUFFEL, J. W., *Bull. Phys. Soc.*, V 3, p 408, (1958).
 68. SENS, J. C., *Phys. Rev.*, V 113, p 679 (1959).
 69. SENS, J. C., SWANSON, R. A., TELEGDI, V. L., and YOVANOVICH, D. D., *ibid.*, V 107, p 1464 (1957).
 70. YOVANOVITCH, D. D., *ibid.*, V 117, p 1580 (1960).
 71. LUNDY, R. A., SENS, J. C., SWANSON, R. A., TELEGDI, V. L., and YOVANOVITCH, D. D., *Phys. Rev. Lett.*, V 1, p 102 (1958).
 72. LATHROP, J. F., LUNDY, R. A., TELEGDI, V. L., WINSTON, R., and YOVANOVITCH, D. D., *ibid.*, V 7, p 107 (1961).

73. ASTBURY, A., KEMP, M. A. R., LIPMAN, H. H., MUIRHEAD, H., VOSS, R. G. P., ZANGGER, C., and KIRK, A., Proc. Phys. Soc., V 72, p 494 (1959).
74. ASTBURY, A., HUSSAIN, M., KEMP, M. A. R., LIPMAN, H. H., MUIRHEAD, H., VOSS, R. G. P., and KIRK, A., Proc. Phys. Soc., V 73, p 314 (1959).
75. REITER, R. A., ROMANOWSKI, T. A., et al., see Chapter 2; TENNENT, R. M., 'Progress in elementary particle and cosmic ray physics', V 5, p 365, North-Holland Publishing Company (1960).
76. BERTRAM, W. J., Jr., REITER, R. A., ROMANOWSKI, T. A., and SUTTON, R. B., Phys. Rev. Lett., V 5, p 61 (1960).
77. CRAMER, W. A., TELEGDI, V. L., and WINSTON, R., Nuovo Cim., V 24, p 546 (1962).
78. FIELDS, T. H., McILWAIN, R. L., and FETKOVICH, J. G., Bull. Am. phys. Soc., V 4, p 81 (1959).
79. WHEELER, J. A., Rev. Mod. Phys., V 21, p 133 (1949).
80. HILLAS, A. M., Thesis, University of Leeds (1958).
81. TELEGDI, V. L., Phys. Rev. Lett., V 8, p 327 (1962).
82. PORTER, C. E., and PRIMAKOFF, H., Phys. Rev., V 83, p 849 (1951).
83. MUTO, T., Prog. theor. Phys. (Kyoto), V 8, p 13 (1952).
84. GILINSKY, V., and MATHEWS, J., Phys. Rev., V 120, p 1450 (1960).
85. ÜBERALL, H., *ibid.*, V 119, p 365 (1960); Nuovo Cim., V 15, p 163 (1960).
86. TERENT'EV, M. V., Zh. eksp. teor. Fiz., V 39, p 1735 (1960).
87. HUFF, R., Ann. Phys., V 16, p 288 (1961); JOHNSON, W. R., O'CONNELL, R. F., and MULLIN, C. J., Phys. Rev., V 124, p 904 (1961).
88. KRUEGER, L., and ROTHLEITNER, J., Z. Phys., V 164, p 330 (1961).
89. LEDERMAN, L. M., and WEINRICH, M., Proc. Int. Conf. High-Energy Accelerators and Ion Physics, CERN, Geneva, V 2, p 427 (1956).
90. KEUFFEL, J. W., Proc. Int. Conf. on High-Energy Phys., p 544, Rochester (1960).
91. CHILTON, F., Phys. Rev. Lett., V 7, p 31 (1961).
92. ALLABY, J. V., CHISHOLM, A., EADES, J., and TOWNES, B. M., Phys. Rev., V 125, p 2077 (1962).
93. CULLIGAN, G., HARTING, D., LIPMAN, N. H., and TIBEL, G., Conf. Int. on Elementary Particles, Aix-de-Provence, V 1, p 143 (1961).
94. IGNATENKO, A. E., YEGOROV, L. B., KUPTSOV, A. V., and PETRASHKU, M. G., Zh. eksp. teor. Fiz., V 43, p 1149 (1962).
95. DIAZ, J. A., KAPLAN, S. N., and PYLE, R. V., Data presented at the A.P.S. Meeting in Los-Angeles (Dec. 1961).
96. BERNSTEIN, J., LEE, T. D., YANG, C. N., and PRIMAKOFF, H., Phys. Rev., V 111, p 313 (1958).
97. ÜBERALL, H., *ibid.*, V 114, p 1640 (1959).
98. TELEGDI, V. L., Phys. Rev., Lett., V 3, p 59 (1959).
99. WINSTON, R., and TELEGDI, V., *ibid.*, V 7, p 105 (1961).
100. CULLIGAN, G., LATHROP, J., TELEGDI, V. L., and WINSTON, R., *ibid.*, V 7, p 458 (1961).
101. HUANG, K., YANG, C. N., and LEE, T. D., Phys. Rev., V 108, p 1440 (1957).
102. SHAPIRO, P. S., DOLINSKY, E., and BLOKHINTSEV, L. D., Nucl. Phys., V 4, p 273 (1957).
103. ÜBERALL, H., Nuovo Cim., V 6, p 533 (1957).
104. AKIMOVA, M. K., BLOKHINTSEV, L. D., and DOLINSKII, E., Zh. eksp. teor. Fiz., V 39, p 1806 (1960).
105. DOLINSKII, E., and BLOKHINTSEV, L. D., *ibid.*, V 35, p 1488 (1958).
106. BLOKHINTSEV, L. D., *ibid.*, V 36, p 258 (1959).
107. BAKER, W. F., and RUBBIA, C., Phys. Rev. Lett., V 3, p 179 (1959).
108. ASTBURY, A., BLAIR, D. M., and HUSSAIN, M., et al., *ibid.*, V 3, p 476 (1959).
109. ASTBURY, A., BARTLEY, J. H., BLAIR, I. M., KEMP, M. A. R., MUIRHEAD, H., and WOODHEAD, T., Preprint (1962).
110. TELEGDI, V. L., Proc. 10th Rochester Conf., p 713 (1960).

111. KOMAROV, V. A., YEVSEEV, V. S., KUSH, V. Z., ROGANOV, V. S., CHERNOGOROVA, V. A., and SCHIMCHAK, M. M., *Zh. eksp. teor. Fiz.*, V 41, p 306 (1961).
112. MORITA, M., and GREENBERG, D., *Phys. Rev.*, V 119, p 435 (1960).
113. ROSE, M. E., and GOOD, R. H., Jr., *Ann. Phys.*, V 9, p 211 (1960).
114. WOLFENSTEIN, L., *Nuovo Cim.*, V 13 (1959).
115. SHAPIRO, I. S., and BLOKHINTSEV, L. D., *Zh. eksp. teor. Fiz.*, V 39, p 1113 (1960).
116. CANTWELL, see 118.
117. BERNSTEIN, J., *Phys. Rev.*, V 115, p 694 (1959).
118. CONFORTO, G., CONVERSI, M., and DI LELLA, L., *Proc. Int. Conf. on High-Energy Physics, CERN*, p 427 (1962).

CHAPTER 4

1. MARSHAK, M. E., 'Meson physics' (1962).
2. COOPER, L. N., and HENLEY, E. M., *Phys. Rev.*, V 92, p 801 (1953).
3. FLÜGGE, S. W., and ADLER, F. T., *Naturwiss.*, V 40, p 601 (1953).
4. FITCH, V. L., and RAINWATER, J., *Phys. Rev.*, V 92, p 789 (1953).
5. CHANG, W. Y., *Rev. Mod. Phys.*, V 21, p 166 (1949).
6. BUTEMENT, F. D. S., *Phil. Mag.*, V 44, p 208 (1953).
7. JOHNSON, C. S., HINCKS, E. P., and ANDERSON, H. L., Preprint (1961).
8. WEST, D., et al., *Proc. Phys. Soc.*, V A68, p 801 (1955).
9. BUTEMENT, F. D. S., *Phil. Mag.*, V 46, p 1136 (1955).
10. HILL, D. L., and FORD, K. W., *Phys. Rev.*, V 94, p 1617 (1954).
11. KOSLOV, S., FITCH, V., and RAINWATER, J., *ibid.*, V 95, p 291 (1954).
12. STEARNS, M., STEARNS, M. B., DEBENEDETTI, S., and LEIPUNER, L., *ibid.*, V 95, p 1353 (1954); V 96, p 804 (1954); V 97, p 240 (1955).
13. BEARDEN, A. J., *Phys. Rev. Lett.*, V 4, p 240 (1960).
14. PETERMANN, A., and YAMAGUCHI, Y., *ibid.*, V 2, p 359 (1959).
15. LATHROP, J., LUNDY, R. A., TELEGDI, V. L., WINSTON, R., and YOVANOVITCH, D. D., *Nuovo Cim.*, V 17, pp 109 and 113 (1960).
16. DEVONS, S., GIDAL, G., LEDERMAN, L. M., and SHAPIRO, G., *Phys. Rev. Lett.*, V 5, p 330 (1960).
17. BURBIDGE, G. R., and DE BORDE, A. H., *Phys. Rev.*, V 89, p 189 (1953).
18. DE BORDE, A. H., *Proc. Phys. Soc.*, V A67, p 57 (1954).
19. RUDERMAN, M. A., *Phys. Rev.*, V 118, p 1632 (1960).
20. FERREL, R. A., *Phys. Rev. Lett.*, V 4, p 425 (1960).
21. EISENBERG, Y., and KESSLER, D., *Nuovo Cim.*, V 6, p 1195 (1961).
22. EISENBERG, Y., and KESSLER, D., *Phys. Rev.*, V 123, p 1472 (1961).
23. BERNSTEIN, J., and WU, T. Y., *Phys. Rev. Lett.*, V 2, p 404 (1959).
24. KRALL, N. A., and GERJUOY, E., *ibid.*, V 3, p 142 (1959).
25. STEARNS, M. B., and STEARNS, M., *Phys. Rev.*, V 105, p 1573 (1957).
26. STEARNS, M. B., STEARNS, M., and LEIPUNER, L., *ibid.*, V 108, p 445 (1957).
27. LATHROP, J., LUNDY, R. A., TELEGDI, V. L., and WINSTON, R., *Phys. Rev. Lett.*, V 7, p 148 (1961).
28. COSYNS, M. G. E., DILWORTH, C. C., OCCHIALINI, G. P. S., and SHOENBERG, M., *Proc. Phys. Soc.*, V A62, p 801 (1949).
29. BONETTI, A., and TOMASINI, G., *Nuovo Cim.*, V 8, p 693 (1951).
30. FRY, W. F., *Phys. Rev.*, V 83, p 594 (1951); *Nuovo Cim.*, V 10, p 490 (1953).
31. WEISSENBERG, A. O., Dissertation (1961).
32. PEVSNER, A., STRAND, R., and MADANSKY, L., *Nuovo Cim.*, V 19, p 409 (1961).
33. RAWITSCHER, G. H., *Phys. Rev.*, V 101, p 423 (1956).
34. MASEK, G. E., and PANOFSKY, W. K. H., *ibid.*, V 101, p 1094 (1956).

35. MASEK, G. E., LAZARUS, A. J., and PANOFSKY, W. K. H., *ibid.*, V 103, p 374 (1956).
36. ALBERIGI-QUARANTA, A., et al., *Phys. Rev., Lett.*, V 9 (5), p 226 (1962).
37. HOFFSTADTER, R., *Rev. Mod. Phys.*, No. 4, p 693 (1957).
38. FOWLER, G. N., and WOLFENDALE, A. W., 'Progress in elementary particle and cosmic ray physics', V 4, Chapter 3, North-Holland Publishing Company (1960).
39. MASEK, G. E., HEGGIE, L. D., KIM, Y. B., and WILLIAMS, R. W., *Phys. Rev.*, V 122, p 937 (1961).
40. CONOLLY, P. L., McEWEN, J. G., and OREAR, J., *Phys. Rev. Lett.*, V 6, p 554 (1961).
- 40'. RAWITSCHER, G. H., *Phys. Rev.*, V 112, p 1274 (1958).
41. COOPER, L. N., and RAINWATER, J., *ibid.*, V 97, p 492 (1955).
42. SCHWARTZ, C. L., and DRELL, S. D., *ibid.*, V 112, p 568 (1958).
43. MASEK, G. E., TOUTONGHI, J. P., and WILLIAMS, R. W., *ibid.*, V 124, p 555 (1961).
44. FRIEDMAN, J. I., *ibid.*, V 116, p 1257 (1959).
45. KARPLUS, R., and KROLL, N. M., *ibid.*, V 77, p 536 (1950).
46. SOMMERFIELD, C. M., *ibid.*, V 107, p 328 (1957).
47. PETERMANN, A., *Helv. phys. Acta.*, V 30, p 407 (1957).
48. COHEN, E. R., CROWE, K. M., and DUMOND, J. W. M., 'Fundamental constants of physics', published in New York (1957).
49. SCHUPP, A. A., PIDD, R. W., and CRANE, H. R., *Phys. Rev.*, V 121, p 1 (1961).
50. CASSELS, J. M., O'KEEFE, T. W., RIGBY, M., WETHERELL, A. M., and WORMALD, J. R., *Proc. Phys. Soc.*, V 2A70, p 543 (1957).
51. COFFIN, T. GARWIN, R. L., PENMAN, S., LEDERMAN, L. M., and SACHS, A. M., *Phys. Rev.*, V 109 p 973 (1958).
52. LUNDY, R. A., SENS, J. C., SWANSON, R. A., TELEGDI, V. L., and YOVANOVITCH, D. D., *Phys. Rev. Lett.*, V 1, p 38 (1958).
53. GARWIN, R. L., HUTCHINSON, D. P., PENMAN, S., and SHAPIRO, G., *Phys. Rev.*, V 118, p 271 (1960); GARWIN, R. L., LEDERMAN, L. M., and WEINRICH, M., *ibid.*, V 105, p 1415 (1957).
54. HUTCHINSON, D. P., MENES, J., SHAPIRO, G., PATLACH, A. M., and PENMAN, S., *Phys. Rev. Lett.*, V 7, p 129 (1961).
55. FORD, K. W., HUGHES, V., and WILLS, J., *ibid.*, V 7, p 134 (1961).
56. CHARPAK, G., FARLEY, F. J. M., GARWIN, R. L., MULLER, T., SENS, J. C., TELEGDI, V. L., and ZICHICHI, A., *ibid.*, V 6, p 128 (1961).
57. CHARPAK, G., FARLEY, F. J. M., GARWIN, R. L., MULLER, T., SENS, J. C., and ZICHICHI, A., *ibid.*, V 1, p 16 (1962).
58. BERESTETSKY, V. B., KROKIN, O. N., and KHLEBNIKOV, A. K., *Zh. eksp. teor. Fiz.*, V 30, p 788 (1956).
59. BERESTETSKY, V., *ibid.*, V 39, p 1427 (1960).
60. DE TOLLIS, B., *Nuovo Cim.*, V 16, p 203 (1960).
61. CHASMAN, C., RESTINEN, R. A., COHEN, R. C., DEVONS, S., and NISSIM-SABAT, C., *Phys. Rev. Lett.*, V 14 (6), p 181 (1965).
62. COTE, R. E., GUSO, R., RABOY, S., CARRIGAN, R. A., GAIGALAS, A., SUTTEN, R. B., and TRAIL, C. C., *ibid.*, V 19 (1), p 18 (1965).
63. WHEELER, T. A., *Phys. Rev.*, V 92, p 812 (1953).
64. FRATI, W., and RAINWATER, J., *ibid.*, V 128 (5), p 2360 (1962).
65. ANDERSON, H. L., JOHNSON, C. S., and HINCKS, E. P., *ibid.*, V 136 (6), p 2468 (1963).
66. BACKENSTOSS, G., GOEBEL, K., STADLER, B., HEGEL, N., and QUITMANN, D., *Nucl. Phys.*, V 62, p 449 (1965).
67. QUITMANN, D., ENGFER, R., HEGEL, U., BRIX, R., BECKENSTOSS, G., GOEBEL, K., and STADLER, B., *ibid.*, V 51, p 609 (1964).
68. FORD, K. W., and WILLIS, J. G., *ibid.*, V 35, p 295 (1962).
69. PUSTOVALOV, G. E., and KRECHKO, M. S., *ibid.*, V 19, p 337 (1960).

70. FEINBERG, G., and LEDERMAN, L.M., *A. Rev. Nucl. Sc.*, V 13, p466 (1965).
71. DEPAGTER, J.K., BOYARSKI, A., GLASS, G., FRIEDMAN, J.I., KENDALL, H.W., GETTNER, M., LARRABEE, J.R., and WEINSTEIN, R., *Phys. Rev. Lett.*, V 12 (26), p739 (1964).
72. KOTELCHUK, D., McEWEN, G., and OREAR, J., *Phys. Rev.*, V 129 (2), p876 (1963).
73. CITRON, A., DE-LORME, C., FRIES, D., GOLDZAHL, L., HEINTZE, J., MICHAELIS, E.D., RICHARD, C., and OOERAS, H., *Phys.*, V 1, p175 (1962).
74. DAVIS, H.F., EVART, T.E., MASEK, G.E., PLATNER, E.D., TAUTONGHI, J.P., and WILLIAMS, R.W., *Phys. Rev.*, V 131 (5), p2192 (1963).
75. COOL, R., MASCHKE, A., LEDERMAN, L.M., TANNENBAUM, M., ELSWORTH, R., MELISSINOS, A., TINLOT, J.H., YAMANOUCHI, T., *Phys. Rev. Lett.* V 14, p724 (1965).
76. HAND, L., MILLER, D., and WILSON, R., *Rev. Mod. Phys.*, V 35, p335 (1965).
77. ACKER, H.L., BACKENSTOSS, G., DAUM, C., SENS, J.C., and DE WIT, S.A., CERN preprint (1966).

CHAPTER 5

1. ALVAREZ, L.W., BRADNER, H., CRAWFORD, F.S., et al., *Phys. Rev.*, V 105, p1127 (1957).
2. FRANK, F.C., *Nature, Lond.*, V 160, p525 (1947).
3. SAKHAROV, A.D., FIAN Report (1948).
4. ZEL'DOVICH, Ya.B., *Dokl. Akad. Nauk. SSSR*, V 95, p493 (1954).
5. DZHELEPOV, V.P., *Atom. Energiya*, V 14, p27 (1963).
6. SCHIFF, M., *Nuovo Cim.*, V 22, p66 (1961).
7. BELYAEV, V.B., GERSHTEIN, S.S., ZAKHAROV, B.N., and LOMNEV, S.P., *Zh. eksp. teor. Fiz.*, V 37, p1652 (1959).
8. DZHELEPOV, V.P., YERMOLAEV, P.F., KUSHNIRENKO, E.A., MOSKALEV, V.I., and GERSHTEIN, S.S., *ibid.*, V 42, p439 (1962).
9. CRESTI, M., GOTTSTEIN, K., ROSENFELD, A.H., and TICHO, H.K., Atomic Energy Commission Report, HCRL 3782 (1957).
10. FETKOVICH, J.G., FIELDS, T.H., YODH, G.B., and DERRICK, M., *Phys. Rev. Lett.*, V 4, p570 (1960).
11. ASHMORE, A., NORDHAGEN, R., STRAUCH, K., and TOWNES, B.M., *Proc. Phys. Soc.*, V 71, p161 (1958).
12. BLESER, E., LEDERMAN, L.M., ROSEN, J., ROTHBERG, J., and ZAVATTINI, E., *Phys. Rev. Lett.*, V 8, p128 (1962); COHEN, S., JUDD, D.L., and RIDDELL, R.J., Jr., *Phys. Rev.*, V 119, p397 (1960).
13. ZEL'DOVICH, Ya., and GERSHTEIN, S., *Usp. fiz. Nauk.*, V 71, p581 (1960).
14. MIZUNO YUKIO, *J. phys. Soc., Japan*, V 16, p1043 (1961).
15. ZEL'DOVICH, Ya.B., and GERSHTEIN, S.S., *Zh. eksp. teor. Fiz.*, V 35, p649 (1958).
16. COHEN, S., JUDD, D.L., and RIDDELL, R.J., Jr., *Phys. Rev.*, V 119, pp384, 397 (1960).

CHAPTER 6

1. GOL'DMAN, I.I., *Zh. eksp. teor. Fiz.*, V 34, p1017 (1958).
2. WERLE, J., *Nuovo Cim.*, V 7, p255 (1958).
3. HAYAKAWA, S., *Phys. Rev.*, V 108, p1533 (1957).
4. CLARK, G.W., and HERSIL, J., *ibid.*, V 108, p1538 (1957).

5. FOWLER, J., PRIMAKOFF, H., and SARD, R., *Nuovo Cim.*, V 9, p 1027 (1958).
6. BARMIN, V. V., KANAVETS, V. P., and MOROZOV, B. V., *Zh. eksp. teor. Fiz.*, V 39, p 986 (1960).
7. DOLGOSHEIN, B. A., Dissertation (1962).
8. ALIKHANYAN, A. I., ASATIANI, T. L., SHARKHATUNYAN, R. O., Paper read at the All-Union Conf. on Cosmic Rays (1961).
9. CLARK, G. W., Paper read at the Int. Conf. on Cosmic Rays, Kyoto, Japan (1961).
10. KOCHARYAN, N. M., *Zh. eksp. teor. Fiz.*, V 38, p 18 (1960).
11. JOHNSON, C., Paper read at the Int. Conf. on Cosmic Rays, Moscow (1959).
12. ALIKHANYAN, A. I., ASATIANI, T. L., MATEVOSYAN, E. M., and SHARKHATUNYAN, R. O., *Zh. eksp. teor. Fiz.*, V 42, p 127 (1962).
13. FRIEDMAN, J. I., and TELEGDI, V. L., *Phys. Rev.*, V 106, p 1290 (1957).
14. CASTAGNOLI, C., FRANZINETTI, C., and MANFREDINI, A., *Nuovo Cim.*, V 5, p 684 (1957).
15. CASTAGNOLI, C., MANFREDINI, A., and MERRISON, A. W., *ibid.*, V 9, p 186 (1958).
16. FOWLER, P. H., FREIER, P. S., LATTES, C. M. G., NEY, E. P., and ST. LORAN, S. J., *ibid.*, V 6, p 63 (1957).
17. BOGGILD, J. K., HANSEN, K. H., and SCHARFF, M., *ibid.*, V 8, p 1695 (1958).
18. BHOWMIK, B., EVANS, D., and PROWSE, D. J., *ibid.*, V 5, p 1663 (1957).
19. BISWAS, N. N., CECCARELLI, M., and CRUSSARD, J., *ibid.*, V 5, p 756 (1957).
20. DAVIS, D. F., ENGLER, A., CORBEL, C. J., HOANG, T. E., KAPLON, M. F., and KLARMAN, I., Preprint (1957).
21. WEISSENBERG, A. O., SMIRNITSKY, V. A., and RABIN, N. V., *Zh. eksp. teor. Fiz.*, V 36, p 1860 (1959).
22. GUREVICH, I. I., KATUKOVA, V. M., MISHAKOVA, A. P., NIKOL'SKY, B. A., and SURKOVA, L. V., *ibid.*, V 34, p 280 (1958).
23. IVANOV, Yu. M., and FESENKO, A. P., *ibid.*, V 35, p 1297 (1958).
24. CHADWICK, G. B., DURRANI, S. A., EISBERG, L. M., JONES, P. B., WIGNALL, J. W. G., and WILKINSON, D. H., *Phil. Mag.*, V 2, p 684 (1957).
25. IVANOV, Yu. M., and FESENKO, A. P., *Zh. eksp. teor. Fiz.*, V 39, p 1492 (1960).
26. WEISSENBERG, A. O., Dissertation (1961).
27. SWANSON, R. A., *Phys. Rev.*, V 112, p 580 (1958).
28. CASSELS, J. M., O'KEEFE, T. W., RIGBY, M., WETHERELL, A. M., and WORMALD, J. R., *Proc. Phys. Soc.*, V A70, p 543 (1957).
29. WEINRICH, M., Preprint (1957).
30. FORD, G. W., and MULLIN, C. J., *Phys. Rev.*, V 108, p 477 (1958).
31. BINCER, A. M., *ibid.*, V 107, p 1434 (1957).
32. WENTZEL, G., *ibid.*, V 75, p 1810 (1949).
33. YAKOVLEVA, I. V., *Zh. eksp. teor. Fiz.*, V 35, p 968 (1958).
34. FEHER, G., PREPOST, R., and SACHS, A. M., *Phys. Rev. Lett.*, V 5, p 515 (1960).
35. BREIT, G., and HUGHES, V. W., *Phys. Rev.*, V 106, p 1293 (1957).
36. FERRELL, R. A., *ibid.*, V 110, p 1355 (1958).
37. FERRELL, R. A., and CHAOS, F., *ibid.*, V 107, p 1322 (1957).
38. FERRELL, R. A., LEE, Y., and PAL, M., *ibid.*, V 118, p 317 (1950).
39. BARKAS, W. H., GILES, P. C., HECKMAN, H. H., INMAN, F. W., and SMITH, F. M., *ibid.*, V 107, p 911 (1957).
40. OREAR, J., LYNCH, G. R., and ROSENDORFF, S., *ibid.*, V 108, p 284 (1960).
41. ALI-ZADE, S. A., GUREVICH, P. P., DOBRETsov and NIKOL'SKY, B. A., *Zh. eksp. teor. Fiz.*, V 36, p 1327 (1959).
42. GUREVICH, P. P., NIKOL'SKY, B. A., and ALI-ZADE, S. A., *ibid.*, V 40, p 452 (1961).
43. WEISSENBERG, A. O., and SMIRNITSKY, V. A., *ibid.*, V 39, p 242 (1960).
44. WEISSENBERG, A. O., RABIN, N. V., and SMIRNITSKY, V. A., *ibid.*, V 36, p 1680 (1959).

45. SENS, J. C., SWANSON, R. A., TELEGDI, V. L., and YOVANOVITCH, D. D., *Phys. Rev.*, V 107, p1465 (1957).
46. PREPOST, R., HUGHES, V. W., and ZIOCK, K., *Phys. Rev. Lett.*, V 6, p19 (1961).
47. HUGHES, V. W., McCOLM, D. W., and ZIOCK, K., *ibid.*, V 5, p63 (1960).
48. McCOLM, D. W., HUGHES, V. W., LURIO, A., and PREPOST, R., *Bull. Am. phys. Soc.*, V 4, p82 (1959).
49. BAILEY, J., CLELAND, W., HUGHES, V. W., and ZIOCK, K., *Proc. 1962 Int. Conf. on High-energy Physics, CERN*, p 473; ZIOCK, K., HUGHES, V. W., PREPOST, R., BAILEY, J., and CLELAND, W., *Phys. Rev. Lett.*, V 8, p103 (1962).
50. SHMUSHKEVICH, I. M., *Nucl. Phys.*, V 11, p419 (1959).
51. DZHRBASHYAN, V. A., *Zh. eksp. teor. Fiz.*, V 36, p277 (1959).
52. MANN, R. A., and ROSE, M. E., *Phys. Rev.*, V 121, p293 (1961).
53. ÜBERALL, H., *ibid.*, V 114, p1640 (1959).
54. LUBKIN, E., *Phys. Rev.*, V 119, p315 (1960).
55. BUKHVOSTOV, A. P., and SHMUSHKEVICH, I. M., *Zh. eksp. teor. Fiz.*, V 41, p1898 (1961); GERSHTEIN, S. S., *ibid.*, V 34, p463 (1958).
56. IGNATENKO, A. E., YEGOROV, L. B., KHALUPA, B., and CHULTEM, D., *ibid.*, V 35, p792 (1959).
57. PREPOST, R., HUGHES, V. W., PENMAN, S., McCOLM, D. W., and ZIOCK, K., *Bull. Am. phys. Soc.*, V 5, p75 (1960).
58. ASTBURY, A., HATTERSLEY, P. M., and HUSSAIN, M., et al., *Proc. Phys. Soc.*, V 78, p1145 (1961).
59. YAKOVLEVA, I. V., *Dissertation* (1962).
60. ZICHICHI, A., *Annual Report, CERN*, p59 (1964).
61. BABAEV, A. P., BALATS, M. Ya., MYASISHCHEVA, G. G., OBUKHOV, Yu. V., KOGANOV, V. F., and FIRSOV, V. G., *Zh. eksp. teor. Fiz.*, No. 1, p3 (1966).
62. GUREVICH, I. I., MAKARIYNA, L. A., NUKOL'SKY, B. A., SOKOLOV, B. L., SURKOVA, L. V., KHAKUMOV, S. Kh., SHESTAKOV, V. D., DOBRETSOV, Yu. P., and AKHMANOV, V. V., *Phys. Lett.*, V 11 (2) (1964).
63. NOSOV, V. G., and YAKOVLEVA, N. V., *Zh. eksp. teor. Fiz.*, V 43, p1751 (1962).

CHAPTER 7

1. PUPPI, G., 'Progress in cosmic ray physics', V 3, p336, North-Holland Publishing Company (1958).
2. ROSSI, B., *Rev. Mod. Phys.*, V 20, p537 (1948).
3. GLASER, D. A., HAMERMESH, B., and SAFONOV, G., *Phys. Rev.*, V 80, p625 (1950).
4. ALIKHANYAN, A. I., ALIKHANOV, A. I., and WEISSENBERG, A. O., *Zh. eksp. teor. Fiz.*, V 18, p322 (1948).
5. CARO, D. E., PARRY, J. K., and RATHGEBER, H., *Aust. J. scient. Res.*, V A4, p16 (1950).
6. OWEN, B. G., and WILSON, J. G., *Proc. Phys. Soc.*, V A68, p409 (1955).
7. HYAMS, B. D., MYLROI, M. G., OWEN, B. G., and WILSON, J. G., *ibid.*, V A63, p53 (1950).
8. PINE, J., DAVISSON, R. J., and GREISEN, K., *Nuovo Cim.*, V 14, p1181 (1959).
9. HOLMES, J. E. R., OWEN, B. G., and RODGERS, A. L., *Proc. Phys. Soc.*, V 78, p505 (1961).
10. ASHTON, F., BROOKE, G., GARDENER, M., HAYMAN, P. J., and JONES, D. G., et al., *Nature, Lond.*, V 185, p364 (1960).
11. HOLMES, J. E. R., OWEN, B. G., RODGERS, A. L., and WILSON, J. G., *Proc. Phys. Soc.*, V 78, p496 (1961).

12. ASHTON, F., KISDNASAMY, S., and WOLFENDALE, A. W., *Nuovo Cim.*, V 8, p 615 (1958).
13. ALLEN, J. E., and APOSTOLAKIS, A. J., *Proc. R. Soc.*, V A265 (1320), p 117 (1961).
14. JAKEMAN, D., *Can. J. Phys.*, V 34, p 432 (1956).
15. WILSON, B. G., *ibid.*, V 37, p 19 (1959).
16. ASHTON, F., and WOLFENDALE, A. W., *Int. Conf. Cosmic Rays in Japan (Kyoto)*, 1961 Preprints, nn. 111 - 5 - 3.
17. SHELDON, W. R., and DULLER, N. M., *Nuovo Cim.*, V 23, p 63 (1962).
18. WEISSENBERG, A. O., *Zh. eksp. teor. Fiz.*, V 32, p 417 (1957).
19. FOTINO, M., *Phys. Rev.*, V 117, p 243 (1960).
20. CONVERSI, M., *ibid.*, V 79, p 749 (1950).
21. SUBRAMANIAN, A., NARANAN, S., RAMANAMURTHY, P. V., SAHIAR, A. B., and LAL, S., *Nuovo Cim.*, V 7, p 110 (1958).
22. DEL-ROSARIO, L., and DAVILA-APONTE, J., *Phys. Rev.*, V 88, p 998 (1952).
23. MISHRA (BASU), N., and SINHA, M. S., *Proc. Indian Acad. Sci.*, V 41, p 335 (1959).
24. ALIKHANYAN, A. I., and WEISSENBERG, A. O., *Zh. eksp. teor. Fiz.*, V 32, p 413 (1957).
25. FILOSOFO, I., POHL, E., and POHL-RÜLING, J., *Nuovo Cim.*, V 12, p 809 (1954).
26. MORONEY, J., and PARRY, J., *Aust. J. Phys.*, V 7, p 423 (1954).
27. BRODE, R. B., and WEBER, M. J., *Phys. Rev.*, V 99, p 610 (1955).
28. EHMERT, A., *Z. Phys.*, V 106, p 751 (1937).
29. CLAY, J., *Rev. Mod. Phys.*, V 11, p 128 (1939).
30. WILSON, V. C., *Phys. Rev.*, V 53, p 337 (1938).
31. AVAN, L., and AVAN, M., *C.r.*, V 241, p 1122 (1955).
32. RANDALL, C. A., and HAZEN, W. E., *Phys. Rev.*, V 81, p 144 (1951).
33. BOLLINGER, L. M., *ibid.*, V 79, p 207 (1950).
34. BARTON, J. C., *Phil. Mag.*, V 6, p 1271 (1961).
35. ASHTON, F., *Proc. Phys. Soc.*, V 77, p 587 (1961).
36. GEORGE, E. P., 'Progress in cosmic ray physics', V 1, North-Holland Publishing Company (1954).
37. BARRETT, P. H., BOLLINGER, L. M., COCCONI, G., EISENBERG, Y., and GREISEN, K., *Rev. Mod. Phys.*, V 24, p 133 (1952).
38. GEORGE, E. P., and EVANS, J., *Proc. Phys. Soc.*, V A63, p 1248 (1950); V A64, p 193 (1951); V A68, p 829 (1955).
39. FOWLER, G. N., and WOLFENDALE, A. W., *op. cit.*, Chapter 4.
40. DAYON, M. I., and POTAPOV, L. P., *Zh. eksp. teor. Fiz.*, V 36, p 697 (1959).
41. ASHTON, F., NASH, W. F., and WOLFENDALE, A. W., *Proc. Phys. Soc.*, V A253, p 163 (1959).
42. COUSINS, J. E., and NASH, W. F., *Nuovo Cim.*, V 23 p 307 (1962).

SUBJECT INDEX

- Alpha particle 128, 129
- Alpha particle model 127
- Alvarez 130
- Angular momentum 295
- Asymmetry coefficient 36, 39, 45, 61, 62, 67, 185, 186, 191, 192, 249, 261, 289, 295, 302
- Asymmetry in electron angular distribution 64, 283, 287
- Asymmetry parameter 38, 63, 64, 66
- Auger electrons 200, 220, 222, 224, 225, 227
- Axial vector coupling constant 135, 136, 147, 186

- Bertram 177
- Beta decay 51, 53, 83, 84, 85, 87, 143
 - electrons 148
 - Fermi's theory 23
 - nuclear 28, 50, 52, 53, 72, 135, 136
 - nuclear, Hamiltonian for 135
- Bohr magneton, muonic 12
- Bohr radius 292
- Bohr radius of muon orbit 169
- Bohr theory 200, 201
- Born approximation 12, 238
- Boson, intermediate 108
- Breit-Rabi diagram 294, 302
- Breit relativistic effect 293

- Bremsstrahlung 12, 67, 72, 73, 97, 273, 276, 325
 - interval 98, 103
 - photons 229
- Bubble chamber
 - deuterium 273
 - freon 31, 100, 109
 - helium 57
 - hydrogen 63, 66, 91, 130, 273
 - nitrogen 130

- Cerenkov counter 44, 95, 110, 183, 205, 222, 237, 242
- Charge conjugation 41, 42, 75
- Charge invariance 75
- Chew-Goldberg distribution 132
- Cloud chamber, diffusion 267
- Compton cross section 71, 74
- Compton electrons 183
- Compton electron pairs 175
- Compton scattering 67, 72
- Conversi 117
- Conversion probability 181
- Conversion transitions 181
- Cosmic radiation 1, 234
- Cosmic radiation, primary 308, 320
- Cosmic rays 306, 307
 - flux 323
 - muons 3, 76, 77, 306, 316, 320

- Cosmic rays - *continued*
 pions 280
 Coulomb barrier 122, 128, 268, 271
 Coulomb cross section for muons on nuclei 236
 Coulomb field 117, 171, 172, 199, 221, 256
 of nucleus 200, 269, 290
 Coulomb interaction 292
 Coulomb potential 201
 Coulomb scattering 79, 291
 Coupling
 axial vector 88
 j-j 150
 pseudoscalar 88
 C.P. transformation 262
 C.P.T. invariance 262
 C.P.T. theorem 49
 Creation operator
 electron 47
 neutrino 47
- Decay electrons, angular asymmetry 191, 258
 Decay positrons scattering 289
 Decay probability, three electron 115
 Decay schemes, rare 118
 Delayed coincidence, method 13, 15
 Depolarization interaction 61
 Deuterium nuclei 130
 Deuteron 136
 Dirac equation 199, 200, 245, 247
 for particles of zero rest mass 40
 Dirac particles 13, 36
 Dirac spin matrix 23
 Dirac spinors, four component 47
 Doppler effect 70
 Doppler broadening 86
 Doppler shift 172
 Dunaitsev 95
- Eckstein 101
 Electromagnetic interactions of muons 198
 Electron asymmetry 63, 65
 Electrons, energy spectrum of decay 54, 172
 Electron, helicity of 43, 72
 Electron magnetic moment 246
 Electron neutrino 119
 helicity 69, 70
 Electron-positron pair 103
 production cross section 227
 Elementary particle 1, 272
 Evaporation theory 127
- Fermi and Teller, Z law 227
 Fermi constant 84, 146, 151, 171, 179, 180, 184, 185
 Fermi density effect 325
 Fermi function 144
 Fermi gas model 127, 132, 188, 189
 Fermi interaction 86, 87, 94, 121, 134
 theory 113
 universal 22, 24, 25, 27, 46, 83, 84, 94
 weak, constant 143
 Fermion 23, 24, 25
 Fermions, interaction with magnetic field 23
 Fermi's theory of β -decay 23
 Fermi transition 52, 85, 137
 Feynman diagram 88, 97, 108
 Fialho 106
 Fine structure constant 96, 245
 Form factor
 electron 244
 electron-neutron 233
 electron-nucleus 233
 lepton 244
 nuclear 239
 photon 239
 proton 239
 Fry 106, 132
- Gamma ray
 background 189
 counter 112
 internal conversion 114
 showers 75, 76, 78
 spectrometer 7
 spectrum 175
 Gamma rays 71, 73, 112, 122, 229, 276
 from negative muon capture 133
 Gammow-Teller constant 84, 146, 179, 180, 184, 185
 Gammow-Teller transitions 38, 49, 84, 85, 137, 143, 147
 Geiger counter 309
 telescope 307, 323
 Gell-Mann 136
 Gyromagnetic ratio 246, 256
- Hamiltonian 23, 24, 46, 52, 98, 137, 151, 171, 179, 196, 197
 for beta decay interaction 50, 51, 87
 for four fermion process 134
 for nuclear beta decay 135
 Hildebrand 139
 Hoffstadter 146
 Hyperfine structure states 295

- Interaction
 - axial vector 49, 50, 51, 53, 69, 85, 107, 135
 - axial vector, constant 151
 - constant, pseudoscalar 136
 - cross section 30
 - electromagnetic 12, 53, 198, 200, 213, 233, 234, 245
 - electromagnetic, constant 109
 - four fermion 96, 107, 135, 185
 - Hamiltonian 50, 51, 96, 147, 186
 - momentum 117
 - muon 327
 - nuclear 325, 326
 - of negative muons with nuclei 14
 - pseudoscalar 150
 - short range 199
 - strong 24, 87, 94, 136, 186
 - vector 50, 51, 53, 69, 85, 107, 135
 - V-A 138, 150, 172, 180, 186, 194, 283
 - V-A, Hamiltonian for 167
 - weak 3, 17, 25, 27, 33, 49, 94, 98, 107, 118, 120, 170, 197, 309
 - weak, constant 27, 109, 138, 168, 194
 - weak, non-conservation of parity in 33, 38
 - weak, theory 53, 69, 107, 283
 - weak, universal nature of 88
- Ioffe 106
- Isotopic effect 209
 - in nuclear negative muon capture 177

- K-electron capture 25, 70
- K-shell 221, 222, 303, 304
 - mesonic 153
- Kaon 33, 308
 - decay 3, 29, 34, 309
 - mass 107
- Kinematic analysis 11
- Kinematic depolarisation 61, 62, 63, 283, 287, 303
 - of cosmic rays 286
 - of muons 283, 284, 285
 - of neutrons 187, 191
- Kinematic parameter 69
- Kinematic transformation 284

- Lamb shift 216
- Larmor frequency 291
- Lee 107
- Leptons 25, 27, 83, 96
 - conservation 44, 83
 - law of conservation 46
- Lorentz transformation 62

- Macq 73
- Magnetic moment 12
 - anomalous 136
- Meson
 - heavy 2
 - spin precession frequency 3
- Mesonic atom 17, 20, 130, 140, 141, 142, 152, 153, 181, 206, 211, 222, 224, 255, 265, 268, 269, 282
 - helium 146
 - hydrogen 179
 - spectroscopy 206
 - transition 210
 - transition energy 213
 - triplet and singlet states 179, 186
- Mesonic Bohr radius 202
- Mesonic molecule 21, 140, 141, 268, 269
 - Mesonic molecule
 - ortho- 141, 142
 - para- 141, 142
- Mesotron 1
- Michel parameter 48, 55, 56, 57, 60, 64, 66, 93, 107, 108, 176
 - measurement 53
- Molière distribution 239
- Momentum,
 - angular 12
 - conservation 10
- Monte Carlo method 91
- Moroz 81
- Mott formula 242
- Mott scattering 79, 81, 246
 - cross section 80, 257
- Multiple scattering, method of 11
- Muon
 - decay probability 152, 172, 178, 274
 - decay scheme 8
 - discovery 1
 - energy spectrum 310, 314
 - interactions 327
 - neutrino 27, 119
 - orbit, Bohr radius of 169
 - pair production 198
 - pair production cross section 232
 - spin precession frequency 45, 249
 - velocity 284
 - wave function 135, 202
- Muonic atom 198, 199, 205, 298, 307
 - energy levels 200, 201
 - Bohr magnetron 12
- Muonium 62, 293, 297, 299
 - Bohr orbit 293
 - triplet state 298, 302
- Muons
 - capture probabilities in heavy and light isotopes 178

Muons - *continued*

- cosmic ray 3
- cosmic ray, slow 226
- decay 25, 50, 91, 100, 314
- depolarisation 290
- dipole moment 262
- energy 106, 172, 284
- free, decay probability 20, 47
- free, lifetime 52
- gyromagnetic ratio 35
- helicity 43, 75, 79
- lifetime 13, 15, 48, 152
- longitudinal polarisation 61, 73
- magnetic moment 199, 215, 245, 247, 250
- mass 4, 7, 215, 219, 255, 256
- mean momentum 6
- momentum 6, 106, 142, 316
- monochromatic 3, 6, 103
- rare decay modes 107
- reduced mass 200
- slow 323
- slow, interaction of, with nuclei 14
- spin 12, 61, 63, 185, 195, 260
- weak interaction current of 108, 145
- Muons, negative 19, 230
 - absorption probability 16
 - binding energy 171
 - capture by C^{12} nuclei 147
 - capture by F_9^{19} 184
 - capture by He^3 nuclei 20
 - capture by impurity nuclei in hydrogen 280
 - capture by light nuclei 226, 227
 - capture by Ne nuclei 130
 - capture by protons 18, 20, 25, 179, 185
 - capture by spinless nuclei 194
 - capture 151, 175, 180, 182
 - capture probability in C 166
 - capture probability in H 166
 - capture probability in tritium 166
 - capture probability 133, 140, 146, 153, 159, 168, 169, 181, 186
 - capture time 152
 - cosmic ray 204
 - decay probability in bound state 171, 174
 - decay probability 133, 159, 182, 270
 - depolarisation 302
 - helicity of 195
 - interactions with nuclei 14
 - lifetime 153, 166
 - magnetic moment 255, 256
 - mass 6
 - momentum 232
 - positive helicity 82
 - slow cosmic ray 148
- Muons, positive 63
 - cyclotron frequency 261
 - decay probability 16, 133
 - depolarisation 61, 62, 295
 - dipole moment 263
 - lifetime 52
 - magnetic moment 255, 256
 - mass 6
 - momentum 232
 - polarisation 295
 - polarisation effect of magnetic field 293
 - polariser of 38
 - spin 300
- Neutrino 3, 8, 10, 17, 25, 27, 40, 60, 108, 308
 - anti- 8, 26, 27, 40, 60, 185
 - energy spectrum 29
 - helicity 40
 - interaction 32
 - law of conservation 69
 - lifetime 86
 - momentum 18, 43, 195, 196
 - theory, single 118
 - theory, two component 40, 54, 60, 64, 65, 66, 67, 71, 73, 96, 99, 185
 - wave function 50
- Neutron 17
 - asymmetry 189, 190, 194
 - mass 18
 - mass reduced 127
- Nuclear charge 203, 220
- Nuclear disintegrations 326
- Nuclear excitation 175
 - function 132
- Nuclear form factor 227
- Nuclear magneton 255
- Nuclear photo effect 326
- Nuclear radius 199, 202
- Nuclear time 16
- Nucleon mass, reduced 127
- Nucleus
 - Coulomb field 116
 - effective charge 168
 - light 196
 - relaxation 197
- Orbital angular momentum 224
- Orbital electron capture 17, 22
- Parity
 - non-conservation 13, 25, 33, 34, 35, 38, 43, 46, 48, 49, 76, 88, 172, 190, 194, 195, 197, 302

- Parity - *continued*
 non-conservation in nuclear negative muon capture 185
 spatial, conservation 190
- Paschen-Back effect 63
- Pauli's principle 55, 168
- Pauli spin matrix 40
- Periodic table 17
- Perturbation theory, first order 96, 97, 202
- Phase space 168
- Photon 10, 205
 spectrum 98
 internal conversion 104
- Pion 3
 decay 28, 65, 87, 91, 94, 103, 309
 mass 3, 4, 7, 215
 negative 230
 negative, lifetime 153
 negative, mass 7
 positive, photo pair, production 23
 primary 1
 slow decay 323
 spinless decay 43
- Pionic atom 224
- Positron 1, 57
 decay spectrum 55, 91
 telescope 34
- Potential, vector and scalar 23
- Pratt 101
- Primakoff 137, 138, 139, 141
- Primakoff's formula 167, 170, 178
- Proton-Antinucleon pair 106
- Proton
 knock-on 183
 magnetic moment 246
 spin 141
- Pseudoscalar constant 196, 197
- Pseudoscalar coupling 197
- Puppi triangle 24
- Quadrupole effect, static 209
- Quantum electrodynamics 23, 199, 261, 262
- Quantum number, principal 221, 224
- Radiative corrections 96, 255
- Radiative decay 109, 115
 probability 98, 99, 106, 197
 process 101
- Rose-Gorter method 38
- Rudik 106
- Scattering
 electron-position pairs 101
- Scattering - *continued*
 multiple 11
 of muons by nuclei 233
 positron-electron 11
 resonance 71
- Schiff 130, 132
- Shell model 150, 180, 187, 188
- Sosnovskii 86
- Space reflection 41, 42
- Spark chamber 29, 55, 111, 116, 117
- Spinless nuclei 188
- Spin-orbit interaction 80
- Sum rule 180
- Telegdi 171
- Time dilation 172, 316
- Time reversal 49
- Tiomno 106
- Transition
 amplitude 23
 Auger, probability 220, 221
 cascade 199, 304
 non-radiative 227
 nuclear 145
 probability 144, 149, 151
 radiative 220, 222, 224, 227
- Überall 176, 180, 192
- Universal Fermi interaction 22, 24, 25, 27, 46, 83, 94
- V-A theory 51
- V-A interaction constants 99, 186
- Vector boson
 charged 107
 intermediate 113, 118
- Vector coupling constant 136, 186
- Weak magnetism 138, 150, 194
 constant of 136
- Weizsäcker-Williams theory 326
- Wilson cloud chamber 1, 2, 8, 55, 123, 133, 204, 309
- X-ray absorption coefficient 213
- X-ray, mesonic 7, 215
- Yang 107
- Yukawa meson 16
- Zeeman transition 299

